INFORMATION TO USERS

This manuscript has been reproduced from the microfilm master. UMI films the text directly from the original or copy submitted. Thus, some thesis and dissertation copies are in typewriter face, while others may be from any type of computer printer.

The quality of this reproduction is dependent upon the quality of the copy submitted. Broken or indistinct print, colored or poor quality illustrations and photographs, print bleedthrough, substandard margins, and improper alignment can adversely affect reproduction.

In the unlikely event that the author did not send UMI a complete manuscript and there are missing pages, these will be noted. Also, if unauthorized copyright material had to be removed, a note will indicate the deletion.

Oversize materials (e.g., maps, drawings, charts) are reproduced by sectioning the original, beginning at the upper left-hand corner and continuing from left to right in equal sections with small overlaps.

ProQuest Information and Learning
300 North Zeeb Road, Ann Arbor, MI 48106-1346 USA
800-521-0600

UNIVERSITY OF OKLAHOMA

GRADUATE COLLEGE

KINEMATIC, DYNAMIC, AND THERMODYNAMIC IMPACTS OF HOOK-ECHO HYDROMETEORS, INCLUDING EXPLORATIONS INTO THE UTILIZATION OF POLARIMETRIC RADAR DATA

A Dissertation

SUBMITTED TO THE GRADUATE FACULTY

In partial fulfillment of the requirements for the

degree of

Doctor of Philosophy

By

MARK ANTHONY ASKELSON
Norman, Oklahoma
2002

UMI Number: 3070631

UMI Microform 3070631

ProQuest Information and Learning Company
300 North Zeeb Road
P.O. Box 1346
Ann Arbor, MI 48106-1346

KINEMATIC, DYNAMIC, AND THERMODYNAMIC INFLUENCES OF HOOK-ECHO HYDROMETEORS, INCLUDING EXPLORATIONS INTO THE UTILIZATION OF POLARIMETRIC RADAR DATA

A Dissertation APPROVED FOR THE
SCHOOL OF METEOROLOGY

BY

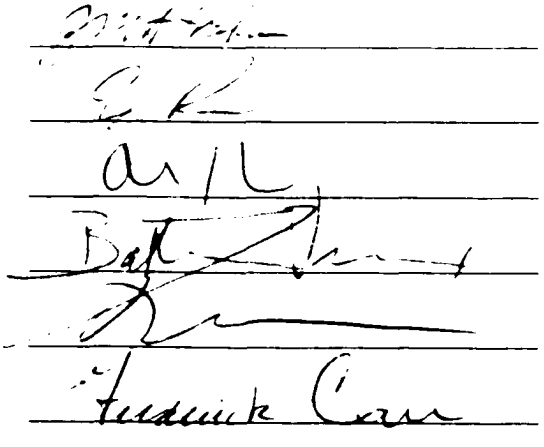

Acknowledgements

I am grateful to numerous individuals who have put forth great effort to help me complete this work. Foremost are my principal advisors, Drs. Jerry Straka and Dušan Zrnić. The amount of support an effort like this requires is staggering. I am forever in their debt.

I would also like to thank the rest of my committee, Drs. Frederick Carr, Alan Shapiro, Erik Rasmussen, and Baxter Vieux, for their efforts. They have not only skillfully advised this work, but have also helped identify important new research avenues.

Through discussion and encouragement, Dr. Charles Doswell III functionally served as a committee member. This work has benefited greatly from his involvement.

I am indebted to Dr. Paul Markowski, who provided important VORTEX data, and to Dr. Patricia Pauley who provided some of the data plotted in Fig. 2.10 and who has helped immensely in the development of the response function work.

This would be horribly lacking if I did not acknowledge the staff at the University of Oklahoma School of Meteorology. Celia Jones, Marcia Pallutto, Andrea Wilson, and Nancy Agrawal have answered countless questions and have gone out of their way to help me finish this Ph.D. remotely.

A Ph.D. education requires a tremendous effort from numerous individuals at numerous organizations. I would like to thank the teachers at the University of Oklahoma, the University of North Dakota, and the Detroit Lakes, MN, public schools

who have worked so hard to provide a quality education. It is my experience that teachers are oftentimes deserving of praise but tend receive very little of it.

Finally, I am grateful to my family and friends. They have provided both support and, at times, much needed diversions. I would especially like to thank my parents, who have waited quite patiently for my completion of the Ph.D., and my wife Amy, who has not only taken on extra duties so that I could finish but has also helped with the processing of some of the soundings used in this research. I can neither express how important her help and support have been nor sufficiently thank her.

Table of Contents

List of Tables

List of Illustrations

Abstract

Given their infrequent occurrence, supercell thunderstorms produce an inordinate amount of death and damage. As a result, they have been studied intensely for the past forty years. Even so, numerous important questions concerning supercells remain. One such question regards tornadoes and observations of supercells that appear to be similar but exhibit very different tornadic behavior. Recently, analyses of data from the VORTEX project revealed that the thermodynamic properties of the rear flank downdraft (RFD) may dictate whether or not a supercell becomes tornadic. Since hydrometeors are thought to be an important driving force for the RFD, it is postulated that they may be important to its thermodynamic properties and, possibly, to tornadogenesis.

The role hook-echo hydrometeors play in driving RFDs is investigated by estimating hook-echo hydrometeor types and amounts from polarimetric radar data and by using that information to drive a relatively simple downdraft model. Soundings for the individual cases are used to initialize the downdraft model in order to replicate the environments of the storms as closely as possible.

Since this effort and others like it require the quantitative utilization of radar data, issues pertaining to this are explored. One common research need is the estimation of radar data on a rectangular Cartesian grid. An exploration of the coordinate transformation equations reveals that the equivalent earth model, which is commonly used to compute the heights of radar data, is not needed. The heights of radar data can be easily computed using commonly applied assumptions without resorting to the equivalent earth model.

Moreover, properties of a new method for estimating radar data on rectangular Cartesian grid are explored. This method, the adaptive Barnes (A-B) scheme, adapts to the

following characteristics of radar data: 1) the spacing of radar data depends on direction and 2) radar data density systematically decreases with range. It is found that the A-B scheme not only adapts to these characteristics and thus affords the opportunity to retain more information when analyzing radar data, but also avoids phase shifts of input waves and offers advantages for the post-analysis computation of derivatives. As is the case with any objective analysis technique, the A-B scheme should be used with care in order to avoid misinterpretations of analysis results.

The study of the A-B scheme led to the difficult problem of response functions for arbitrary weight functions and data distributions. A novel approach to this problem was devised, with the principal result being that the local response function for distance dependent weighted averaging schemes is the complex conjugate of the normalized Fourier transform of the effective weight function. This result provides a framework for efforts like evaluating observation network efficacy and applying the response function to filter design for irregularly spaced observations.

The simulations of hydrometeor driven RFDs show that hydrometeor fields inferred from radar data are able to drive significant downdrafts without the influence of vertical perturbation pressure gradients. Moreover, they reveal that above the boundary layer supercell environments are relatively resistant to downdrafts whereas within the boundary layer they are generally supportive of downdrafts. It appears that in many supercell environments relatively large hail (≥1 cm in diameter) or vertical perturbation pressure gradients may be needed to drive deep midlevel downdrafts that penetrate into the boundary layer. Because the boundary layer is an important downdraft generation/intensification layer, its θ_e profile appears to be important to the surface RFD θ_e deficit and, consequently, to tornadogenesis. To further examine these issues, analyses using idealized soundings that represent multiple possible RFD environments and analyses of the complete set of VORTEX cases are planned.

Chapter 1: Introduction

Considering their infrequent occurrence, supercells[1,2] cause an inordinate amount of death and damage (Moller et al. 1994). Often, supercells cause these through severe winds (tornadic or otherwise) and hail. Destructive supercell winds tend to produce both loss of life and property, while destructive supercell hailfalls typically result only in loss of property [hailfalls have, nevertheless, caused deaths (e.g., Flora 1956, 6-9)]. Supercell flooding may also cause loss of life and property. Herein the focus will be on severe winds produced by supercells.

Past supercell events underscore their destructive potential. Two of the more deadly tornado outbreaks of the past 40 years, the Palm Sunday outbreak of 11-12 April 1965 and the Superoutbreak of 3-4 April 1974, both of which consisted of numerous supercells, resulted in 256 and 315 (tornado-related) deaths, respectively (Grazulis 1993). Destructive supercell winds also cause a great deal of property damage. Grazulis (2001, p. 206) lists 16 U.S. tornadoes that occurred in the past 104 years that caused ≥ $200 million in damage each (values inflation adjusted to 1999). The most damaging in this list, the 3 May 1999 tornado that affected the Oklahoma City, Oklahoma, area, caused $1.2 billion in damage. These numbers are impressive

---

[1] Herein, a supercell is defined as a convective storm that has certain distinguishing characteristics. The most prominent characteristic, a deep (significant fraction of storm depth), persistent (relative to the convective time scale defined by the residence time of an updraft parcel) mesocyclone, has been used in most recent definitions of supercells (e.g., Doswell and Burgess 1993). Other characteristics, which in this work are not rigorously enforced, include the requirements that mesocyclones have vertical vorticity of at least 10^{-2} s^{-1} and that the updraft and mesocyclone (vertical vorticity) are positively correlated (e.g., Davies-Jones and Brooks 1993; Moller et al. 1994).

[2] It is of historical interest to note that the original use of the term 'supercell' by Browning (1962) also indicated the persistence of storm characteristics. Originally, however, the persistent features were the radar echo pattern and the airflow pattern, which was inferred partially from the radar echo pattern (Browning and Ludlam 1962).

considering that they concern only individual tornadoes and do not include losses from other damaging tornadoes that occurred in the same outbreaks. Moreover, they only concern supercell tornadoes and do not consider supercell straight-line wind events, the damage from which is much tougher to quantify.[3]

Owing in part to the loss of life and property associated with them, supercells have been studied intensely for approximately the past 40 years [cf. Rotunno (1993) for a concise account of the history of supercell studies]. Even so, many scientific questions concerning supercells remain. Examples include: 1) what are the hydrometeor structures (types and amounts) of hook echoes?, and 2) do hook-echo hydrometeors play a significant role in driving rear flank downdrafts in supercells? Both of these questions relate to severe supercell winds, with the latter having particular relevance to tornadogenesis.

It is believed that, owing to recent developments in polarimetric weather radar technologies and applications (e.g., Doviak and Zrnić 1993; Straka et al. 2000), significant progress towards answering these questions can be made at this time. Straka et al. (2000) have provided a thorough review of the utilization of polarimetric radar (PR) data for classification and quantification of bulk hydrometeor fields. While difficulties and ambiguities certainly exist, the use of PR data in combination with physical insight (gained from previous observational and theoretical studies, cf. appendix C) provides a valuable method for inferring bulk hydrometeor field characteristics. Examples of successful applications of this technique (deemed so

[3] This statement is based upon the fact that to quantify this type of damage one needs to first verify that a supercell caused it. Since straight-line wind damage can result from various forms of convection,

through *in situ* verification) include the studies of Bringi et al. (1986a,b), Balakrishnan and Zrnić (1990b), and Ramachandran et al. (1996). As indicated by Straka et al. (2000), a fair amount of confidence may be placed in PR-based hydrometeor identifications while PR-based estimations of hydrometeor amounts are not as certain. (For more information concerning the classification and quantification of bulk hydrometeor fields using PR data, see appendices C and D).

The purpose of this study is to investigate hydrometeor distributions in hook echoes of supercells and kinematic, dynamic, and thermodynamics consequences thereof. Because these efforts require the quantitative utilization of radar data, aspects of this are intensively studied in chapter 2. The interaction of hydrometeors with rear flank downdrafts is then examined in chapter 3, with a summary concluding this work in chapter 4.

---

including squall lines, and since supercells are not always easy to identify (Moller et al. 1990; Doswell and Burgess 1993), this is not a simple task.

Chapter 2: Quantitative Utilization of Radar Data

2.1 Coordinate Transformation Equations for Weather Radars

2.1.1 Height and Great Circle Distance

The quantitative utilization of radar data often requires knowledge of the locations of radar data within the atmosphere. In this section the purpose is to determine the above ground level height z and great circle distance s (cf. Fig. 2.1) of a radar datum for radars for which the elevation $\theta = 0^\circ$ is in a direction that is perpendicular to the line emanating from the center of the earth through the radar. This problem has been considered in detail by previous investigators (e.g., Doviak and Zrnić 1993, 14-28). A common approach to determining z and s is the use of the equivalent earth model, which is comprised of two components (Shelleng et al. 1933; Bean and Dutton 1966, 56-59; Doviak and Zrnić 1993, 18-21). The first is the assumption that radar rays follow paths of constant curvature. This occurs under the following conditions (Doviak and Zrnić 1993, 18-21): 1) temperature and humidity are horizontally homogeneous (i.e., the atmosphere is spherically stratified), 2) refractive index n is smoothly changing [i.e., within a wavelength the relative changes in refractivity N, where $N = (n-1)\times 10^6$, are small], 3) $z << a$, where a is the radius of the earth, and 4) n is linearly dependent upon height. The second component is the transformation from the actual spatial configuration to one in which the ray path is straight, implying a "bending" of both the ray path and of the earth's surface (cf. Fig. 2.1). In this spatial transformation the radius of a fictitious "equivalent" earth is

determined so that z and s are essentially unchanged. With this model, Doviak and Zrnić obtain the relations

$$z = \left[r^2 + (k_e a + h_a)^2 + 2r(k_e a + h_a)\sin\theta\right]^{1/2} - (k_e a) \tag{2.1}$$

and

$$s = (k_e a)\sin^{-1}\left[\frac{r\cos\theta}{(k_e a) + z}\right], \tag{2.2}$$

where r is range, k_e is the constant in the equivalent earth model (usually it is assumed that $k_e = 4/3$), and the situation where the (above ground level) antenna height h_a is nonzero has been incorporated.

A fundamental assumption in the equivalent earth model is that radar rays follow paths of constant curvature. It will be shown herein that with this assumption the height and great circle distance of a datum can be determined directly, without drawing upon the equivalent-earth-model spatial transformation.

The problem is shown in Fig. 2.1. The assumption that radar rays follow paths of constant curvature implies that the curved ray path from R to D (from the radar location to the datum location) is an arc of a circle of radius r_c. Doviak and Zrnić obtain the approximate relation for this radius $r_c \approx 1/(-dn\ dz)$. (The assumption that radar rays follow paths of constant curvature, therefore, is consistent with the assumption that the refractive index is linearly dependent upon height.) Doviak and Zrnić (1993, p. 21) indicate that a typical value of $dn\ dz$ is $-1/4a$, so that $r_c \approx 4a$.

Armed with knowledge of r_c, relations for z and s in terms of radar-measurable parameters can be determined. The strategy for determining z is to apply the law of

cosines to the triangle ORD. To execute this strategy, however, one needs both γ and r'. The value of r' can be obtained by noting, from the circle sector $O'RD$, that $\beta = r/2r_e$. With this,

$$r' = 2r_e \sin(r/2r_e). \tag{2.3}$$

The value of γ can be determined by noting that the angle between OR and RI is $\pi/2 + \theta$ and thus that $\gamma = \pi/2 + \theta - \delta$. From the triangle with vertices at O', R, and the mid-point of the line RD and the fact that $O'R$ and RI are perpendicular, $\delta = \beta = r/2r_e$. Thus, $\gamma = \pi/2 + \theta - r/2r_e$ and application of the law of cosines to the triangle ORD results in

$$z = \left[r'^2 + (a + h_a)^2 + 2r'(a + h_a)\sin(\theta - r/2r_e)\right]^{1/2} - a, \tag{2.4a}$$

with r' given by (2.3).

Equation (2.4a) can be simplified by noting that because $r/2r_e = r/8a$ is very small for typical weather radar applications ($r < \sim 500$ km), $\sin(r/2r_e) \approx r/2r_e$ and $r' \approx r$. With this simplification, (2.4a) is

$$z \approx \left[r^2 + (a + h_a)^2 + 2r(a + h_a)\sin(\theta - r/2r_e)\right]^{1/2} - a. \tag{2.4b}$$

By expanding $\sin(\theta - r/2r_e) = \sin\theta\cos(r/2r_e) - \cos\theta\sin(r/2r_e)$ and by making the approximations $\cos(r/2r_e) \approx 1$ and $\sin(r/2r_e) \approx r/2r_e$, (2.4b) becomes

$$z \approx \left[r^2 + (a + h_a)^2 + 2r(a + h_a)\left(\sin\theta - \frac{r}{2r_e}\cos\theta\right)\right]^{1/2} - a. \tag{2.4c}$$

Height values with $h_a = 0$ km, $a = 6370$ km, $r_e = 4a$, and $k_e = 4/3$ (consistent with the assumption $r_e = 4a$) have been computed using (2.1) and (2.4a-c).

Comparisons for an altitude of approximately 20 km [not less than 20 km according to (2.4a)] and for different elevations are provided in Fig. 2.2. The altitude of 20 km was chosen since this is approximately the highest altitude of interest in weather-radar applications and since differences (at a fixed elevation) between the various height formulations increase with increasing altitude (range). As shown in Fig. 2.2, the differences between (2.1) and (2.4a) range from +8.8 m at 0.0° elevation to +0.004 m at 90.0° elevation. Differences between (2.4b) and (2.4a) range from +1.03 m at 0.0° elevation to +0.001 m at 90.0° elevation; differences between (2.4c) and (2.4a) range from +0.88 m at 0.0° elevation to +0.004 m at 90.0° elevation. The new height formulation (2.4a), therefore, agrees very closely with the standard formulation (2.1) and (2.4b) and (2.4c) are very good approximations to (2.4a).

The value of k_e used in the above calculations was varied in order to determine if the standard (2.1) and new (2.4a) formulations could be brought into perfect agreement. The attempt was unsuccessful. These two formulations are very nearly, but not exactly, equivalent.

Removal of the $r/2r_e$ term from (2.4b) or the $r/2r_e \cos\theta$ term from (2.4c) results in the relation one would obtain if it were assumed that the ray-path is straight (and thus that the atmosphere is non-refractive). The r' and $r/2r_e$ terms in (2.4a) and the $r/2r_e$ terms in (2.4b,c), therefore, incorporate height corrections owing to atmospheric refractivity.

At the beginning of this investigation four conditions were established in order to facilitate height determination. The first of these conditions results in no refraction

of radar rays when $\theta = \pm 90.0^\circ$. When $\theta = \pm 90.0^\circ$, then, the geometry pictured in Fig. 2.1 breaks down and the radar ray does not travel in a path of constant curvature, it travels in a straight line. In that situation, when $\theta = +90.0^\circ$, $z = h_a + r$, and when $\theta = -90.0^\circ$, $z = h_a - r$. Equations (2.1) and (2.4c) produce these results while (2.4a,b) do not. Thus, (2.4c) may be preferable to (2.4a,b) because it produces the correct results when $\theta = \pm 90.0^\circ$.

A relation for s can be obtained by applying the law of sines to the RD and OD sides of triangle ORD. The result is

$$s = a \sin^{-1}\left[\frac{r' \cos(\theta - r\ 2r_e)}{a + z}\right]. \tag{2.5a}$$

With the approximation $r' \approx r$, this becomes

$$s \approx a \sin^{-1}\left[\frac{r \cos(\theta - r\ 2r_e)}{a + z}\right]. \tag{2.5b}$$

Another relation for s results from an application of the law of cosines to the triangle ORD, with the result

$$s = a \cos^{-1}\left[\frac{(a + h_a)^2 + (a + z)^2 - r'^2}{2(a + h_a)(a + z)}\right]. \tag{2.5c}$$

The approximation $r' \approx r$ applied to (2.5c) produces

$$s \approx a \cos^{-1}\left[\frac{(a + h_a)^2 + (a + z)^2 - r^2}{2(a + h_a)(a + z)}\right]. \tag{2.5d}$$

Values of s have been computed using (2.2) [with z computed using (2.1)], (2.5a) [with z computed using (2.4a)], (2.5b) [with z computed using (2.4b)], and (2.5d) [with z computed using (2.4c)]. [Note that (2.5a,c) are exact solutions and produce

equivalent results for elevations from $-\pi/2 + r/2r_e$ to $\pi/2 + r/2r_e$. Equations (2.5a,c) do not agree for elevations greater than $\pi/2 + r/2r_e$ and less than $-\pi/2 + r/2r_e$ because the cos() function in the numerator of (2.5a,b) becomes negative in these regions. This results in s values computed using (2.5a,b) being negative for elevations greater than $\pi/2 + r/2r_e$ and less than $-\pi/2 + r/2r_e$.] The h_a, a, r_e, and k_r values that were used are the same as those used in the height tests. Differences between (2.2), (2.5b,d) and (2.5a,c) are plotted in Fig. 2.3 as a function of elevation for an altitude of ~20 km [not less than 20 km according to (2.4a)]. As with the height formulations, differences, at a fixed elevation, between the great circle distance formulations increase with increasing altitude (range). In contrast with the respective height formulations, the standard (2.2) and new (2.5a,c) formulations differ by what may be considered to be a significant amount for some elevations. As shown in Fig. 2.3, at an altitude of ~20 km the difference between (2.2) and (2.5a,c) ranges from +152.7 m at 0.0° elevation to -12.22 m at 90.0° elevation. For elevations greater than about 8.5° (and an altitude of ~20 km), the magnitude of the difference between (2.2) and (2.5a,c) is less than about 50 m. Differences between (2.5b,d) and (2.5a,c), on the other hand, are much smaller. As shown in Fig. 2.3, differences between (2.5b) and (2.5a,c) range from +12.77 m at 0.0° elevation to $+4.88\times10^{-7}$ m at 90.0° elevation. The corresponding differences between (2.5d) and (2.5a,c) are +12.78 m and -12.22 m. The new great circle distance formulation (2.5a,c), therefore, contains some significant differences relative to the standard formulation (2.2). These differences are reflected in the approximations (2.5b,d) since they are close approximations to (2.5a,c).

As with the height formulations, the r' and $r/2r_e$ terms in (2.5a), the $r/2r_e$ term in (2.5b), and the r' term in (2.5c) incorporate corrections owing to atmospheric refractivity. The approximation (2.5d) does not contain any refraction-correction terms. While this approximation performs well without any of these correction terms, ignoring these terms in (2.5a) [i.e., approximating $r'\cos(\theta - r/2r_e)$ as $r\cos\theta$] does not result in as accurate of an approximation. Differences between (2.5a) [with z from (2.4a)] and (2.5a) with refraction-correction terms ignored [with z from (2.4a)], for an altitude of ~20 km, range from +51.45 m at 0.0° elevation to –81.5 m at 2.5° elevation to –10.01 m at 55.0° elevation to –12.22 m at 90.0° elevation.

The no-refraction condition when $\theta = \pm 90.0°$ requires that s is zero. Equations (2.2) and (2.5d) [when z is calculated using (2.4c)] satisfy this requirement while (2.5a-c) do not. The coordinate-transformation equations (2.4c) and (2.5d), therefore, are arguably the most useful because of their satisfaction of the no-refraction condition when $\theta = \pm 90.0°$ and because of their close adherence to the exact constant-curvature solutions.

It is noted that s can be determined directly from radar-measurable parameters without computing z. From the law of sines applied to the sides *OR* and *RD* of triangle *ORD* [the angle at *D* is $\pi/2 - (s/a + \theta - r/2r_e)$],

$$s = a\tan^{-1}\left[\frac{r'\cos(\theta - r/2r_e)}{a + h_a + r'\sin(\theta - r/2r_e)}\right]. \qquad (2.6a)$$

By expanding $\cos(\theta - r/2r_e) = \cos\theta\cos(r/2r_e) + \sin\theta\sin(r/2r_e) \approx \cos\theta + (r/2r_e)\sin\theta$, ignoring $(r/2r_e)\sin\theta$ relative to $\cos\theta$, and applying the approximation $r' \approx r$, (2.6a) becomes

$$s \approx a\tan^{-1}\left[\frac{r\cos\theta}{a + h_a + r\sin(\theta - r\ 2r_e)}\right]. \tag{2.6b}$$

While (2.6b) satisfies the no-refraction condition when $\theta = \pm 90.0°$, it is not a very good approximation to (2.5a,c) and (2.6a), with difference values for an altitude of ~20 km that are very close to those that result from approximating the $r'\cos(\theta - r/2r_e)$ in (2.5a) as $r\cos\theta$. Ignoring the $r/2r_e$ term in (2.6b) results in a much worse approximation to (2.5a,c) and (2.6a) at low elevations.

Shelleng et al. (1933), who apparently advanced the use of the equivalent earth model (Bean and Dutton 1966, p. 56), indicate that the spatial transformation utilized in the equivalent earth model results in negligibly small errors. The agreement between (2.1) and (2.4a-c) and (2.2) and (2.5a-d) further confirms their conclusion. Moreover, the agreement between (2.1) and (2.4a-c) and (2.2) and (2.5a-d) validates the relations obtained herein since the equivalent earth model relations perform well under standard refractive conditions (Doviak and Zrnić 1993, p. 23). It may be argued, however, that (2.4a-c), (2.5a-d), and (2.6a-b) are preferable to (2.1) and (2.2) since they do not require the slightly imperfect spatial transformation utilized in the equivalent earth model and since they are less complicated conceptually.

It is of interest to compare results obtained using (2.4c) to those obtained using

$$z = h_a + r\sin\theta \tag{2.7}$$

and

$$z = h_a + r\sin\theta + \frac{r^2\cos^2\theta}{2(k_e a)}. \qquad (2.8)$$

Equation (2.7) results from assuming that the earth is flat and that the atmosphere is homogeneous (non-refractive), while (2.8) is a slight modification (h_a has been incorporated) of an approximation obtained by Bent et al. (1950). [To obtain (2.8), Bent et al. (1950) utilized the equivalent earth model and made several simplifying assumptions.] Differences between (2.4c) and (2.7) are shown in Fig. 2.4a. Except for low ($< 15^\circ$) elevations and moderate to large (> 60 km) ranges, these differences are relatively small. At $\theta = 0^\circ$, the no-refraction, flat-earth model (2.7) provides unsavory results since it indicates that data at this elevation are located at ground level. With the assumed standard refractive conditions, however, the curvature of the earth's surface results in data with $\theta = 0^\circ$ being located above ground level. On the contrary, (2.8) correctly indicates that data collected at $\theta = 0^\circ$ are located above the earth's surface. In fact, (2.8) provides a very good approximation to (2.4c) (Fig. 2.4b). Figure 2.4b, in addition to illustrating the adequacy of (2.8), seems to provide a clue concerning the origin of the slight differences between (2.8) and (2.4c). Because the differences at $z = 20$ km between (2.1) and (2.4c) (Fig. 2.2) and (2.8) and (2.4c) (Fig. 2.4b) are so similar, it appears as if the $z \le 20$ km differences in Fig. 2.4b result primarily from the use, in (2.8), of the equivalent earth model spatial transformation [and not from the other approximations applied to obtain (2.8)]. In any case, it is apparent that for tropospheric data ($z \le 20$ km), (2.8) is an accurate approximation of (2.4c) [and (2.1)],

whereas (2.7) provides less palatable results, especially at low elevations and moderate to large ranges.

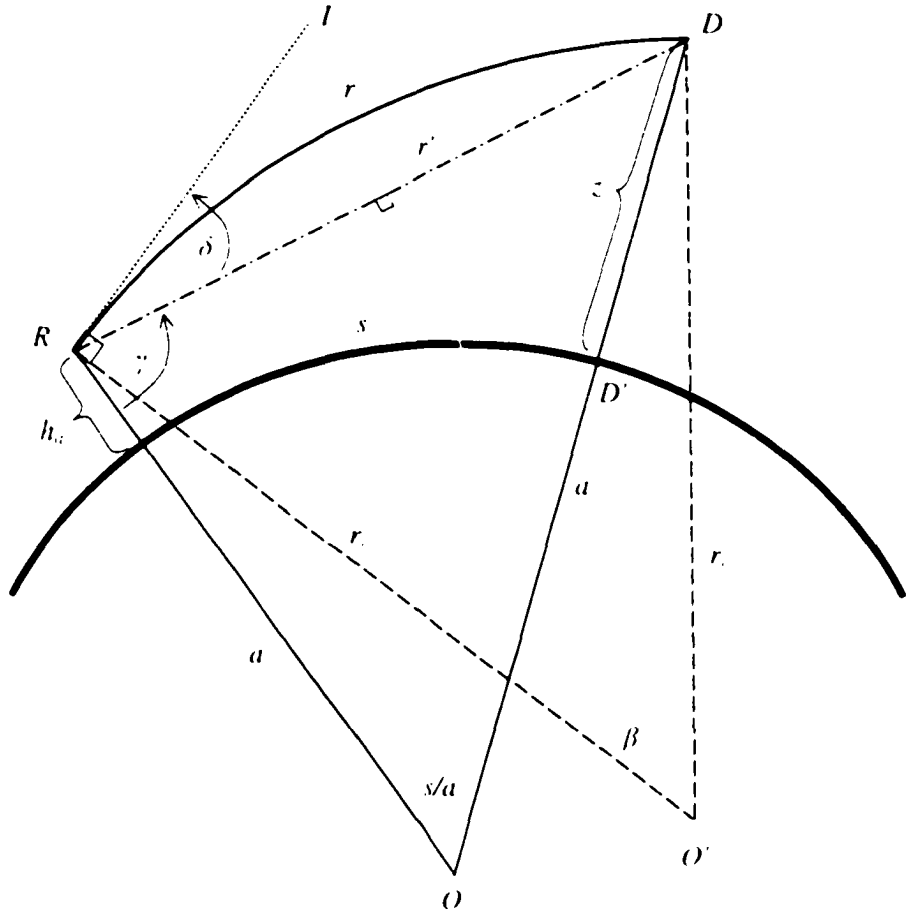

FIG. 2.1. Illustration of the height z and great-circle distance s determination problem for a ray propagating in an atmosphere in which the refractive index n decreases linearly with height. In this situation the ray follows a path of constant curvature with a radius of curvature r_c. R denotes the radar location, h_a is the (radar) antenna height, r is the (slant) range, D denotes the datum location, r' is the length of the chord RD, RI denotes the ray path in a homogeneous (non-refractive) atmosphere, γ is the angle between the lines OR and RD, δ is the angle between the lines RD and RI, D' denotes the projection of the datum location to the earth's surface, a is the radius of the earth, O denotes the center of the earth, O' denotes the center of the circle that contains the arc RD, and β is half of the angle between $O'R$ and $O'D$. For illustration purposes, features like antenna height h_a and the relative curvatures of the Earth's surface and of the arc RD are not drawn to scale.

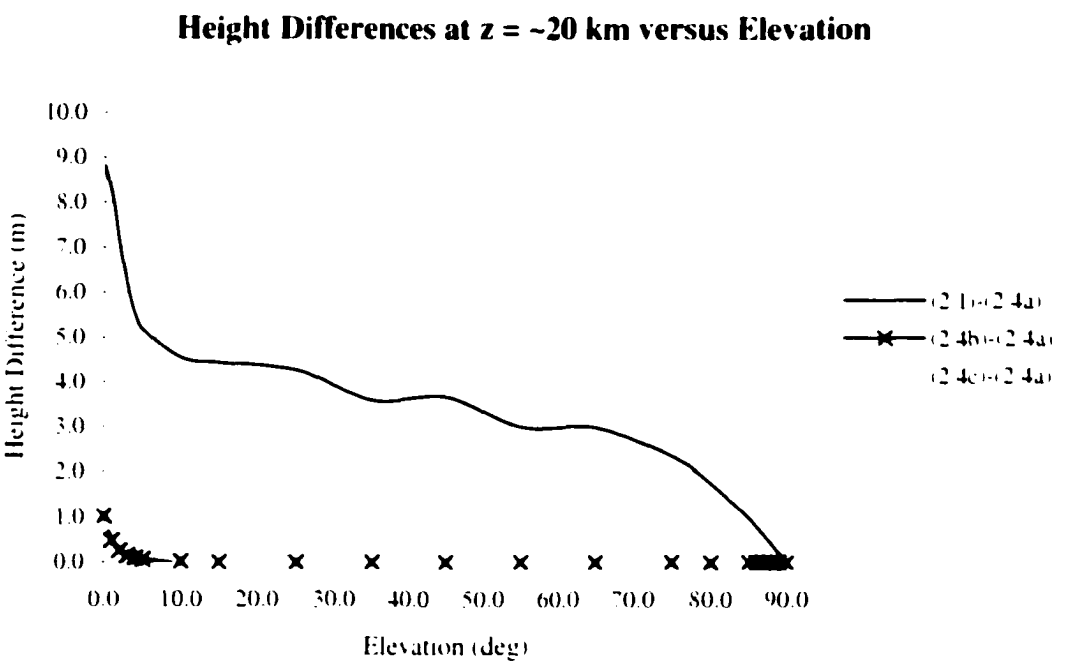

FIG. 2.2. Differences, as a function of elevation and at approximately 20 km altitude, between radar data heights estimated using (2.1) and (2.4a-c). The parameter values are $h_0 = 0$ km, $a = 6370$ km, $r_e = 4a$, and $k_e = 4/3$.

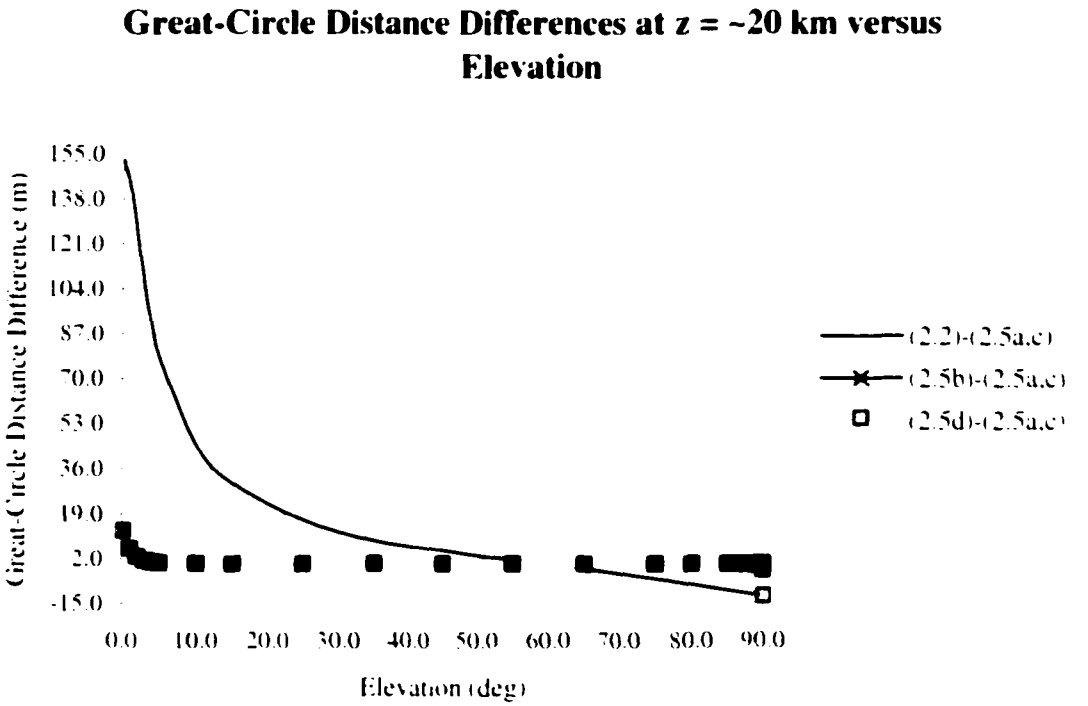

FIG. 2.3. Differences, as a function of elevation and at approximately 20 km altitude, between radar-data great circle distances estimated using (2.2) and (2.5a-d). In (2.2) z was computed using (2.1), in (2.5a,c) z was computed using (2.4a), in (2.5b) z was computed using (2.4b), and in (2.5d) z was computed using (2.4c). The parameter values are $h_i = 0$ km, $a = 6370$ km, $r_c = 4a$, and $k_e = 4/3$.

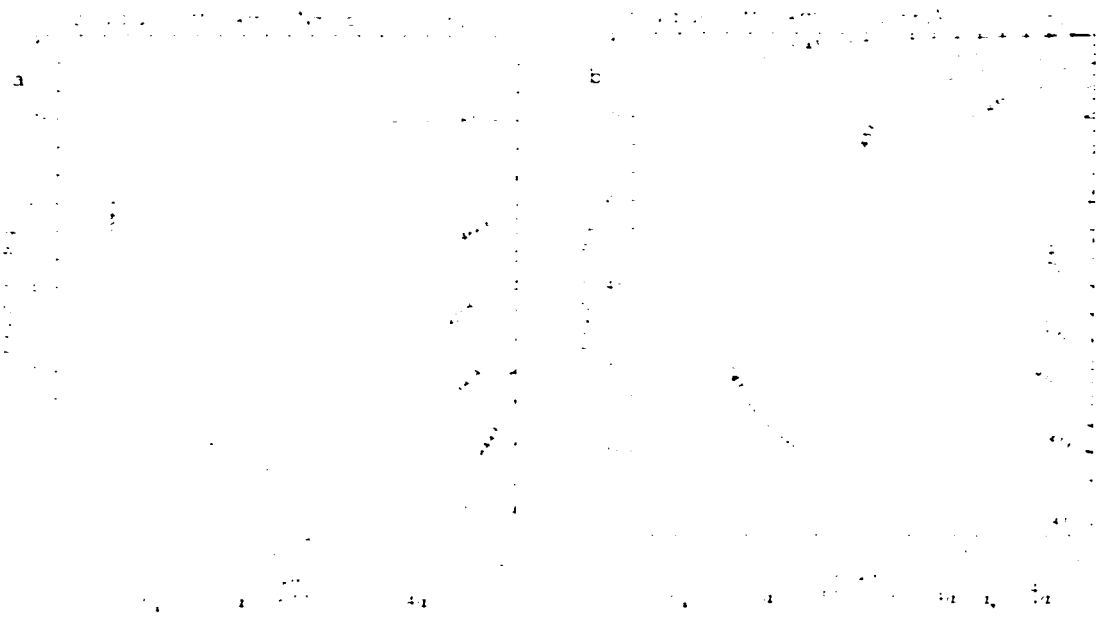

FIG. 2.4. (a) Differences between z values (km) obtained using the no-refraction, flat-earth [NR,FE; Eq. (2.7)] and the constant curvature, spherical earth, direct solution [CC,SE,DS; Eq. (2.4c)] models as a function of range and elevation. (b) Differences between z values (km) obtained using the constant curvature, spherical equivalent earth, approximate solution [CC,SEE,AS; Eq. (2.8)] and the constant curvature, spherical earth, direct solution [CC,SE,DS; Eq. (2.4c)] models as a function of range and elevation. In both (a) and (b) positive contours are indicated by solid lines, negative contours are indicated by dashed lines, $z = 20$ km [calculated using (2.4c)] is indicated by the dotted line, the antenna height is $h_a = 0.0$ km, the earth radius is $a = 6370.0$ km, the ray radius of curvature is $r_c = 4a$, and the equivalent earth radius $a_e = k_e a$ is $a_e = (4/3)a$.

2.1.2 Radar to Spherical Curvilinear Coordinates

When converting from the radar coordinate system to an (x, y, z)-type of coordinate system, the "flat-earth" approximation is often used to determine x and y. In this situation x and y are given by

$$x = s \sin \phi \tag{2.9}$$

and

$$y = s \cos \phi , \tag{2.10}$$

where ϕ is azimuth. In the flat-earth approximation the earth's surface is treated as a plane (cf. Ayres 1954, p. 189). While this approximation may not generally result in egregious errors when working with radar data, errors could be significant for certain applications [e.g., relating earth-relative features (hailswaths, tornado damage paths, etc.) to storm structure]. Moreover, it is of interest to explore the results of using a more contemporary model (spherical instead of flat) for the earth's shape.

The goal is to determine x, y, and z using r, ϕ, θ, a, radar latitude φ_r, and radar longitude λ_r. Relations for z (and s) have been provided in the previous section. In the following it will be assumed that the azimuth $\phi = 0°$ and elevation $\theta = 0°$ corresponds to the +y-direction (north), the +x-direction is to the east, and positive rotation in r,ϕ and r,θ surfaces is clockwise and towards the zenith, respectively.

In the coordinate system typically used in meteorology, x represents the distance along latitude circles and y represents the distance along meridians (Dutton 1995, p. 230). With these conventions, the problem of determining x and y on a spherical earth

is illustrated in Fig. 2.5. Because the arcs RP_n, P_nD', and $D'R$ in Fig. 2.5 are all arcs of great circles, RP_nD' is a spherical triangle (Ayres 1954, p. 147). Note that $RD'E$ is not a spherical triangle because ER is an arc of a small circle instead of a great circle (Ayres 1954, p. 147). As is customary in spherical trigonometry, both the angles and the sides of the spherical triangle RP_nD' are expressed in angular measure (Ayres 1954, 148-149).

Three elements of RP_nD', the vertex φ and the two sides $\pi/2-\varphi_r$ and s/a, are known. As will be subsequently shown, knowledge of P_n and $\pi/2-\varphi_d$ allows one to determine x, x', and y (since the north pole P_n is at one of the vertices of the spherical triangle RP_nD' the symbol P_n is used to represent the spherical angle at that vertex). From the law of cosines for sides for oblique spherical triangles (Ayres 1954, p. 168)

$$\pi/2-\varphi_d=\cos^{-1}\left[\cos(\pi/2-\varphi_r)\cos(s/a)+\sin(\pi/2-\varphi_r)\sin(s/a)\cos\varphi\right]. \quad (2.11)$$

With knowledge of $\pi/2-\varphi_d$ one can determine P_n using the law of sines for oblique spherical triangles (Ayres 1954, p. 168):

$$P_n=\sin^{-1}\left[\frac{\sin(s/a)}{\sin(\pi/2-\varphi_d)}\sin\varphi\right]. \quad (2.12)$$

Now that P_n and $\pi/2-\varphi_d$ are known, x, x', and y can be determined. The simplest value to determine is y. Because

$$y=a(\varphi_d-\varphi_r)=a\left[\pi/2-\varphi_r-(\pi/2-\varphi_d)\right], \quad (2.13)$$

$$y=a\left\{\pi/2-\varphi_r-\cos^{-1}\left[\cos(\pi/2-\varphi_r)\cos(s/a)+\sin(\pi/2-\varphi_r)\sin(s/a)\cos\varphi\right]\right\}, \quad (2.14)$$

where (2.11) has been utilized.

To determine x and x', consider Fig. 2.6, in which the situation pictured in Fig. 2.5 is redrawn. By definition, the spherical angle P_n is measured by the angle at O,

which equals the angles at O_R and O_D (Ayres 1954, p. 147). With this equivalence it is apparent that $x = R_r P_n$ and $x' = R_d P_n$. Expressions for R_r and R_d are readily ascertained by considering Fig. 2.7, which is drawn in the plane defined by the points O, O_R, and E. From Fig. 2.7, $R_r = a\cos(\varphi_r)$ and, analogously, $R_d = a\cos(\varphi_d)$. The relations for x and x', therefore, are

$$x = a\cos(\varphi_r)P_n = a\cos(\varphi_r)\sin^{-1}\left[\frac{\sin(s/a)}{\sin(\pi/2 - \varphi_d)}\sin\sigma\right] \tag{2.15}$$

and

$$x' = a\cos(\varphi_d)P_n = a\cos(\varphi_d)\sin^{-1}\left[\frac{\sin(s/a)}{\sin(\pi/2 - \varphi_d)}\sin\sigma\right], \tag{2.16}$$

where (2.12) has been utilized.

It is useful to recognize that from the above information both λ_d, the longitude of the datum, and φ_d can be determined. The relatively trivial relations are

$$\lambda_d = \lambda_r + P_n \tag{2.17}$$

and

$$\varphi_d = \pi/2 - (\pi/2 - \varphi_d), \tag{2.18}$$

where the term in parentheses on the rhs of (2.18) is available from (2.11).

At this point it is appropriate to consider the possible dependencies of (2.11)-(2.18) upon the azimuthal quadrant of the datum. (In Fig. 2.5 the case for quadrant 1 is considered. Quadrants 1, 2, 3, and 4 are to the northeast, southeast, southwest, and northwest, respectfully, of the radar location.) A simple check of the different quadrants indicates that (2.11), (2.13), (2.14), and (2.18) hold regardless of the quadrant

of ϕ. The relation for P_n is more complicated. Determination of the relation for P_n for azimuthal quadrants 3 and 4 indicates that for these azimuthal quadrants a negative sign should precede both the right-hand sides of (2.12), (2.15), and (2.16) and the P_n term in (2.17). It turns out, however, that this negative sign serves to keep P_n nonnegative in these quadrants. [In spherical trigonometry both the angles and the sides are considered to be nonnegative (Ayres 1954, p. 146)]. Because in the third and fourth azimuthal quadrants $\lambda_{s_1} < \lambda_{s_2}$, a negative P_n value is appropriate for the coordinate system used herein. Consequently, (2.11)-(2.18) hold regardless of the azimuthal quadrant.

A comparison of results obtained using the flat earth [(2.9)-(2.10)] and the spherical earth [(2.16) and (2.13)] approximations, with s and z calculated using (2.5d) and (2.4c), respectively, is provided in Fig. 2.8. In this figure differences are plotted as a function of r and ϕ, which have been converted into polar x and y coordinates, and at an elevation of $\theta = 5.0°$. Because differences at a constant range increase with decreasing elevation (increasing s), the differences in Fig. 2.8 are indicative of the largest differences between the flat earth and spherical earth models. As is apparent in Fig. 2.8a, (2.9) closely approximates (2.16). Maximum differences at $r = 200$ km are ~0.016 km. Figure 2.8b, however, indicates that (2.10) is not as good of an approximation to (2.13). Maximum differences at $r = 200$ km are ~2.21 km, while at ranges of 25, 50, 100, and 150 km the maximum differences are approximately 0.037, 0.143, 0.559, and 1.25 km, respectively. [The difference of 0.143 km at $r = 50$ km corresponds roughly to the length of a city block (0.134 km) and is nearly equal to the magnitude of the difference between (2.4c) and (2.7) at this range and elevation]. For

some applications, like relating earth-relative features (hailswaths, tornado damage paths, etc.) to storm structure, differences of this magnitude may be important. For typical weather radars with beamwidths of ~ 1.0°, however, these differences constitute a fraction of the beamwidth and thus are not expected to be of significant consequence.

The differences in Fig. 2.8b, which are symmetric about the meridian of the radar, increase with range (and s), and are largest for the 90° and 270° azimuths, provide clues concerning their principal cause. From this pattern, it appears as if the differences in Fig. 2.8b may arise primarily from the effect illustrated in Fig. 2.9. As is shown in Fig. 2.9b, latitude lines on the earth's surface curve toward the north pole. In the spherical curvilinear coordinate system, this results in data with $\lambda \neq \lambda_r$ having y values that are smaller than in the rectangular Cartesian case (Fig. 2.9a). Because this effect is symmetric about the meridian of the radar, increases with range, and should be largest for the 90° and 270° azimuths, it appears to explain the difference pattern in Fig. 2.8b.

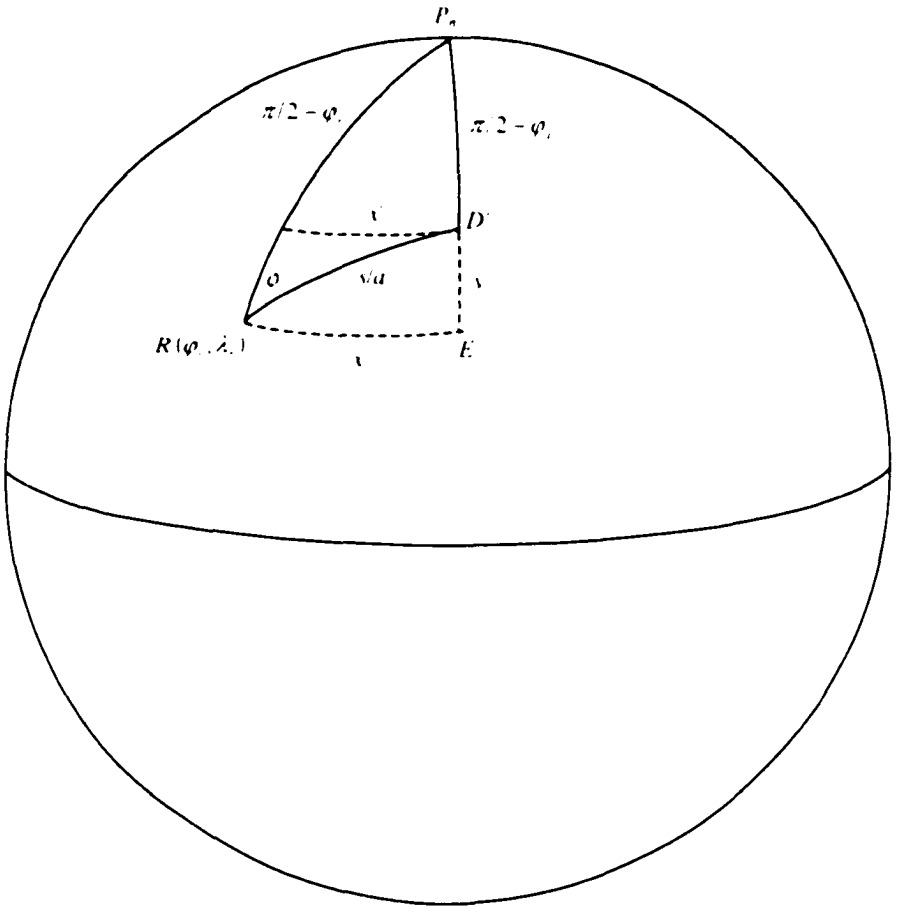

FIG. 2.5. The problem of determining the x, x', and y of a radar datum, on a spherical earth, given the datum's great circle distance s and azimuth ϕ, the latitude and longitude of the radar φ_r and λ_r, and the radius of the earth a. The variable x is the distance from the meridian of the radar to the meridian of the datum along the latitude circle of the radar, x' is the distance from the meridian of the radar to the meridian of the datum along the latitude circle of the datum, and y is the distance from the latitude of the radar to the latitude of the datum. Radar location is denoted by $R(\varphi_r, \lambda_r)$. P_n indicates the north pole, D' indicates the projection of the datum location to the surface of the earth, E indicates the intersection of the meridian of the datum with the latitude circle of the radar, and φ_d is the latitude of the datum.

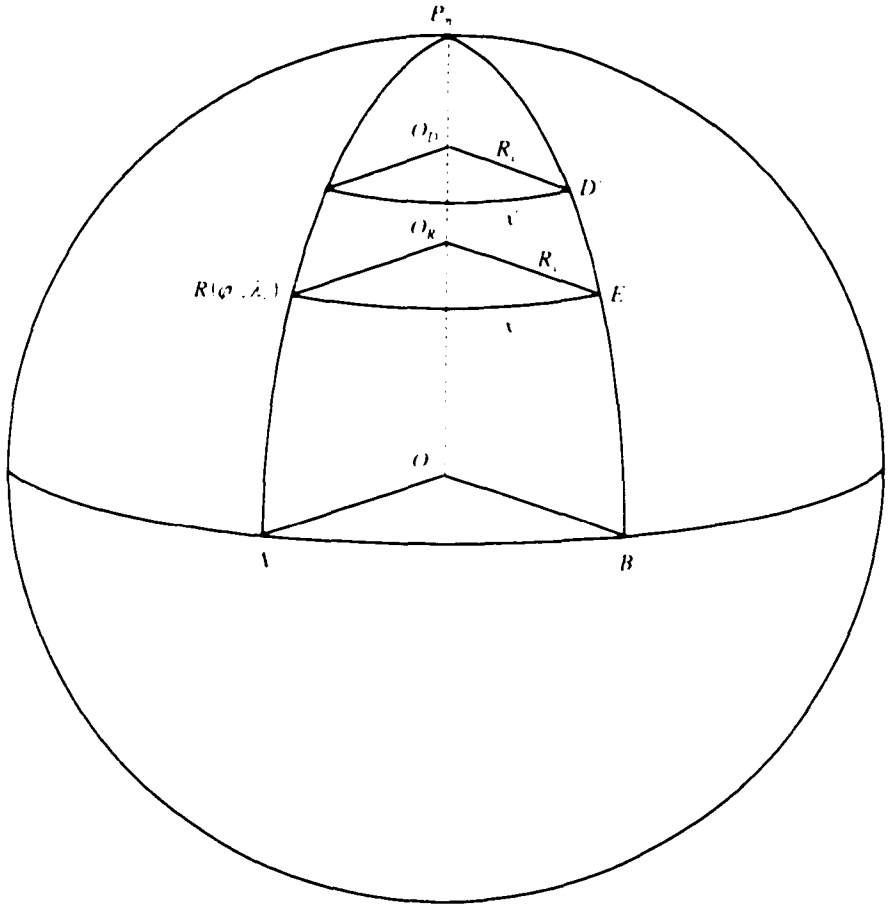

FIG. 2.6. The problem of determining the x and x' of a radar datum, on a spherical earth, given P_n. The symbol A indicates the intersection of the meridian of the radar with the equator, B is the intersection of the meridian of the datum with the equator, O is the center of the earth, $R(\varphi_r, \lambda_r)$ is the radar location, E is the intersection of the meridian of the datum with the latitude circle of the radar, O_R is the intersection of the plane associated with the radar latitude circle with the axis of the earth, D' is the projection of the datum location to the surface of the earth, O_D is the intersection of the plane associated with the datum latitude circle with the axis of the earth, P_n is the north pole, R_1 is the radius of the radar latitude circle, and R_2 is the radius of the datum latitude circle.

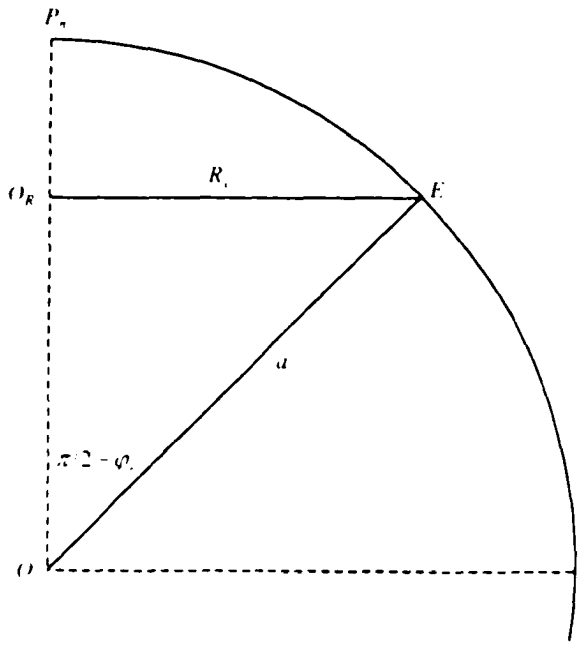

FIG. 2.7. The plane that includes the center of the earth O, O_R (the intersection of the plane associated with the radar latitude circle with the axis of the earth), and E (the intersection of the meridian of the datum with the latitude circle of the radar). P_n is the north pole, R_c is the radius of the radar latitude circle, a is the radius of the earth, and φ_r is the radar latitude.

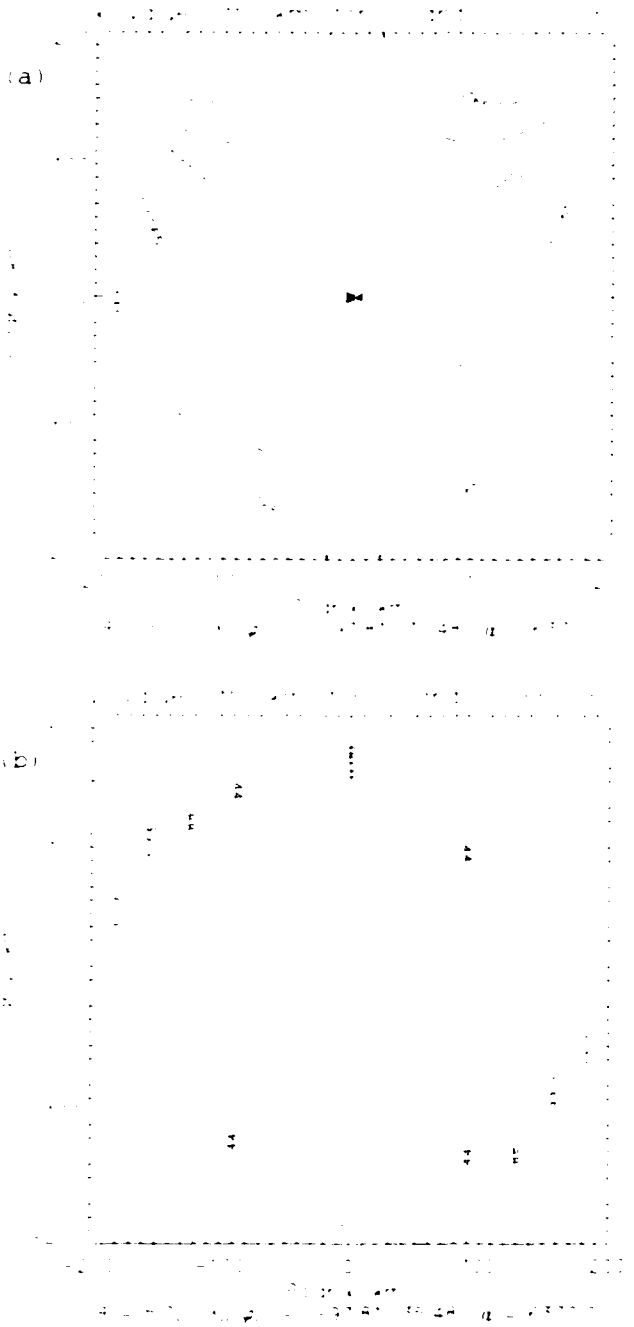

FIG. 2.8. (a) Differences between x values (km) obtained using the flat earth [FE, Eq. (2.9)] and the spherical earth [SE, Eq. (2.16)] approximations as a function of azimuth and range. (b) Differences between y values obtained using the flat earth [FE, Eq. (2.10)] and the spherical earth [SE, Eq. (2.13)] approximations as a function of azimuth and range. In both (a) and (b) s was computed using (2.5d) [with z from (2.4c)], azimuth and range have been converted into polar x and y values, positive contours are indicated by solid lines, negative contours are indicated by dashed lines, the elevation is $\theta = 5.0°$, the radar longitude and latitude are $(\lambda_r, \varphi_r) = (-97.81°, 35.48°)$, the antenna height is $h_a = 0.0$ km, the earth radius is $a = 6370.0$ km, and the ray radius of curvature is $r_e = 4a$.

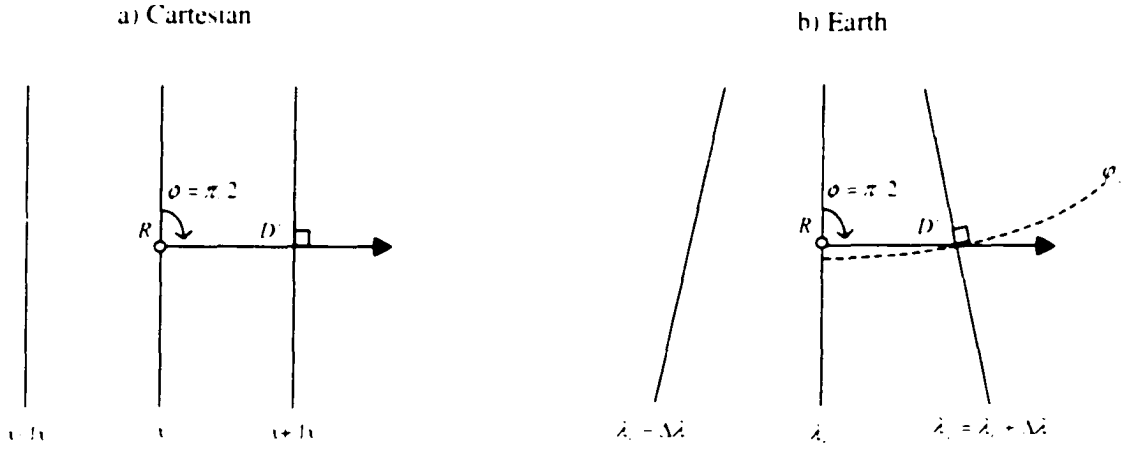

FIG. 2.9. Horizontal surfaces in (a) a rectangular Cartesian coordinate system and (b) a spherical curvilinear coordinate system (e.g., the earth's surface). R indicates the radar location, D' is the projection of a datum location to the surface, ϕ is azimuth, λ is longitude (λ_r is the radar longitude), and φ is latitude (φ_d is the datum latitude). The arrows indicate the projection of a radar beam with $\phi = \pi/2$ onto the surface and the dashed arc in b indicates the latitude circle of the datum.

2.1.3 Spherical Curvilinear to Radar Coordinates

With the $(r,\phi,\theta)\rightarrow(x,y,z)$ transformation relations established, it is prudent to investigate the $(x,y,z)\rightarrow(r,\phi,\theta)$ transformation. In this case P_n and $\pi/2-\varphi_{tt}$ are easily ascertained from x or x' and y:

$$\pi/2-\varphi_{tt}=\pi/2-\varphi_r-y/a \tag{2.19}$$

and

$$P_n=\frac{x}{a\cos(\varphi_r)} \tag{2.20}$$

or

$$P_n=\frac{x'}{a\cos(\varphi_{tt})}. \tag{2.21}$$

At this point the vertex P_n and the sides $\pi/2-\varphi_r$ and $\pi/2-\varphi_{tt}$ of the spherical triangle pictured in Fig. 2.5 are known. From the law of cosines for sides for oblique spherical triangles (Ayres 1954, p. 168),

$$s/a=\cos^{-1}\left[\cos(\pi/2-\varphi_r)\cos(\pi/2-\varphi_{tt})+\sin(\pi/2-\varphi_r)\sin(\pi/2-\varphi_{tt})\cos(P_n)\right]. \tag{2.22}$$

From the law of sines for oblique spherical triangles (Ayres 1954, p. 168),

$$\phi_{int}=\sin^{-1}\left[\frac{\sin(P_n)\sin(\pi/2-\varphi_{tt})}{\sin(s/a)}\right], \tag{2.23}$$

where this azimuthal value is labeled as ϕ_{int} (ϕ-intermediate) because this azimuthal value will oftentimes be located in the incorrect quadrant. Information concerning the quadrant of a datum is needed to determine its ϕ.

Because of the nature of the spherical curvilinear coordinate system, determining the azimuthal quadrant of a datum is more complicated than in the case of plane-trigonometry. Specifically, determining whether a datum is in either quadrant two or three is more complicated than in the plane-trigonometry case. One cannot simply use the test $y < 0$ as in plane trigonometry. The reason for this complication is illustrated in Fig. 2.9. In the case of a Cartesian coordinate system (Fig. 2.9a) the projection of the $\theta = \pi/2$ radar beam coincides with the $+x$-direction. For the coordinate system used herein (Fig. 2.9b), however, the projection of the $\theta = \pi/2$ radar beam coincides with the $+x$-direction only at the location of the radar R. This results in negative y-values for data at azimuths slightly less than and equal to $\pi/2$ and for data at azimuths slightly greater than and equal to $3\pi/2$. Consequently, the test $y < 0$ would incorrectly place some points that are in quadrants one and four into quadrants two and three, respectively.

The y-value y_v that divides azimuthal quadrants one and two and three and four is needed. It can be determined using (2.14) with $\theta = \pi/2$ or $\theta = 3\pi/2$. The result is

$$y_v = a\{\pi/2 - \varphi_r - \cos^{-1}[\cos(\pi/2 - \varphi_r)\cos(s/a)]\}, \qquad (2.24)$$

with the quantity s/a available from (2.22). For a given earth radius and radar location, (2.24) provides the y-values that divide azimuthal quadrants one and two and three and four as a function of the s/a values of the data. It can be seen from (2.24) that y_v is typically negative since, for $0 < s/a \le \pi/2$, $\cos(\pi/2 - \varphi_r)\cos(s/a)$ is nonnegative and less than $\cos(\pi/2 - \varphi_r)$, resulting in $\cos^{-1}[\cos(\pi/2 - \varphi_r)\cos(s/a)] > \pi/2 - \varphi_r$.

One may wonder if the test $x<0$ can also fail to correctly indicate whether a datum is in either azimuthal quadrant three or four. Fortunately, this test does correctly indicate a datum's location within either azimuthal quadrant three or four. This can be verified by considering (2.12) and (2.15) or (2.16). At $o=0$ and $o=\pi$, P_n and thus x and x' equal zero. On either side of these azimuths the sign of both x and x' varies according to the sign of P_n.

By recognizing that the sign of the argument to the $\sin^{-1}(\ )$ function in (2.23) varies according to the sign of P_n, by assuming that the $\sin^{-1}(\ )$ function in (2.23) produces the principal values, and by considering the case for each azimuthal quadrant, one obtains the relation

$$\begin{aligned} o &= o_{int} && x \geq 0,\ y \geq y_s \\ o &= \pi - o_{int} && y < y_s \\ o &= 2\pi + o_{int} && x < 0,\ y \geq y_s . \end{aligned} \tag{2.25}$$

Thus, once P_n, $\pi/2-\varphi_a$, and s/a are known, (2.23)-(2.25) are required to compute the correct value of o.

A relation for r,

$$r = \left[(a+h_a)^2 + (a+z)^2 - 2(a+h_a)(a+z)\cos(s/a)\right]^{1/2}, \tag{2.26}$$

arises from solving (2.5d) for r. In this equation s is available from (2.22). The elevation of a datum can be determined from the relation

$$\begin{aligned} \theta = \sin^{-1}\left[\frac{(a+z)^2-(a+h_a)^2-r^2}{2r(a+h_a)}\right] + r/2r_e = \\ \sin^{-1}\left[\frac{(z-h_a)(z+h_a+2a)-r^2}{2r(a+h_a)}\right] + r/2r_e . \end{aligned} \tag{2.27}$$

which arises from solving (2.4b) for θ and uses r from (2.26). In the height determination section it was stated that (2.4c) and (2.5d) might be preferable to the other relations because of their satisfaction of the no-refraction condition when $\theta = \pm 90.0^\circ$ and because of their close adherence to the exact constant-curvature solutions. Consequently, (2.26) and (2.27) are provided with the assumption that (2.4c) and (2.5d) are used for $(r, \phi, \theta) \rightarrow (x, y, z)$ transformations. Because of the difficulty associated with solving for θ in (2.4c), θ in (2.27) is obtained from (2.4b). Since (2.4b) and (2.4c) are nearly equivalent (Fig. 2.2), with the largest difference for the conditions of Fig. 2.2 being +29 cm, the consequences of using (2.4b) [instead of (2.4c)] to determine θ are expected to be minimal. The only situation in which the use of (2.4b) instead of (2.4c) for the determination of θ is expected to potentially make a difference is when r is very small.

The relations obtained herein may fail in extreme circumstances. Potential failure conditions include:

i. If $\pi/2 < \theta < 3\pi/2$, where θ is expressed such that $0 \le \theta \le 2\pi$, s becomes negative when calculated using (2.2) or (2.6b) because of the $\cos\theta$ term. This is an unlikely problem because elevations are almost always reported in the range $-\pi/2 \le \theta \le \pi/2$.

ii. If $\pi/2 + r\ 2r_e < \theta < 3\pi/2 + r/2r_e$, where θ is expressed such that $0 \le \theta \le 2\pi$, s becomes negative when calculated using (2.5a,b) or (2.6a) because of the $\cos(\theta - r/2r_e)$ term. Because elevations are almost always reported in the range

$-\pi/2 \le \theta \le \pi/2$, this problem is likely to arise only for elevations very near (within $r/2r_e$ of) $-\pi/2$.

iii. If $\varphi_r = \pi/2$, the spherical triangle RP_nD' collapses into the arc of a great circle. In that case $\pi/2 - \varphi_{ii} = s/a$ and $P_n = \phi$. Consequently, from (2.15) $x = 0$, from (2.16) $x' \ge 0$ (assuming the values of ϕ are reported such that $0 \le \phi \le 2\pi$), and from (2.13) $y = -s$. The physical meanings of x, x', and y break down in this situation. Moreover, a division by zero occurs in (2.20). These relations, therefore, do not hold for the situation where the radar is at a pole.

iv. If $\varphi_{ii} = \pi/2$, division by zero occurs in (2.12), (2.15), (2.16), and (2.21). These relations do not hold in situations where data points may be at either of the poles.

v. If $r \ge \sim O(a)$ the geometry of Fig. 2.5 breaks down. The relations provided herein are intended for conditions in which $r << a$.

vi. If $r = 0$, then $z = h_{ii}$, $\varphi_{ii} = \varphi_r$, and $s = P_n = x = x' = y = 0$. This results in division by zero in both (2.23) and (2.27).

vii. If $\theta = \pm\pi/2$, $z = h_{ii} \pm r$ [assuming (2.1) or (2.4c) are used], $\varphi_{ii} = \varphi_r$, and $s = P_n = x = x' = y = 0$ [assuming (2.2), (2.5d), or (2.6b) are used]. This results in division by zero in (2.23).

2.1.4 A Spherical Curvilinear Grid for the Spatial Objective Analysis of Radar Data

The establishment of a spherical curvilinear grid for the spatial objective analysis of radar data requires careful consideration. If the grid is established relative to

the radar location using x (2.15) and y (2.13) for east-west and north-south displacements, then lines of constant north-south displacement will coincide with latitude lines while lines of constant east-west displacement will coincide with meridians. The drawback of this system is the convergence of meridians with increasing latitude (decreasing latitude in the southern hemisphere). Assuming the grid does not traverse either the equator or a pole, this convergence of meridians results in lines of constant east-west displacement being closer to each other in the northern part of the grid (southern part for the southern hemisphere) than they are in the southern part of the grid (northern part for the southern hemisphere).

An alternative is to define the east-west displacement using x' (2.16). In this system, lines of constant north-south displacement still coincide with latitude lines while lines of constant east-west displacement are roughly parallel to the meridian of the radar. A difficulty arises, however, if one wishes to perform multiple-Doppler analyses. In that situation, defining east-west displacements using x' results in lines of constant east-west displacement that are different for each radar (unless, of course, the longitudes of the radars are equal). Consequently, even if the centers of the analysis grids (at ground level) for the different radars were collocated, the grids would not coincide because the east-west displacement lines are defined relative to the longitude of each radar.

A solution to this problem is to define east-west and north-south displacements relative to the center of the analysis grid. If the east-west displacements are then defined as the distance along the latitude circle of the datum (not the grid center), lines of constant north-south displacement coincide with latitude lines while lines of constant

east-west displacement are roughly parallel to the meridian of the center of the analysis grid. Note that in this coordinate system only the set of grid points along $x' = 0$ are parallel to a meridian.

The relations for the east-west and north-south displacement of a datum relative to the center of the grid, x'_{ct} and y_{ct}, are obtained from the same reasoning used to derive (2.13), (2.15), and (2.16):

$$x'_{ct} = a\cos(\varphi_t)(\lambda_{st} - \lambda_{ct}) \tag{2.28}$$

and

$$y_{ct} = a(\varphi_{st} - \varphi_{ct}). \tag{2.29}$$

In (2.28) and (2.29) λ_{ct} is the longitude of the center of the analysis grid and φ_{ct} is the latitude of the center of the analysis grid. For the transformation $(x'_{ct}, y_{ct}, z) \rightarrow (r, \varphi, \theta)$, it can be helpful to express (2.24) and (2.25) in terms of latitude and longitude differences:

$$dlat_t = y_t / a = \pi/2 - \varphi_r - \cos^{-1}[\cos(\pi/2 - \varphi_r)\cos(s/a)], \tag{2.30}$$

$$\begin{array}{ll} \varphi = \varphi_{int} & P_n \geq 0, \varphi_{st} - \varphi_r \geq dlat_t \\ \varphi = \pi - \varphi_{int} & \varphi_{st} - \varphi_r < dlat_t \\ \varphi = 2\pi + \varphi_{int} & P_n < 0, \varphi_{st} - \varphi_r \geq dlat_t. \end{array} \tag{2.31}$$

It is enlightening to note that the analysis grid defined herein appears to be equivalent to that used by Brown et al. (1981). As Brown et al. (1981) indicate, this coordinate system is one in which each horizontal two-dimensional grid level is part of a spherical surface, each of which is concentric about the earth's center. Vertical columns of grid points are normal to the earth's surface (i.e., are "radiating" outward

from the earth's center). The analyzed data can be displayed by deforming the analysis grid into a rectangular-Cartesian grid. As noted by Brown et al. (1981), the errors that result from this deformation are negligible because of the limited domain size (horizontal extent typically less than ~60 km and vertical extent less than ~20 km).

2.2 Objective Analysis

Spatial objective analyses of radar data are oftentimes performed to estimate radar data on a rectangular Cartesian grid. Three important motivations for doing so are the removal of noise, the incorporation of radar data into numerical weather prediction models, and phenomenological studies. The latter reason arises in part because the analysis of radar data is simplified for coordinate systems that are aligned with physical processes. The melting of hydrometeors, for example, tends to progress as those hydrometeors fall towards the Earth. This physical process is approximately aligned with the -z direction but is not aligned with any of the directions of the spherical coordinate system that underlies most radar data.

Spatial objective analyses of radar data are used in this study to enhance analyses of physical processes. In the application of spatial objective analyses to radar data numerous issues arose that deserved investigation. These issues are considered presently.

2.2.1 The Adaptive Barnes Scheme

The investigation of a new filter for the objective analysis of radar data was motivated by the following two fundamental characteristics of the spatial density of

radar data. 1) Data spacing depends on direction: Because data spacing in the radial direction is fixed (e.g., every 150 m) whereas data are spaced in the azimuthal and elevational directions at angular intervals, data spacing depends on direction. 2) Data density systematically decreases with increasing range: Data in the azimuthal and elevational directions are collected at angular intervals and the distances associated with these intervals increase with increasing range.

Because of these characteristics it has been proposed (Askelson et al. 2000) that the following weight function be utilized in distance-dependent weighted averaging (DDWA) spatial objective analyses of radar data:

$$w(r_{ik}, \phi_{ik}, \theta_{ik}, \kappa_r, \kappa_\phi, \kappa_\theta) = \exp\left[-\frac{r_{ik}^2}{\kappa_r} - \frac{\phi_{ik}^2}{\kappa_\phi} - \frac{\theta_{ik}^2}{\kappa_\theta}\right], \tag{2.32}$$

where r_{ik} is the radial distance between the i^{th} analysis location and the k^{th} observation location, ϕ_{ik} and θ_{ik} are the azimuthal and elevational differences between the i^{th} analysis point and the k^{th} observation, and κ_r, κ_ϕ, and κ_θ are the smoothing parameters in the radial, azimuthal, and elevational directions, respectively. With (2.32) the weight assigned to an observation depends upon the *differences in the coordinates* of the observation and the analysis point. Moreover, the form of (2.32) allows the specification of anisotropic weight functions. The weight function (2.32) is referred to as both the adaptive-Barnes (A-B) weight function and the A-B filter.

The implications of using (2.32) have been thoroughly investigated. Because of the timing of the work in this area, the decision was made to move forward with the publication of this research, which is contained in Askelson et al. (2000). A brief summary of their findings, taken directly from their conclusions section, is:

"1) The A-B filter can directly account for the dependence of radar data spacing on direction and for the tendency of radar data density to decrease with range. Within the confines of one-pass DDWA schemes, the A-B filter facilitates the retention of the maximum amount of information.

2) Consistent with the anisotropy of radar data spacing, more information concerning waves with short to medium wavelengths in the highly resolved direction can be retained by decreasing the smoothing in that direction using the direction-splitting design of the A-B filter. This occurs without egregious phase shifts or orientation changes of input waves.

3) Because the weight assigned to an observation depends upon the differences in the coordinates of the observation and analysis points, the A-B filter automatically adapts to the systematically decreasing radar data density with range. With the A-B filter information content at close ranges does not have to be sacrificed because of poor resolution at more distant ranges.

4) Windowing weight functions produces ringing in their response functions. Effects on the main lobe of the one-dimensional, Barnes response function are small when the weight function is windowed at or below 0.05.

5) For radar data, postanalysis gradient fields of analyses produced using an isotropic weight function will generally suffer from contributions by gradients in the analysis weights. Because of its consistency with radar data, the direction-splitting A-B filter, when applied away from data boundaries and to radar data that are at regular radial, azimuthal, and elevational intervals, results in postanalysis gradient fields that have virtually no contribution from gradients in analysis

weights. However, even when the additional restriction of collocated observation and analysis points is imposed, postanalysis gradients are not equal to analyses of gradients because of the scale factors associated with the spherical coordinate system of radar data.

6) The A-B filter should be used with caution since imbalances in the data, including preferential orientation of finescale structure and decreasing finescale structure with range, can be retained by the A-B filter. The retention of these imbalances is what ironically produces both the potential benefits and detriments of the A-B scheme. Potential detriments arise since retention of data imbalances could lead unwary analysts to form incorrect conclusions concerning the phenomena being studied. Isotropic schemes, at the cost of information loss, attempt to normalize these imbalances."

In the above summary, windowing at a certain level means treating the non-normalized weight function as if it were zero when its value is below that level. Because computational resources are finite, limits must be placed on the amount of information that is used to obtain analysis values. In DDWA objective analyses, these limits are enforced through windowing. The traditional strategy is to ignore data for which the weight function is small since those data have little influence upon analysis values. Windowing, through either design or data limits, is inherent to most objective analyses.

One finding that is not listed above is that for data with infinite and continuous domains, the DDWA is a cross correlation, not a convolution. In this context cross correlation is the composition of two functions as defined by Papoulis (1962, p. 244)

and Bracewell (2000, p. 46). This distinction is important when considering the phase modulations experienced during DDWA objective analyses (Askelson et al. 2000).

A frustration encountered during this work was the response function for arbitrary weight functions and data distributions. Lack of knowledge concerning this issue precluded certain avenues of investigation. Consequently, this issue has been investigated, as discussed presently.

2.2.2 Response Functions for Arbitrary Weight Functions and Data Distributions

2.2.2.1 Introduction

Distance-dependent weighted averaging (DDWA) can be viewed as a fundamental process in most of the objective analysis techniques that are commonly employed in meteorology (Thiébaux and Pedder 1987, 5-6; Daley 1991, 30-31). In one-pass schemes that use prescribed distance-dependent weight functions (e.g., Barnes 1964), analysis values are produced directly through DDWA. Furthermore, multiple-pass schemes using prescribed distance-dependent weight functions (successive-correction schemes) can be rewritten as DDWA (Caracena 1987; Doswell and Caracena 1988). Similarly, schemes that employ least-squares function fitting also obtain analysis values through a process that is equivalent to DDWA (Thiébaux and Pedder 1987, 22-23; Daley 1991, p. 49). Statistical objective analysis schemes utilize the spatial correlation structure of the variables used in the analysis to construct a DDWA scheme that minimizes analysis-error variance. Variational schemes, while possibly not generally expressible in terms of DDWA, often utilize techniques that are equivalent to DDWA to facilitate solution (e.g., Testud and Chong 1983).

Given the importance of DDWA to the spatial objective analysis techniques used in meteorology, it is prudent to understand the effects DDWA has upon the data. These effects can be expressed through the response function[4]. As typically defined in meteorology, the response function is the ratio of the Fourier transforms of the post- and pre-analysis fields. Assuming one-dimensional fields and denoting (direct) Fourier transforms with non-script capital letters, the response function $\mathcal{R}(\nu)$ is $\mathcal{R}(\nu) = F_a(\nu)/F(\nu)$, where $F_a(\nu)$ is the Fourier transform of the analysis field $f_a(x)$, $F(\nu)$ is the Fourier transform of the observation field $f(x)$, and ν denotes the frequency dependence. Herein, the one-dimensional (direct) Fourier transform is defined to be $F(\nu) = \mathrm{FT}[f(x)] = \int_{-\infty}^{\infty} f(x)\exp(-j2\pi\nu x)dx$, where $j = \sqrt{-1}$. The response function is a generally complex-valued function that provides information concerning amplitude and phase changes undergone during analysis.

The response function for DDWA analyses of continuous, infinite data has been understood for some time (e.g., Barnes 1964). Observations, however, are rarely continuous or infinite; observations are typically discrete, bounded, and irregularly distributed. Of these three characteristics, the discrete nature of observations is the most straightforward to address in terms of the response function. Numerous texts (e.g., Hamming 1998) and journal articles (e.g., Jones 1972) examine the situation where the observations are both regularly-distributed and collocated with the analysis points. A common approach used to determine the response function in this situation is the eigenfunction approach (e.g., Weaver 1983, 259-260). The efficacy of this approach is

[4] The response function is known by other names, including transfer function and system function.

diminished, however, when either the analysis points are not collocated with the observations or the observations are irregularly distributed.

Pauley and Wu (1990) considered a special case of non-collocated analysis and observation points. They determined the response function for the situation where analysis points are located midway between observations that are discrete, regularly distributed, and infinite in number. The case of irregularly distributed observations was beyond the scope of their investigation.

For irregularly distributed observations, the response function can be viewed from two standpoints. The first standpoint is a domain-wide response function, which is some sort of average response function that characterizes the domain-wide spectral effects of an analysis. Domain-wide response functions for specific data-point distributions have been investigated (e.g., Yang and Shapiro 1973; Buzzi et al. 1991), as have domain-wide response functions for random data-point distributions (Stephens and Polan 1971).

The second standpoint is the local response function, which is the subject of this study. As discussed by Thiébaux and Pedder (1987, p. 105) and Buzzi et al. (1991), the response function for DDWA analyses of discrete, irregularly distributed data depends upon both frequency and location. Others (e.g., Jones 1972; Yang and Shapiro 1973; Schlax and Chelton 1992) have derived the local response function for DDWA analyses of discrete, irregularly distributed data by using what is termed here the back-substitution approach. In this approach a spectral representation of the observation field is first substituted into an expression for a DDWA analysis. Then, the result of this operation is manipulated to obtain the response function. Herein, an alternative

approach, labeled the convolution-theorem approach and based upon the approach outlined by Caracena et al. (1984), is utilized to obtain the response function for DDWA analyses of discrete, irregularly distributed data.

The purpose here is to outline a method for determining the local response function for DDWA analyses of arbitrarily distributed data using arbitrary weight functions. In doing so, the response function for DDWA analyses of discrete, irregularly-distributed data is derived. Although this response function is the same as that determined previously (e.g., Jones 1972; Yang and Shapiro 1973; Schlax and Chelton 1992), the method outlined herein is enlightening because of the additional insights it provides. In order to provide a logical progression to the final result and to clarify issues pertaining to a previous result obtained by Pauley (1990) (henceforth P90), the steps taken to obtain the response function for discrete, irregularly-distributed data are retraced in the chronological order in which they were discovered. Consequently, the response function for continuous, bounded data is first derived and tested in section 2.2.2.2 and then the response function for discrete, irregularly-distributed data is derived and tested in section 2.2.2.3. An extension to multiple dimensions is provided in section 2.2.2.4. Results are discussed in section 2.2.2.5 and conclusions are presented in chapter 4.

2.2.2.2 Continuous, Bounded Data

2.2.2.2.1 The Problem

Whereas response functions for DDWA schemes applied to data away from data boundaries are relatively well understood (e.g., Pauley and Wu 1990), less is known

concerning the response functions for DDWA schemes applied near data boundaries. Even though this topic has been the subject of past investigations by P90 and Achtemeier (1986), problems with these earlier papers motivate further examination.

For one-dimensional, continuous, bounded data with boundaries at x_L and x_R, the first-pass, DDWA analysis field $f_1(x)$ is given by

$$f_1(x) = \frac{\int f(x_o) w(x_o - x) dx_o}{\int w(x_o - x) dx_o} = \frac{\int f(x_o) p(x_o) w(x_o - x) dx_o}{n(x)}, \qquad (2.33)$$

where $f(x_o)$ denotes the observations, $w(x_o - x)$ is the weight function, $n(x) = \int w(x_o - x) dx_o$ is the normalization factor, $p(x_o)$ is the pulse function given by

$$p(x_o) = \begin{cases} 1 & x_L \le x_o \le x_R \\ 0 & \text{otherwise} \end{cases}, \qquad (2.34)$$

x_o depicts observation locations, and x depicts analysis locations.[5] With the substitution $x' = x_o - x$, (2.33) becomes

$$f_1(x) = \frac{\int f(x + x') w(x') dx'}{n(x)} = \frac{\int f(x + x') p(x + x') w(x') dx'}{n(x)}. \qquad (2.35)$$

As indicated in (2.35), *both* $n(x)$ *and* $p(x + x')$ *are functions of* x (position in the analysis domain).

[5] It is noted that in DDWA analyses observation and analysis domains are distinct. This is true even though they can share some, or even all, locations.

Examples of the dependence of $n(x)$ on x [for the Gaussian weight function given by $w(x) = \exp(-x^2/\kappa_1)$, with $\kappa_1 = 3$] are provided in Fig. 2.10 for a continuous, bounded case (Fig. 2.10a), three discrete, regularly-distributed cases (Fig. 2.10b), and a discrete, irregularly-distributed case (Fig. 2.10c). The dependence of $n(x)$ upon both analysis type (continuous versus discrete) and location x, as illustrated in Fig. 2.10, requires some explanation. In the continuous case (Fig. 2.10a), $n(x)$ is nearly constant in the center of the observational domain at a value that agrees with the infinite domain value if the boundaries are sufficiently removed from each other, decreases to half the infinite domain value at the boundaries, and shrinks to near zero outside of these boundaries. This pattern arises because, as the analysis point (and weight function peak) approaches and passes a boundary, the area under the portion of the weight function that resides within the observational domain decreases.

The same pattern is also present in the discrete, regularly-distributed cases (Fig. 2.10b). In these cases, however, $n(x)$ increases with decreasing data spacing [the data spacing is 1.0 (dotted line), 0.5 (thin-dashed line), and 0.25 (solid line)]. This can be understood by considering that DDWA schemes produce weighted averages using, in the one-dimensional discrete case, equations of the form

$$f_1(x) = \frac{\sum_{i=1}^{N} f(x_{oi}) w(x_{oi} - x)}{\sum_{i=1}^{N} w(x_{oi} - x)}, \tag{2.36}$$

where $f_1(x)$ is the analysis field, $f(x_{oi})$ denotes the i^{th} observation, and N is the total number of observations. As the data density increases, so does the number of times the

weight function is sampled, which leads to an increase in the normalization factor. [This situation is similar to that of a running mean. As the data density increases, the number of values within the averaging interval (the normalization factor for the running mean) increases.] Because of this and because the Gaussian weight function is largest for small values of x', peaks in $n(x)$ are also expected in conjunction with clusters of observations in the discrete, irregularly distributed case (Fig. 2.10c).

The final aspect of Fig. 2.10 that requires explanation is the relative magnitudes of $n(x)$ for the continuous and the discrete cases. Despite the use of the same weight function, $n(x)$ values in the discrete cases often exceed those in the continuous case. The reason for this can be ascertained by considering (2.36). Multiplication of both the numerator and the denominator of (2.36) by $\Delta x = 1$ converts both into Riemann sums (sums of products of function values and intervals), while neither analysis nor normalization-factor values are altered. The Riemann sum in the denominator, however, is generally an *improper* approximation to the integral of the weight function because observational intervals are not generally equal to one. When the data spacing is less than one, as is often the case (cf. Figs. 2.10b,c), intervals overlap and overestimation results. In the regularly distributed cases of Fig. 2.10b, the normalization factor can be converted into a *proper* Riemann-sum approximation of the integral of the weight function by multiplying by the actual data spacing. Doing so for the cases in Fig. 2.10b results in all of the curves being nearly identical to that for the case with a data spacing of 1.0 and to that for the continuous case.

In her equation (P2a) P90 expresses the first-pass, Barnes, DDWA analysis field for one-dimensional, continuous, bounded data as

$$g_0(x) = \frac{\int \exp\left(\frac{-x'^2}{\lambda_0^2}\right) f(x+x')\,dx'}{\int \exp\left(\frac{-x'^2}{\lambda_0^2}\right) dx'}. \qquad \text{(P2a)}$$

where $g_0(x)$ is the analysis field, $\exp(-x'^2/\lambda_0^2) = w(x', \lambda_0)$ is the (Barnes) weight function, and $f(x+x')$ denotes the observations. [Equations from P90 are labeled with a P followed by the corresponding equation number in P90]. In order for (P2a) to be consistent with (2.35), x_1 must equal $x_1 - x$ and x_2 must equal $x_R - x$.

P90 derived the response function for the Barnes scheme applied to one-dimensional, continuous, bounded data by taking the Fourier transform of (P2b). Equation (P2b), which resulted from introducing a pulse function into (P2a), is

$$g_0(x) = \frac{\int \exp\left(\frac{-x'^2}{\lambda_0^2}\right) f(x+x')\,p(x')\,dx'}{\int \exp\left(\frac{-x'^2}{\lambda_0^2}\right) p(x')\,dx'}. \qquad \text{(P2b)}$$

The pulse function in (P2b), however, was set up incorrectly. Data boundaries should be expressed in terms of observation space—x_n as used herein or X as used in Pauley and Wu (1990). This means that the pulse function $p(x')$ in (P2b) should be written as $p(x+x')$, as in (2.35). The numerator on the rhs of (2.35) [and (2.33)], therefore, is the *cross correlation* of $w(x)$ and the function $f(x)p(x)$, denoted as $w(x)\bigstar f(x)\,p(x)$. As shown by Papoulis (1962, p. 244), $w(x)\bigstar f(x)\,p(x) = w(-x) * f(x)\,p(x)$, where $*$ denotes convolution. This result can also be obtained directly by recognizing that the numerators of (2.33) and (2.35) are the convolution of $w(-x)$ and $f(x)p(x)$. Thus, a concise expression of (2.33) and (2.35) is

$$f_1(x) = \frac{w(x) \bigstar f(x)\, p(x)}{n(x)} = \frac{w(-x) * f(x)\, p(x)}{n(x)}. \qquad (2.37)$$

Attempting to obtain the response function by taking the Fourier transform of (2.37)[6], which is the corrected version of (P2b), results in difficulties. Taking the Fourier transform of (2.37) produces

$$F_1(v) = \int_{\xi=-\infty}^{\xi=\infty} M(\xi) N_I(v-\xi)\, d\xi, \qquad (2.38)$$

where $M(v) = \mathrm{FT}[w(-x) * f(x)p(x)]$, $N_I(v) = \mathrm{FT}[1/n(x)]$, ξ denotes frequency dependence, and the product theorem[7] (Weaver 1983, p. 73) has been applied. Using the convolution[8] (Weaver 1983, p. 72), similarity[9] (Bracewell 2000, p. 108), and product theorems, $M(v)$ can be expressed as $M(v) = W(-v) \int_{\psi=-\infty}^{\psi=\infty} F(\psi) P(v-\psi)\, d\psi$ [10], where ψ denotes frequency dependence. Substituting this result into (2.38) results in

$$F_1(v) = \int_{\xi=-\infty}^{\xi=\infty} \left(\int_{\psi=-\infty}^{\psi=\infty} F(\psi) P(\xi-\psi)\, d\psi \right) W(-\xi) N_I(v-\xi)\, d\xi. \qquad (2.39)$$

---

[6] The domain of the analysis field is considered to be continuous and infinite; both within and outside of the observation domain, analysis values are determined using (2.37). Consequently, Fourier theory for one-dimensional, continuous, infinite domains applies to this problem.

[7] The form of the product theorem used here states that if two functions $f(x)$ and $g(x)$, the domains of which are infinite and continuous, have Fourier transforms given by $F(v)$ and $G(v)$, respectively, then the Fourier transform of the product of $f(x)$ and $g(x)$ is given by the convolution of $F(v)$ and $G(v)$.

[8] The form of the convolution theorem used here states that if two functions $f(x)$ and $g(x)$, the domains of which are infinite and continuous, have Fourier transforms given by $F(v)$ and $G(v)$, respectively, then the Fourier transform of the convolution of $f(x)$ and $g(x)$ is given by $F(v)G(v)$.

[9] The one-dimensional similarity theorem states that if the Fourier transform of the infinite, continuous domain function $f(x)$ is $F(v)$, then the Fourier transform of $f(ax)$ is $\frac{1}{|a|} F\left(\frac{v}{a}\right)$.

The response function cannot be expressed explicitly using (2.39) because $F(\nu)$ is bound within convolution integrals. That is, $F(\nu)$ cannot be taken outside the integrals (de-convolved), preventing the solution for $F_1(\nu)/F(\nu)$. Moreover, rearranging (2.37) prior to applying the Fourier transform does not help because the numerator on the rhs of (2.37) is the cross correlation of $w(x)$ and $f(x)p(x)$. No matter how (2.37) is expressed, upon application of the Fourier transform, this cross correlation results in a convolution between $F(\nu)$ and $P(\nu)$.

P90, however, did obtain an explicit expression for the response function through a process similar to that outlined above, albeit as a consequence of the incorrect specification of the pulse function in (P2b). As stated above, the pulse function is used to describe the distribution of the observations and thus is a function of observation location, $x_o = x + x'$. P90 incorrectly casted the pulse function as a function of x', the local coordinate system centered on the analysis point x. Because of this error, the pulse function in the normalization factor of (P2b) is not a function of x as it should be, and so $n(x)$ passes through the Fourier transform as a constant in P90.[11] Furthermore,

---

[10] The Fourier transform $P(\nu)$ can be evaluated either directly or through the evaluation of the Fourier transform of the shifted pulse function, that is centered upon the origin (e.g., Bracewell 2000, p. 137), and the subsequent application of the shift theorem (Bracewell 2000, p. 111).

[11] In P90 the normalization factor was erroneously treated as a constant, with a value appropriate for the particular analysis location of interest (as explained further in this, and in the following, sections). P90's treatment did correct the error in Achtemeier (1986), in which (in effect) the pulse function was not included in the normalization factor and so led to a constant value of $n(x)$, regardless of location. Even so, P90's treatment is inconsistent with (2.37) because of the previously described error that was made in defining the pulse function.

the (incorrect) numerator of (P2b) is a cross correlation of $w(x)p(x)$ and $f(x)$ [12], rather than a cross correlation of $w(x)$ and $f(x)p(x)$ as in (2.37). The Fourier transform of the latter binds $F(v)$ within integrals and so does not readily lead to a response function.

Interpretation is facilitated using the concept of a *window*, which is defined at each analysis point as the effective "view" of the data. For one-dimensional, continuous, bounded data, the window at an analysis point is the product of the pulse function and the normalized weight function, $p(x + x')[w(x')/n(x)]$, and extends from $x_L - x$ to $x_R - x$. Examples of unnormalized [i.e., not divided by $n(x)$] windows for this situation are provided in Fig. 2.11a. [It should be noted that this analysis holds for any $w(x')$. The $w(x')$ in Fig. 2.11 is simply an example, which has been made asymmetric in order to avoid the implication of special characteristics.] As is obvious from Fig. 2.11a, the analyses at points A and B "see" the data through different windows. In fact, the window is generally different for each analysis point. If, on the other hand, the analysis somehow would view the data through the *same* window at each analysis point (Fig. 2.11b), $n(x)$ would be constant and the pulse function would only depend upon x', resulting in the numerator of the rhs of (2.37) being a cross correlation of $w(x)p(x)$ and $f(x)$. Because of the fixed data boundaries at x_L and x_R, however, the scenario pictured in Fig. 2.11b does not hold and the problem investigated by P90 needs to be reexamined.

---

[12] P90 treated the numerator on the rhs of (P2b) as a *convolution* of $w_{x_0}(x)$ and $f(x)$, where $w_{x_0}(x) = w(x, \lambda_0)p(x)$, when it is actually a *cross correlation* of $w_{x_0}(x)$ and $f(x)$. The two operations

would be equal if $w_{j,n}(-x) = w_{j,n}(x)$. This does not hold, however, for (P2b).

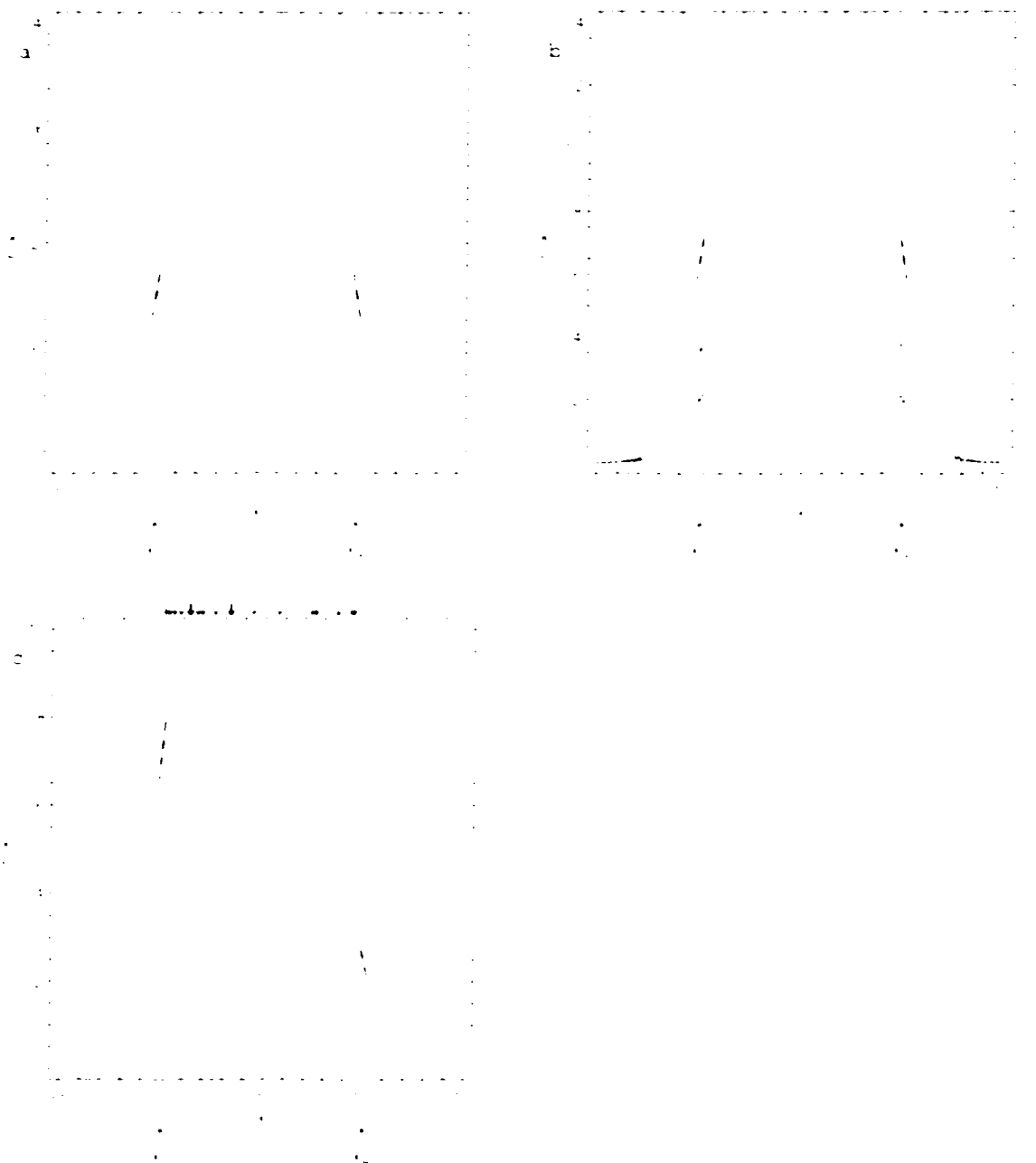

FIG. 2.10. Examples of the spatial dependence of the normalization factor $n(x)$ for (a) a continuous, bounded case, (b) three discrete, regularly-distributed cases, and (c) a discrete, irregularly-distributed case. Thick-dashed lines indicate observational domain boundaries in (a) and (b) and the limits of the possible observation locations in (c), with actual observation locations in (c) denoted by arrows. In (b), the dotted, thin-dashed, and solid lines are for observational spacings of 1, 0.5, and 0.25, respectively. The figure in (a) corresponds to the analysis results shown in Fig. 2.12 while (c) corresponds to the analysis results shown in Fig. 2.13. Data for (b) are courtesy of P. Pauley. The weight function for (a-c) is $w(x) = \exp(-x^2/\kappa_d)$, with $\kappa_d = 3$.

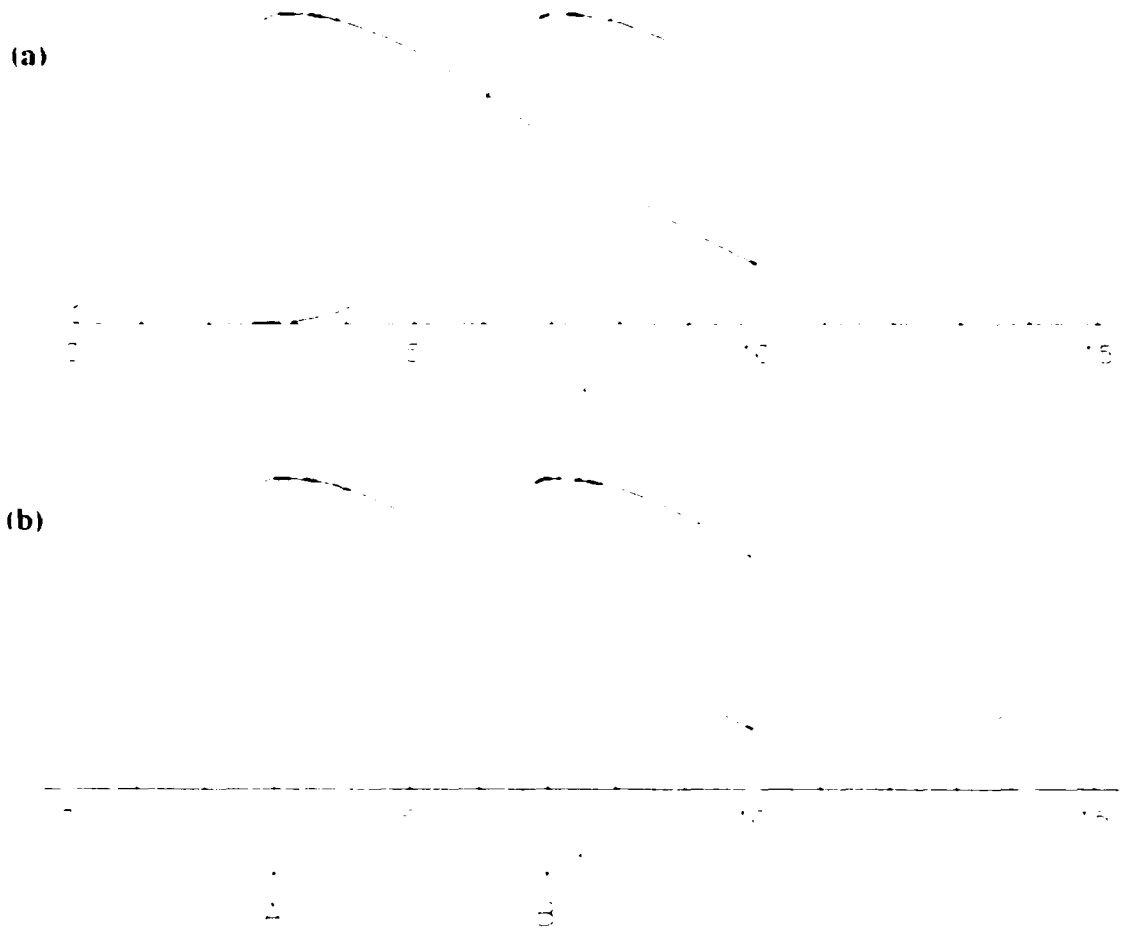

FIG. 2.11. Illustrations of two types of unnormalized [not divided by $n(x)$] windows for DDWA analyses of one-dimensional, continuous, bounded data. (a) Examples of unnormalized windows at points A and B for an actual analysis. (b) Examples of (equivalent) theoretical unnormalized windows at points A and B. In (a), the thick-dashed line represents the pulse function. In (b), the thick-dashed line represents the pulse function for point A and the thick-dotted line represents the equivalent pulse function at point B. In both (a) and (b) the solid line represents $w(x')$ for point A and the thin-dashed line represents $w(x')$ for point B. The $w(x')$ shown in (a) and (b) is not special; in this analysis $w(x')$ is arbitrary.

2.2.2.2.2 The Solution

This quandary can be resolved by defining a hypothetical analysis for which the scenario in Fig. 2.11b holds—that is, the same window applies across the entire analysis domain. Owing to its equivalent treatment of data across the analysis domain, such an analysis is called herein an "equivalent analysis". To produce an equivalent analysis for this situation, consider the actual analysis at some point, like point A in Fig. 2.11. Further, suppose that observations are available not just *within* the observational domain (i.e., from x_I to x_R) but *throughout* the equivalent analysis domain $(-\infty,\infty)$. The equivalent analysis field $f_{EA}(x, x_{ref} = \mathrm{A})$ is then produced by using, throughout the entire equivalent analysis domain, the same weight and pulse functions (i.e., the same window) that are used in the actual analysis at point A. (The symbol x_{ref} represents the reference location, in this case point A, for which a response function is desired.) In this imaginary analysis, therefore, each point in the infinite domain "sees" the same relative distribution of observations as the actual analysis "sees" at point A. Because of its equal treatment across an infinite domain, this construction allows an explicit expression of the response function using Fourier theory for one-dimensional, continuous, infinite data.

Mathematically, the equivalent analysis field can be expressed as

$$f_{EA}(x, x_{ref}) = \frac{\int_{x_I - x}^{x_R - x} f(x_o) w(x_o - x)\, dx_o}{\int_{x_I - x}^{x_R - x} w(x_o - x)\, dx_o}. \qquad (2.40)$$

Note that the hypothetical equivalent analysis value at each x is different for each equivalent analysis (i.e., each reference location x_{ref}). Because within each equivalent analysis x_R, x_L, and x_{ref} are constant, the normalization factor in the denominator of (2.40) is constant. This is more obvious when (2.40) is transformed using the substitution $x' = x_i - x$, which results in

$$f_{EA}(x, x_{ref}) = \frac{\int f(x + x') w(x') dx'}{n_{EA}(x_{ref})} = \frac{\int f(x + x') p_{EA}(x', x_{ref}) w(x') dx'}{n_{EA}(x_{ref})}, \quad (2.41)$$

where

$$n_{EA}(x_{ref}) = \int w(x') dx' = \int p_{EA}(x', x_{ref}) w(x') dx' \quad (2.42)$$

is the equivalent analysis normalization factor and the equivalent analysis pulse function $p_{EA}(x', x_{ref})$ is given by

$$p_{EA}(x', x_{ref}) = \begin{cases} 1 & x_L - x_{ref} \le x' \le x_R - x_{ref} \\ 0 & \text{otherwise} \end{cases}. \quad (2.43)$$

Because within each equivalent analysis x_{ref} is constant, $p_{EA}(x', x_{ref})$ depends only upon x'. Consequently, for each equivalent analysis, the numerator and denominator on the rhs of (2.41) are

$$\int f(x + x') p_{EA}(x', x_{ref}) w(x') dx' = w(x) p_{EA}(x, x_{ref}) \bigstar f(x)$$

$$= w(-x) p_{EA}(-x, x_{ref}) * f(x)$$

$$= w_{eff}(-x, x_{ref}) * f(x) \quad (2.44)$$

and

$$n_{EA}(x_{ref}) = \int_{-\infty}^{\infty} w_{eff}(x', x_{eff})\,dx'. \tag{2.45}$$

respectively. The "effective" weight function $w_{eff}(x, x_{ref}) = w(x)\,p_{EA}(x, x_{ref})$, which is the product of the weight function and the pulse function, embodies the actual weights that are applied to the observations during equivalent analyses [cf. (2.41)].

Using (2.44), (2.41) can be expressed as

$$f_{EA}(x, x_{ref}) = \frac{w(-x)\,p_{EA}(-x, x_{ref}) * f(x)}{n_{EA}(x_{ref})} = \frac{w_{eff}(-x, x_{ref}) * f(x)}{n_{EA}(x_{ref})}. \tag{2.46}$$

This expression illustrates an important difference between the actual and equivalent analyses. In the actual analysis (2.37), the pulse function is associated with the observation field $f(x)$; in the equivalent analysis (2.46), the pulse function is associated with weight function $w(x)$. The equivalent analysis construct results in the pulse function moving across the convolution symbol.

The Fourier transform of (2.46) and the application of the convolution theorem produce the response function

$$\mathcal{R}(\nu, x_{ref}) = \frac{F_{EA}(\nu, x_{ref})}{F(\nu)} = \frac{\mathrm{FT}[w_{eff}(-x, x_{ref})]}{n_{EA}(x_{ref})}, \tag{2.47}$$

where the fact that $n_{EA}(x_{ref})$ is constant for each x_{ref} has been used. The term $\mathrm{FT}[w_{eff}(-x, x_{ref})]$ can be expressed in a more useful form by using the similarity theorem, the definition of the Fourier transform, and the definition of $p_{EA}(x, x_{ref})$. From the similarity theorem, if $\mathrm{FT}[w_{eff}(x, x_{ref})] = W_{eff}(\nu, x_{ref})$, then

$\mathrm{FT}[w_{c_{x_{c_x}}}(-x, x_{c_x})] = W_{c_{x_{c_x}}}(-v, x_{c_x})$. Using the definitions of the Fourier transform and of $p_{EA}(x, x_{c_x})$, $W_{c_{x_{c_x}}}(v, x_{c_x})$ can be expressed as

$$W_{c_{x_{c_x}}}(v, x_{c_x}) = \int w(x)\cos(2\pi v x)\,dx + j\left[-\int w(x)\sin(2\pi v x)\,dx\right]. \qquad (2.48)$$

Substituting $-v$ for v in (2.48) to get $\mathrm{FT}[w_{c_{x_{c_x}}}(-x, x_{c_x})]$, as dictated by the similarity theorem, and inserting the result into (2.47) produces

$$\mathcal{R}(v, x_{c_x}) = \frac{\int w(x)\cos(2\pi v x)\,dx}{n_{EA}(x_{c_x})} - j\frac{-\int w(x)\sin(2\pi v x)\,dx}{n_{EA}(x_{c_x})}. \qquad (2.49)$$

This is the response function for DDWA analyses of one-dimensional, continuous, bounded data. The only assumption concerning the weight function is that the integrals in (2.40)-(2.42) and (2.44)-(2.49) exist. A well-known (e.g., Caracena et al. 1984; Achtemeier 1986; P90) consequence of data boundaries is indicated in (2.49): *when data are bounded, the response function depends upon the weight function* $w(x)$, *the frequency* v, *and the location* x_{c_x}.

At this point it is instructive to relate this result to that of P90. P90 applied the Fourier transform to (P2b) and then utilized the convolution theorem and the pulse function definition for (P2b) to obtain an explicit expression for the response function. It has already been shown [cf. (2.39)] that when the correct version of (P2b), namely (2.37), is used, this methodology does not result in an explicit expression for the response function. How, then, did P90 obtain an explicit expression for the response function? The answer is that the incorrect definition of the pulse function in (P2b)

emulates equivalent analyses. To examine the local response function for analysis points located at or near a boundary, P90 utilized a pulse function that fixed the boundaries relative to each analysis point. The difficulty is, in DDWA analyses boundaries relate to observation, rather than analysis, locations. The concept of an equivalent analysis, as in (P2b), allows the boundaries to be specified relative to analysis locations.

With the incorrect definition of the pulse function, the normalization factor in (P2b) is constant and the pulse function depends only upon x'. In fact, with $x_1 = x_I - x_{n_x}$ and $x_2 = x_R - x_{n_x}$, P90's response function (P4), which in slightly modified form is given by

$$\mathcal{R}(\nu, x_{n_x}) = \frac{\int_{x_1}^{x_2} w(x)\cos(2\pi\nu x)\,dx}{\int_{x_1}^{x_2} w(x)\,dx} + j\frac{\int_{x_1}^{x_2} w(x)\sin(2\pi\nu x)\,dx}{\int_{x_1}^{x_2} w(x)\,dx}, \qquad \text{(P4)}$$

is equivalent to (2.49). This equivalence is somewhat puzzling, however, since P90 incorrectly regarded (P2b) as a convolution rather than a cross correlation, which should lead to a negative sign in the imaginary term in (P4). P90 does not give sufficient detail in the derivation of (P4) to definitively resolve this sign problem. It is possible that a sign error was made when P90 set up the Fourier integrals. If so, this error resulted in (P90) obtaining the correct response function. Another possibility is that the alternative definition of the (direct) Fourier transform $F_{WLT}(\nu) = \int_{x=-\infty}^{x=\infty} f(x)\exp(j2\pi\nu x)\,dx$ was used and that no sign error was committed when the Fourier integrals were set up. Considering that Pauley and Wu (1990) used the same (direct) Fourier transform as

used herein, however, this seems unlikely. In any case, despite the pulse function problems, if (P2b) were correctly treated as a cross correlation, if the Fourier integrals were correctly set up, and if the same (direct) Fourier transform were used, (P4) would be equivalent to (2.49). The incorrect treatment of (P2b) as a convolution leads to a sign error in the imaginary term of the response function. The consequence is a difference in the sign of the phase shift undergone during analysis, as illustrated presently.

2.2.2.2.3 Verification

The application of the similarity theorem in the derivation of (2.49) resulted in a change in the sign of the imaginary term. Consequently, (2.49) is the complex conjugate of $\mathrm{FT}[w_{r,w}(x,x_{rc})]/n_{FA}(x_{rc}) = W_{r,w}(v,x_{rc})/n_{FA}(x_{rc}) = W_{\zeta}(v,x_{rc})$ and is denoted here as $W_{\zeta}^{*}(v,x_{rc})$. The important result that *the local response function is the complex conjugate of the normalized Fourier transform of the effective weight function* is succinctly expressed as

$$\mathcal{R}(v,x_{rc}) = W_{\zeta}^{*}(v,x_{rc}). \tag{2.50}$$

In (2.50), $W_{\zeta}^{*}(v,x_{rc}) = W_{\zeta\,\mathrm{Re}}(v,x_{rc}) - jW_{\zeta\,\mathrm{Im}}(v,x_{rc})$.

Using the definition of the response function, the Fourier coefficients of the equivalent analysis field can be expressed in polar form as

$$F_{FA}(v,x_{rc}) = |F(v)||W_{\zeta}^{*}(v,x_{rc})|\exp[j(\varphi_{F(v)} + \varphi_{W_{\zeta}^{*}(v,x_{rc})})], \tag{2.51}$$

where $|F(v)|$ and $|W_{\zeta}^{*}(v,x_{rc})|$ are the magnitudes of $F(v)$ and $W_{\zeta}^{*}(v,x_{rc})$ and $\varphi_{F(v)} = \arg[F(v); F_{\mathrm{Re}}(v), F_{\mathrm{Im}}(v)]$ and

$\varphi_{W_\nu^*(\nu,x_{ref})} = \arg\left[W_\nu^*(\nu,x_{ref}),W_{\nu\,\mathrm{Re}}(\nu,x_{ref}),-W_{\nu\,\mathrm{Im}}(\nu,x_{ref})\right]$ are the phases, or arguments, of $F(\nu)$ and $W_\nu^*(\nu,x_{ref})$.[13] Using (A10) from appendix A, $f_{\Delta I}(x,x_{ref})$ can be written as

$$f_{\Delta I}(x,x_{ref}) = \int_{\nu=0}^{\infty} \frac{2}{1+\delta^0(\nu)} |F(\nu)| |W_\nu^*(\nu,x_{ref})| \cos\left(2\pi\nu x + \varphi_{F(\nu)} - \varphi_{W_\nu^*(\nu,x_{ref})}\right) d\nu, \quad (2.52)$$

where $\delta^0(\nu)$ is 0 except for at $\nu = 0$, where it is 1, and the fact that $\varphi_{W_\nu^*(\nu,x_{ref})} = -\varphi_{W_\nu(\nu,x_{ref})}$ has been utilized. Equation (2.52) shows exactly what happens to each Fourier coefficient during an analysis. During an analysis, the amplitude of each Fourier coefficient is modified by the factor

$$|W_\nu^*(\nu,x_{ref})| = |W_\nu(\nu,x_{ref})| = \left[W_{\nu\,\mathrm{Re}}(\nu,x_{ref})^2 + W_{\nu\,\mathrm{Im}}(\nu,x_{ref})^2\right]^{1/2} \quad (2.53)$$

and the phase of each Fourier coefficient is altered by

$$-\varphi_{W_\nu(\nu,x_{ref})} = -\arg\left[W_\nu(\nu,x_{ref}),W_{\nu\,\mathrm{Re}}(\nu,x_{ref}),W_{\nu\,\mathrm{Im}}(\nu,x_{ref})\right]. \quad (2.54)$$

The response function (2.49) can now be verified by using it to predict analysis values and by comparing these predicted analysis values to actual analysis values obtained using (2.33) or (2.36). This has been accomplished using "observation" fields of the form

$$f(x_j) = A_i \cos(2\pi\nu_i x_j), \quad (2.55)$$

where A_i is the amplitude and $\nu_i > 0$ is the frequency of the input field. To perform these tests, knowledge of $F_{\mathrm{Re}}(\nu)$ and $F_{\mathrm{Im}}(\nu)$ is needed to evaluate $|F(\nu)|$ and $\varphi_{F(\nu)}$,

[13] The representation of the argument function arg in the form $\arg\left[F(\nu),F_{\mathrm{Re}}(\nu),F_{\mathrm{Im}}(\nu)\right]$ means the argument of $F(\nu)$, which depends upon $F_{\mathrm{Re}}(\nu)$ and $F_{\mathrm{Im}}(\nu)$. The argument of $F(\nu)$ is the angle $\varphi_{F(\nu)}$ such that $|F(\nu)|\cos\varphi_{F(\nu)}$ is the real part of $F(\nu)$ and $|F(\nu)|\sin\varphi_{F(\nu)}$ is the imaginary part of $F(\nu)$; it is the

[since (2.52) is to be utilized, only v values greater than or equal to zero are of concern]. For the input field (2.55) with $v_i > 0$, $F_{Re}(v) = \frac{A_i}{2}\delta(v - v_i)$ and $F_{Im}(v) = 0$, where $\delta(x)$ is the Dirac distribution (Bracewell 2000, 74-85).[14,15] These result in $|F(v)| = \frac{|A_i|}{2}\delta(v - v_i)$ and $\varphi_{F(v)} = 0, \pi$, depending upon whether A_i is positive or negative, respectively. For the input field (2.55) with $v_i > 0$, therefore, (2.52) becomes

$$f_{FA}(x, x_{ref}) = |A_i||W_v^*(v_i, x_{ref})|\cos(2\pi v_i x + \varphi_{F(v_i)} - \varphi_{W_v^*(v_i, x_{ref})}), \qquad (2.56)$$

where the sifting property of the Dirac distribution, $\int_{-\infty}^{\infty}\delta(x-a)f(x)dx = f(a)$ (Bracewell 2000, p. 79), has been exploited and the fact that $\delta^{(1)}(v_i) = 0$ if $v_i \neq 0$ has been utilized. Because the response in (2.49) and (2.50) is valid only at $x = x_{ref}$, $f_{FA}(x, x_{ref})$ values from (2.56) are relevant to the actual analysis values only when $x = x_{ref}$ in (2.56).

Actual and predicted analysis fields for $x_I = 0$, $x_R = 10$, $A_i = 1$, $v_i = 1/3$, and $w(x) = \exp(-x^2/\kappa_x^2)$, with $\kappa_x = 3$, are shown in Fig. 2.12a. This figure confirms the

---

angle in the complex plane that the vector, originating from zero and ending at $F(v)$, makes with the positive x-axis.

[14] The real component of $F(v)$ for an input field given by (2.55) is $F_{Re}(v) = \frac{A}{2}\delta(v - v_i) + \frac{A}{2}\delta(v + v_i)$, which can be expressed as $F_{Re}(v) = \frac{A}{2}\delta(|v| - |v_i|)$. Since the one sided spectrum is being utilized ($v \geq 0$) and since $v_i > 0$, the second term is zero and $F_{Re}(v) = \frac{A}{2}\delta(v - v_i)$.

[15] The terms Dirac distribution and comb distribution (next section) are used instead of the terms Dirac delta-function and comb function since, strictly speaking, these are not functions, but are *distributions* (or generalized functions). Distribution theory is beyond the scope of this study. Fortunately, for the

veracity of (2.49) since it shows that the predicted analysis values (plus-sign symbols), obtained using (2.49), match the actual analysis values (solid line).

Predicted analysis values obtained using a response function derived under the incorrect assumption that DDWA entails convolution, instead of cross correlation, are illustrated by the thin-dashed line in Fig. 2.12a. As this line indicates, this incorrect response function, given by (P4) with a negative sign preceding the imaginary component, does not correctly predict analysis values. The difference between (2.49) and this incorrect response function can be understood by noting that a repetition of the above analysis for the incorrect response function results in a positive, rather than negative, sign in front of $\varphi_{W_\zeta(\nu,x_{\alpha_0})}$ in (2.52) and (2.56). The response function that results from incorrectly treating DDWA as a convolution correctly specifies the amplitude modulation and the phase shift magnitude but incorrectly specifies the sign of the phase shift. It results in an incorrect response function that is the complex conjugate of the correct response function (2.50).

The amplitude $|W_\zeta^*(\nu,x_{\alpha_0})|$ (solid line, left axis), phase $\varphi_{W_\zeta(\nu,x_{\alpha_0})}$ (thin-dashed line, right axis), and ideal-amplitude (dotted line, left axis) modulations for the test illustrated in Fig. 2.12a are shown in Fig. 2.12b. The ideal amplitude modulation is the response function for infinite, continuous data and is thus also referred to as the ideal response function. [For the weight function used in these tests, the ideal response function is $\mathcal{R}_1(\nu)=\exp\left[-\kappa_d(\pi\nu)^2\right]$ (Barnes 1964).] As Fig. 2.12b indicates, the

---

operations used herein the distributions considered behave much like functions. For those who are interested, Bracewell (2000) provides a relatively straightforward introduction to distribution theory.

response is nearly ideal in the central portions of the observational domain. For $x \leq \sim 3$ and $x \geq \sim 7$, however, the boundaries affect the analysis and force non-ideal results.

The phase shifts experienced near and outside of the observational domain boundaries are particularly illuminating. Since positive values of $\varphi_{w_{\lambda}(x_0,t_0)}$ result in shifting the input wave to the right while negative values of $\varphi_{w_{\lambda}(x_0,t_0)}$ result in leftward shifts [cf. (2.56)], it is apparent that near the boundaries the analysis obtains information from towards the center of the observational domain. This also holds true outside of the observational domain up to a certain distance from the domain boundaries. At that point the phase shift changes from $\pm 180^\circ$ to $\mp 180^\circ$, with the phase-shift values oscillating with increasing distance from the domain boundaries. These oscillations result from the constraint that $-180^\circ \leq \varphi_{w_{\lambda}(x_0,t_0)} \leq 180^\circ$, which was imposed during the calculations. This constraint does not necessarily produce the correct value of $\varphi_{w_{\lambda}(x_0,t_0)}$. Strictly speaking, any $\varphi_{w_{\lambda}(x_0,t_0)} = \varphi + n(360^\circ)$, where $-180^\circ \leq \varphi \leq 180^\circ$ and n is an integer, could be considered valid at any point since 360°-increment changes in $\varphi_{w_{\lambda}(x_0,t_0)}$ do not alter the results of (2.56). Within the observational domain it appears as if the restricted $\varphi_{w_{\lambda}(x_0,t_0)}$ values are correct since the analysis does not need to look very far away to obtain information. This is not true, however, for analysis points outside of the observational domain. Consider the situation at $x = 12$, where (the restricted) $\varphi_{w_{\lambda}(x_0,t_0)} = -68.69^\circ$. Since the nearest information is two units away, which corresponds to 240° for this wave (wavelength of $\lambda = 3$), it seems that the correct phase shift value at this point is $+291.31^\circ$. Note that this value implies a physically

plausible rightward migration of information for this point. From reasoning that is supported by the phase shift values near the data boundaries, consequently, it appears that the correct phase shift values for points outside of the observational domain result from incrementing the restricted phase shift values by an appropriate multiple of 360°. To the right (left) of the observational domain, the corrected phase-shift values increase (decrease) monotonically with increasing distance from the rightmost (leftmost) data boundary.

The interpretation of analysis consequences in terms of the amplitudes and phases of the Fourier components, therefore, facilitates understanding. For the analysis illustrated in Fig. 2.12, for example, extrapolation is achieved by shifting information contained within the observational domain to points outside of the observational domain. This statement, moreover, appears to be fundamental to *all* extrapolations. A further consequence of the extrapolation illustrated in Fig. 2.12 is decreasing filtering with increasing extrapolation distance. This is indicated in Fig. 2.12b by the increasing amplitude modulation with increasing distance from the observational domain. It is not known if this is a fundamental attribute of all extrapolation schemes.

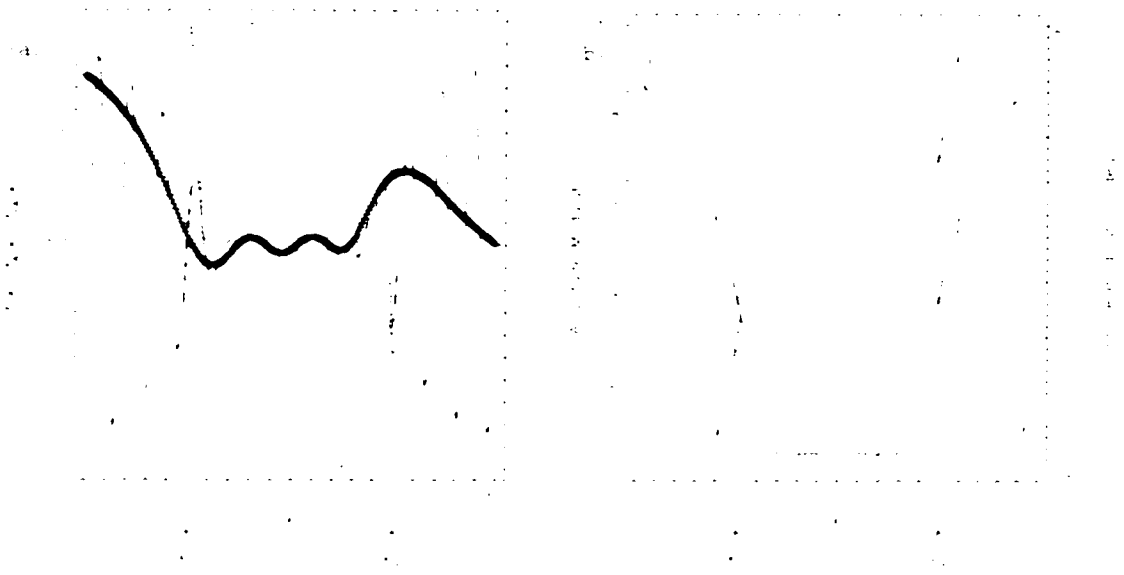

FIG. 2.12. (a) The input field (dotted line) and actual (solid line), response-function predicted (plus-sign symbols), and complex conjugate response-function predicted (thin-dashed line) analysis fields for a DDWA analysis of one-dimensional, continuous, bounded data. (b) The amplitude (solid line, left axis) and phase (thin-dashed line, right axis) modulation functions and the ideal response function (dotted line, left axis) for the test shown in (a). In both (a) and (b) the thick-dashed lines indicate the observational domain boundaries. The observational field is given by $f(x) = A_1 \cos(2\pi\nu_1 x)$, with $A_1 = 1$, $\nu_1 = 1/3$, and the weight function is given by $w(x) = \exp(-x^2/\kappa_a)$, with $\kappa_a = 3$.

2.2.2.3 Discrete, Irregularly-Distributed Data

2.2.2.3.1 Derivation

For simplicity, the problem considered is again one-dimensional. In this situation, the analysis field $f_A(x)$ is determined using (2.36), which is repeated here for convenience and is

$$f_A(x) = \frac{\sum_{i=1}^{N} f(x_{o_i}) w(x_{o_i} - x)}{\sum_{i=1}^{N} w(x_{o_i} - x)}, \tag{2.57}$$

where $f(x_{o_i})$ denotes the i^{th} observation and N is the total number of observations. (Note that this derivation is designed for the case where the number of observations is finite. It could easily be modified for analyses involving an infinite number of observations.) As in Caracena et al. (1984) and Pauley and Wu (1990), the observation locations can be described using a comb distribution (rather than a pulse function). Comb distributions are typically defined (e.g., Weaver 1983, p. 131) as infinite trains of equally-spaced Dirac distributions. In this case, however, the irregular data spacing requires what is called here an *irregular* comb distribution, which is given by

$$\text{icomb}(x_{o_i}) = \sum_{i=1}^{N} \delta(x_{o_i} - x_{o_i}), \tag{2.58}$$

where $\delta(x)$ is the Dirac distribution. The sifting property of the Dirac distribution, together with (2.58), allows (2.57) to be expressed in the form

$$f_A(x) = \frac{\int_{x_{o_i}=-\infty}^{x_{o_i}=\infty} f(x_{o_i})\,\text{icomb}(x_{o_i})\,w(x_{o_i} - x)\,dx_{o_i}}{n(x)}, \tag{2.59}$$

where the normalization factor $n(x)$ is given by $n(x) = \sum_{1}^{k} w(x_{ij} - x)$.

With the substitution $x' = x_{ij} - x$, (2.59) can be rewritten as

$$f_1(x) = \frac{\int f(x + x')\,\mathrm{icomb}(x + x')\,w(x')\,dx'}{n(x)}. \tag{2.60}$$

As in the bounded, continuous case, both $n(x)$ and $\mathrm{icomb}(x + x')$ depend upon x. In this situation, the numerators of (2.59) and (2.60) are $w(x)\bigstar f(x)\mathrm{icomb}(x) = w(-x) * f(x)\mathrm{icomb}(x)$. Thus, a succinct expression for (2.59) and (2.60) is

$$f_1(x) = \frac{w(-x) * f(x)\mathrm{icomb}(x)}{n(x)}. \tag{2.61}$$

Attempting to determine an explicit expression for the response function by taking the Fourier transform of (2.61)[16] produces

$$F_1(v) = \int M(\xi)\,N_I(v - \xi)\,d\xi, \tag{2.62}$$

where $M(v) = \mathrm{FT}[w(-x) * f(x)\mathrm{icomb}(x)]$, $N_I(v) = \mathrm{FT}[1/n(x)]$, ξ denotes frequency dependence, and the product theorem has been applied. Using the convolution, similarity, and product theorems, $M(v)$ can be expressed as

[16] As in the case for continuous, bounded data, the domain of this analysis field is considered to be continuous and infinite.

$M(\nu) = W(-\nu) \int_{\psi=-\infty}^{\psi=\infty} F(\psi)\mathrm{ICOMB}(\nu-\psi)d\psi$ [17], where ψ denotes frequency dependence.

Substituting this into (2.62) results in

$$F_1(\nu) = \int_{\xi=-\infty}^{\xi=\infty} \left[\int_{\psi=-\infty}^{\psi=\infty} F(\psi)\mathrm{ICOMB}(\xi-\psi)d\psi \right] W(-\xi)N_I(\nu-\xi)d\xi. \qquad (2.63)$$

As with (2.39), the response function cannot be expressed explicitly using (2.63). Moreover, rearranging (2.61) prior to applying the Fourier transform does not help produce an explicit expression for the response function.

Again, the artifice of an equivalent analysis allows the determination of the local response function. Consider the hypothetical situation in which the observation field is known everywhere and an equivalent analysis field $f_{EA}(x, x_{ref})$ is produced using, for all points in the equivalent-analysis domain $(-\infty,\infty)$, the same relative distribution of observations and weights that is used to produce an actual analysis value at the point x_{ref}. The non-weight component of the window through which the observations are "seen" is, in this case, a sliding irregular comb, as opposed to the sliding pulse function employed earlier in the equivalent analyses of continuous, bounded data. This equivalent analysis field is given by

$$f_{EA}(x, x_{ref}) = \frac{\int_{x'=-\infty}^{x'=\infty} f(x+x')\,\mathrm{icomb}_{EA}(x', x_{ref})w(x')dx'}{n_{EA}(x_{ref})}. \qquad (2.64)$$

---

[17] The Fourier transform of the product of a function $f(x)$ and a comb distribution can be interpreted using the sifting property of the Dirac distribution, as shown in Bracewell (2000, p. 138). In the case

where

$$n_{EA}(x_{ref}) = \sum_{n=1}^{N} w(x_n - x_{ref}) = \int_{x'=-\infty}^{\infty} \text{icomb}_{EA}(x', x_{ref})\, w(x')\, dx' \tag{2.65}$$

is the equivalent analysis normalization factor and the equivalent analysis irregular comb distribution is

$$\text{icomb}_{EA}(x', x_{ref}) = \sum_{n=1}^{N} \delta[x' - (x_n - x_{ref})]. \tag{2.66}$$

Within each equivalent analysis x_{ref} and $n_{EA}(x_{ref})$ are constant and $\text{icomb}_{EA}(x', x_{ref})$ depends only upon x'. Hence, in this situation the numerator and denominator of (2.64) are

$$\begin{aligned} \int_{x'=-\infty}^{\infty} f(x + x')\, \text{icomb}_{EA}(x', x_{ref})\, w(x')\, dx' &= w(x)\, \text{icomb}_{EA}(x, x_{ref}) \bigstar f(x) \\ &= w(-x)\, \text{icomb}_{EA}(-x, x_{ref}) * f(x) \\ &= w_{eq}(-x, x_{ref}) * f(x) \end{aligned} \tag{2.67}$$

and

$$n_{EA}(x_{ref}) = \int_{x'=-\infty}^{\infty} w_{eq}(x', x_{ref})\, dx'. \tag{2.68}$$

respectively. The effective weight function $w_{eq}(x, x_{ref}) = w(x)\, \text{icomb}_{EA}(x, x_{ref})$ embodies not only the structure of the weight function but also the distribution of the observations about the point x_{ref}.

---

where $f(x) = 1$, this produces the Fourier transform of the comb distribution. For the comb distribution given by (2.58), $\text{ICOMB}(\nu) = \sum_{n=1}^{N} \exp(-j2\pi\nu x_n)$.

The following determination of the response function proceeds as in the continuous, bounded case. With (2.67), (2.64) can be expressed as

$$f_{EA}(x, x_{ref}) = \frac{w(-x)\text{icomb}_{EA}(-x, x_{ref}) * f(x)}{n_{EA}(x_{ref})} = \frac{w_{eff}(-x, x_{ref}) * f(x)}{n_{EA}(x_{ref})}. \qquad (2.69)$$

As in the continuous, bounded case, (2.69) illustrates an important difference between the actual and equivalent analyses. In the actual analysis (2.61), the irregular comb distribution is associated with the observation field $f(x)$; in the equivalent analysis (2.69), the irregular comb distribution is associated with the weight function $w(x)$. The equivalent analysis construct, in a manner similar to that in the continuous, bounded case, results in the irregular comb distribution moving across the convolution symbol.

The Fourier transform of (2.69) and the application of the convolution theorem produce the response function

$$\mathcal{R}(v, x_{ref}) = \frac{F_{EA}(v, x_{ref})}{F(v)} = \frac{\text{FT}[w_{eff}(-x, x_{ref})]}{n_{EA}(x_{ref})}. \qquad (2.70)$$

where the fact that $n_{EA}(x_{ref})$ is constant for each x_{ref} has been used. The similarity theorem indicates that if $\text{FT}[w_{eff}(x, x_{ref})] = W_{eff}(v, x_{ref})$, then $\text{FT}[w_{eff}(-x, x_{ref})] = W_{eff}(-v, x_{ref})$. Using the definitions of the Fourier transform and of $\text{icomb}_{EA}(x, x_{ref})$, $W_{eff}(v, x_{ref})$ can be expressed as (see footnote 17)

$$\begin{aligned} W_{eff}(v, x_{ref}) = &\sum_{n=1}^{N} w(x_n - x_{ref})\cos[2\pi v(x_n - x_{ref})] \\ &+ j\left\{-\sum_{n=1}^{N} w(x_n - x_{ref})\sin[2\pi v(x_n - x_{ref})]\right\}. \end{aligned} \qquad (2.71)$$

Substituting $-v$ for v in (2.71) to get $\mathrm{FT}[w_{em}(-x, x_{ei})]$, as dictated by the similarity theorem, and inserting the result into (2.70) produces

$$\mathcal{R}(v, x_{ei}) = \frac{\sum_{n=1}^{N} w(x_n - x_{ei})\cos[2\pi v(x_n - x_{ei})]}{n_{EA}(x_{ei})} - j\frac{-\sum_{n=1}^{N} w(x_n - x_{ei})\sin[2\pi v(x_n - x_{ei})]}{n_{EA}(x_{ei})} \tag{2.72}$$

As in the case for continuous, bounded data, the response function for DDWA analyses of discrete, irregularly-distributed data depends upon *the weight function* $w(x)$, *the frequency* v, *and the location* x_{ei}.

2.2.2.3.2 Verification

The response function (2.72) is tested by using it to predict analysis values and by comparing these values to actual analysis values obtained using (2.57). As in the continuous, bounded case, the input to these tests is prescribed by (2.55). Furthermore, since in this case $\mathcal{R}(v, x_{ei}) = \mathrm{FT}[w_{em}(-x, x_{ei})]/n_{EA}(x_{ei}) = W_\zeta^*(v, x_{ei})$, as in the continuous, bounded case [(2.49) and (2.50)], the analysis from (2.50) to (2.56) applies here also. In this case, of course, $W_\zeta^*(v, x_{ei})$ is given by (2.72) rather than by (2.49).

Actual and predicted analysis fields for $A_1 = 1$, $v_1 = 1/5$, $N = 20$, and $w(x) = \exp(-x^2/\kappa_w^2)$, with $\kappa_w = 3$, are shown in Fig. 2.13a. (Each x_n was obtained using a pseudo-random number generator and was restricted such that $x_L \le x_n < x_R$, with $x_L = 0$ and $x_L = 10$.) In this figure the limits of the possible x_n values are

indicated by thick-dashed lines, the input field is indicated by the dotted line, observations are indicated by diamond symbols, observation locations are indicated by the small arrows at the top of the figure, the analyzed field is indicated by the solid line, and the predicted [using (2.56)] analysis values are indicated by the plus-sign symbols. As this figure shows, (2.72) is correct since it predicts actual analysis values.

The amplitude $|W_\lambda^*(\nu, x_{ref})|$ and phase $\varphi_{W_\lambda(\nu, x_{ref})}$ modulations for the test illustrated in Fig. 2.13a are shown in Fig. 2.13b. Except for the arrows that indicate observation locations along the top of this figure, the elements of Fig. 2.13b are as in Fig. 2.12b, with the amplitude modulation field (left axis) indicated by the solid line, the phase modulation field (right axis) indicated by the thin-dashed line, and the ideal amplitude modulation field, or ideal response, (left axis) indicated by the dotted line. In this case, amplitude modulations are generally far from ideal and significant phase shifts are common. (The presence of significant phase shifts in Fig. 2.13b is consistent with the misalignment in Fig. 2.13a of the maxima and minima of the input and analysis fields.) Figure 2.13 illustrates well the impact an irregular observational distribution can have. When observations are irregularly distributed, the response can be far from ideal both within and outside of the observational domain limits.

The phase shift values that are outside of the observational domain limits in Fig. 2.13b behave similarly to the phase shift values that are outside of the observational domain limits in Fig. 2.12b. Because the $\varphi_{W_\lambda(\nu, x_{ref})}$ values plotted in Fig. 2.13b were restricted as they were in Fig. 2.12b, i.e. such that $-180^\circ \le \varphi_{W_\lambda(\nu, x_{ref})} \le 180^\circ$, the extrapolation phase shift discussion of section 2.2.2.2.3 applies here as well. A plot of

corrected $\varphi_{w,\ldots,\ldots}$ values would thus indicate monotonically increasing (decreasing) phase shifts with increasing distance to the right (left) of the rightmost (leftmost) observational domain limit. As with the continuous, bounded case, extrapolation is achieved by shifting information contained within the observational domain to points outside of the observational domain.

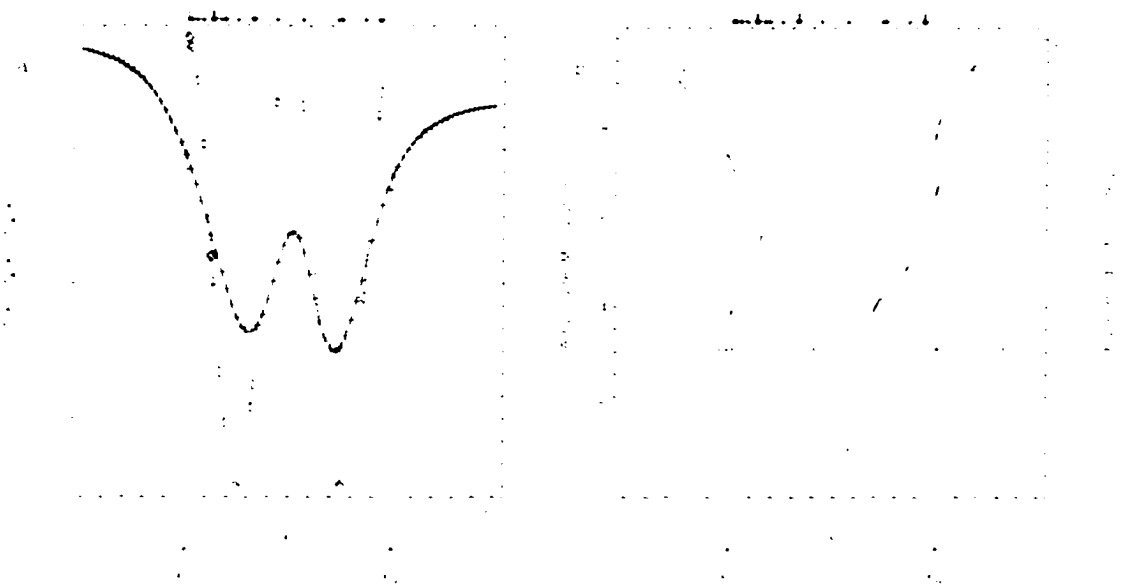

FIG. 2.13. (a) The input field (dotted line), observations (diamond symbols), and actual (solid line) and response-function predicted (plus-sign symbols) analysis fields for a DDWA analysis of one-dimensional, discrete, irregularly-distributed data. (b) The amplitude (solid line, left axis) and phase (thin-dashed line, right axis) modulation functions and the ideal response function (dotted line, left axis) for the test shown in (a). In both (a) and (b) the thick-dashed lines indicate the limits of possible observation locations and the arrows denote actual observation locations. The observational field is given by $f(x) = A_1 \cos(2\pi\nu_1 x)$, with $A_1 = 1$, $\nu_1 = 1/5$, and the weight function is given by $w(x) = \exp(-x^2/\kappa_d)$, with $\kappa_d = 3$.

2.2.2.4 Extension to Multiple Dimensions

2.2.2.4.1 Derivation

The purpose is to extend the general response function framework to multidimensional problems. To illustrate how this can be accomplished, the simplest multidimensional problem, that concerning two dimensions, is considered here. The extension to three or more dimensions can be accomplished by generalizing the methods presented herein.

In this analysis the direct Fourier transform of $f(x, y)$ is defined to be

$$F(u,v) = \mathrm{FT}[f(x,y)] = \int_{-\infty}^{\infty}\int_{-\infty}^{\infty} f(x,y)\exp[-j2\pi(ux+vy)]dx\,dy\,. \qquad (2.73)$$

where u and v denote frequency and $j = \sqrt{-1}$. The corresponding indirect Fourier transform is defined by

$$f(x,y) = \int_{-\infty}^{\infty}\int_{-\infty}^{\infty} F(u,v)\exp[j2\pi(ux+vy)]du\,dv\,. \qquad (2.74)$$

To illustrate the application of the general response function framework in two-dimensions, the two-dimensional, discrete, irregularly-distributed case is analyzed. To proceed, the expression for distance-dependent weighted averaging (DDWA) analyses of such data must be expressed in a form to which Fourier theory for infinite, continuous data can be applied. The DDWA analysis of discrete, irregularly-distributed, two-dimensional data can be expressed as

$$f_A(x,y) = \frac{\sum_{i=1}^{N} f(x_{in}, y_{in}) w(x_{in} - x, y_{in} - y)}{\sum_{i=1}^{N} w(x_{in} - x, y_{in} - y)}. \tag{2.75}$$

where $f_A(x,y)$ is the analysis field, $f(x_{in}, y_{in})$ denotes the i^{th} observation, N is the total number of observations, and $w(x_{in} - x, y_{in} - y)$ is the weight function. To manipulate (2.75) into the desired form, the two-dimensional impulse symbol (Bracewell 2000, p. 89),

$$^2\delta(x,y) = \delta(x)\delta(y) = \begin{cases} 0 & x^2 + y^2 \neq 0 \\ \infty & x^2 + y^2 = 0, \end{cases} \tag{2.76}$$

is required. This impulse symbol is defined (cf. Bracewell 2000) such that

$$\int_{-\infty}^{\infty}\int_{-\infty}^{\infty} {}^2\delta(x,y)\,dx\,dy = 1 \tag{2.77}$$

and

$$\int_{-\infty}^{\infty}\int_{-\infty}^{\infty} {}^2\delta(x-a, y-b) f(x,y)\,dx\,dy = f(a,b). \tag{2.78}$$

This latter sifting property means that (2.75) can be expressed as

$$f_A(x,y) = \frac{\int_{-\infty}^{\infty}\int_{-\infty}^{\infty} f(x_{in}, y_{in})\, {}^2\mathrm{icomb}(x_{in}, y_{in})\, w(x_{in} - x, y_{in} - y)\,dx_{in}\,dy_{in}}{n(x,y)}, \tag{2.79}$$

where

$${}^2\mathrm{icomb}(x_{in}, y_{in}) = \sum_{i=1}^{N} {}^2\delta(x_{in} - x_{in}, y_{in} - y_{in}) \tag{2.80}$$

and $n(x,y)$ is the normalization factor given by $n(x,y) = \sum_{i=1}^{N} w(x_{in} - x, y_{in} - y)$.

With the substitutions $x' = x_{\alpha} - x$ and $y' = y_{\alpha} - y$, (2.79) can be rewritten as

$$f_A(x,y) = \frac{\int\int f(x+x', y+y') \stackrel{2}{\star} \text{icomb}(x+x', y+y') w(x', y') dx' dy'}{n(x,y)}. \quad (2.81)$$

The numerator on the rhs of (2.81) is the two-dimensional *cross correlation* of $w(x,y)$ with the composite function $f(x,y) \stackrel{2}{\star} \text{icomb}(x,y)$ and is denoted as $w(x,y) \star\star f(x,y) \stackrel{2}{\star} \text{icomb}(x,y)$. By substituting $w(x,y) = w_p(-x,-y)$, thereby defining $w_p(x,y) \equiv w(-x,-y)$, and by subsequently performing the change of variables $X = x + x'$ and $Y = y + y'$, one obtains the result $w(x,y) \star\star f(x,y) \stackrel{2}{\star} \text{icomb}(x,y) = w(-x,-y) ** f(x,y) \stackrel{2}{\star} \text{icomb}(x,y)$, where ** denotes a two-dimensional convolution (Bracewell 2000, p. 331). Thus, (2.81) can be expressed as

$$f_A(x,y) = \frac{w(-x,-y) ** f(x,y) \stackrel{2}{\star} \text{icomb}(x,y)}{n(x,y)}. \quad (2.82)$$

Attempting to determine an explicit expression for the response function by taking the Fourier transform of (2.82) fails because the Fourier transform of $f(x,y)$ becomes bound within convolution integrals, preventing one from obtaining $\mathcal{R}(u,v) = F_A(u,v)/F(u,v)$. One can obtain the response function, however, if the concept of an equivalent analysis is applied. Consider the hypothetical situation in which the observation field is known everywhere and an equivalent analysis field $f_{EA}(x, y, x_{ref}, y_{ref})$ is produced using, for all points in the equivalent-analysis domain, the same relative distribution of observations and weights that is used to produce an

actual analysis value at the point (x_{ref}, y_{ref}). The non-weight component of the window through which the observations are "seen" is, in this case, a sliding, irregular, two-dimensional comb distribution. This equivalent analysis field is given by

$$f_{EA}(x, y, x_{ref}, y_{ref}) = \frac{\int_{-\infty}^{\infty}\int_{-\infty}^{\infty} f(x+x', y+y')\,\text{icomb}_{EA}(x', y', x_{ref}, y_{ref})\,w(x', y')\,dx'dy'}{n_{EA}(x_{ref}, y_{ref})}, \tag{2.83}$$

where

$$\begin{aligned} n_{EA}(x_{ref}, y_{ref}) &= \sum_{i=1}^{N} w(x_i - x_{ref}, y_i - y_{ref}) \\ &= \int_{-\infty}^{\infty}\int_{-\infty}^{\infty} \text{icomb}_{EA}(x', y', x_{ref}, y_{ref})\,w(x', y')\,dx'dy' \end{aligned} \tag{2.84}$$

and

$$\text{icomb}_{EA}(x', y', x_{ref}, y_{ref}) = \sum_{i=1}^{N} \delta[x' - (x_i - x_{ref}), y' - (y_i - y_{ref})]. \tag{2.85}$$

Recognizing that the numerator on the rhs of (2.83) is a cross-correlation and using the same transformation between a two-dimensional cross-correlation and a two-dimensional convolution that was used previously, (2.83) can be expressed as

$$f_{EA}(x, y, x_{ref}, y_{ref}) = \frac{w(-x, -y)\,\text{icomb}_{EA}(-x, -y, x_{ref}, y_{ref}) ** f(x, y)}{n_{EA}(x_{ref}, y_{ref})}. \tag{2.86}$$

Note that in the equivalent analysis (2.86) $\text{icomb}_{EA}(x, y, x_{ref}, y_{ref})$ is associated with $w(x, y)$, whereas in the actual analysis (2.82) $\text{icomb}(x, y)$ is associated with $f(x, y)$. The equivalent analysis results in the two-dimensional irregular comb distribution

moving across the convolution symbol, which is the key alteration that enables the determination of the response function.

Taking the Fourier transform of (2.86) and applying the convolution theorem for two-dimensional Fourier transforms[18] (Bracewell 2000, p. 332),

$$\begin{aligned}\mathcal{R}(u,v,x_{ref},y_{ref}) &= \frac{\mathrm{FT}\left[w(-x,-y)\,\hat{}\mathrm{icomb}_{FA}(-x,-y,x_{ref},y_{ref})\right]}{n_{FA}(x_{ref},y_{ref})} \\ &= \frac{\mathrm{FT}\left[w_{cw}(-x,-y,x_{ref},y_{ref})\right]}{n_{FA}(x_{ref},y_{ref})}\end{aligned} \quad . \qquad (2.87)$$

where $w_{cw}(-x,-y,x_{ref},y_{ref}) = w(-x,-y)\,\hat{}\mathrm{icomb}_{FA}(-x,-y,x_{ref},y_{ref})$. The similarity theorem for two-dimensional Fourier transforms[19] (Bracewell 2000, p. 332) states that if $\mathrm{FT}\left[w_{cw}(x,y,x_{ref},y_{ref})\right] = W_{cw}(u,v,x_{ref},y_{ref})$, then $\mathrm{FT}\left[w_{cw}(-x,-y,x_{ref},y_{ref})\right] = W_{cw}(-u,-v,x_{ref},y_{ref})$. From the definitions of the two-dimensional Fourier transform and of $\hat{}\mathrm{icomb}_{FA}(x,y,x_{ref},y_{ref})$,

$$\begin{aligned}&W_{cw}(u,v,x_{ref},y_{ref}) = \\ &\sum_{n=1}^{N} w(x_n - x_{ref}, y_n - y_{ref})\cos\left\{2\pi\left[u(x_n - x_{ref}) + v(y_n - y_{ref})\right]\right\} \\ &+ j\left\{-\sum_{n=1}^{N} w(x_n - x_{ref}, y_n - y_{ref})\sin\left\{2\pi\left[u(x_n - x_{ref}) + v(y_n - y_{ref})\right]\right\}\right\}.\end{aligned} \qquad (2.88)$$

---

[18] The two-dimensional convolution theorem states that if two functions $f(x,y)$ and $g(x,y)$, the domains of which are infinite and continuous, have Fourier transforms given by $F(u,v)$ and $G(u,v)$, respectively, then the Fourier transform of the convolution of $f(x,y)$ and $g(x,y)$ is given by $F(u,v)G(u,v)$.

[19] The two-dimensional similarity theorem states that if the Fourier transform of the infinite, continuous domain function $f(x,y)$ is $F(u,v)$, then the Fourier transform of $f(ax,by)$ is $\frac{1}{|ab|}F\left(\frac{u}{a},\frac{v}{b}\right)$.

Substitution of $-u$ for u and $-v$ for v in (2.88), as dictated by the similarity theorem, and insertion into (2.87) results in

$$\mathcal{R}(u,v,x_{ref},y_{ref}) = \frac{\sum_{i=1}^{N} w(x_{in}-x_{ref},y_{in}-y_{ref})\cos\{2\pi[u(x_{in}-x_{ref})+v(y_{in}-y_{ref})]\}}{n_{EA}(x_{ref},y_{ref})} - \frac{j\left\{-\sum_{i=1}^{N} w(x_{in}-x_{ref},y_{in}-y_{ref})\sin\{2\pi[u(x_{in}-x_{ref})+v(y_{in}-y_{ref})]\}\right\}}{n_{EA}(x_{ref},y_{ref})}. \quad (2.89)$$

This is the response function for DDWA analyses of discrete, irregularly-distributed, two-dimensional data.

2.2.2.4.2 Verification

As in the one-dimensional case, the local response function is the complex conjugate of the normalized Fourier transform of the effective weight function, which in two dimensions is succinctly expressed as

$$\mathcal{R}(u,v,x_{ref},y_{ref}) = W_S^*(u,v,x_{ref},y_{ref}). \quad (2.90)$$

In (2.90) $W_S^*(u,v,x_{ref},y_{ref}) = W_{S\,\mathrm{Re}}(u,v,x_{ref},y_{ref}) - jW_{S\,\mathrm{Im}}(u,v,x_{ref},y_{ref})$, where $W_S(u,v,x_{ref},y_{ref}) = \mathrm{FT}[w_{eff}(x,y,x_{ref},y_{ref})]/n_{EA}(x_{ref},y_{ref})$.

From the definition of the response function, the Fourier coefficients of the equivalent analysis field can be expressed in polar form as

$$F_{EA}(u,v,x_{ref},y_{ref}) = |F(u,v)||W_S^*(u,v,x_{ref},y_{ref})|\exp[j(\varphi_{F(u,v)} + \varphi_{W_S^*(u,v,x_{ref},y_{ref})})], \quad (2.91)$$

where $|F(u,v)|$ and $|W_\zeta^*(u,v,x_{ref},y_{ref})|$ are the magnitudes of $F(u,v)$ and $W_\zeta^*(u,v,x_{ref},y_{ref})$ and $\varphi_{F(u,v)}$ and $\varphi_{W_\zeta^*(u,v,x_{ref},y_{ref})}$ are the phases of $F(u,v)$ and $W_\zeta^*(u,v,x_{ref},y_{ref})$. Using (B12) of appendix B and (2.91), $f_{EA}(x,y,x_{ref},y_{ref})$ can be written as

$$f_{EA}(x,y,x_{ref},y_{ref}) = \int_{v=0}^{v=\infty}\int_{u=-\infty}^{u=\infty}\left\{\frac{2}{1+\delta^{(0)}(v)}|F(u,v)||W_\zeta^*(u,v,x_{ref},y_{ref})|\times \cos\left[2\pi(ux+vy)+\varphi_{F(u,v)}-\varphi_{W_\zeta^*(u,v,x_{ref},y_{ref})}\right]\right\}dudv, \tag{2.92}$$

where $\delta^{(0)}(v)$ is 0 except for at $v=0$, where it is 1, and the fact that $\varphi_{W_\zeta^*(u,v,x_{ref},y_{ref})} = -\varphi_{W_\zeta(u,v,x_{ref},y_{ref})}$ has been utilized. As in the one-dimensional case, (2.92) shows exactly what happens to each Fourier coefficient during an analysis. During an analysis, the amplitude of each Fourier coefficient is modified by the factor

$$\begin{aligned}|W_\zeta^*(u,v,x_{ref},y_{ref})| &= |W_\zeta(u,v,x_{ref},y_{ref})| \\ &= \left[W_{\zeta\,\mathrm{Re}}(u,v,x_{ref},y_{ref})^2 + W_{\zeta\,\mathrm{Im}}(u,v,x_{ref},y_{ref})^2\right]^{1/2}\end{aligned} \tag{2.93}$$

and the phase of each Fourier coefficient is altered by

$$\begin{aligned}&-\varphi_{W_\zeta(u,v,x_{ref},y_{ref})} = \\ &-\arg\left[W_\zeta(u,v,x_{ref},y_{ref});W_{\zeta\,\mathrm{Re}}(u,v,x_{ref},y_{ref}),W_{\zeta\,\mathrm{Im}}(u,v,x_{ref},y_{ref})\right]\end{aligned} \tag{2.94}$$

where $\arg[W_\zeta(u,v,x_{ref},y_{ref});W_{\zeta\,\mathrm{Re}}(u,v,x_{ref},y_{ref}),W_{\zeta\,\mathrm{Im}}(u,v,x_{ref},y_{ref})]$ means the argument of $W_\zeta(u,v,x_{ref},y_{ref})$, which depends upon $W_{\zeta\,\mathrm{Re}}(u,v,x_{ref},y_{ref})$ and $W_{\zeta\,\mathrm{Im}}(u,v,x_{ref},y_{ref})$.

To verify (2.89), an input field similar to that used for discrete, irregularly-distributed, one-dimensional data is used:

$$f(x_{in}, y_{in}) = A_i \cos[2\pi(u_i x_{in} + v_i y_{in})]. \tag{2.95}$$

In (2.95) A_i is the amplitude and u_i and v_i are the input frequencies. For the input field (2.95), $F_{Re}(u,v) = \frac{A_i}{2} {}^2\delta(u-u_i, v-v_i) + \frac{A_i}{2} {}^2\delta(u+u_i, v+v_i)$ and $F_{Im}(v) = 0$, which can be verified by insertion into (2.74). These result in $|F(u,v)| = \frac{|A_i|}{2} {}^2\delta(u-u_i, v-v_i) + \frac{|A_i|}{2} {}^2\delta(u+u_i, v+v_i)$ and $\varphi_{F(u,v)} = 0, \pi$, depending upon whether A_i is positive or negative, respectively. For these tests both u_i and v_i are greater than zero. Since in (2.92) $v > 0$, only the first term in $|F(u,v)|$ contributes and thus for an input of the form (2.95) and for u_i and v_i both greater than zero (2.92) becomes

$$\begin{aligned} &f_{FA}(x, y, x_{ro}, y_{ro}) = \\ &|A_i||W_2^*(u_i, v_i, x_{ro}, y_{ro})|\cos[2\pi(u_i x + v_i y) + \varphi_{F(u_i,v_i)} - \varphi_{W_2(u_i, v_i, x_{ro}, y_{ro})}], \end{aligned} \tag{2.96}$$

where the sifting property of ${}^2\delta(x,y)$ has been exploited and the fact that $\delta^{(1)}(v_i) = 0$ if $v_i \neq 0$ has been utilized. Because the response in (2.89) is valid only at (x_{ro}, y_{ro}), $f_{FA}(x, y, x_{ro}, y_{ro})$ values from (2.96) are relevant to the actual analysis values only when $(x, y) = (x_{ro}, y_{ro})$ in (2.96).

Test results for $A_i = 1$, $u_i = 1/4$, $v_i = 1/10$, and $w(x,y) = \exp(-x^2/\kappa_1 - y^2/\kappa_2)$, with $\kappa_1 = \kappa_2 = 2$, are provided in Fig. 2.14. From Figs. 2.14b,c it is apparent that the analysis field and response-function predicted analysis field appear to be equivalent. In fact, the greatest difference between these two fields has a magnitude of 1.00136×10^{-5}, which is within the expected accuracy for single-precision computations. This correct prediction of analysis values, therefore, verifies (2.89).

Of particular interest are the differences between the actual analysis (Fig. 2.14b) and the analysis field for infinite, continuous data (Fig. 2.14d). As these indicate, the actual analysis is far from replicating what is obtained in the ideal situation of infinite, continuous data. Figures 2.14b,d, coupled with the amplitude (Fig. 2.14e) and phase (Fig. 2.14f) modulations, illustrate how strongly the distribution of the observations affects the analysis. If the data were infinite and continuous, the amplitude modulation would have a constant value of 0.24 and the phase modulation would be zero. Instead, the amplitude modulation varies significantly, having a maximum of 0.937 and a minimum of 0.015, and the phase modulation is considerable over much of the analysis domain. The causes of these non-ideal amplitude and phase modulations and, thus, of an analysis field that differs significantly from the ideal case, are the irregular distribution of the discrete observations and the data boundaries. Considering that on average there are about 2.3 observations per wavelength of the input wave, the irregular distribution of the observations should strongly affect analysis fidelity. In fact, in the nomenclature of Doswell and Caracena (1988), this is an inadequately-sampled wave. When the wave is well-resolved, in which case the number of observations per wavelength meets or exceeds 12 (Doswell and Caracena 1988), the analysis resembles the ideal analysis much more closely, although the effects of the data boundaries are still significant (not shown).

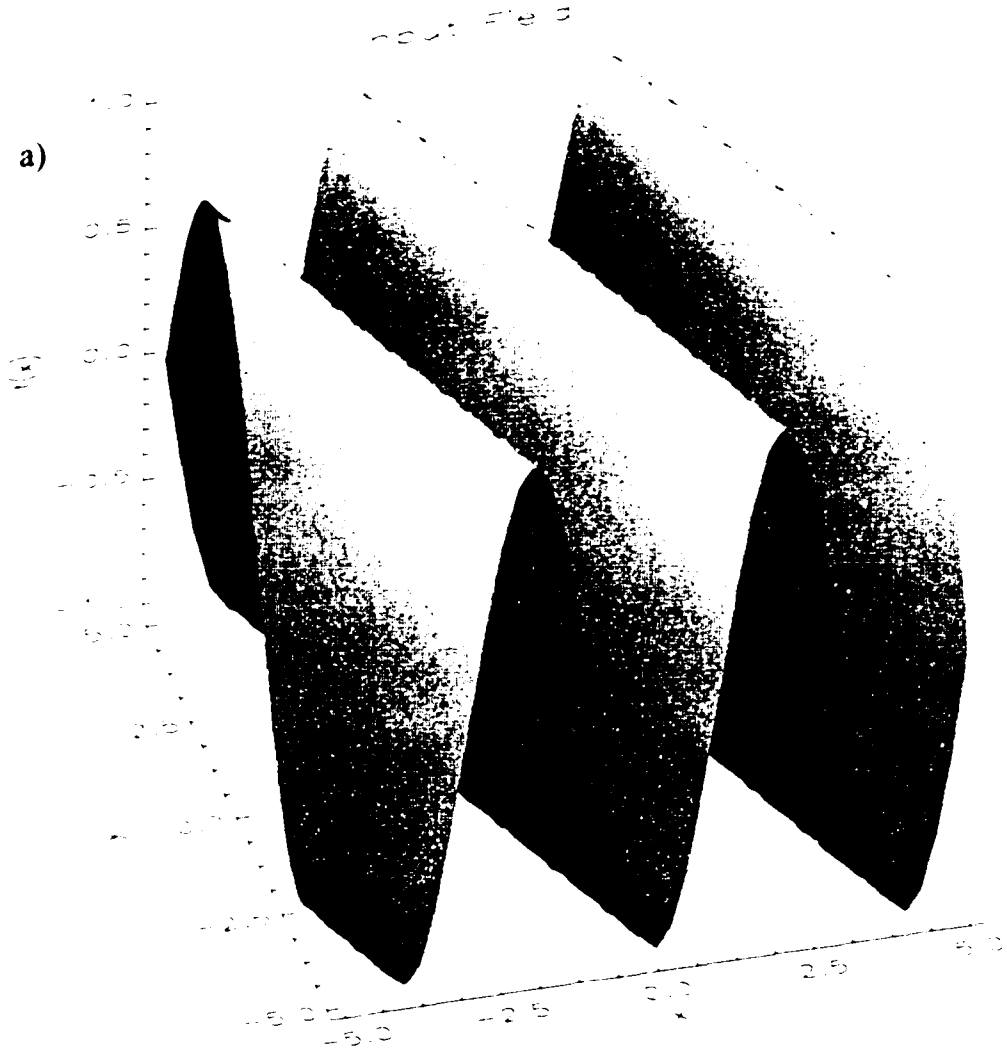

FIG. 2.14. The (a) input field, (b) analysis field, (c) response-function predicted analysis field, (d) analysis field for infinite, continuous data, (e) amplitude modulation, (f), phase modulation, and (g) observation distribution for a DDWA analysis of two-dimensional, discrete, irregularly-distributed data. The observational field is given by $f(x,y) = A_i \cos[2\pi(u_i x + v_i y)]$, with $A_i = 1$, $u_i = 1/4$, and $v_i = 1/10$, and is sampled at the 40 random locations (restricted to be in the domain $[-5,5]\times[-5,5]$) shown in (g). The weight function is given by $w(x,y) = \exp(-x^2/\kappa_x^2 - y^2/\kappa_y^2)$, with $\kappa_x = \kappa_y = 2$. In (e) the theoretical amplitude modulation is the amplitude modulation that would be realized for infinite, continuous observations.

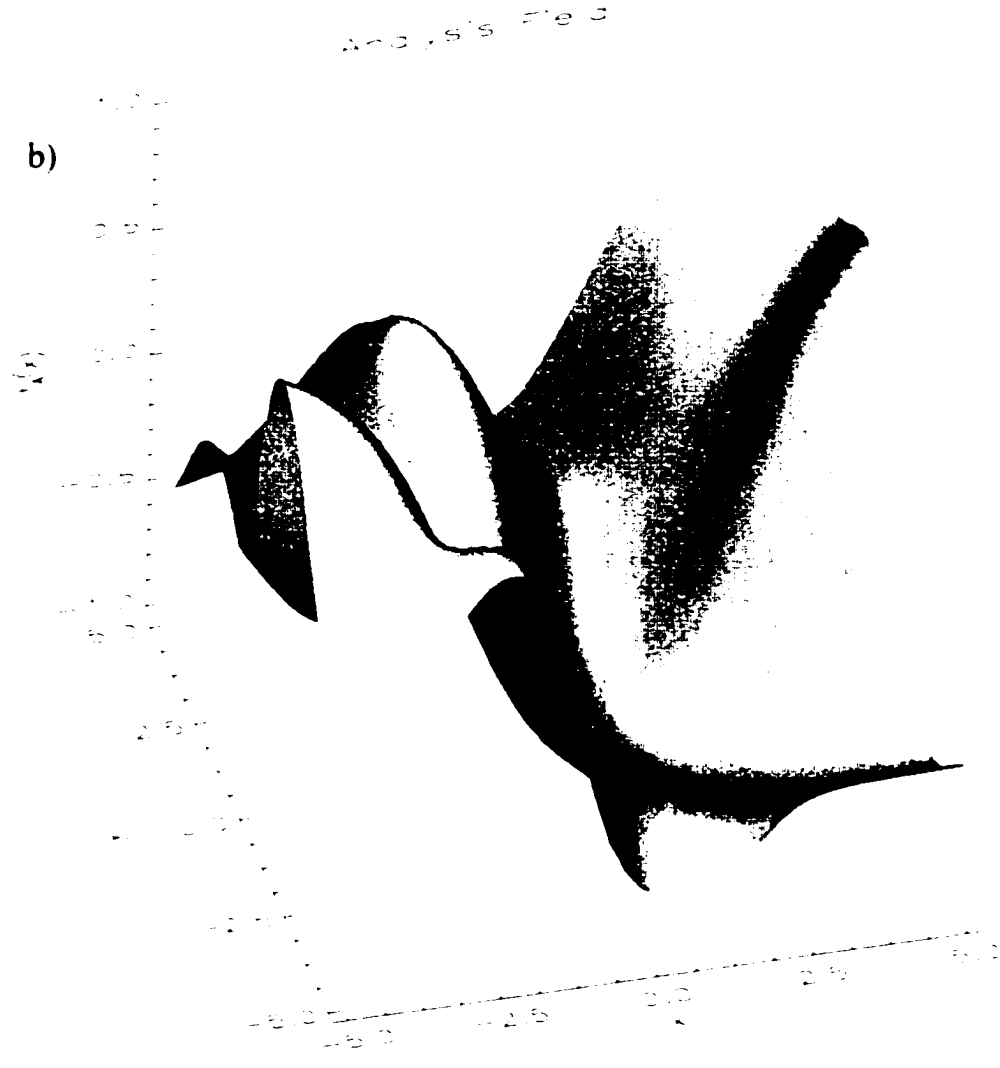

FIG. 2.14. (*cont.*)

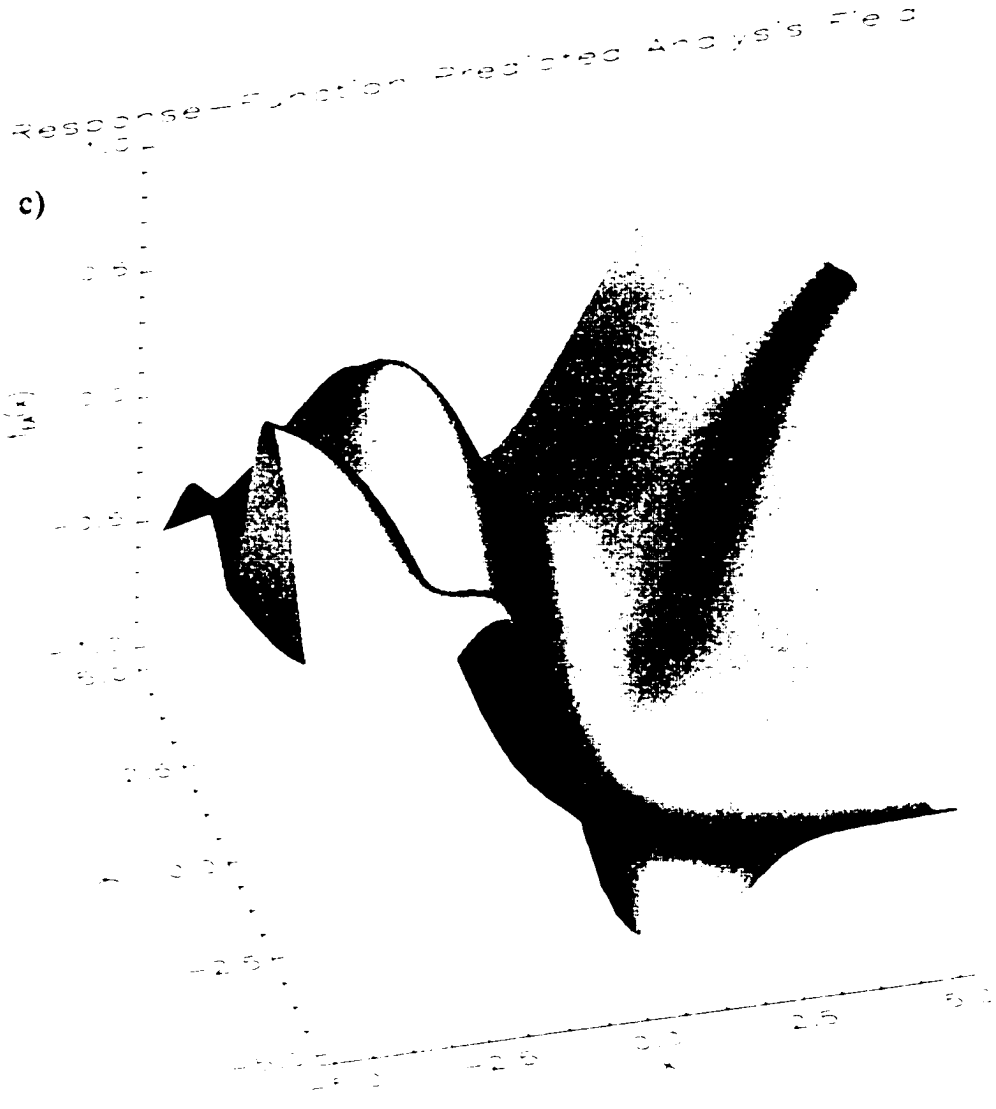

FIG. 2.14. (*cont.*)

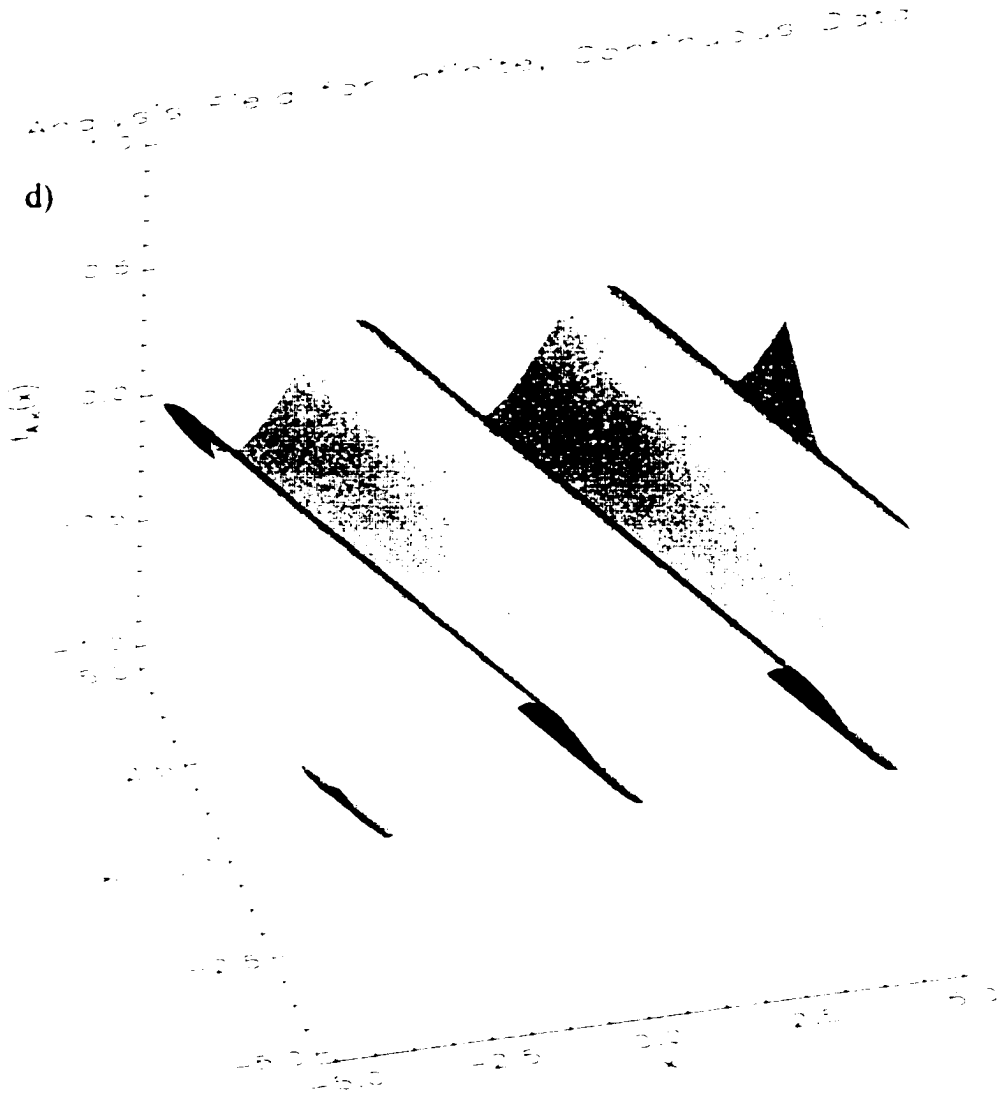

FIG. 2.14. (*cont.*)

FIG. 2.14. *(cont.)*

FIG. 2.14. (*cont.*)

g)

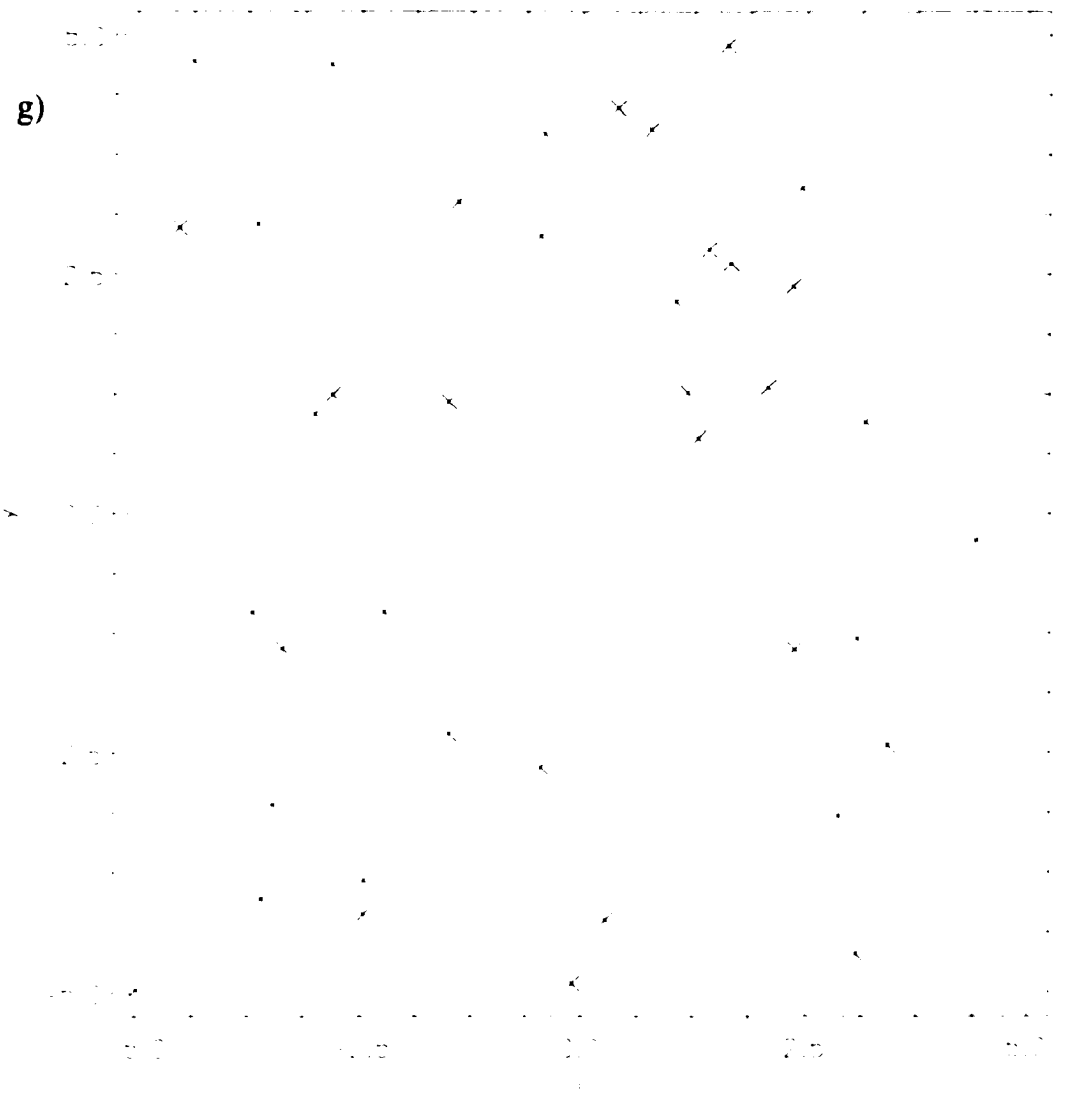

FIG. 2.14. (*cont.*)

2.2.2.5 Discussion

As indicated in section 2.2.2.1, the response function can be viewed from either a domain-wide or a local perspective. In some situations, like the use of a fixed weight function in the DDWA analyses of continuous, infinite data, these are equivalent. Generally, however, they are not. The local response function concerns spectral effects at a particular location while the domain-wide response function denotes some sort of average response. This is a very important distinction, as illustrated presently. For the purpose of illustrating this distinction, the domain-wide response function is defined as being composed of the domain-wide average amplitude and phase modulations.[20] Given this, consider Fig. 2.12. In Fig. 2.12b, the average of the phase modulations is zero. From a phase-shift standpoint, this implies a good analysis (no domain-wide phase shift). This is a misleading measure of analysis quality, however, since local phase shifts are significant both near and outside of the observational domain boundaries. In fact, the impact of these phase shifts is apparent in the differences in the locations of the extremes of the analysis and input fields near the boundaries of the observational domain (Fig. 2.12a). The local response function, therefore, appears to be a superior measure of local analysis fidelity.

Differences between domain-wide and local response functions are also illuminated by the factors that affect post-analysis Fourier content, which can be examined using (2.39), (2.63), (2.49), and (2.72). Equation (2.39) indicates that for continuous, bounded data the post-analysis, domain-wide Fourier content results from

[20] This measure of the domain-wide response function is similar to one of the forms suggested by Buzzi et al. (1991). In their form, however, they applied the averaging operator prior to the calculation of amplitude and phase.

three steps: 1) the convolution of the input Fourier content with the Fourier transform of the pulse function, 2) the multiplication of the result of 1) with the Fourier transform of $w(-x)$, and 3) the convolution of the result of 2) with the Fourier transform of $1/n(x)$. Equation (2.63) indicates that the situation is much the same for discrete, irregularly-distributed data, the only difference being that the input Fourier content is first convolved with the Fourier transform of the irregular comb distribution. Consequently, the analysis scheme affects the post-analysis, domain-wide Fourier content through the Fourier content of both $w(-x)$, the reflection of the weight function about $x = 0$, and $1/n(x)$, the inverse of the normalization factor. The observation distribution affects the post-analysis, domain-wide Fourier content through the Fourier content of the pulse function (continuous, bounded data) or irregular comb distribution (discrete, irregularly-distributed data) and the Fourier content of $1/n(x)$ [both the analysis scheme and the observation distribution affect $n(x)$]. The post-analysis, local Fourier content, defined here to be the Fourier content under the conditions of an equivalent analysis, is specified by either (2.49) or (2.72). From the analyses preceding these equations [cf. (2.47) and (2.70)], it is apparent that the post-analysis, local Fourier content results from two steps: 1) the convolution of the Fourier content of $w(-x)$ with the Fourier content of either $p_{E\Lambda}(-x, x_{r_e})$ or $\text{icomb}_{E\Lambda}(-x, x_{r_e})$ and 2) the multiplication of the result of 1) with $F(v)/n_{E\Lambda}(x_{r_e})$. As opposed to the situation for post-analysis, domain-wide Fourier content, the normalization factor has a relatively minor affect on the post-analysis, local Fourier content since it only serves to normalize that Fourier content.

Equations (2.39), (2.49), (2.63), and (2.72) provide a basis for studying the effects observation distributions and analysis schemes have upon response functions. While a rigorous exploration of this topic is beyond the scope of this work, a brief indication of research progress is appropriate.

The effects rectangular windows have on domain-wide spectral content are discussed in both textbooks (e.g. Weaver 1983, 134-137; Hamming 1998, chapter 5) and articles (e.g., Caracena et al. 1984), as are the effects infinite regular comb distributions have on domain-wide spectral content (e.g., Weaver 1983, 131-134; Pauley and Wu 1990). The impact of finite regular comb distributions has also been considered (e.g., Caracena et al. 1984). With respect to local spectral content, the impact of pulse functions (Achtemeier 1986; Pauley 1990), infinite regular comb distributions (e.g., Pauley and Wu 1990), finite regular comb distributions (e.g., Jones 1972), and finite irregular comb distributions (e.g., Jones 1972; Schlax and Chelton 2002) have all been considered to varying degrees.

The effects weight functions have on Fourier content have been considered by numerous investigators (e.g., Barnes 1964; Stephens 1967; Koch et al. 1983). However, the role the normalization factor plays in domain-wide spectral content, as indicated by (2.39) and (2.63), has not been considered previously.

As discussed in section 2.2.2.1, the response function (2.72) has been derived in one form or another by others (Jones 1972; Yang and Shapiro 1973; Thiébaux and Pedder 1987, p. 105; Buzzi et al. 1991; Schlax and Chelton 1992). To obtain the equivalent of (2.72), these investigators substituted a spectral representation of the observation field into their expressions for DDWA analyses and subsequently

manipulated that result. This 'back-substitution method' differs from the 'convolution-theorem approach' used herein. Since both techniques produce the same response function, one may contend that little has been gained in this exposition. On the contrary, it is argued that the convolution-theorem approach provides insights into DDWA analyses that are not available from the back-substitution method. Specifically, 1) the convolution-theorem approach provides an infrastructure for interpreting *both the separate and combined* impacts that data distributions and weight functions have upon analyses and 2) the convolution-theorem approach illustrates exactly what the local response function for DDWA analyses is: *the local response function is the complex conjugate of the normalized Fourier transform of the effective weight function.*

Similarly, the response function (2.89) has been derived previously (Buzzi et al. 1991). As in the one-dimensional case, the convolution-theorem approach has the advantages of providing an infrastructure for interpreting the impacts data distributions and weight functions have upon analyses and of illustrating exactly what the local response function for (two-dimensional) DDWA analyses is. In two dimensions, the local response function is as it is in one dimension—the complex conjugate of the normalized Fourier transform of the effective weight function.

While other methods for interpreting the response function exist (e.g., Achtemeier 1986), the most straightforward interpretation seems to be in terms of amplitude and phase modulation as described in detail in this study. With this approach, the effects of a DDWA analysis scheme are described quite simply by how the analysis scheme changes the intensity of input waves (amplitude modulation) and by how the analysis scheme moves input waves around (phase modulation). Because in

real DDWA analyses the inhomogeneous distribution of observations generally results in phase shifts (Pauley 1990, Buzzi et al. 1991), phase modulation information should be included in addition to amplitude modulation information in the evaluation of response functions. Unfortunately, as Buzzi et al. (1991) indicate, phase modulation has received less scrutiny than it would seemingly warrant. Its importance has been increasingly noted, however, in numerous analyses and discussions, including Achtemeier (1986), Pauley (1990), Buzzi et al. (1991), Carr et al. (1995), and Askelson et al. (2000). In fact, Buzzi et al. (1991) provide illustrations of amplitude and phase modulations (their Figs. 3 and 4) that are essentially of the same form as Figs. 2.12 and 2.13 of this study.

The technique outlined herein has numerous potential applications. The most obvious is the evaluation of the amplitude and phase fidelity of DDWA analysis schemes. In this regard, an interesting use would be the evaluation of the filtering properties of statistical objective analysis (SOA) schemes. It would be particularly interesting to determine whether SOA schemes, in their procurement of a DDWA analysis that minimizes analysis-error variance, also minimize phase shifts.

Another potential use is the evaluation of observation networks. Doswell and Lasher-Trapp (1997) have suggested the use of the gradient of the normalization factor to characterize the degree of irregularity of observation networks. It seems that phase modulation could be used in much the same manner since nonzero phase shifts arise from the inhomogeneity of observation distributions. A potential complication, however, would be the $\pm n2\pi$ ambiguity in the determination of phase shift values, which is discussed in section 2.2.2.2.3.

Amplitude modulation could also be quite useful in the evaluation of observation networks. Its principal utility is probably its ability to indicate how well DDWA schemes retain signal while repressing noise (e.g., Jones 1972; Schlax and Chelton 2002). By characterizing filtering potential, the technique outlined herein could be especially useful for networks that are limited in both extent and number of observations, for which the determination of network viability is particularly difficult.

It is noted that the technique outlined in this study is sufficiently general so that it should be applicable to arbitrary weight functions and data distributions as long as the concomitant integrals and summations are defined. Extension to situations where combinations of discrete and continuous data are available should be possible by combining pulse functions and comb distributions.

Finally, an exciting potential use is in the design of filters that will replicate prescribed amplitude and phase modulations as closely as possible given an observation distribution. This could be a very useful filter design technique, especially considering the difficulties in applying SOA to situations where error covariances are uncertain or background estimates are unavailable. Work on the design of such a filter is currently underway.

Chapter 3: Interactions of Hydrometeors with Rear Flank Downdrafts

3.1 Background

Numerous theories exist for supercell tornadogenesis [in an unpublished manuscript, Rasmussen and Straka (1997) outline 11 tornadogenesis hypotheses]. Recently, the roles downdrafts, especially the rear flank downdraft (RFD) (Lemon and Doswell 1979), may play have received more attention (e.g., Walko 1993; Davies-Jones and Brooks 1993; Davies-Jones 2000). Davies-Jones (1982) sparked increased interest in the downdraft when he found that it probably plays a critical role in establishing vertical vorticity near the ground. As Davies-Jones (1982) and Davies-Jones and Brooks (1993) reason, in an environment with negligible background vertical vorticity an "in, up, and out" circulation driven primarily by forces aloft could not establish significant vorticity near the ground since in this process parcels that obtain vertical vorticity are significantly elevated. To produce, in this type of circulation, significant vertical vorticity near the ground through updraft tilting of horizontal vorticity, an abrupt upward turning of streamlines, strong pressure gradients, and large vertical velocities are needed near the ground. [Alternatively, eddies could transport vertical vorticity downward against the flow. This process, however, has not been observed (e.g., Walko 1993).] While these features do arise in updrafts in axisymmetric tornado models, it is doubtful that they arise in supercells without the influences of downdrafts (Davies-Jones and Brooks 1993). [These features can be present along gust fronts and can result in significant near ground vertical vorticity in updrafts (e.g., Adlerman et al.

1999). For these gust fronts to arise, however, downdrafts are generally needed.] Thus, it seems that downdrafts may be crucial to tornadogenesis. Specifically, the RFD is a principal downdraft suspect in the tornadogenesis mystery. Incriminating evidence includes observations of low-level cyclonic-anticyclonic vorticity couplets straddling the RFD and hook echo (suggesting vorticity production by the RFD through tilting) just prior to and at the time of tornadogenesis [e.g., Fig. 4 of Brandes (1978) and Figs. 9 and 10 of Dowell and Bluestein (1997)], and observations showing that supercellular tornadoes typically form along the interface of the updraft and the RFD (e.g., Lemon and Doswell 1979). Moreover, simulations indicate that RFD air flows into areas of low-level rotation (Wicker and Wilhelmson 1995; Adlerman et al. 1999) and both observational (e.g., Lemon and Doswell 1979; Brandes 1981) and numerical (e.g., Adlerman et al. 1999) studies show that the evolution of low-level rotation and the RFD are linked.

A partial understanding of RFD dynamics can be gained through the consideration of the vertical component of the equation of motion expressed in the perturbation (hydrostatic base state) form:

$$\frac{dw}{dt} = -\frac{1}{\rho_0}\frac{\partial p'}{\partial z} + g\left(\frac{\theta_v'}{\theta_{v0}} - \frac{c_v}{c_p}\frac{p'}{p_0} - r_H\right) + F_z . \tag{3.1}$$

In (3.1) perturbations are indicated by single-primes, the base state is indicated by a subscript zero, w is vertical velocity, ρ is density, p is pressure, z is the vertical coordinate, g is the acceleration due to gravity, θ_v is virtual potential temperature, c_v is the specific heat of dry air at constant volume, c_p is the specific heat of dry air at

constant pressure, r_H is the total hydrometeor mixing ratio (cloud r_c, rain r_r, and ice r_i), and F_i represents the viscous and eddy stress terms (e.g., Houze 1993, 35-36). The first and second (of three total) terms on the rhs of (3.1) are the vertical gradient of the perturbation pressure field and the buoyancy $B = g\left(\frac{\theta'}{\theta_{00}} - \frac{c_v}{c_p} \frac{p'}{p_0} - r_H \right)$, respectively. (In the buoyancy term it is assumed that the hydrometeors are falling at their terminal velocities and thus that the drag that they exert upon an air parcel is equal to their weight, resulting in the r_H term.) As indicated in (3.1), the RFD may be driven by vertical perturbation pressure gradients, buoyancy, viscous and eddy stresses (believed to be of secondary importance to this problem), or a combination thereof.

Numerous investigators have illustrated the importance of vertical perturbation pressure gradients to supercell evolution. As background for the consideration of these studies, it is noted that with the anelastic assumption

$$\nabla \cdot (\rho_0 \mathbf{v}) = 0 \tag{3.2}$$

($\mathbf{v}$ is vector velocity) and the assumption that Coriolis forces are insignificant [relatively good approximations for deep convection (Klemp and Rotunno 1983; Emanuel 1994, §1.3)], the pressure perturbation field p' can be split into two components p'_B and p'_D. The pressure perturbation owing to buoyancy p'_B is defined by

$$\nabla^2 p'_B = \frac{\partial(\rho_0 B)}{\partial z}, \tag{3.3}$$

whereas the pressure perturbation owing to dynamic forcing p'_D is defined by

$$\nabla^2 p'_D = -\nabla \cdot (\rho_0 \mathbf{v} \cdot \nabla \mathbf{v}) + \nabla \cdot (\rho_0 \mathbf{F}), \tag{3.4}$$

where **F** is the viscous and eddy stress vector (cf. Klemp and Rotunno 1983; Houze 1993, §7.2). With this decomposition, (3.1) can be expressed as

$$\frac{dw}{dt} = -\frac{1}{\rho_0}\frac{\partial p'_D}{\partial z} + \left(-\frac{1}{\rho_0}\frac{\partial p'_B}{\partial z} + B \right) + F_z . \tag{3.5}$$

In this form, the first term on the rhs of (3.5) represents dynamic forcing [related to the flow field and to viscous and eddy stresses, (3.4)] while the second term represents the net forcing due to buoyancy.

Rotunno and Klemp (1982, 1985) and Weisman and Klemp (1984) have underscored the importance of dynamic forcing to supercell updraft maintenance and evolution. Rotunno and Klemp (1982) found that dynamic pressure perturbations resulting from the impingement of sheared environmental flow upon the updraft (termed herein linear pressure forcing) can favor right moving storms in veering wind profiles (thus explaining why right moving storms are favored in these wind profiles). Further, Rotunno and Klemp (1982, 1985) found that dynamic forcing plays a fundamental role in supercell splitting while both Weisman and Klemp (1984) and Rotunno and Klemp (1985) found it to also be important to supercell propagation. Weisman and Klemp further found that in addition to being important on supercell updraft peripheries, dynamic forcing can be significant (responsible for up to ~60% of the updraft magnitude) in supercell updraft cores.

With regard to downdrafts, Klemp and Rotunno (1983) simulated what they termed an 'occlusion downdraft' that arose at the time of low-level gust front occusion and that was driven primarily by dynamic pressure perturbations (owing to strong low-level rotation). They found the occlusion downdraft to be distinct from the storm scale

rear flank downdraft. Wicker and Wilhelmson (1995) and Adlerman et al. (1999) also simulated occlusion downdrafts that were forced by dynamic pressure perturbations. In their studies the occlusion downdraft was either initially distinct from the RFD and then subsequently merged with it (Wicker and Wilhemson 1995) or it developed on the eastern fringe of the RFD (Adlerman et al. 1999).

Evidence indicates that dynamic pressure perturbations may also play a role in driving the storm scale RFD. Both Brandes (1984) and Hane and Ray (1985) display retrieved pressure perturbation fields that support this statement. The principal cause of these downward-directed pressure perturbation forces is probably linear pressure forcing, which was elucidated by Rotunno and Klemp (1982) and was considered by Lemon and Doswell (1979) to be the mechanism that may initiate storm scale RFDs.

Even though, as the foregoing discussion indicates, dynamic pressure perturbations provide significant up- and downdraft forcing in supercells, they do not solely dictate vertical motions within these types of storms. In fact, buoyancy forcing is considered by many to be the primary forcing mechanism of the storm scale RFD (e.g., Browning 1964; Barnes 1978a,b; Lemon and Doswell 1979; Brooks et al. 1994; Adlerman et al. 1999), although further research is needed to conclusively prove this assertion. The evidence for this conclusion is oftentimes based upon the association between the RFD and precipitation in the rear-flank. Dowell et al. (1997), however, do provide evidence that buoyancy is principally responsible for the storm scale RFD in one of the storms (the Woodward storm) they analyze.

The negative buoyancy associated with storm scale RFDs is thought to be provided principally by hydrometeors. Hydrometeors produce negative buoyancy

through θ_i' (cooling through melting, sublimation, and evaporation) and through their drag (r_{ii} in B).

Hydrometeors are capable of driving intense downdrafts. In fact, in their comprehensive review Knupp and Cotton (1985) found that precipitation-driven downdrafts are among the largest and strongest downdrafts associated with convective clouds. Some relatively simple, one-dimensional downdraft models have successfully elucidated hydrometeor-driven downdraft properties. These models have evolved from steady state models (Hookings 1965; Kamburova and Ludlam 1966; Das and Subba Rao 1972; Betts and Silva Dias 1979) to time-dependent models (Srivastava 1985, 1987). Key findings of these efforts include 1) cooling by evaporation is most efficient when the raindrops are small (e.g., Hookings 1965; Srivastava 1985), 2) cooling by melting is more efficient when the ice-hydrometeors are small (Srivastava 1987), 3) downdraft descent is oftentimes somewhere between dry and moist adiabatic (e.g., Das and Subba Rao 1972), and 4) downdrafts are more vigorous the closer the environmental temperature profile is to dry-adiabatic (e.g., Kamburova and Ludlam 1966), the smaller the hydrometeors are, and the larger the liquid- and ice-water contents are (e.g., Srivastava 1987).

In addition to its mere existence, thermodynamic properties of the RFD also appear to be important to tornadogenesis (Markowski et al. 2002). Analyses of VORTEX (Rasmussen et al. 1994) data have indicated that surface RFD air associated with strong supercellar tornadoes (≥F2 intensity and lasting >5 minutes) is relatively buoyant (θ_i and θ_e deficits relative to the environment typically <2 K and <4 K, respectively) while surface RFD air associated with non-tornadic supercells tends to

have little buoyancy (θ_v and θ_e deficits relative to the environment typically >5 K and >10 K, respectively).[21] These findings led Markowski et al. (2002) to conclude that evaporative cooling and entrainment of potentially cold, midlevel air may play smaller roles in the formation of RFDs associated with tornadic supercells as compared to those associated with nontornadic supercells.

The purpose of this research is to infer kinematic and thermodynamic properties of RFDs associated with tornadic and non-tornadic supercells. Specifically, answers to the following questions are sought: 1) How strongly do hook-echo hydrometeors drive the RFDs of tornadic and nontornadic supercells and 2) Could hydrometeors affect tornadogenesis through their modulation of RFD strength and thermodynamic properties? In order to answer these questions (at least tentatively), polarimetric radar (PR) data are used to infer properties (phase, size distribution, amount) of hydrometeor populations observed within the hook echoes of tornadic and nontornadic supercells. This information is then used to drive a one-and-a-half-dimensional downdraft model similar to that described by Srivastava (1985, 1987). With these results, the kinematic and thermodynamic properties of hook-echo-hydrometeor-driven model-RFDs associated with tornadic and nontornadic supercells can be analyzed and compared. A description of both the one-and-a-half-dimensional downdraft model and the PR-based hydrometeor classification and quantification techniques used herein follows.

---

[21] Markowski et al. (2002) used the $\theta_v = \theta(1 + .61r_v - r_l)$ definition of virtual potential temperature, where θ is potential temperature and r_v is water vapor mixing ratio. Since $T_v = T(1 + .61r_v)$, this definition differs from the $\theta_v = T\left(\frac{p_{00}}{p}\right)^{R_d/c_p}$ definition of virtual potential temperature, where R_d is the gas constant for dry air and p_{00} is a reference pressure, by the quantity $-\theta r_l$.

3.2 1.5D Downdraft Model

3.2.1 Dynamics

The dynamic framework of the one-and-a-half-dimensional downdraft model used herein follows that of Asai and Kasahara (1967), Ogura and Takahashi (1971), and Ogura and Takahashi (1973). The downdraft is assumed to be circular and to have a time- and height-independent radius a. Relevant equations are expressed in cylindrical coordinates (r, λ, z), are written in flux form using the continuity equation, and then averaged over the area of the downdraft. By defining

$$\overline{A} = \frac{1}{\pi a^2} \int_0^{2\pi} \int_0^a A r \, dr \, d\lambda \,, \tag{3.6}$$

$$\tilde{A}_a = \frac{1}{2\pi} \int_0^{2\pi} A \, d\lambda \qquad \text{at } r = a \,, \tag{3.7}$$

$$A' = A - \overline{A} \,, \tag{3.8}$$

and

$$A_a'' = A - \tilde{A}_a \,, \tag{3.9}$$

where A is a general quantity, relations for the rate of change $\overline{A}$ can be obtained. The relation for $\overline{w}$ is

$$\frac{\partial \overline{w}}{\partial t} = -\overline{w}\frac{\partial \overline{w}}{\partial z} - \frac{2\alpha^2}{a}|\overline{w}|\overline{w} + \frac{2}{a}\tilde{u}_a(\overline{w} - \tilde{w}_a) + B \,, \tag{3.10}$$

where α^2 is the lateral mixing coefficient and it is assumed that there is no vertical motion in the environment of the downdraft. The first term on the right hand side of (3.10) is advection, the second is mixing owing to lateral eddy exchange, the third is

dynamic entrainment (required to satisfy mass continuity), and the fourth is buoyancy. Buoyancy is computed from

$$B = g\left(\frac{T_v'}{T_{v0}} - r_H \right), \tag{3.11}$$

where r_H is the total hydrometeor mixing ratio, the subscript zero indicates environmental values, *and the perturbation pressure contribution has been dropped since no mechanism exists for its computation in this model* (Ogura and Takahashi 1971). By using the relation between T_v and θ_v to relate the differential of T_v to that of θ_v, it can be verified that the form of buoyancy in (3.11) is consistent with the form discussed in §3.1.

Radial inflow/outflow on the boundary of the downdraft $\tilde{u}_a$ is diagnosed from the continuity equation

$$\tilde{u}_a = -\frac{a}{2}\left(\frac{\bar{w}}{\rho_0}\frac{\partial \rho_0}{\partial z} + \frac{\partial \bar{w}}{\partial z} \right). \tag{3.12}$$

The dynamic entrainment term for a general variable A is computed, following Asai and Kasahara (1967), Ogura and Takahashi (1971), and Ogura and Takahashi (1973), according to

$$\begin{aligned} \tilde{A}_a &= A_0, \quad \text{if } \tilde{u}_a < 0 \\ \tilde{A}_a &= \bar{A}, \quad \text{if } \tilde{u}_a > 0. \end{aligned} \tag{3.13}$$

This results in dilution of the downdraft when there is inflow from the environment and no effect on the downdraft when there is outflow to the environment. Mixing is parameterized in the form of lateral eddy exchange terms, but is restricted to the horizontal since vertical mixing is neglected in this model.

The conservation equations for the other prognostic variables have forms similar to (3.10). The thermodynamic equation is

$$\frac{\partial \bar{T}}{\partial t} = -\bar{w}\left(\frac{\partial \bar{T}}{\partial z} + \Gamma_d\right) - \frac{2\alpha^2}{a}|\bar{w}|(\bar{T} - T_0) + \frac{2}{a}\tilde{u}_a(\bar{T} - \tilde{T}_a) + \frac{q}{c_p}, \tag{3.14}$$

where Γ_d is the dry adiabatic lapse rate, q is the specific heating rate, and c_p is the heat capacity of dry air.[22] Diabatic processes that contribute to q include thermal diffusion between hydrometeors and their environments and are discussed in the next section.

The conservation equations for water vapor mixing ratio r_v and cloud water mixing ratio r_c are

$$\frac{\partial \bar{r}_v}{\partial t} = -\bar{w}\frac{\partial \bar{r}_v}{\partial z} - \frac{2\alpha^2}{a}|\bar{w}|(\bar{r}_v - r_{v0}) + \frac{2}{a}\tilde{u}_a(\bar{r}_v - \tilde{r}_{va}) + S_{rv,\,cond} \tag{3.15}$$

and

$$\frac{\partial \bar{r}_c}{\partial t} = -\bar{w}\frac{\partial \bar{r}_c}{\partial z} - \frac{2\alpha^2}{a}|\bar{w}|\bar{r}_c + \frac{2}{a}\tilde{u}_a(\bar{r}_c - \tilde{r}_{ca}) + S_{rc,\,cond}, \tag{3.16}$$

where $S_{rv,\,cond}$ and $S_{rc,\,cond}$ are sources/sinks for r_v and r_c owing to condensation/evaporation (discussed in the next section). In (3.16), the fall speeds of cloud droplets are ignored and the environment is assumed to be non-cloudy.

Because details of rain and graupel/hail size distributions may be very important to downdraft properties, the prognostic variables for rain and graupel/hail are number concentration densities—the number of hydrometeors of a certain size per unit volume per unit size interval. The prognostic equations can be derived by applying Leibnitz's rule and the divergence theorem (e.g., Reddy and Rasmussen 1990, 97-103) to a

[22] The weak dependence of c_p on water vapor mixing ratio is ignored.

population of hydrometeors of the same size. Following the same set of operations that are applied to the other variables, the equations become

$$\frac{\partial \overline{N}(D_r)}{\partial t} = -(\overline{w} - v_{tr})\frac{\partial \overline{N}(D_r)}{\partial z} + \overline{N}(D_r)\frac{\overline{w}}{\rho_0}\frac{\partial \rho_0}{\partial z} - \frac{2\alpha^2}{a}|\overline{w}|\overline{N}(D_r) + \frac{2}{a}\tilde{u}_a\left[\overline{N}(D_r) - \tilde{N}_a(D_r)\right] + \overline{N}(D_r)\frac{\partial v_{tr}}{\partial z} + S_{N(D_r)\text{evap}} + S_{N(D_r)\text{melt}} \tag{3.17}$$

and

$$\frac{\partial \overline{N}(D_{eh})}{\partial t} = -(\overline{w} - v_{teh})\frac{\partial \overline{N}(D_{eh})}{\partial z} + \overline{N}(D_{eh})\frac{\overline{w}}{\rho_0}\frac{\partial \rho_0}{\partial z} - \frac{2\alpha^2}{a}|\overline{w}|\overline{N}(D_{eh}) + \frac{2}{a}\tilde{u}_a\left[\overline{N}(D_{eh}) - \tilde{N}_a(D_{eh})\right] + \overline{N}(D_{eh})\frac{\partial v_{teh}}{\partial z} + S_{N(D_{eh})\text{cond}} + S_{N(D_{eh})\text{melt}} \tag{3.18}$$

where $N(D_r)$ is the number of drops of diameter D_r per unit volume per unit size interval, v_{tr} is the terminal velocity of a raindrop, $S_{N(D_r)\text{evap}}$ is a source/sink of $\overline{N}(D_r)$ owing to evaporation, $S_{N(D_r)\text{melt}}$ is a source/sink of $\overline{N}(D_r)$ owing to the complete melting of ice hydrometeors, $N(D_{eh})$ is the number of graupel/hail of diameter D_{eh} per unit volume per unit size interval, v_{teh} is the terminal velocity of a graupel/hailstone, $S_{N(D_{eh})\text{cond}}$ is a source/sink of $\overline{N}(D_{eh})$ owing to condensation/evaporation, and $S_{N(D_{eh})\text{melt}}$ is a source/sink of $\overline{N}(D_{eh})$ owing to melting. As with cloud water, the environment is assumed to contain neither rain nor graupel/hail. In addition, condensation onto raindrops is not included since, relative to cloud droplets, the growth rate of raindrops by condensation is quite small (this issue is discussed further in the next section). Finally, it is noted that (3.17) contains the extra term $\overline{N}(D_r)(\partial v_{tr}/\partial z)$

relative to the similar equation given by Ogura and Takahashi (1973) because here a dependence of terminal velocity on altitude is included, as illustrated presently.

3.2.2 Microphysics

3.2.2.1 Terminal Velocities

The terminal velocities of raindrops can be estimated using multiple techniques. These include the Davies number approach (e.g., Davies 1945; Berry and Pranger 1974; Beard 1980), the Beard (1976) approach, and adjustment factor approaches (Beard 1977; Beard 1980; Beard 1985). As Foote and Du Toit (1969) point out, the Davies number approach is strictly valid only for rigid bodies, for which the drag coefficient C_D depends only upon the Reynolds number N_{Re}.[23] This motivated Beard (1976) to develop a more rigorous method for determining terminal velocities of raindrops. Unfortunately, this approach is quite complex. Consequently, Beard (1977, 1980, 1985) investigated an alternative approach in which changes in terminal velocities owing to changes in air density and viscosity can be easily incorporated using adjustment factors. In this study, the relation used to determine the terminal velocity of raindrops v_{tr} is

$$v_{tr}(D_r, \rho) = v_{tr0}(D_r)(\rho_0/\rho)^m, \tag{3.19}$$

where v_{tr0} is the terminal velocity at a reference density ρ_0, D_r is in mm, and v_{tr} and v_{tr0} are in m s^{-1}. The $v_{tr0}(D_r)$ relation used in (3.19) is

---

[23] The terminal velocity of a hydrometeor v_t is the fall speed at which the drag force F_D balances the buoyancy force of the hydrometeor F_{BH}. For steady, axisymmetric flow and for a rigid body, Pruppacher and Klett (1997, section 10.2.2) show that the drag force can be expressed as $F_D = \frac{1}{2}\rho v^2 A C_D$, where ρ is the density of the air, A is the cross section of the hydrometeor normal to the air flow, and C_D depends only upon the Reynolds number $N_{Re} = \rho D v / \eta$, with D being hydrometeor diameter and η being the

$$v_{t,0}(D_r) = [9.65 - 10.3\exp(-0.6D_r)]. \qquad (3.20)$$

which is the terminal velocity relation obtained by Atlas et al. (1973) that closely fits the Gunn and Kinzer (1949) data. Since the Gunn and Kinzer (1949) data are for an air density of 1.2 kg m^{-3}, ρ_0 has this value in (3.19). The m value is set at 0.45, which falls approximately in the middle of the range of m values (0.4 to 0.5) suggested by Beard (1985) and represents a compromise between the values appropriate for small drops (~0.4) and for large drops (~0.5). The form (3.19) is a simplified version of the adjustment factor approach. It is expected to be the quite accurate for most raindrops but to incorporate significant errors for drops smaller than about 1 mm in diameter. The method for determining raindrop terminal velocities encapsulated in (3.19) and (3.20) represents a compromise between complex, highly accurate techniques (e.g., Beard 1976) and simple, inaccurate techniques that do not include adjustments for changes in atmospheric conditions. It requires only one equation for the calculation of raindrop terminal velocities, as opposed to the several that are required in the accurate form of the adjustment factor method (Beard 1980). In addition, in (3.20) it incorporates a dependence upon D_r that is much more accurate than power-law relations and yet is still convenient when computing moments of raindrop size distributions that involve v_{tr}.[24]

The terminal velocities of hailstones and graupel are even more complicated. At first sight, the problem seems to be simplified by the rigidity of these hydrometeors, which seemingly makes Davies number approaches viable. While this is true for

---

dynamic viscosity. The buoyancy force of a hydrometeor is given by $F_{buH} = (\rho - \rho_H)V_H g$, where ρ_H and V_H are the density and volume of the hydrometeor, respectively.

[24] This statement regarding convenience is based upon the expectation of using either gamma or exponential distributions as models for raindrop size distributions. In that case, as with power-law

hailstones and graupel that are not experiencing significant changes owing to wet growth, melting, etc., the wide variety of graupel/hailstone shapes alters C_D-N_{Re} relations and complicates the picture. Furthermore, melting also significantly alters terminal velocities and presumably C_D-N_{Re} relations of graupel and hailstones (Rasmussen and Heymsfield 1987). These complications imply that accounting for all effects in the calculation of the terminal velocities of graupel and hailstones is a daunting task.

The most sophisticated techniques for computing terminal velocities of graupel and hail (e.g., Beard 1980; Rasmussen and Heymsfield 1987; Böhm 1989) use the Davies number approach, in which the pivotal step is the application of an effective C_D-N_{Re} relation. Herein, a simplified adjustment factor approach similar to (3.19) is used. An important component of this approach is the relation for terminal velocities at the reference density ρ_0. To provide guidance concerning this relation, v_t-C_D and C_D-N_{Re} relations are examined subsequently.

As indicated earlier in footnote 23, the terminal velocity of a hydrometeor is reached when the drag force balances the buoyancy force of the hydrometeor. This balance results in

$$v_{th} = \left[\frac{2(\rho_h - \rho)V_h g}{\rho A_r C_D} \right]^{1/2}, \tag{3.21}$$

relations for v_{tm}, (3.20) enables the use of the gamma function in the computation of moments of raindrop size distributions involving v_t.

where v_{th} is the terminal velocity of the hailstone and ρ_h and V_h are the density and volume of the hailstone, respectively. Since $\rho << \rho_h$, ρ is typically dropped from the numerator, resulting in

$$v_{th} \approx \left(\frac{2\rho_h V_h g}{\rho A_c C_D} \right)^{1/2}. \tag{3.22}$$

For hail that is spherical, an assumption that is applied to both hail and graupel in this study, (3.22) becomes

$$v_{th} \approx \left(\frac{4\rho_h g}{3\rho C_D} \right)^{1/2} D_h^{1/2}, \tag{3.23}$$

where D_h is the diameter of the hailstone.

From (3.23), it is apparent that if C_D is constant, v_{th} depends upon $D_h^{1/2}$. However, theory for the drag coefficient of spheres (Abraham 1970), results for graupel and hailstone models (Macklin and Ludlam 1961; List and Schemenauer 1971; List et al. 1973), and studies of actual graupel and hailstones (Heymsfield 1978; Matson and Huggins 1980; Knight and Heymsfield 1983) indicate that for hailstones having diameters smaller than ~2.5 cm C_D generally decreases with N_{Re}. Since $N_{Re} = \rho D_h v_{th} / \eta$, where η is the dynamic viscosity, N_{Re} should increase with D_h, all else (ρ and η) being equal. Thus, C_D should decrease with increasing D_h, all else being equal, and v_{th} should have a greater than square root dependence upon D_h. In fact, a fairly simple C_D-N_{Re} relation that holds roughly for the diameter range of 0.05 to 2.5 cm is $C_D = aN_{Re}^b$ [cf. (B3) of Rasmussen and Heymsfield (1987), Matson and Huggins (1980), and Beard (1980)]. Inserting this into (3.23) results in

$$v_{tn} \approx a^{(1/2-b)}\left(\frac{4\rho_n g}{3}\right)^{\frac{1}{2-b}} \rho^{(1-b)/(2-b)} \eta^{(b/2-b)} D_n^{(1-b)/(2-b)}. \qquad (3.24)$$

which agrees with the findings of Beard (1980) concerning correction factors for an assumed C_D-N_{Re} relation of the form $C_D = aN_{Re}^b$. With typical values of b being -0.2,[25] (3.24) illustrates that for C_D-N_{Re} relations typical of hailstones, v_{th} does have a greater than square root dependence on D_h. In fact, with b = -0.2, v_{th} is proportional to $D_h^{0.67}$.

Curiously, both Matson and Huggins (1980) and Knight and Heymsfield (1983) obtain v_{th}-D_h relations that are not consistent with their C_D-N_{Re} relations. Matson and Huggins (1980) obtain $v_{tn}\,(\mathrm{m\,s^{-1}}) = 11.45 D_n^{0.5}$ (cm) and Knight and Heymsfield (1983) obtain $v_{tn}\,(\mathrm{m\,s^{-1}}) = 8.445 D_n^{0.653}$ (cm). To be consistent with their C_D-N_{Re} relations, they should have D_h exponents of 0.64 and 0.84, respectively.

As indicated earlier, a simplified adjustment factor approach is used to determine the terminal velocities of graupel and hail. In the simplified adjustment factor approach used herein,

$$v_{tgh}(D_{gh}, \rho) = v_{tgh0}(D_{gh})(\rho_0/\rho)^m, \qquad (3.25)$$

where v_{tgh} is the terminal velocity of a graupel or hailstone, v_{tgh0} is the terminal velocity of a graupel or hailstone at the reference density ρ_0, and D_{gh} is the diameter of a graupel or hailstone. For this method to perform well, it is important that an accurate v_{tgh0} relation is used. As indicated in the above discussion, such a relation should depend approximately on $D_{gh}^{0.67}$ for graupel and hailstones having diameters between 0.05 to 2.5

[25] Knight and Heymsfield (1983) obtained b = -0.367, Matson and Huggins (1980) obtained b = -0.1689, and (B3) of Rasmussen and Heymsfield corresponds to b = -0.19.

cm. Since this size range encapsulates most of the graupel and hail considered in this study (see below), this dependence is appropriate here. Interestingly, empirical terminal velocity relations for graupel and hail tend to have exponents that are either above or below this value (Pruppacher and Klett 1997, section 10.5.2). Moreover, slight inconsistencies between v_{th}-D_h and C_D-N_{Re} relations arise in studies of hailstone characteristics (Matson and Huggins 1980; Knight and Heymsfield 1983). It seems that these may result from scatter in the original data. In fact, by drawing a curve to the Matson and Huggins (1980) v_{th}-D_h data that seems to represent those data better than their least squares fit, the following v_{tgh0}-D_{gh} relation was obtained:

$$v_{tgh0}(D_{gh}) = 11.6 D_{gh}^{0.71}, \tag{3.26}$$

where v_{tgh0} is in m s^{-1} and D_{gh} is in cm. This v_{tgh0} relation is more in line with what is expected from both theory and observations of C_D-N_{Re} curves. Since the evidence concerning these curves is quite extensive and since observational scatter likely compromised empirical v_{tgh0}-D_{gh} relations, (3.26) is used to calculate graupel and hailstone terminal velocities. Because (3.26) is from the Matson and Huggins (1980) data, ρ_0 in (3.25) is their 0.993 kg m^{-3} value. The value of m in (3.25) is set at 0.42, which is represents a compromise between the adjustment factor appropriate for relatively small graupel (0.34 for ~0.05 cm diameter graupel) and the adjustment factor for large hail (0.5).[26]

Although melting significantly impacts terminal velocities of graupel and hail (Rasmussen et al. 1984b), no efforts like those of Rasmussen and Heymsfield (1987) were made to adjust for these effects. Once a graupel or hailstone completely melts, it

is added to the raindrop population and falls with the appropriate terminal velocity. Although this approximates a naturally smooth terminal velocity transition with an abrupt one, it is expected that the consequences for these modeling efforts are minor.

3.2.2.2 Microphysical Processes

The source/sink term that is considered first is $S_{r_c\,\mathrm{cond}}$, the source/sink of r_c owing to condensation/evaporation. This term is handled using the Soong and Ogura (1973) saturation adjustment scheme, with saturation vapor pressure given by equation (4.4.13) of Emanuel (1994). In this scheme, supersaturated air is adjusted to the point of saturation, with the excess water vapor condensing into cloud water. Alternatively, if cloud water is present and the air is not saturated, that cloud water is depleted until it is either completely gone or the air is saturated. It is noted that when supersaturated conditions occur, all excess water vapor is assumed to condense onto cloud drops, as in Ogura and Takahashi (1971). The justification for this simplification is that the growth rate of raindrops is much smaller than the growth rate of cloud drops. For graupel/hail condensation still occurs, which means that if supersaturated conditions arise, total water mass is not conserved. The impact of this is likely small owing to the relatively small condensational growth rates of graupel/hail (which are nonetheless important to the energy balance of each hailstone). It is of no consequence here, however, since saturated conditions do not arise in these simulations.

The $S_{r_c\,\mathrm{cond}}$ term is comprised of contributions owing to condensation/evaporation of cloud drops, which is handled using saturation adjustment,

---

[26] These values were determined using Fig. 3 and Table 1 of Beard (1980).

evaporation of raindrops, and condensation/evaporation of melting graupel/hail. The evaporation rate of raindrops is calculated using

$$\frac{dD_r}{dt} = \frac{4}{\rho_w R_v} D_v \frac{f_v}{D_r}\left(\frac{\bar{e}}{\bar{T}} - \frac{e_{vr}}{T_r}\right), \tag{3.27}$$

where ρ_w is the density of liquid water, R_v the gas constant for water vapor, D_v is the diffusivity of water vapor in air, f_v is the ventilation coefficient for mass, $\bar{e}$ and $\bar{T}$ are the (model) vapor pressure and temperature (the values in the environment of a raindrop), and e_{vr} and T_r are the saturation vapor pressure and temperature at the surface of a raindrop (Rogers and Yau 1989, chapter 7). The relation of Hall and Pruppacher (1976),

$$D_v = \left(2.11\times10^{-5}\ \mathrm{m^2 s^{-1}}\right)\left(\frac{T}{273.15\ \mathrm{K}}\right)^{1.94}\left(\frac{1013.25\ \mathrm{mb}}{p}\right), \tag{3.28}$$

is used to compute D_v. The ventilation coefficient for mass f_v is computed using

$$f_v = \begin{cases} 1.0 + 0.108X_v^2 & X_v \le 1.4 \\ 0.78 + 0.308X_v & 1.4 < X_v \end{cases}, \tag{3.29}$$

where $X_v = N_{Sc}^{1/3} N_{Re}^{1/2}$, with N_{Sc} the Schmidt number and N_{Re} the Reynolds number for a raindrop (Beard and Pruppacher 1971; Pruppacher and Rasmussen 1979). Since curvature and solute effects are small for raindrops (cf. Rogers and Yau 1989, chapter 6), they are ignored in the computation of e_{vr}. The raindrop temperature T_r is assumed to be equal to the thermodynamic wetbulb temperature T_w, which is a commonly applied simplification (e.g., Srivastava 1985). Regarding this simplification, Srivastava and Coen (1992) warn that T_w and T_r can differ by several degrees celsius. This is substantiated by the comparisons of T_w and T_r provided by Ludlam (1980), which show

that while T_w and T_r are nearly equivalent for most conditions, differences on the order of a degree Celsius can occur. Although the impact of this assumption is likely very small, it will be considered in future work.

To compute the contribution of raindrop evaporation to S_{n_cond} one could compute raindrop evaporation rates as described above, convert these values into rates of changes of mass, compute the total amount of evaporation in a model time step for each raindrop size, sum the contributions from all raindrop sizes, and convert this result to a mixing ratio change by dividing by the (model) dry-air density. This is not the approach taken herein, however, since in addition to computing S_{n_cond}, one also needs to compute $S_{N(D_r)\_evap}$. $S_{N(D_r)\_evap}$ can be computed by relating $S_{N(D_r)\_evap}$ to the evaporation rates of individual raindrops given by (3.27). The relation is

$$S_{N(D_r)\_evap} = -\frac{\partial}{\partial D_r}\left[\bar{N}(D_r)\frac{dD_r}{dt}\right], \tag{3.30}$$

as given by Ogura and Takahashi (1973). It can be derived by applying the Leibnitz rule to $\int_{D_{r\_min}}^{D_r} \bar{N}(D_r)dD_r'$, which is a constant since evaporation (and condensation) does not alter the total number of hydrometeors. The contribution of raindrop evaporation to S_{n_cond}, $S_{n\_evap\_rain}$, is obtained by computing $S_{N(D_r)\_evap}$ and subsequently summing the effect of evaporation across the raindrop size distribution:

$$S_{n\_evap\_rain} = -\frac{\sum_i \left(S_{N(D_r)\_evap}\right)\Delta D_r \left(\frac{\pi}{6} D_r^3 \rho_w\right)}{\bar{\rho}_d}, \tag{3.31}$$

where ΔD_r is the width of the i^{th} raindrop size bin and ρ_d is the density of the dry air.

Before proceeding, it is noted that melting graupel and hail are modeled as having cores composed of ice water and air inclusions surrounded by liquid water coats, as observed by Rasmussen et al. (1984b). In addition, graupel and hailstones are assumed to be spherical, with spherical cores and spherical water coats. This assumption may seem unjustified considering the observations of Rasmussen et al. (1984b). Because the equations that are used to obtain condensation and melting rates of graupel and hail are formulated in terms of equivalent radii, however, this is the correct approach (Rasmussen et al. 1984a,b; Rasmussen and Heymsfield 1987). Srivastava (1987) also assumed that graupel and hailstones are spherical, with spherical cores and spherical water coats.

Condensation/evaporation for graupel/hail is computed using the relations of Rasmussen and Heymsfield (1987), which apply only for melting graupel and hail.[27] These relations are based upon both experimental and theoretical studies and together comprise the most complete treatment of the subject to date. The equation for condensation/evaporation of graupel/hail has a form similar to (3.27) and is given by

$$\frac{dm_{gh}}{dt} = \frac{2\pi}{R_v} D_v D_{gh,ul} f_v \left(\frac{\bar{e}}{\bar{T}} - \frac{e_{s,gh}}{T_{gh}} \right), \tag{3.32}$$

where m_{gh} is the total mass of a graupel/hailstone, $D_{gh,ul}$ is either the total diameter of the melting graupel/hailstone D_{gh} (diameter of the unmelted portion plus the diameter of the liquid water coat) or the diameter of the unmelted portion D_{ul} (composed of ice and air), $e_{s,gh}$ is the saturation vapor pressure at the surface of the melting graupel/hailstone, and T_{gh} is the temperature at the surface of the melting graupel/hailstone. The exact

form of dm_{gh}/dt depends on the Reynolds number of the graupel/hailstone. For all Reynolds numbers except those in the range $3.0\text{x}10^3$-$6\text{x}10^3$, T_{gh} is 273.15 K; for Reynolds numbers in the range $3.0\text{x}10^3$-$6\text{x}10^3$, T_{gh} is determined by solving an implicit equation for T_{gh} derived by Mason (1956). For Reynolds numbers in the range $2.5\text{x}10^2$-$6\text{x}10^3$, f_v is computed using (3.29). Outside this range, f_v exhibits different dependencies owing to convective effects within the liquid water coat, shedding, or enhanced ventilation owing to surface roughness effects. For Reynolds numbers greater than $6\text{x}10^3$, D_{sh} is used because nearly the entire water coat is shed. Otherwise, D_{gh} is used.

The contribution of graupel/hail condensation/evaporation to $S_{rv\ cond}$, $S_{rv\ cond\ gh}$, is simply the sum of the contributions from all of the graupel/hail bins

$$S_{rv\ cond\ gh} = -\frac{\sum\left(\frac{dm_{gh}}{dt}\right)\bar{N}(D_{gh})\Delta D_{gh}}{\bar{\rho}_d}. \tag{3.33}$$

In (3.33), ΔD_{gh} is the width of the i^{th} graupel/hail size bin.

The source/sink of $\bar{N}(D_{gh})$ owing to condensation/evaporation, $S_{\bar{N}(D_{gh})\ cond}$, is easily calculated once condensation/evaporation growth rates are known from (3.32). Since the condensation/evaporation of graupel/hail does not alter the total number of graupel/hail,

$$S_{\bar{N}(D_{gh})\ cond} = -\frac{\partial}{\partial D_{gh}}\left[\bar{N}(D_{gh})\frac{dD_{gh}}{dt}\right]. \tag{3.34}$$

---

[27] This is a limitation of this model, which was designed for downdrafts in which the graupel and hail are melting. This model cannot presently be used for situations in which the graupel/hail are not melting.

with dD_{gh}/dt, the rate of change of D_{gh} owing to condensation/evaporation, computed from

$$\frac{dD_{gh}}{dt} = \frac{2}{\pi \rho_w D_{gh}^2} \frac{dm_{gh}}{dt}. \tag{3.35}$$

The density of liquid water is needed in (3.35) because the condensation/evaporation growth of a melting graupel/hailstone occurs on its liquid water coat.

To compute $S_{\bar{N}(D_r)\,\mathrm{melt}}$ and $S_{\bar{N}(D_{gh})\,\mathrm{melt}}$, sources/sinks of $\bar{N}(D_r)$ and $\bar{N}(D_{gh})$ owing to the complete melting of graupel/hail, one must track the amount of ice in a melting graupel/hailstone. This is accomplished by computing $f_{i,m}$, the mass fraction of ice in a melting graupel/hailstone. From the definition of $f_{i,m}$, its rate of change is

$$\frac{df_{i,m}}{dt} = \frac{1}{m_{gh}} \frac{dm_i}{dt} - \frac{f_{i,m}}{m_{gh}} \frac{dm_{gh}}{dt}, \tag{3.36}$$

where m_i is the mass of the ice core and dm_{gh}/dt is available from (3.32). The rate of melting of the ice core dm_i/dt is computed from the energy balance of the graupel/hailstone following Rasmussen and Heymsfield (1987). The three processes important to this energy balance are conductive heating, heating owing to condensation/evaporation, and melting/freezing. The conductive heating rate of a single graupel/hailstone Q_{cdn} is given by

$$Q_{cdn} = 2\pi D_{gh,\mathrm{melt}} k_a f_h \left(\bar{T} - T_{gh}\right), \tag{3.37}$$

where k_a is the thermal conductivity, f_h is the ventilation coefficient for heating, and the units of Q_{cdn} are J s^{-1}. The thermal conductivity k_a is computed using the Beard and Pruppacher (1971) relation

$$k_a(T) = 2.382 \times 10^{-2} + 7.032 \times 10^{-5} T. \tag{3.38}$$

where k_a has units of J m^{-1} s^{-1} K^{-1} and T is in °C. The ventilation coefficient for heating generally has the same dependence as f_v with the Prandtl number N_{Pr} replacing the Schmidt number N_{Sc} (Pruppacher and Klett 1997, p. 541). Thus,

$$f_h = \begin{cases} 1.0 + 0.108 X_h^2 & X_h \le 1.4 \\ 0.78 + 0.308 X_h & 1.4 < X_h \end{cases},$$

where $X_h = N_{Pr}^{1/3} N_{Re}^{1/2}$. The evaluation T_{gh}, f_h, and D_{ghmd} in (3.37) follow the same Reynolds number rules as for T_{gh}, f_v, and D_{ghmd} in (3.32). With the conductive heating rate (3.37) and the condensational heating rate given by $L_v(T_{gm})(dm_{gm}/dt)$, where $L_v(T_{gh})$ is the enthalpy of vaporization at T_{gh}, the heat balance of a graupel/hailstone results in (Rasmussen and Heymsfield 1987)

$$\frac{dm_i}{dt} = -\frac{1}{L_f(273.15\ \mathrm{K})}\left[Q_{cdn} + L_v(T_{gm})\frac{dm_{gm}}{dt}\right], \tag{3.39}$$

where $L_f(273.15\ \mathrm{K})$ is the enthalpy of fusion at 273.15 K. At first glance it appears as if (3.39) neglects heat storage effects since all excess heating goes towards melting the ice core and none is applied towards altering the thermal structure of the melting graupel/hailstone. However, because the equations of Rasmussen and Heymsfield (1987) are verified against observations, heat storage effects are implicitly included in (3.39). Whether heat storage is included or not, its impact appears to be minimal (Pellet and Dennis 1974).

The computation of $f_{i,m}$ can be accomplished in an Eulerian framework in the following manner. First, allow $\bar{N}(D_{gm})$ to evolve through the dynamic terms in (3.18) (i.e., excluding the source/sink terms). Then, for each location and each graupel/hail

bin that has a nonzero $\overline{N}(D_{gh})$, estimate the $f_{i,m}$ that a particular graupel/hailstone started with at the previous time step before arriving at that location. Then, (3.36), (3.32), and (3.39) are used to estimate the current value of $f_{i,m}$. If $f_{i,m}$ drops below zero, these graupel/hailstones are removed from $\overline{N}(D_{gh})$ and redistributed into $\overline{N}(D_r)$. In this process, mass is conserved so as to conserve loading and internal energy. This is the manner in which $S_{\overline{N}(D_r),\text{melt}}$ and one of the two terms in $S_{\overline{N}(D_{gh}),\text{melt}}$ are computed.

A second $S_{\overline{N}(D_{gh}),\text{melt}}$ term exists because the melting of the ice core of a graupel/hailstone results in a change in D_{gh} owing to the differences in the densities of the liquid water coat and the ice core. Since during melting the total number of graupel/hail is conserved, this second term, $S_{\overline{N}(D_{gh}),\text{melt},2}$, is computed from

$$S_{\overline{N}(D_{gh}),\text{melt},2} = -\frac{\partial}{\partial D_{gh}}\left[\overline{N}(D_{gh})\frac{dD_{gh,m}}{dt}\right], \tag{3.40}$$

where $dD_{gh,m}/dt$ is the rate of change of D_{gh} owing to melting. $dD_{gh,m}/dt$ is computed from

$$\frac{dD_{gh,m}}{dt} = \left(\frac{2}{\pi}\right)\left(\frac{\rho_w - \rho_{ic}}{\rho_w \rho_{ic}}\right)\left(\frac{1}{D_{gh}^2}\right)\frac{dm_i}{dt}, \tag{3.41}$$

where ρ_{ic} is the density of the core. Equation (3.41) can be derived by equating the rate of change of the mass of the core to the rate of change of the mass of the water coat.

The only source/sink term in (3.10)-(3.18) that is not specified is q, the specific heating rate, which is composed of three terms. The first is the specific heating rate owing to condensation/evaporation of cloud water. This term is handled in the

saturation adjustment scheme. The second term is the specific heating rate owing to the evaporation of raindrops. This term is

$$q_{evap\ rain} = -S_{n\ evap\ rain}\left(\frac{\bar{\rho}_d}{\bar{\rho}}\right)L_v(T_a). \tag{3.42}$$

The third term is the specific heating rate owing to the concomitant condensation/evaporation and melting/freezing of graupel/hailstones. The only portion of this energy balance that contributes to this term is conduction since this is the mechanism by which a graupel/hailstone exchanges thermal energy with its environment. Consequently, this term is

$$q_{cond\ gh} = -\frac{\sum Q_{cgh}\ \bar{N}(D_{gh})\Delta D_{gh}}{\bar{\rho}}. \tag{3.43}$$

3.2.3 Initialization

3.2.3.1 Environmental Initialization

In order to perform downdraft experiments, the model must be initialized using appropriate environmental soundings. While this may seem like a straightforward task, difficulties do arise. Thus, a description of the methods used is provided here.

First, data from mandatory and significant levels at which total pressure p, temperature T, and dewpoint temperature T_d are available are retrieved from a sounding. Then, the hypsometric equation is used to calculate the altitude of each of these levels. The hypsometric equation is based on the hydrostatic assumption and the equation of state and is given by

$$Z_2 = Z_1 + \frac{R_d}{g_0}\bar{T}_v \ln(p_1/p_2). \tag{3.44}$$

where

$$\bar{T}_v = \int_{p_1}^{p_2} T_v \, d\ln p \Big/ \int_{p_1}^{p_2} d\ln p, \tag{3.45}$$

Z represents geopotential height,[28] R_d is the dry gas constant (287.04 J kg^{-1} K^{-1}), $g_0 = 9.80665$ m s^{-2}, T_v is virtual temperature, and subscripts 1 and 2 represent two levels in the atmosphere (1 represents a smaller altitude than 2). The altitude of each level is computed even though altitude estimates are provided in many of the soundings in order to ensure hydrostatic consistency within the model.

To compute altitudes, information concerning the variation of T_v between levels is required. The assumption that T_v varies linearly with ln$p$ between levels,

$$T_v = T_{v1} + \frac{T_{v2} - T_{v1}}{\ln p_2 - \ln p_1}(\ln p - \ln p_1), \tag{3.46}$$

is justified by both theoretical considerations [cf. Richner and Viatte (1995) and references therein] and by our comparisons of computed [assuming (3.16)] and provided (computed using the full-resolution radiosonde data) mandatory-level geopotential heights. With (3.45) and (3.46), (3.44) becomes

$$Z_2 = Z_1 + \frac{R_d}{g_0}\left(\frac{T_{v1} + T_{v2}}{2}\right)\ln(p_1/p_2). \tag{3.47}$$

The altitudes of sounding levels where p, T, and T_d are available are calculated using (3.47).

At this point one must estimate p, T, r_v, and T_v at the model locations z_m using the p, T, and T_d values at the sounding locations Z. First, vapor pressure e, r_v, and T_v are computed at the sounding locations. Then, using the assumption that T_v varies linearly with $\ln p$ between sounding levels [(3.46)], the height z_m of a model point that lies between sounding levels Z_i and Z_{i+1} is related, through (3.47), to the temperature and pressure fields by

$$\frac{T_{v_{i+1}} - T_{v_i}}{\ln(p_{i+1}/p_i)}\left[\ln(p_i/p)\right]^2 + 2T_{v_i}\ln(p_i/p) - \frac{2g_0(z_m - Z_i)}{R_d} = 0, \qquad (3.48)$$

where p is the pressure at z_m. Since everything in (3.48) but p is known, this quadratic equation can be solved for p, resulting in

$$p = \begin{cases} p\exp\left[\dfrac{T_{v_i} \mp \sqrt{T_{v_i}^2 + \dfrac{2g_0}{R_d}\dfrac{T_{v_{i+1}} - T_{v_i}}{\ln(p_{i+1}/p_i)}(z_m - Z_i)}}{\dfrac{T_{v_{i+1}} - T_{v_i}}{\ln(p_{i+1}/p_i)}}\right] & T_{v_{i+1}} \neq T_{v_i} \\ p\exp\left[\dfrac{g_0(Z_i - z_m)}{R_d T_{v_i}}\right] & T_{v_{i+1}} = T_{v_i} \end{cases}. \qquad (3.49)$$

The solution for p must split according to whether or not $T_{v_{i+1}}$ is equal to T_{v_i} in order to avoid division by zero [(3.48) is no longer quadratic in this case]. Calculations show that the negative root in (3.49) produces viable values.

With p known at the model points, environmental T_v values are determined by linearly interpolating T_v as a function of $\ln p$ from the sounding data. At this point, the

[28] The geopotential heights computed herein are treated as actual heights. Considering the relatively small heights (< 5 km) of the model domain, this approximation results in negligible errors (e.g., List 1951, 217-223).

environmental variables that remain to be determined are T and r_v. These cannot be determined directly from T_v since only one piece of information is available concerning two values. In order to close this problem, the assumed linear variation of T_v with ln$p$ is utilized. By utilizing the approximation $T_v \approx T(1 + .608 r_v)$ and through some algebraic manipulation, it can be shown that the assumption that T_v varies linearly with ln$p$ is consistent with linear variations of T and r_v with ln$p$. Consequently, environmental T values are determined by linearly interpolating them as a function of ln$p$ from the sounding data. Environmental r_v values are then calculated using

$$r_v = \frac{T_v - T}{1 \varepsilon - T_v - T}, \tag{3.50}$$

where $\varepsilon = R_d / R_v$, with R_v the gas constant for water vapor (461.5 J kg^{-1} K^{-1}).

3.2.3.2 Microphysical Initialization

The first step required in the microphysical initialization of this model is the assumption of size distributions for rain and graupel/hail. This is necessary in order to reduce the degrees of freedom associated with size distributions to a manageable number that can be inferred using radar data. A common form used for the distribution of rain is the gamma distribution

$$N(D_r) = N_{0r} D_r^{\mu_r} \exp(-\Lambda_r D_r), \tag{3.51}$$

where D_r is the equivolume diameter (the diameter of a spherical drop that has the same volume as an actual drop), $N(D_r)$ is the number of drops of diameter D_r per unit

volume per unit size interval.[29] N_{0r} is the intercept, μ_r is the shape parameter, and Λ_r is the slope (Ulbrich 1983) (subscript r indicates rain). Another common form used for raindrop size distributions is the exponential distribution (Battan 1973, §7.2), which is described by (3.51) with $\mu_r = 0$. Herein, it is assumed that raindrop sizes are distributed exponentially.

For hail, the Cheng-English exponential distribution (Cheng and English 1983; Cheng et al. 1985), in which the intercept and slope are related, has gained some acceptance and will be used herein. [Note that numerous studies (e.g., Federer and Waldvogel 1975; Xu 1983; Cheng and English 1983; Cheng et al. 1985) indicate that hail is exponentially distributed, although exceptions (power law, gamma) have been documented (Auer 1972; Ziegler et al. 1983).] The relation between the intercept and slope that is used is that of Cheng et al. (1985), $N_{0gh} = (100\ \mathrm{m}^{-3}\ \mathrm{mm}^{3.11})\Lambda_{gh}^{4.11}$, with N_{0gh} in $\mathrm{m}^{-3}\ \mathrm{mm}^{-1}$ and Λ_{gh} in mm^{-1} (the subscript ghs indicate graupel/hail). Strictly speaking, the Cheng-English distribution holds only for hail, for which $D \geq 5$ mm. There is evidence, however, that graupel (for which $D < 5$ mm) are also exponentially distributed (Xu 1983). Thus, graupel are assumed to have an exponential distribution and are furthermore constrained to have N_0 and Λ values that are equal to those of the hail size distribution. This results in a single distribution that describes the sizes of both graupel and hail. [The assumption of matching, exponential hail and graupel size distributions is a fairly common one that has been utilized in numerous other computational efforts (e.g., Lin et al. 1983; Bringi et al. 1986a,b; Aydin and Zhao 1990).]

[29] As a matter of convenience, equivolume diameter D, will often be referred to as simply diameter.

In order to relate PR data to size distribution parameters, information concerning raindrop and graupel/hail shapes, canting, and incidence angles (essentially elevation angles) is needed. Raindrops are assumed to have equilibrium shapes approximated by oblate spheroids [shown by Warner and Hizal (1976) to be a good approximation] with axis ratios that vary with size according to the relation found by Green (1975). The degree to which raindrops assume equilibrium shapes is controversial. From an analysis of aircraft data, Chandrasekar et al. (1988) found that the oscillations of raindrops are slight (oscillation amplitudes of 10% of the axis ratio). Zrnić and Doviak (1989) showed that oscillations of this magnitude minimally affect polarimetric measurements. From surface observations in heavy showers (Jones 1959; Jameson and Beard 1982) and a model of collisionally-induced raindrop oscillations (Beard et al. 1983), however, indications are that in moderate to heavy rainfall collisionally-induced oscillations can result in raindrop shapes that deviate from equilibrium (and toward sphericity). Moreover, Andsager et al. (1999) found that even without collisions raindrops may oscillate (apparently from resonance with vortex shedding) strongly enough to alter average raindrop shapes towards sphericity. Since the impacts oscillations have on raindrop shape are not fully understood and since differences are not expected to have a large impact on the results of this study, equilibrium shapes are assumed for raindrops. In addition, raindrops are assumed to experience no canting (Beard and Jameson 1983) and are treated as though the incidence angle is zero [a good approximation for the low-elevation data used herein (Stapor and Pratt 1984; Jameson 1987)]. Graupel/hail are assumed to be spherical (see appendix C). With this assumption, canting and incidence angles are relatively unimportant.

Information concerning maximum and minimum raindrop and graupel/hail diameters is also required for the microphysical initialization of this model. (With this information, two degrees of freedom remain for the interaction of raindrop populations with electromagnetic energy while one remains for graupel/hail populations. Thus, only two measurands are needed to initialize rain and only one is required to initialize graupel/hail.) For raindrops, the minimum diameter $D_{r\,\min}$ is 0.2 mm while the maximum diameter $D_{r\,\max}$ is equal to the approximate spontaneous breakup size limit of 8.0 mm (Komabayasi et al. 1964). The minimum raindrop diameter is based upon the definition of raindrops (or, more precisely, drizzle drops). The maximum raindrop diameter, on the other hand, is believed to be realistic not so much because collisionally-induced breakup is relatively inactive (thus allowing spontaneous breakup to dictate maximum drop size), but because in the raindrop-containing hook echoes considered here the production of large raindrops through the melting of graupel and hail is believed to be significant (e.g., Conway and Zrnić 1993). For graupel/hail, $D_{gh\,\min} = 0.05$ mm and $D_{gh\,\max} = 9.0$ mm. The maximum graupel/hail diameter is set so that a parameterization of shedding would not be needed; Rasmussen et al. (1984b) found that ice particles with diameters smaller than 9 mm do not shed while melting. In future work, shedding will be incorporated in the model and larger hailstones will be allowed.

The PR-based hydrometeor classification and quantification techniques that are used herein are partially described in appendices C and D. To quantify the rain and graupel/hail fields, the reflectivity factors at horizontal polarization for rain Z_{hr} and ice (graupel/hail) Z_{hi} and the reflectivity factors at vertical polarization for rain Z_{vr} and ice

Z_{vl} must be determined. Then Z_{DRr}, the differential reflectivity owing to rain, can be estimated. With the assumptions concerning raindrops, N_{0r} and Λ_r of raindrop size distributions depend only upon Z_{hr} and Z_{DRr} (Seliga and Bringi 1976). Furthermore, with the assumptions concerning graupel/hail, only Z_{hl} is needed for the initialization of graupel/hail.

Two methods are empolyed to estimate Z_{hr}, Z_{hl}, Z_{vr}, and Z_{vl} from PR data. As discussed in appendix C, the measured reflectivity factor at horizontal polarization Z_h and the differential reflectivity Z_{DR} [$Z_{DR}(\text{dB}) = Z_h(\text{dBZ}) - Z_v(\text{dBZ})$, where Z_v is the reflectivity factor at vertical polarization] are used to compute the reflectivity difference Z_{DP} (dBZ), which is defined by

$$Z_{DP} = 10\log(Z_h - Z_v) = 10\log[(Z_{hr} + Z_{hl}) - (Z_{vr} + Z_{vl})], \tag{3.52}$$

where $Z_h > Z_v$, $Z_h = Z_{hr} + Z_{hl}$, $Z_v = Z_{vr} + Z_{vl}$, and linear-units (e.g., $\text{mm}^6\ \text{m}^{-3}$) reflectivity values are used. [Equation (3.52) can be expressed as $Z_{DP} = Z_h + 10\log(1 - 10^{-Z_{DR}/10})$, where $Z_{DR} > 0$ dB, Z_{DP} is in dBZ, Z_h is in dBZ, and Z_{DR} is in dB.] For raindrop size distributions conforming to the gamma distribution, Golestani et al. (1989) found that

$$Z_{hr}(\text{dBZ}) = a\,Z_{DPr} + b, \tag{3.53}$$

where $Z_{DPr}(\text{dBZ}) = 10\log(Z_{hr} - Z_{vr})$ is the Z_{DP} corresponding to rain and a and b are constants. Observations from regions dominated by rain have confirmed the validity of (3.53) (Golestani et al. 1989; Meischner et al. 1991; Conway and Zrnić 1993; Carey and Rutledge 1996; Tong et al. 1998). By using (3.52), (3.53), and the key assumption that the ice-water hydrometeors are effectively isotropic with respect to reflectivity factor

(see appendix C) so that $Z_{hi} = Z_{vi}$ and $Z_{DP} = Z_{DPr}$, one can obtain Z_{hr} from Z_h and Z_v. With this, one can determine Z_{hi} (and Z_{vi} and Z_{vr}).

The second method for separating Z_h into Z_{hr} and Z_{hi} is also discussed in appendix C. It was introduced by Balakrishnan and Zrnić (1990a) and, as with Z_{DP}, depends upon the ice hydrometeors being essentially isotropic with respect to horizontal and vertical polarization states. In this method, however, it is presumed that the ice hydrometeors do not affect the specific differential phase K_{DP} (see appendix C). Then, the utilization of K_{DP}-R and R-Z_{hr} relations, where R is rainrate, produces an estimate of Z_{hr}. From the $R = 37.1(K_{DP})^{0.866}$ K_{DP}-R relation proposed by Sachidananda and Zrnić (1987) and the Marshall-Palmer $Z_{hr} = 200R^{1.6}$ R-Z_{hr} relation (Marshall et al. 1955), Balakrishnan and Zrnić (1990a) obtained

$$Z_{hr} = 64.840(K_{DP})^{1.386}, \tag{3.54}$$

where Z_{hr} is in mm^6 m^{-3} and K_{DP} is in km^{-1} [with Z_{hr} in dBZ (3.54) is $Z_{hr} = 13.86\log(K_{DP}) + 48.12$, which is consistent with (3.57) below].

From the two Z_{hi} estimates available from these two methods, Z_{hiz} (from Z_{DP}) and Z_{hik} (from K_{DP}), we calculate F_{iz}, the fractional contribution of ice to Z_h from Z_{DP}, as

$$F_{iz} = \frac{Z_{hiz}}{Z_h}, \tag{3.55}$$

and F_{ik}, the fractional contribution of ice to Z_h from K_{DP}, as

$$F_{ik} = \frac{Z_{hik}}{Z_h}, \tag{3.56}$$

with the reflectivities having linear units. It is not clear which of these is better. Error sources for F_{iz} estimates include measurement errors in Z_h and Z_{DR} [Tong et al. (1998)

show that the standard error of Z_{DP} is nearly equivalent to that of Z_h], raindrop size distributions that do not conform to the range of gamma distributions considered by Golestani et al. (1989)[30], graupel and hailstones that are not isotropic with respect to reflectivity, and the use of non-calibrated coefficients in (3.53).[31] Error sources for F_{ik} estimates include measurement errors in K_{DP}, inaccuracies in the assumed K_{DP}-R and R-Z_{hr} relations owing to variations in raindrop size distributions [more severe for R-Z_{hr} relations (Doviak and Zrnić 1993, p. 234)], and graupel and hailstones that are not isotropic with respect to differential phase. Based on the work of Balakrishnan and Zrnić (1990a), Straka et al. (2000) argue that F_{ik} should be superior to F_{ic} because anisotropic graupel/hail affect K_{DP} less than they affect Z_{DR} [see Figs. 5 and 6 and associated text of Balakrishnan and Zrnić (1990a)]. While this is true, the utility of F_{ik} relative to F_{ic} is decreased by two factors. The first is the dependence of F_{ik} upon an R-Z_{hr} relation. These relations seem to suffer more from raindrop size distribution variability than do Z_{hr}-Z_{DPr} relations (see preceding footnote). The second is the accuracy with which K_{DP} can be estimated. Because the K_{DP} algorithm used herein is similar to the NSSL K_{DP} algorithm (Brandes et al. 2001), the standard deviation of K_{DP} [SD(K_{DP})] estimates for Cimarron radar data is 0.12 to 0.3 ° km^{-1} (Ryzhkov and Zrnić 1996; Brandes et al. 2001). The upper SD(K_{DP}) value of 0.3 ° km^{-1} equals the expected

[30] Golestani et al. (1989) state that their linear Z_{hr}-Z_{DPr} relation was obtained by varying gamma-distribution parameters over a wide range. They do not, however, indicate the extents of those ranges. Measurements (Golestani et al. 1989; Meischner et al. 1991; Conway and Zrnić 1993; Carey and Rutledge 1996; Tong et al. 1998) and disdrometer-based calculations (Aydin and Giridhar 1992) indicate that linear Z_{hr}-Z_{DPr} relations are typical and may extend to gamma-distributions that may not have been considered by Golestani et al. (1989).

[31] The coefficients in the Z_{hr}-Z_{DPr} relation depend upon calibration (Conway and Zrnić 1993). Because of the number of cases considered here, however, the determination of coefficients for each case is not

K_{DP} value for $Z_{hr} = 40.92$ dBZ, where Z_{hr} is estimated from the Z_{hr}-K_{DP} relation of Balakrishnan and Zrnić (1990a)

$$Z_{hr} = 13.86\log(K_{DP}) + 48.17\,. \tag{3.57}$$

with Z_{hr} in dBZ and (one-way) K_{DP} in ° km^{-1} [as noted earlier, (3.57) is consistent with (3.54)]. For $Z_{hr} = 45$ dBZ, SD(K_{DP}) = 0.3 ° km^{-1} is about half of the expected K_{DP} value. Variations of 0.3 ° km^{-1} about $Z_{hr} = 45$ dBZ, $K_{DP} = 0.6$ ° km^{-1} produce $F_{ik} = 0.61$ ($K_{DP} = 0.3$ ° km^{-1}) and $F_{ik} = 0.0$ ($K_{DP} = 0.9$ ° km^{-1}) when the expected value is $F_{ik} = 0.0$. K_{DP} noisiness at small Z_hs, therefore, significantly limits the utility of F_{ik} for small Z_hs. In comparison, with $\bar{a} = 0.876$ and $\bar{b} = 9.482$ dB, ∓1 dBZ errors in Z_{DP} [equal to the expected standard error for Z_h (Zrnić et al. 1993; Doviak and Zrnić 1993, 128-129), which Tong et al. (1998) show to be a valid approximation] for $Z_{hr} = 45$ dBZ, $Z_{DP} = 40.546$ dBZ ($Z_{DR} = 1.929$ dB) results in $F_{iz} = 0.18$ ($Z_{DP} = 39.546$ dBZ) and $F_{iz} = 0.0$ ($Z_{DP} = 41.546$ dBZ) when the expected value is $F_{iz} = 0.0$.[32,33] Based upon this rather simple error analysis, the fractional contribution

---

feasible. Consequently, averages of the values reported in the literature (see appendix C) are used. These are $\bar{a} = 0.876$ and $\bar{b} = 9.482$ dB.

[32] Note that for physical realizability, when these methods indicate that $Z_{hr} > Z_n$ and thus that Z_{vr} is negative (linear units), Z_{hr} and Z_{vr} are set such that $Z_{hr} = Z_n$ and $Z_{vr} = 0.0$ mm^6 m^{-3}.

[33] Another way of looking at the impacts measurement errors have upon F_{iz} is to consider how 1 dBZ changes in Z_h or Z_v affect F_{iz}. A -1 dBZ error in Z_h with $Z_{hr} = 45$ dBZ, $Z_{vr} = 43.071$ dBZ (meaning the measured Z_h is 44 dBZ) produces $F_{iz} = 0.4$ when the expected value is $F_{iz} = 0.0$. On the other hand, a +1 dBZ error in Z_v with $Z_{hr} = 45$ dBZ, $Z_{vr} = 43.071$ dBZ (meaning the measured Z_v is 44.071 dBZ) produces $F_{iz} = 0.42$ when the expected value is $F_{iz} = 0.0$. These examples are chosen so as to maximize the errors in F_{iz}. The same may be done for the F_{ik} example. A +1 dBZ error in Z_h coupled with a -0.3 ° km^{-1} error in K_{DP} for $Z_{hr} = 45$ dBZ, $K_{DP} = 0.6$ ° km^{-1} (meaning the measured Z_h and K_{DP} values are 46 dBZ and 0.3 ° km^{-1}, respectively, produce $F_{ik} = 0.69$ when the expected value is $F_{ik} = 0.0$.

of ice to Z_h, F_i is herein estimated by averaging F_{iz} and F_{ik} if $Z_h \geq 50$ dBZ and by weighting F_{iz} four times more than F_{ik} if $Z_h < 50$ dBZ.

With an estimate of F_i, measurements of Z_h and Z_{DR}, and the assumption that graupel/hail are isotropic with respect to reflectivity ($Z_{hi} = Z_{vi}$), Z_{hr}, Z_{DRr}, and Z_{hi} can be estimated. As indicated earlier, these are the estimates that are needed to initialize the raindrop and graupel/hail size distributions. The dependence of Z_{hr} and Z_{DRr} on N_{0r} and Λ_r for truncated, exponential raindrop size distributions has been investigated (Seliga and Bringi 1976; Seliga and Bringi 1978; Seliga et al. 1979; Seliga et al. 1981). Curve fits to their $D_{max} = 8.0$ mm results produce

$$\Lambda_r = 3.118 Z_{DRr}^{-0.2155}, \tag{3.58}$$

$$N_{0r} = 10^{0.1 Z_{hr} - 5.378} Z_{DRr}^{-5.516}, \tag{3.59}$$

where Λ_r is in mm $^{-1}$, Z_{DRr} is in dB, N_{0r} is in m $^{-3}$ mm $^{-1}$, and Z_{hr} is in dBZ. The curve (3.58) is consistent with the theoretical result of Ulbrich and Atlas (1984) but differs moderately from the disdrometer-based result of Seliga et al. (1986). These curve fits are used to initialize the rain field.

The initialization of graupel/hail requires one more piece of information beyond that provided by Z_{hi} and the assumptions concerning size distribution, shape, canting, incidence angles, and maximum and minimum sizes. This extra piece of information is the electromagnetic wetness of the graupel/hail. Because the model downdrafts are generally initialized at levels below the melting level, the graupel/hail at these levels are expected to have coatings of liquid water owing to melting (e.g., Rasmussen et al. 1984b). The backscattering of melting graupel and hail has been investigated (e.g.,

Kerker et al. 1951; Herman and Battan 1961). Results indicate that the backscattering cross section of a melting graupel/hailstone lies between that of an all ice/air hydrometeor (electromagnetically dry) and that of a liquid hydrometeor of the same size (electromagnetically wet). Thus,

$$\sigma_{ia,w}(D_{ia,w}, D_{sh}, \rho_{ia}) = \sigma_{ia}(D_{ia,w}, \rho_{ia}) + f\left[\sigma_w(D_{ia,w}) - \sigma_{ia}(D_{ia,w}, \rho_{ia})\right], \quad (3.60)$$

where $\sigma_{ia,w}(D_{ia,w}, D_{sh}, \rho_{ia})$ is the backscattering cross section of a water-coated ice/air hydrometeor of diameter $D_{ia,w}$, D_{sh} is the thickness of the water shell, ρ_{ia} is the density of the ice-air hydrometeor, $\sigma_{ia}(D_{ia,w}, \rho_{ia})$ is the backscattering cross section of an ice/air hydrometeor having diameter $D_{ia,w}$ and density ρ_{ia}, $\sigma_w(D_{ia,w})$ is the backscattering cross section of a liquid hydrometeor having diameter $D_{ia,w}$, and f is the electromagnetic wetness. By relating this to the equivalent reflectivity Z_{he} that is obtained with weather radars,[34] it is shown in appendix D that

$$Z_{ea} \approx \frac{|K_i|^2}{|K_w|^2} \int_{D_{a,m}}^{D_{a,m}} \left(\frac{\rho_{ia}}{\rho_i}\right)^2 (1-f) D_{ia,w}^6 \, N(D_{ia,w}) dD_{ia,w} + \int_{D_{a,m}}^{D_{a,m}} f \, D_{ia,w}^6 \, N(D_{ia,w}) dD_{ia,w} \quad (3.61)$$

where $|K_i|^2 = 0.176$ and $|K_w|^2 = 0.93$ are related to the refractive indices of ice (i) and liquid water (w) (see appendix D), ρ_i is the density of ice, and it is assumed that melt-water does not penetrate into the ice/air hydrometeors (the ice/air hydrometeors are not

[34] The Z_h that is typically obtained with weather radars is more accurately labeled Z_{eh}, the equivalent reflectivity factor at horizontal polarization. This is because Z is determined using the weather radar equation, which requires assumptions concerning the scattering behavior of hydrometeors. It is typically assumed that Rayleigh scattering applies and that the hydrometeors are composed of liquid water. Since these assumptions are not always valid, Z_{he} is what is actually obtained. When dealing with horizontal

porous). The results of Herman and Battan (1961) indicate that for Rayleigh scatterers and for a fixed radar wavelength, f depends upon both D_{sh} and $D_{ta,wa}$. Assuming that ρ_{ta} and ρ_i are independent of $D_{ta,wa}$, defining $\bar{f}$ as

$$\bar{f} = \frac{\int_{D_{a,wa\_min}}^{D_{a,wa\_max}} f\, D_{ta,wa}^{6}\, N(D_{ta,wa})\, dD_{ta,wa}}{\int_{D_{a,wa\_min}}^{D_{a,wa\_max}} D_{ta,wa}^{6}\, N(D_{ta,wa})\, dD_{ta,wa}}, \tag{3.62}$$

and inserting the Cheng-English size distribution results in

$$Z_{hi} \approx (100\ \mathrm{m}^{-3}\,\mathrm{mm}^{3.11})\,\Lambda_{gh}^{2.89}\left[\bar{f} + (1-\bar{f})\frac{|K_i|^2}{|K_w|^2}\left(\frac{\rho_{ta}}{\rho_i}\right)^2\right]\times \left[\gamma(7,\Lambda_{gh} D_{ta,wa\_max}) - \gamma(7,\Lambda_{gh} D_{ta,wa\_min})\right], \tag{3.63}$$

where $\gamma(a,x) = \int_0^x e^{-t} t^{a-1}\, dt$ is the incomplete gamma function, Z_{hi} is in $\mathrm{mm}^6\ \mathrm{m}^{-3}$, Λ_{gh} is in mm^{-1}, and D_{ta,wa_max} and D_{ta,wa_min} are in mm. This can also be expressed as

$$Z_{hi} \approx N_{0gh}\left[\bar{f} + (1-\bar{f})\frac{|K_i|^2}{|K_w|^2}\left(\frac{\rho_{ta}}{\rho_i}\right)^2\right]\int_{D_{a,wa\_min}}^{D_{a,wa\_max}} D_{ta,wa}^{6}\exp(-\Lambda_{gh} D_{ta,wa})\, dD_{ta,wa}, \tag{3.64}$$

which is more amenable to solution [for example, if $\Lambda_{gh} < 0$, then difficulties arise in evaluating $\Lambda_{gh}^{2.89}$ (resolved below) and the incomplete gamma functions in (3.63)].

With knowledge concerning values of Z_{hi}, N_{0gh}, $\bar{f}$, $|K_i|^2$, $|K_w|^2$, ρ_{ta}, ρ_i, D_{ta,wa_min}, and D_{ta,wa_max}, (3.64) can be solved for Λ_{gh}. The Z_{hi} values are determined as discussed above. In order to avoid problems for small or negative Λ_{gh} values, the Cheng et al.

---

polarization, the Z_e and Z_r in appendix D become Z_{he} and Z_{hr} and $Z_{hi} = Z_{he} - Z_{hr}$. (The Z_{hi} used herein is really an equivalent Z_{hi}.)

(1985) N_{0gh}-Λ_{gh} relation is truncated at $\Lambda_{gh} = 0.2$ mm^{-1} (approximately the smallest Λ_{gh} of their data), resulting in

$$N_{0gh} = \begin{cases} 0.134 \text{ m}^{-3} \text{ mm}^{-1} & \Lambda_{gh} < 0.2 \text{ mm}^{-1} \\ (100 \text{ m}^{-3} \text{ mm}^{3.11}) \Lambda_{gh}^{4.11} & \Lambda_{gh} \geq 0.2 \text{ mm}^{-1} \end{cases}. \quad (3.65)$$

As indicated above, f depends upon both D_{sh} and $D_{tot,wc}$. This raises the question of appropriate values for D_{sh}. Because PR methods that depend upon isotropy of graupel and hail are utilized herein, consistency requires D_{sh} values that are small enough so that water-coated ice-air hydrometeors are nearly spherical. According to Chong and Chen (1974), water-coated ice-air hydrometeors are nearly spherical if $D_{sh} \leq \sim 0.2$ mm. Thus, it is assumed in most calculations that $D_{sh} = 0.1$ mm for graupel and hail that are larger than $D_{tot,wc,cut}$. For graupel/hail that are smaller than $D_{tot,wc,cut}$, D_{sh} is initialized in a different manner. This is necessary because water coats D_{sh} thick are not possible for very small graupel since they require more mass than is available from the whole particle. To avoid this problem, the ratio of the mass of the water coat m_{wc} to the mass of the total hydrometeor m_{gh} is held constant for graupel/hail that are smaller than $D_{tot,wc,cut}$. It is not immediately obvious as to what would be an appropriate value for this ratio. A high value means that the small melting particles are principally composed of liquid water while a low value means predominance of ice water. The requirement of polarimetric isotropy does not help here since for small particles the deformation is minimal, even for all liquid-water hydrometeors (Pruppacher and Beard 1970). Without much physical guidance, an arbitrary $f_{wc,m} = m_{wc}/m_{gh} = 0.3$ value is used. This corresponds to the water coat mass fraction

for $D_{sh} = 0.1$ mm, $D_{ial,wc} = 1.0$ mm [with $\rho_{ial} = 870$ kg m^{-3} (see below)]. Thus, the values of D_{sh} are determined using

$$D_{sh} = \begin{cases} D_{ial,wc} - D_{ial,wc}\left[\dfrac{\rho_w\left(1 - f_{wc,m}\right)}{\rho_{ial} f_{wc,m} + \rho_w\left(1 - f_{wc,m}\right)}\right]^{1/3} & D_{ial,wc} < 1.0 \text{ mm} \\ 0.1 \text{ mm} & D_{ial,wc} \geq 1.0 \text{ mm} \end{cases} , \quad (3.66)$$

where the relation for $D_{ial,wc} < 1.0$ mm results from the definition of $f_{wc,m}$, ρ_w is the density of liquid water, and $D_{ial,wc,cut} = 1.0$ mm. With the variation of D_{sh} established, estimations of $\bar{f}$ are now possible. Analysis of the 10-cm wavelength results of Herman and Battan (1961) indicates that f changes monotonically from ~0.74 to ~0.4 for water coated ice air hydrometeors having diameters ranging from 2 to 10 mm and water shells 0.1 mm thick. Moreover, this variation is roughly linear with $f_{wc,m}$, which is consistent with the findings summarized by Battan (1973, §5.1). Because hydrometeors smaller than $D_{ial,wc,cut}$ have a constant $f_{wc,m}$, they may, based on the above, be expected to have a nearly constant f value. From the results summarized by Battan (1973, §5.1), $f = \sim 0.85$ appears appropriate for the small hydrometeors. Given (3.62) and (3.66), the value of $\bar{f}$ is some sort of compromise between the values for the larger ($\geq D_{ial,wc,cut}$) and smaller ($< D_{ial,wc,cut}$) hydrometeors. The appropriate value of $\bar{f}$ depends upon the distribution of both f and $D_{ial,wc}^6 N(D_{ial,wc})$ with $D_{ial,wc}$. Because of the sixth-power weighting in $D_{ial,wc}^6 N(D_{ial,wc})$, it is expected that $\bar{f}$ will be affected most strongly by relatively large graupel/hailstones [see, for instance, Doviak and Zrnić (1993, §8.3.2)]. Thus, an $f = 0.6$ value is used in all computations.

The weak dependencies of $|K_i|^2$ and $|K_w|^2$ upon temperature (e.g., Gunn and East 1954) are ignored, with $|K_i|^2 = 0.176$ and $|K_w|^2 = 0.93$ values used. Similarly, the weak temperature dependence of ρ_i is ignored, with the $\rho_i = 920$ kg m^{-3} value used [corresponds to a temperature of –20 °C (Pruppacher and Klett 1997, 79-80)].

The $\rho_{ai} = 870$ kg m^{-3} value is generally used. This is toward the low end of the values typically observed for hailstones (English 1973) and is consistent with the values reported by Braham (1963) for graupel particles collected during Project Whitetop (Braham 1964). It is believed that the Braham (1963) graupel density values are relevant to the current study because the cases considered herein are from the same geographical region [Oklahoma in this study and Missouri in the Braham (1963) study] and, due to their relatively warm cloud bases [as in the Project Whitetop study (Koenig 1963; Braham 1964; Braham 1986)], should have relatively more (high-density) frozen droplets that develop into graupel (and hail) (Koenig 1963; Braham 1964; Knight 1981). This (relatively high) ρ_{ai} value is also consistent with the previous assumption that the ice/air hydrometeors are not porous, which was used to obtain (3.61).

As stated previously, $D_{gn\_min} = 0.05$ mm and $D_{gn\_max} = 9.0$ mm. These do not necessarily correspond exactly to D_{ai,wc_min} and D_{ai,wc_max}. The Cheng-English distribution applies to *dry* hailstones since, after collection at the ground, they were stored in dry ice (Cheng and English 1983). This would freeze any liquid water either in, or on the surface of, the hailstones. (The frozen water presumably would not have the same density as that of the ice/air hydrometer. Since most of the frozen water is expected to have been shook lose when the hailstones were collected, this is expected to

be of little importance.) Because of the difference in the densities of ice/air hydrometeors and liquid water, water-coated ice/air hydrometeors do not have the same diameters as they did when they were dry (prior to melting). In other words, $D_{ia,wc} \neq D_{ia,init}$. The Cheng-English distribution corresponds to $D_{ia,init}$ while in the model the appropriate diameters are $D_{ia,wc}$. In these experiments, however, initial water-coat mass fractions are assumed to be relatively small (< 0.3) for all sizes (as per the previous discussion concerning D_{sh}). As a consequence, $D_{ia,wc} \approx D_{ia,init}$, with maximum relative differences between $D_{ia,wc}$ and $D_{ia,init}$ being ~1.4%. Therefore, the Cheng-English distribution is assumed to hold for the water-coated ice/air hydrometeors and it is assumed that $D_{ia,wc,min} = 0.05$ mm and $D_{ia,wc,max} = 9.0$ mm.

3.2.4 Boundary Conditions, Initial Conditions, Solution Methods, and Parameters

At the upper and lower boundaries, all model variables, excluding $\overline{w}$, are allowed to evolve through the various processes outlined above. For $\overline{w}$, rigid boundary conditions are applied, with $\overline{w} = 0$ at the upper and lower boundaries.

At time zero, all model fields, except for rain and graupel/hail at one altitude, are equal to environmental values. Diagnosed rain and graupel/hail fields are inserted at one altitude, that at which they are observed, at each time step (including time step zero). This is consistent with steady hydrometeor production in the storms. Situations in which the hydrometeor fields driving the RFD evolve are not considered.

For tornadic cases, observations just prior to the development of the most significant tornado in each data set (not shown) were used. For nontornadic cases,

observations at the time of the strongest low-level mesocyclone, as estimated from Doppler radar data (not shown), were used.

Because of the relative simplicity of the approach used herein, three-dimensional analysis fields are not needed. Consequently, the objective analysis techniques that are developed in chapter 2 and are useful in applications that require the quantitative utilization of radar data are not applied in this particular investigation.

Generally, the model is driven using hydrometeors fields from relatively low altitudes (~1.5 km AGL). There are several reasons for this. As will be shown, above-boundary-layer storm environments are relatively stable to (model) downdrafts driven by precipitation fields typical of this data set. In fact, deep above-boundary-layer downdrafts may depend upon the presence of relatively large hail (> 1.0 cm diameter). Without these relatively large hailstones, a shallow downdraft in which all of the smaller hailstones melt is produced above the boundary layer. Since this model does not include relatively large hail, in part because of uncertainties in identifying maximum hail size from polarimetric radar data, model downdrafts are initialized using data from relatively low altitudes. This way, because the largest hailstones will likely have melted to the point that they are much closer to the maximum size used in the model, more realistic graupel/hail fields are used in the lowest part of the troposphere, which appears to be a very important layer.

Finite differences are used. They are forward in time, upstream for advection terms, and centered in space for non-advection terms. The grid spacing is 0.1 km and the time step is 0.5 s. The finite differences, grid spacing, and time step are all similar

to those used by Srivastava (1985, 1987). Tests were performed to ensure numerical convergence.

Fifty rain and graupel/hail size bins are used. Following Ogura and Takahashi (1971), $\alpha^2 = 0.1$. The radius of the downdrafts a is set at 3 km. This is approximately in the middle of the size range given by Knupp and Cotton (1985) for precipitation-driven downdrafts.

3.2.5 Verification

First, zero forcing was applied to the model to check model veracity. The results at t = 10 minutes are shown in Fig. 3.1. The model drift at this point, at which the maximum downdraft magnitude is 0.01 m s^{-1}, is minimal. Some drift does occur, however, and amplifies with time (not shown). From its structure, this drift appears to be from weak numerical instabilities that are not completely controlled, perhaps because in the case of zero forcing lateral mixing and dynamic entrainment are minimal. Considering that single-precision arithmetic is used and that the case illustrated in Fig. 3.1 is 1200 steps into the simulation, the performance is quite good.

The second test is a comparison to the results of Srivastava (1987) that are illustrated in his Fig. 7 and shown here in Fig. 3.2. In this case, graupel and hail conforming to a Marshall-Palmer size distribution with parameters $N_{0gh} = 8000\ \mathrm{m^{-3}\ mm^{-1}}$ and $\Lambda_{gh} = 1.7\ \mathrm{mm^{-1}}$ are released from an altitude of 4 km AGL in an environment having a temperature lapse rate of 7 °C km^{-1}, a surface temperature of 28 °C, a surface pressure of 870 mb, a constant relative humidity of 70%, and a temperature at the release point of 0 °C. Because this model can only handle

graupel/hail that are melting, graupel/hail had to be released from 3.5 km AGL in these tests. While this will undoubtedly produce differences between the results of Srivastava (1987) and those obtained here, they are expected to be relatively minor since most of the melting occurs once the graupel/hail have fallen about 0.5 km (Fig. 3.2).

Figure 3.3 shows the results of this comparison simulation at t = 2000 s. In this and subsequent plots of vertical velocities, the $\overline{w} = 0$ at z = 0 boundary condition is omitted. The reason for this is the absence of perturbation pressures and the use of an upstream advection scheme means that this boundary condition is not dynamically communicated to the model domain. Consequently, plotting $\overline{w} = 0$ at z = 0 would be purely cosmetic and would imply something that is not dynamically enforced. Therefore, this boundary condition is not depicted.

Somewhat surprisingly, the results illustrated in Fig. 3.3 differ significantly from those obtained by Srivastava (1987). For these conditions Srivastava (1987) simulated a downdraft that is strongest near the ground and that has a maximum strength of about 11.3 m s^{-1}. Here, the downdraft is strongest aloft (2.3 km AGL) and has a maximum strength of 5.62 m s^{-1}. Moreover, in Srivastava's simulation the downdraft strengthens with decreasing altitude, while here the downdraft exhibits more complicated structure. The simulated rain and graupel/hail fields do follow the same patterns, but the peak of the rainwater mixing ratio r_r is much smaller here (~1.2 g kg^{-1}) than in Srivastava's simulation (~3.2 g kg^{-1}). While some of this difference could result from differing altitudes and thus dry-air densities at which these peaks occur, it is doubtful that this is the main cause since the peaks occur at nearly the same altitudes (1.6 km AGL here and ~2.2 km AGL in Srivastava's simulation).

One may suspect that the difference in the graupel/hail release altitudes is the cause of these large differences. This is not likely, however, for the reason given earlier: most of the melting occurs from 3.5 km AGL and down. In fact, the cause is a difference in model formulation. The most important difference between this model and that of Srivastava (1985, 1987) is Srivastava does not include dynamic entrainment. To see whether this is the cause of these differences, a test was performed in which dynamic entrainment was turned off. The results of this test, shown in Fig. 3.4, are quite close to those of Srivastava (1987). The peak downdraft magnitude is 10.6 m s^{-1} as compared to Srivastava's 11.3 m s^{-1}; the peak r_r is 1.975 g kg^{-1} while Srivastava's peak is 3.2 g kg^{-1}. [If the peak r_r value is adjusted for density differences owing to the difference of the heights of the peaks (1.4 km AGL here versus 2.2 km AGL in Srivastava), then the peak r_r values are within 1.08 g kg^{-1}]. The vertical profiles of r_r and r_g are similar in shape. They differ, however, in the altitude of the r_r peak. In addition, the vertical downdraft profiles also have some differences. In Srivastava (1987), the downdraft intensifies all of the way to the ground while here the downdraft intensifies down to about 1.6 km AGL and then weakens from there to the ground. Considering the multitude of physical processes involved, the agreement between this simulation and Srivastava's is excellent.

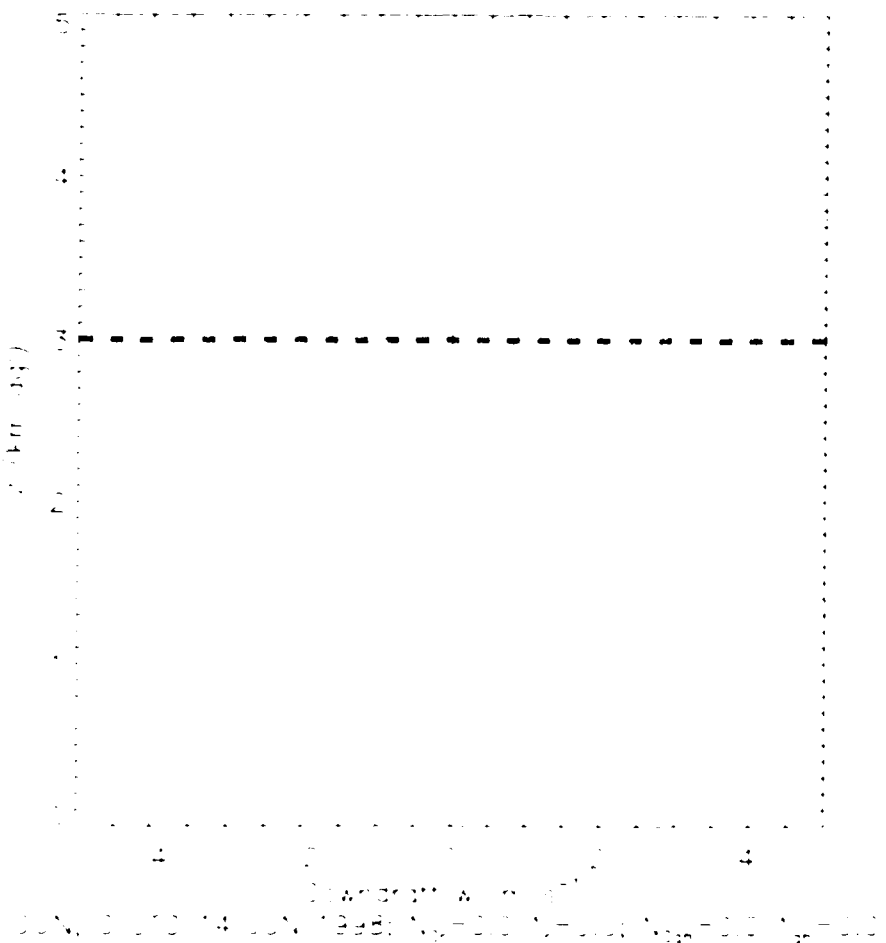

FIG. 3.1. Model results at t = 10 minutes for the case of zero forcing. Downdraft strength in m s^{-1} is plotted on the abscissa and height AGL in km is plotted on the ordinate. The thick, dashed, grey line indicates the precipitation insertion altitude (at which no precipitation was inserted for this simulation). The 00 UTC 14 June 1998 Norman, Oklahoma sounding was used for this test. Maximum downdraft magnitude is 0.01 m s^{-1}.

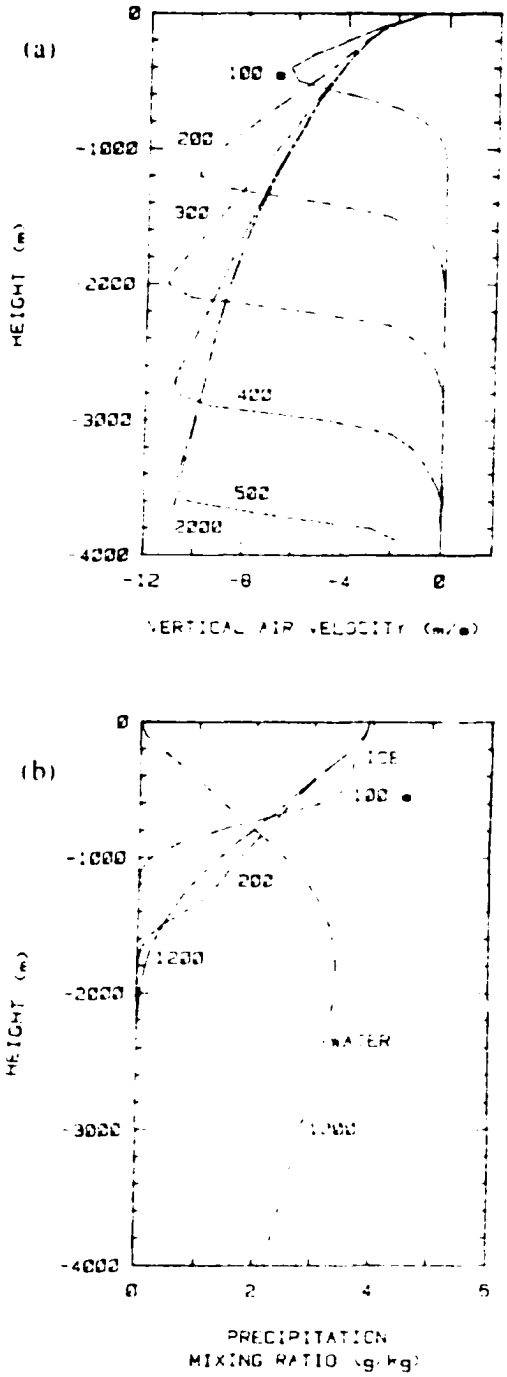

FIG. 3.2. (a) Vertical velocity (m s^{-1}) versus height below the release altitude (m) of graupel/hail. (b) Same as (a) except for mixing ratio of rain (WATER) and graupel/hail (ICE) (g kg^{-1}). The -4000 m height corresponds to the surface. Labels beside plots indicate the times of the simulated values. In (b), a steady state is reached by 1200 s and thus later times are not displayed. [From Srivastava (1987).] *Courtesy of the American Meteorological Society. Copyright 1987.*

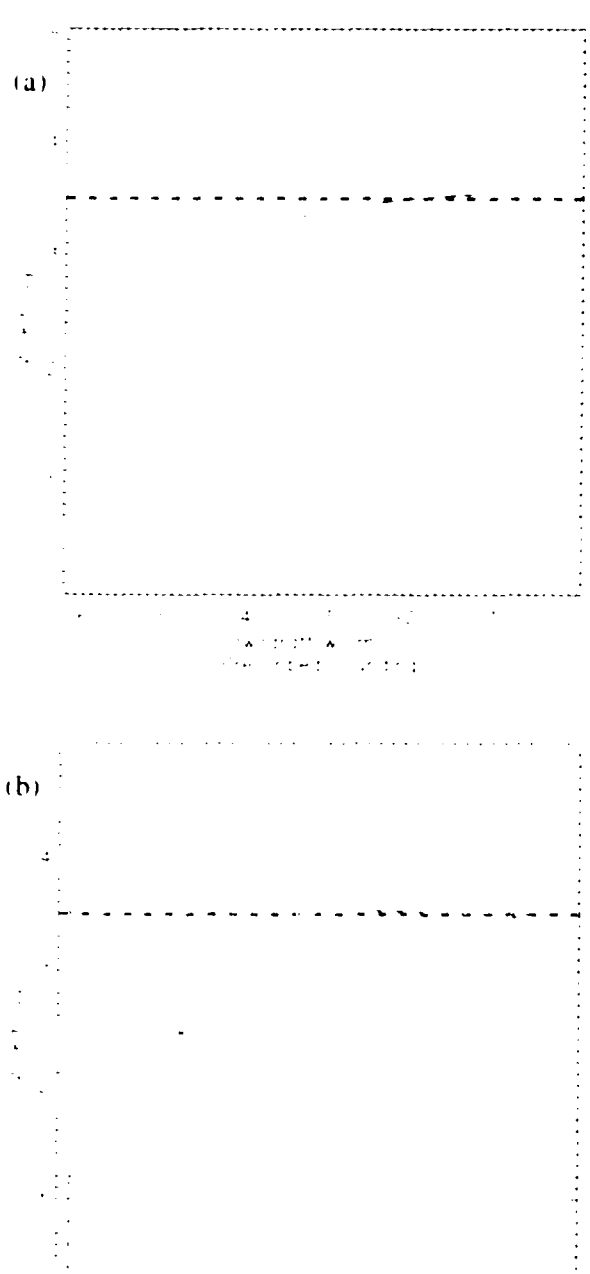

FIG. 3.3. (a) As in Fig. 3.1 except for model results at t = 2000 seconds for the Srivastava (1987) comparison (see text for details concerning the parameters used in this comparison). (b) As in (a) except for mixing ratios of rain (r_r; solid line) graupel/hail (r_{gh}; dashed line), and cloud (r_c; dotted line) in g kg^{-1}.

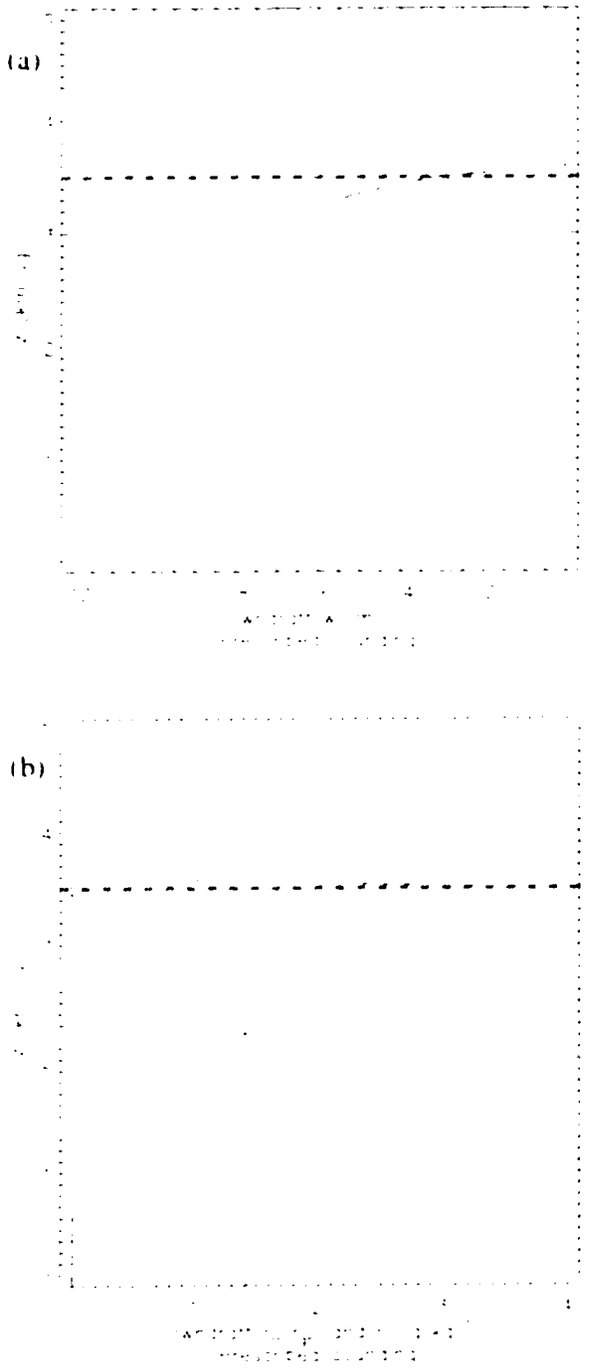

FIG. 3.4. As in Fig. 3.3 except dynamic entrainment is turned off.

3.3 Results

3.3.1 'High' Altitude Release

Before comparing tornadic and nontornadic cases, it is enlightening to consider results for a high altitude release, where the adjective 'high' is used because compared to subsequent simulations the release point of the precipitation is high. The results of such an experiment are shown in Fig. 3.5. The data for this case are from the hook echo of the tornadic supercell that affected the Oklahoma City, Oklahoma, area on 13 June 1998.[35]

At first graupel and hail dominate the precipitation field. Upon insertion, they begin melting and produce a downdraft. They melt into raindrops fairly quickly, however, and the downdraft dissipates. Significant downdraft does not appear again until the hydrometeors reach the boundary layer, at which point the evaporation of raindrops drives the downdraft. It appears, therefore, that in this environment the production of downdraft above the boundary layer depends strongly upon the presence of graupel and hail. Above the boundary layer, evaporation of rain is not sufficient to drive a significant downdraft.

The altitude-dependence of the ability of evaporation of rain to drive downdrafts can be understood by considering the sounding for this case (Fig. 3.6). In the boundary layer, where evaporation of rain is effective in driving a downdraft, the lapse rate is dry adiabatic. Since precipitation-driven downdrafts descend somewhere between dry and

[35] The parameters for this case are: z = 3.7 km AGL, Z_h = 41.0 dBZ, Z_{DR} = 3.7 dB, K_{DP} = 0.1 ° km^{-1}, F_{rr} = 0.0, F_{hh} = 0.79, F_{ii} = 0.16, Z_{hr} = 40.25 dBZ, Z_{DRr} = 4.96 dB, Λ_r = 0.986 mm^{-1}, N_{0r} = 9266.3 m^{-3} mm^{-1}, Z_{hi} = 32.98 dBZ, and Λ_{0i} = 3.01 mm^{-1}

moist adiabatically (Das and Subba Rao 1972), the environment offers minimal resistance to the downdraft there. Above the boundary layer, the environmental lapse rate is between the moist and dry adiabatic lapse rates. There, the environment is more resistant to downdrafts. This temperature structure is quite typical of many supercell environments, including those for the cases analyzed herein. Consequently, it appears as if above-boundary-layer downdrafts in supercell storms may depend strongly upon graupel and hail.

In this simulation, hail diameters are less than or equal to 9.0 mm. Larger hail would take longer to melt and thus could possibly support a much deeper downdraft above the boundary layer. Larger hail is not included here principally because of uncertainties in the determination of maximum hailstone size using polarimetric radar data. (Additionally, the inclusion of larger hail would require a parameterization of shedding.). Given this uncertainty, it was decided to initialize downdrafts using data from relatively low altitudes. At these altitudes the largest hailstones will likely have melted to the point that they are much closer to the maximum size used in the model. Thus, the graupel/hail fields obtained at lower altitudes should be more realistic and are in a position to drive downdrafts from just above and through the boundary layer. As a consequence of this approach, these results are not expected to hold for situations in which graupel and hail are able to drive downdrafts through a deep layer and into the boundary layer.

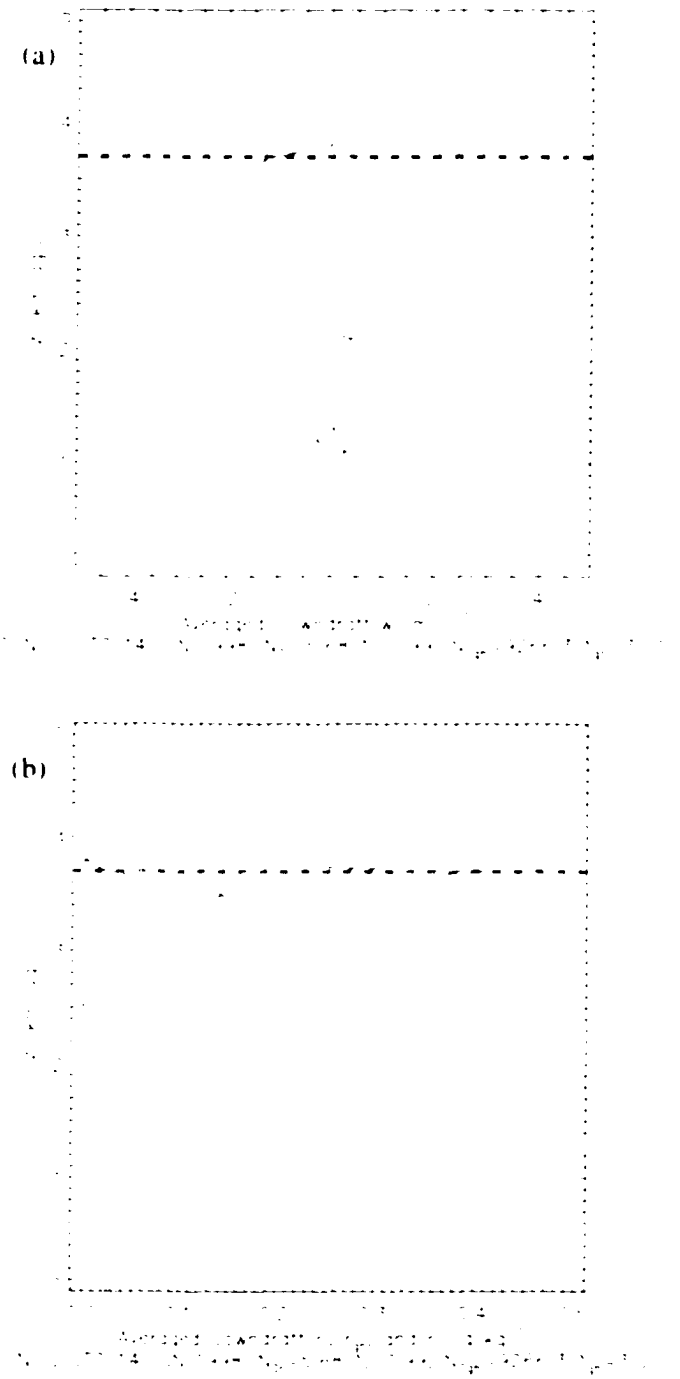

FIG. 3.5. (a) Vertical velocity (m s^{-1}) versus altitude (km AGL) for the high-altitude, 13 June 1998 simulation. In order to decrease the impact of buoyancy oscillations, model results are averaged over a five minute interval from t = 1050 to t = 1350 seconds (centered on t = 20 minutes). The sounding used to initialize the environment is the 00 UTC 14 June 1998 Norman, OK, sounding. (b) As in (a) except for mixing ratios of rain (r_r; solid line) graupel/hail (r_{gh}; dashed line), and cloud (r_c; dotted line) in g kg^{-1}. Thick, dashed, grey lines indicate the precipitation insertion altitude.

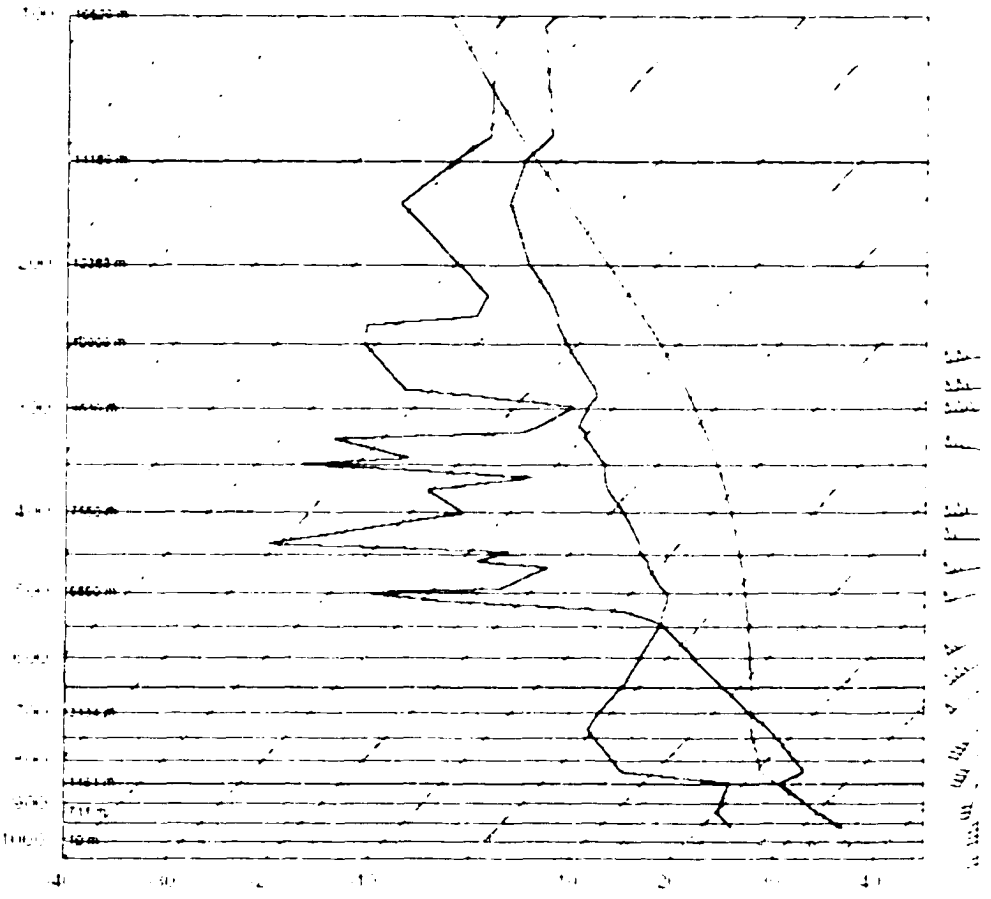

FIG. 3.6. The 00 UTC 14 June 1998 Norman, OK, sounding. Pressure (mb) is along the ordinate, temperature (°C) is along the abscissa, and winds (knots) are plotted on the right.

3.3.2 Polarimetric Cases

The cases considered here are listed in Table 3.1. There are four tornadic (25 May 1997, 13 June 1998, 4 Oct. 1998, and 3 May 1999) and three nontornadic (18 June 1992, 19 Sept. 1993, and 8 June 1998) cases. While this analysis is far from being able to give significant results in a statistical sense, it is hoped that the patterns that arise can be applied to a wider group of storms.

For these simulations, the sounding that was closest to the storm time and location is generally used. Exceptions are when soundings had been modified by convection. Of the four tornadic cases, two, 25 May 1997 and 3 May 1999, had soundings that appeared to have been significantly modified by convection. For 25 May 1997, convection appears to have significantly cooled and moistened the atmosphere near the surface (Fig. 3.7b). Because sounding structure strongly affects downdrafts (see the previous section), the sounding from the previous was used for this case (Fig. 3.7a). This is far from an optimal solution. However, other options, like interpolating conditions from surrounding soundings or using predicted soundings, seem less palatable. At least with this approach the simulated downdraft occurs within an actual sounding. It is hoped that the synoptic setting the day before the event was similar to that the day of the event and thus that the use of the previous day's sounding produces reasonable results. For 3 May 1999, the proximity of the convection appears to have altered the 00 UTC 4 May 1999 Norman, Oklahoma, sounding (Fig. 3.8b). Compared to the 18 UTC sounding obtained six hours earlier, temperatures are significantly greater in a layer centered near 800 mb. This suggests the influence of

compensating sinking motions around the convection. Because of the alteration of the lapse rate of temperature in the boundary layer, this strongly affects the low-level downdraft. The 18 UTC sounding (Fig. 3.8a), therefore, is used in the simulation (the radar data for this case are from 2242 UTC 3 May 2002).

Norman, Oklahoma, soundings are unavailable for the day of the nontornadic 18 June 1992 case. Consequently, the 00 UTC 19 June 1992 Stephenville, Texas, sounding is used (Fig. 3.9a). It is hoped that this sounding adequately approximates the environment of the 18 June 1992 supercell studied here. The use of the previous day's Norman, Oklahoma, sounding produces similar results. As in the 25 May 1997 case, the proximity sounding for 8 June 1998 (Fig. 3.9b) appears to indicate significant cooling near the surface owing to convection. The previous day's sounding is therefore used in this simulation. In addition, polarimetric radar data for the 8 June 1998 case are available only at about 0.5 km AGL. For the results shown here the estimated 0.5 km AGL precipitation fields were inserted at 1.5 km AGL so that the simulated downdraft might draw air from above the boundary layer downward. Because the precipitation was ineffective at doing so, however, the results for 0.5 and 1.5 km AGL insertion points are nearly equivalent below 0.5 km AGL.

Simulated downdraft profiles for the four tornadic cases for which polarimetric radar data are available are shown in Fig. 3.10. With the exception of the 4 October 1998 case, the profiles look similar. In the 4 October 1998 case, the hydrometeor fields appear to be too weak to drive significant downdraft in this model. In the other cases, a short burst in downdraft strength is followed by a zone of little to no downdraft, which is then followed by strengthening downdraft in the boundary layer. The initial bursts in

downdraft strength likely result from rapid evaporation of small raindrops and rapid melting of small graupel/hail (Hookings 1965; Srivastava 1985, 1987). Once these small hydrometeors evaporate and melt, the stability of the above-boundary layer environments significantly weakens the downdrafts. Downdrafts then strengthen again in the boundary layer where the environments are much less resistant to downdrafts.

Simulated downdraft profiles for the three nontornadic cases for which polarimetric radar data are available are shown in Fig. 3.11. These profiles are similar to those for the tornadic cases in Fig. 3.10. As with the tornadic cases, one of the nontornadic cases, 19 September 1993, appears to have had hydrometeor fields that were too weak to drive significant downdraft in this model. In the other two cases, the initial downdraft bursts, subsequent weakening, and final strengthening in the boundary layer are apparent. Owing to the similarity between these downdraft profiles and those for the tornadic cases, it is concluded that the low-level RFDs in tornadic and nontornadic supercells may not differ significantly in their kinematic structure.

Further insight into kinematic structures of modeled downdrafts can be gained by considering a typical buoyancy profile (Fig. 3.12). At the hydrometeor insertion point the total buoyancy is slightly negative and appears to be driven principally by loading. As the incipient downdraft sinks in a resistant environment, the total buoyancy becomes positive and rather large. The main contributor to these positive buoyancies is is temperature differences relative to the environment (thermal buoyancy). This is consistent with the earlier analysis of the high-altitude release simulation performed using the same sounding. The stability of the environment above the boundary layer results in the downdraft descending relatively warm compared to the environment. This

is especially enhanced in areas where the environmental lapse rate is small or even negative (implying increasing temperatures with height), as is the case here in the layer centered near 830 mb (Fig. 3.6). In the boundary layer, the dry adiabatic environmental lapse rate allows the thermal buoyancy, in concert with loading and r_t buoyancy, to drive a significant downdraft.

Differences between downdraft and environmental θ_e and θ_t values for the tornadic cases are depicted in Fig. 3.13. These differences are computed as downdraft value minus environmental value. As in Markowski et al. (2002),[36] the θ_t values are actually pseudoequivalent potential temperature θ_{ep} values (Emanuel 1994, §4.7) that are computed using the formula derived by Bolton (1980). Because the θ_t used herein differs from that used by MSR02 by the term $-\theta r_t$ (footnote 21) and because θ_e differences are generally larger, attention is focused on θ_e deficits.

The θ_t differences for the nontornadic cases are shown in Fig. 3.14. Most of the profiles in Figs. 3.13 and 3.14 are similar, with relative minima in θ_e differences near the surface, relative maxima in θ_e differences just above the surface, and relative minima above those. Three of the four tornadic cases have surface θ_e deficits that are less than the 4 K threshold observed by MSR02 and two of the three nontornadic cases have surface θ_e deficits that are greater than 4 K. Thus, five of the seven cases support the finding of MSR02 that the surface RFDs in tornadic and nontornadic supercells are thermodynamically different. However, the differences between the tornadic and nontornadic cases in this study are not overly great. For instance, average θ_e differences for the lowest 0.5 km in the tornadic cases are -0.12 K for 25 May 1997, -5.06 K for 13

June 1998, -1.1 K for 4 October 1998, and -1.9 K for 3 May 1999. Average θ_e differences for the lowest 0.5 km in the nontornadic cases are -5.83 K for 18 June 1992, -1.99 K for 19 September 1993, and -1.98 K for 8 June 1998. While the low-level nontornadic model downdrafts do appear to be potentially cooler on average than their tornadic counterparts, the differences are not large. Of course, sensitivity to the thermodynamic properties of the low-level RFD could be such that these fairly small differences translate into very large differences in tornado development.

Although on average the differences between tornadic and nontornadic cases are not great, two of the cases are significantly different and may be indicative of an important distinction between tornadic and nontornadic supercells. The θ_e and θ_v differences for these two cases, 25 May 1997 (tornadic) and 19 June 1992 (nontornadic), are shown in Figs. 3.15 and 3.16 along with their corresponding soundings and environmental θ_e profiles. In the 25 May 1997 case the low-level downdraft θ_e is very close to and even greater than that of the environment (Fig. 3.15a). In the 19 June 1992 case, on the other hand, the low-level downdraft θ_e is significantly lower (more than 4 K cooler) than that of the environment (Fig. 3.16a). From Figs. 3.15b and 3.16b it appears as these cases differ primarily because of their environmental θ_e profiles. In the tornadic 25 May 1997 case θ_e decreases slowly with height in the boundary layer whereas in the nontornadic 19 June 1992 case θ_e decreases rapidly. Consequently, the downdraft in the nontornadic 19 June 1992 case is much more able to bring low θ_e values down to the surface.

---

[36] Henceforth this paper will be referred to as MSR02, which stands for Markowski, Straka, and Rasmussen (2002).

The differences in these boundary layer θ_e profiles result from differences in their boundary layer moisture profiles. In the tornadic 25 May 1997 case water vapor mixing ratio r_v is nearly constant up to the top of the boundary layer, which appears to located where the lapse rate of temperature ceases to be dry adiabatic at ~900 mb. In the nontornadic 19 June 1992 case, r_v decreases with height throughout the boundary layer. Since dry-adiabatic, constant-r_v layers have constant θ_e, the θ_e profiles of these dry-adiabatic boundary layers are determined by their r_v profiles.

It seems, therefore, that the boundary-layer θ_e profile may be important to tornado development. In supercell environments the boundary layer, which is an important downdraft genesis/intensification region, is often dry adiabatic (or nearly so). Consequently, the vertical structure of r_v in the boundary layer appears to be an important variable modulating θ_e deficits and thus tornado development. All else being equal, tornado development should be favored when the boundary layer temperature and r_v structure is such that θ_e is constant or even increases with height. Thus, a dry-adiabatic, constant r_v boundary layer having an inverted-V structure should favor tornado development. On the other hand, tornado development should not be favored if r_v decreases significantly with height in a dry adiabatic boundary layer.

These conclusions, of course, must be qualified by the limitations of this study and also by known requirements for tornado development. For instance, if the precipitation field and/or dynamic forcing successfully bring air from above the boundary layer to the surface, then the vertical structure of θ_e in the boundary layer may be relatively unimportant. Since relatively large hail may be required to do this, this study cannot properly address this situation. Moreover, a constant-θ_e boundary layer

that is quite dry will have a high LCL. Despite its constant-θ_e structure, its high LCL will mean that tornado development is unlikely (Rasmussen and Blanchard 1998).

TABLE 3.1. Parameters for each of the polarimetric cases. Cases above the dashed line are tornadic and cases below the dashed line are nontornadic. Double dashes indicate that the value is not relevant. The Fujita rating and duration (in minutes) of each tornado that developed soon after the times of the data used in the simulations are indicated in parentheses in the form Fujita rating/duration.

CASE	z AGL (km)	Z_h (dBZ)	Z_{DR} (dB)	K_{DP} ($^\circ$ km^{-1})	F_L	F_H	F_S	Z_{hr} (dBZ)	Z_{DRr} (dB)	Λ_r (mm^{-1})	N_{0r} (m^{-3}mm^{-1})	Z_{hi} (dBZ)	Λ_{gh} (mm^{-1})
25 May 1997 (F2/4)	1.8	51.0	2.7	1.1	0.0	0.41	0.21	50.0	3.8	1.19	233.27	44.14	1.2
13 June 1998 (F2/3)	1.4	52.0	3.5	2.5	0.0	0.0	0.0	52.0	3.5	1.27	583.5	--	--
4 Oct. 1998 (F3/17)	1.25	40.0	2.25	0.5	0.0	0.0	0.0	40.0	2.25	1.74	424.93	--	--
3 May 1999 (F3/25)	1.8	42.5	2.5	0.35	0.0	0.15	0.03	42.37	2.61	1.57	325.73	27.24	4.76
18 June 1992	1.5	47.0	1.8	0.2	0.1	0.86	0.25	45.74	2.63	1.56	676.43	41.02	1.58
19 Sept. 1993	1.47	32.5	1.65	0.15	0.0	0.0	0.0	32.5	1.65	2.18	420.74	--	--
8 June 1998	0.52	49.5	1.5	0.65	0.27	0.6	0.33	47.75	2.5	1.62	1420.92	44.71	1.13

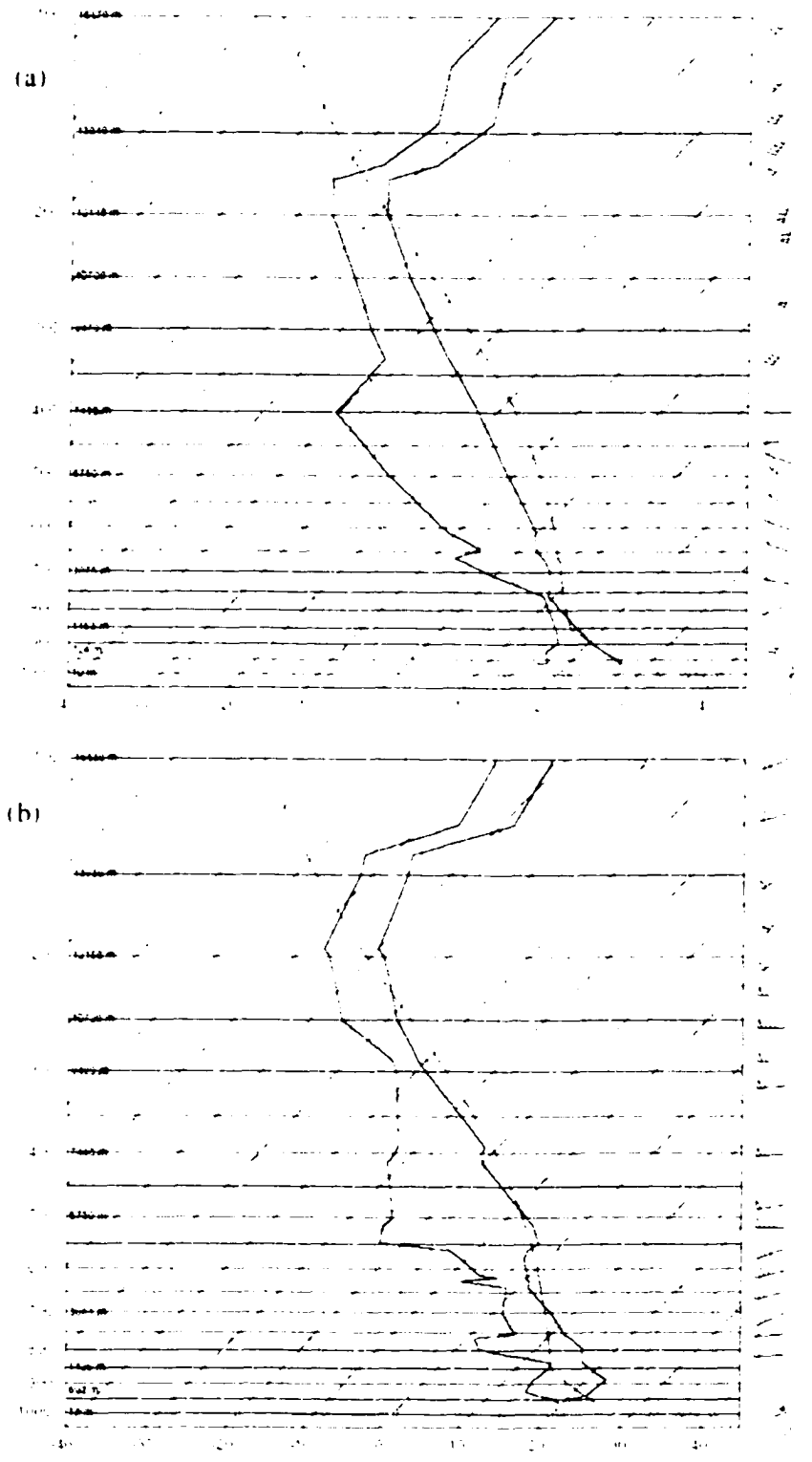

FIG. 3.7. As in Fig. 3.6 except for the (a) 00 UTC 25 May 1997 and (b) 00 UTC 26 May 1997 Norman, OK, soundings.

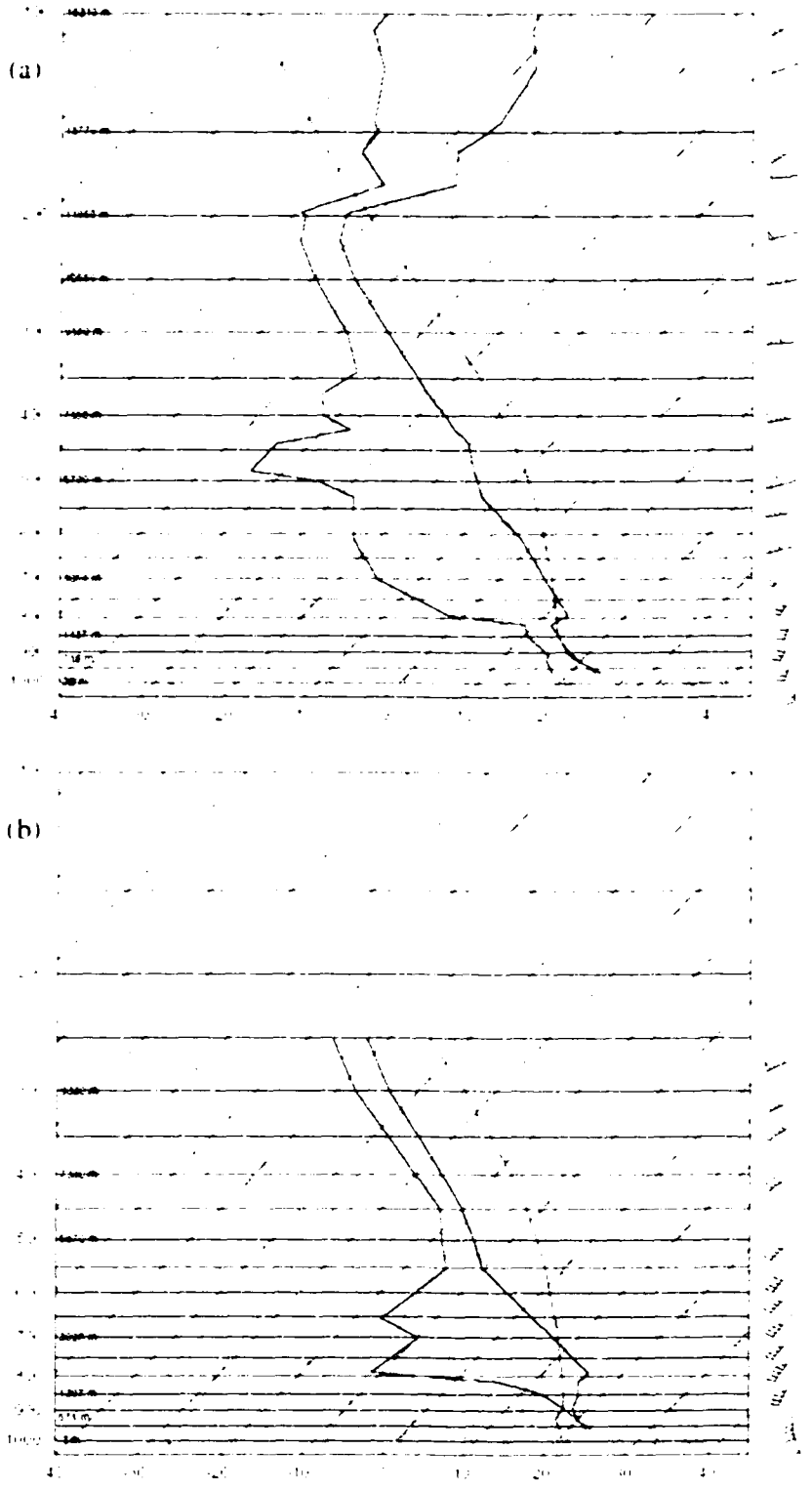

FIG. 3.8. As in Fig. 3.6 except for the (a) 18 UTC 3 May 1999 and (b) 00 UTC 4 May 1999 Norman, OK, soundings.

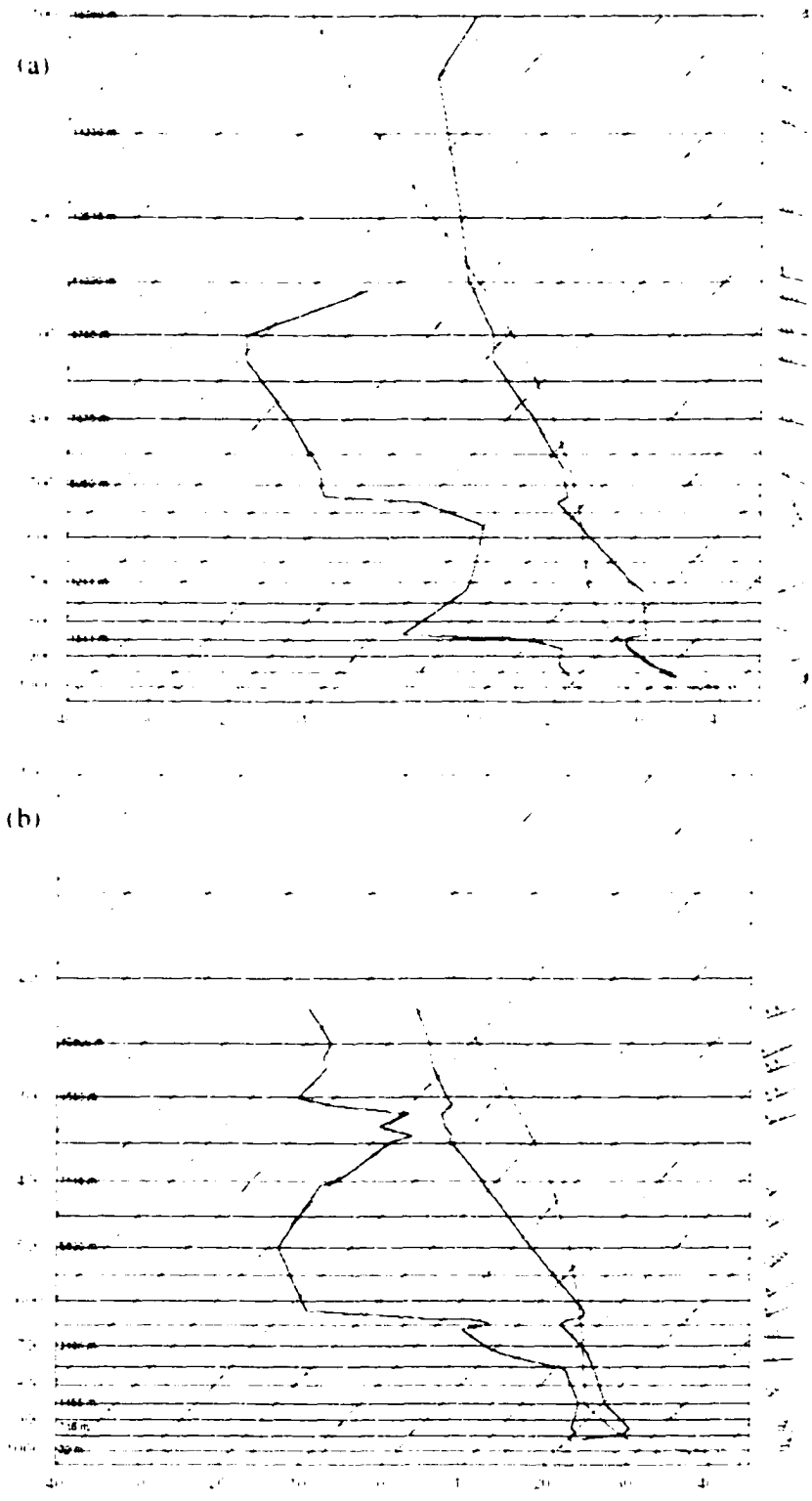

FIG. 3.9. As in Fig. 3.6 except for the (a) 00 UTC 19 June 1992 Stephenville, TX, and (b) 00 UTC 9 June 1998 Norman, OK, soundings.

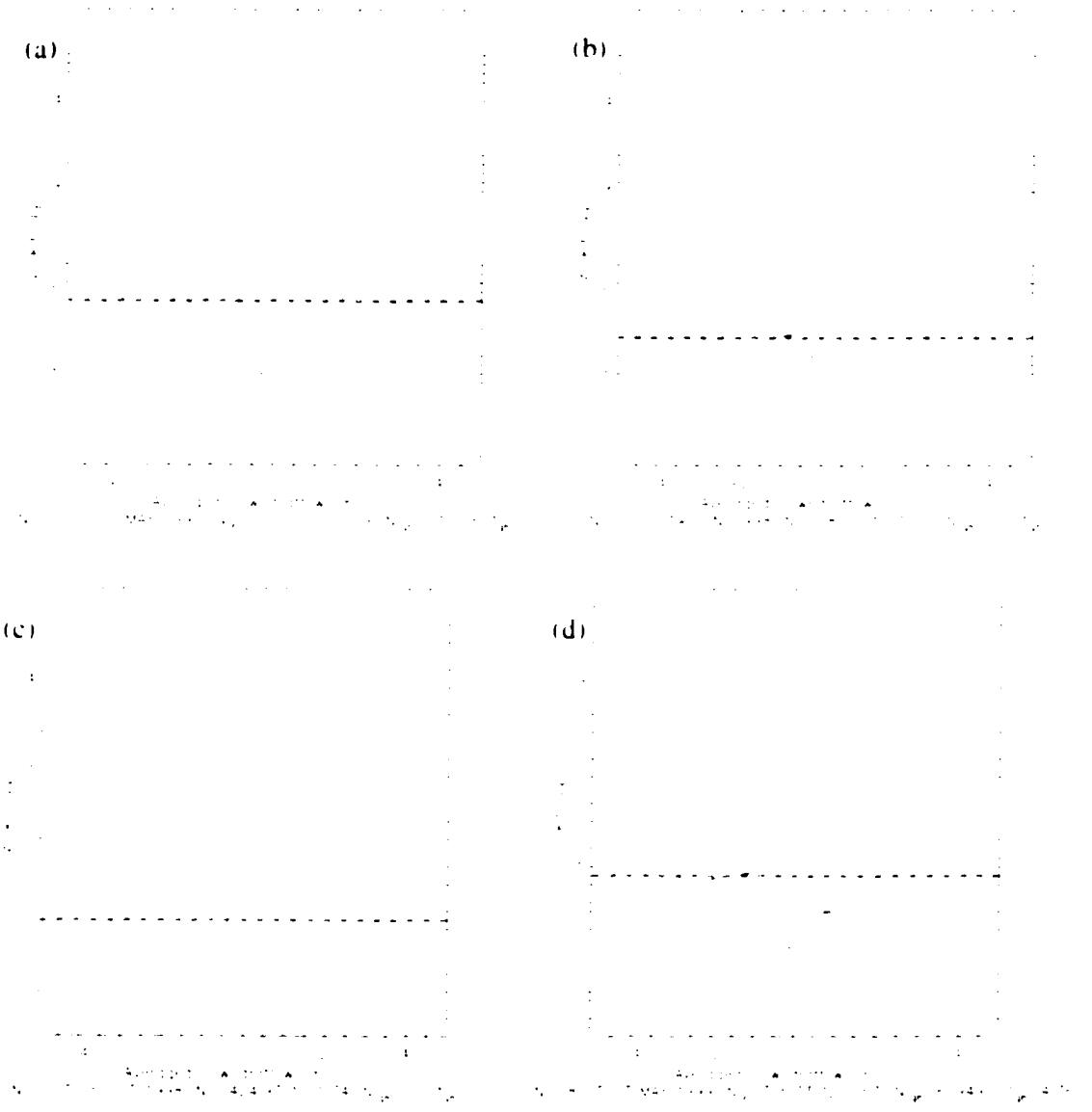

FIG. 3.10. As in Fig. 3.5a except for the tornadic (a) 25 May 1997 case, (b) 13 June 1998 case (low altitude), (c) 4 October 1998 case, and (d) 3 May 1999 case. The soundings used are (a) 00 UTC 25 May 1997 Norman, OK, (b) 00 UTC 14 June 1998 Norman, OK, (c) 00 UTC 5 October 1998 Norman, OK, and (d) 18 UTC 3 May 1999 Norman, OK.

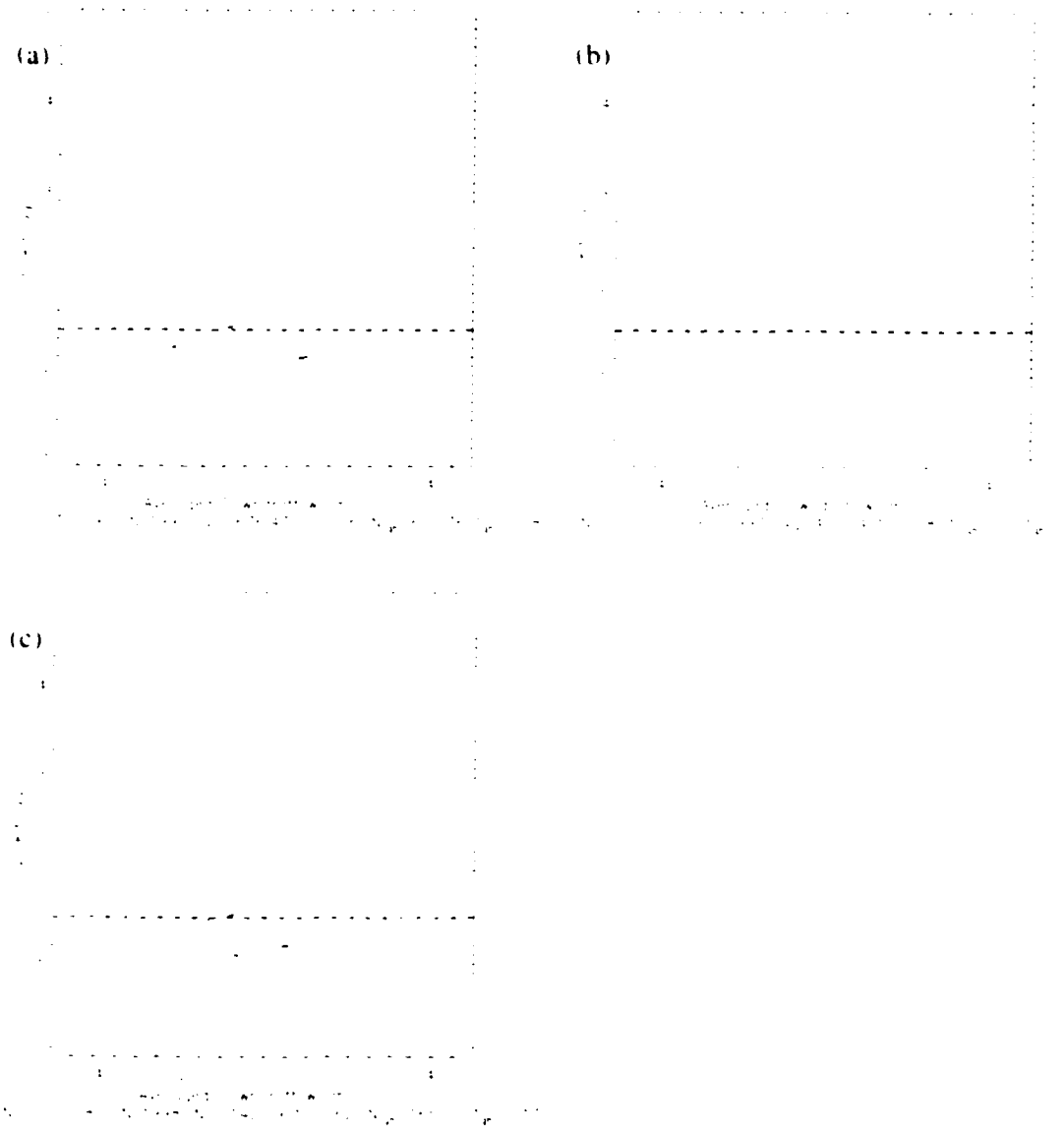

FIG. 3.11. As in Fig. 3.10 except for the nontornadic (a) 18 June 1992 case, (b) 19 September 1993 case, and (c) 8 June 1998 case. The soundings used are (a) 00 UTC 19 June 1992 Stephenville, TX, (b) 00 UTC 20 September 1993 Norman, OK, and (c) 00 UTC 8 June 1998 Norman, OK.

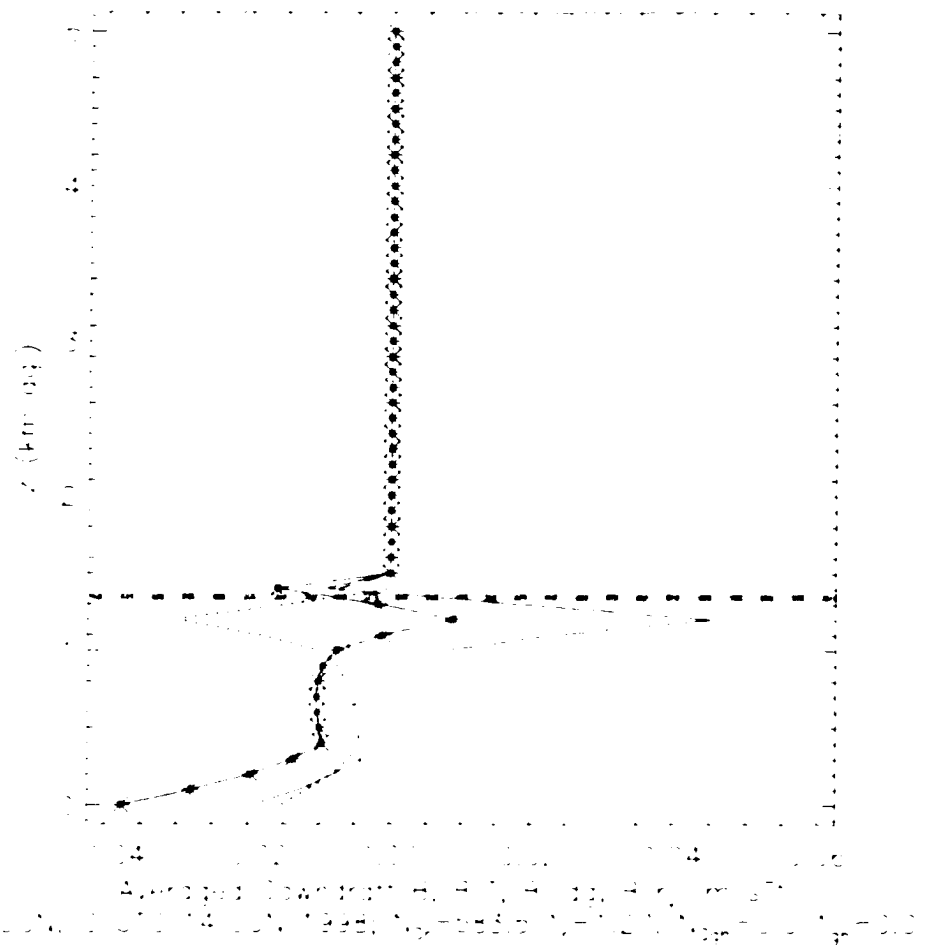

FIG. 3.12. Buoyancy (m s^{-2}) versus altitude (km AGL) for the 13 June 1998 (low altitude) simulation. The buoyancy variables plotted are the total buoyancy B (solid line with asterisks), the buoyancy owing to temperature differences relative to the environment B_T (solid line), the buoyancy owing to hydrometeor loading B_ldg (dashed line), and the buoyancy owing to water vapor mixing ratio differences relative to the environment B_r$_v$ (dotted line).

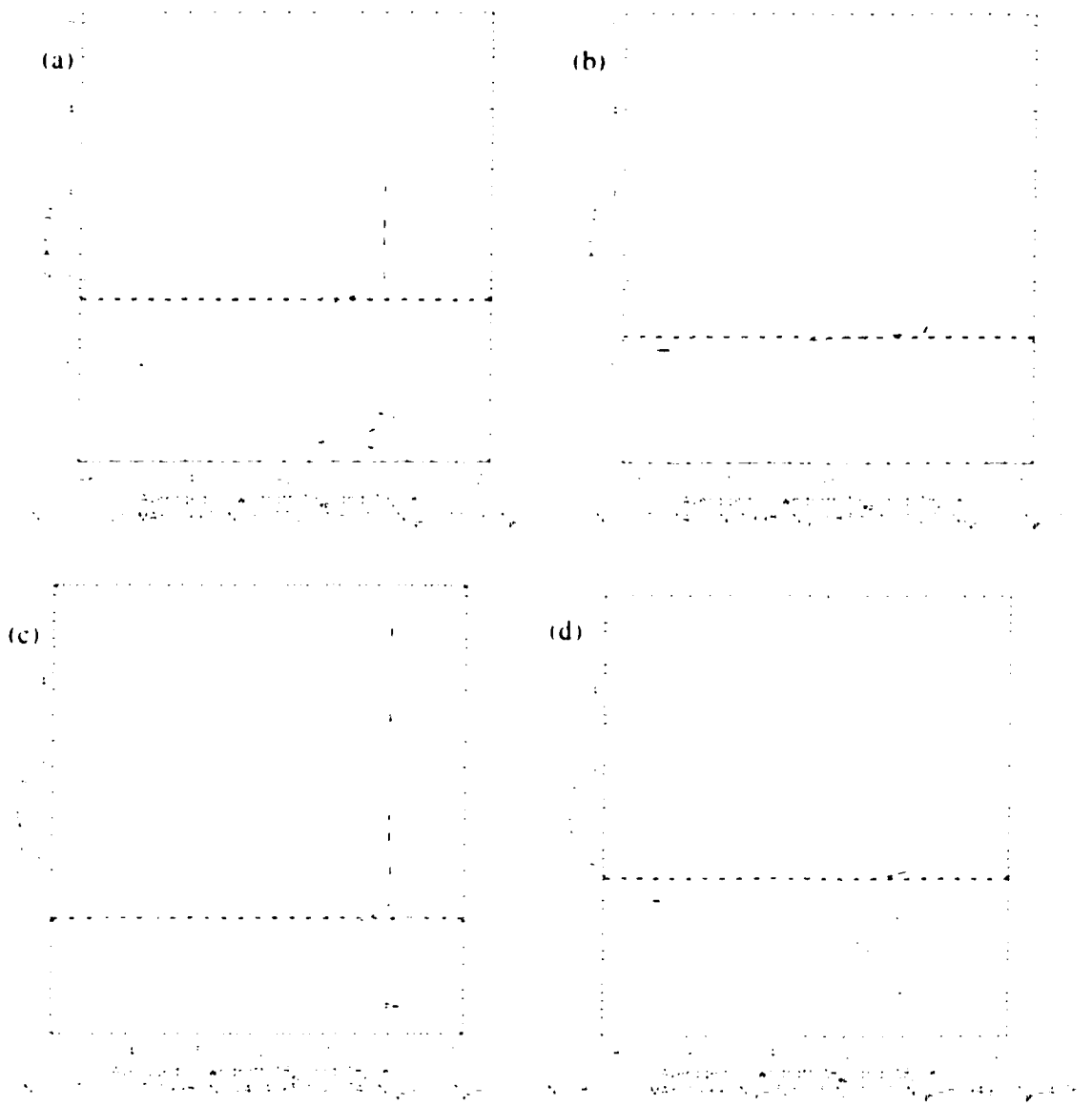

FIG. 3.13. As in Fig. 3.10 except for differences between downdraft and environmental θ_e (solid line) and θ_v (dashed line) values for the tornadic cases. Differences are computed as downdraft value minus environmental value.

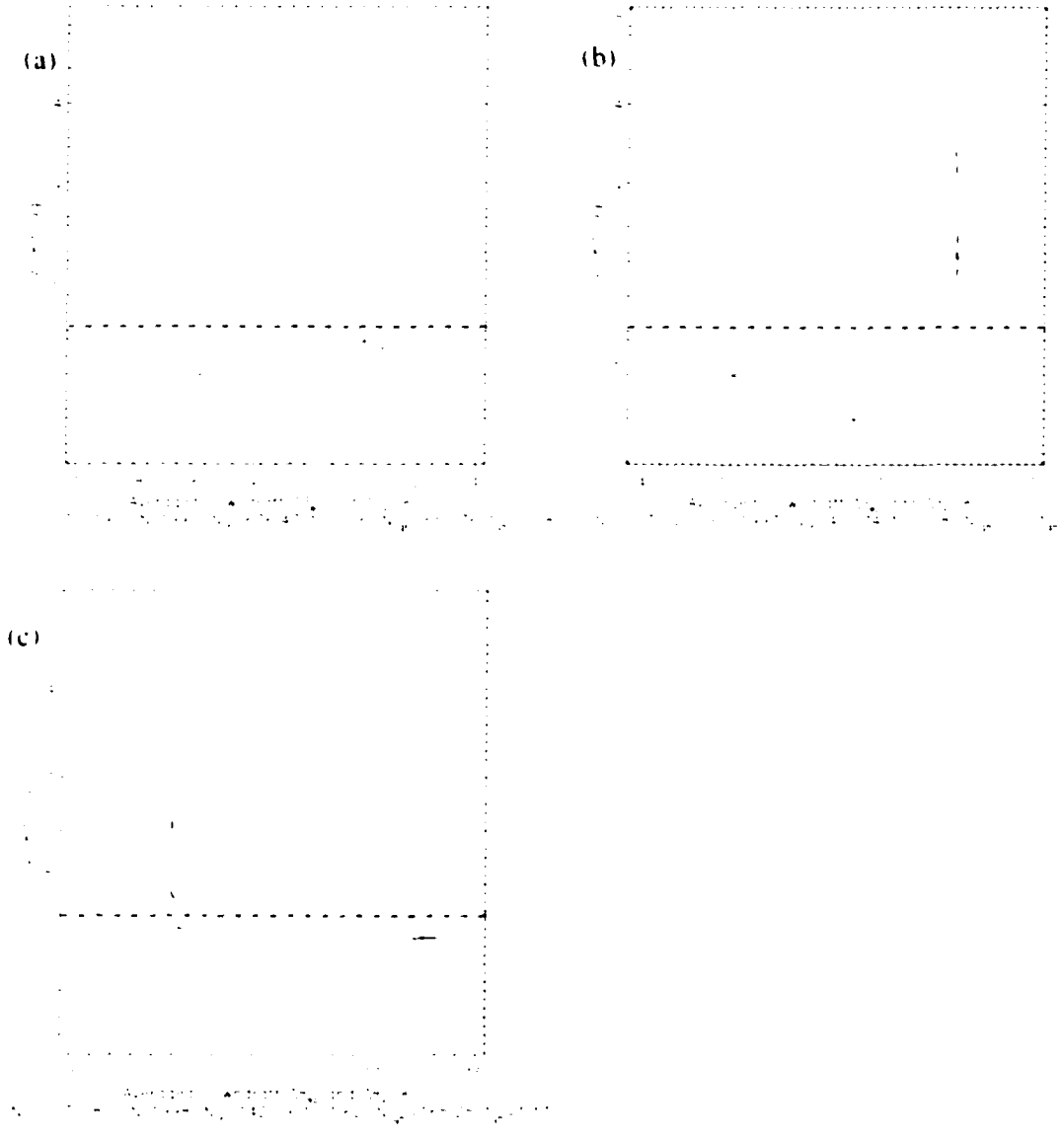

FIG. 3.14. As in Fig. 3.13 except for the nontornadic cases.

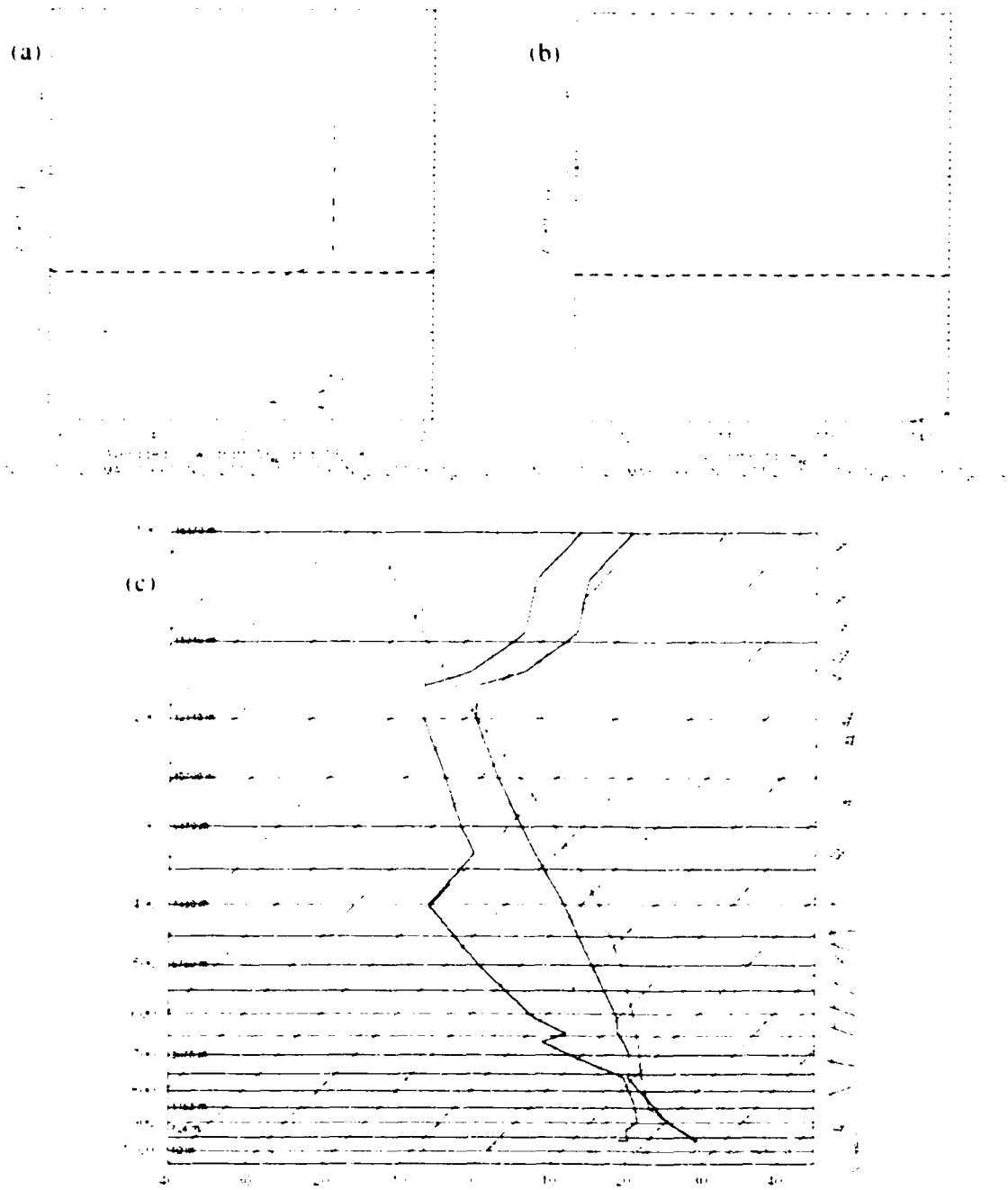

FIG. 3.15. (a) As in Fig. 3.13a. (b) Environmental θ_e profile for the 00 UTC 25 May 1997 Norman, OK sounding (c) used in the 25 May 1997 simulation.

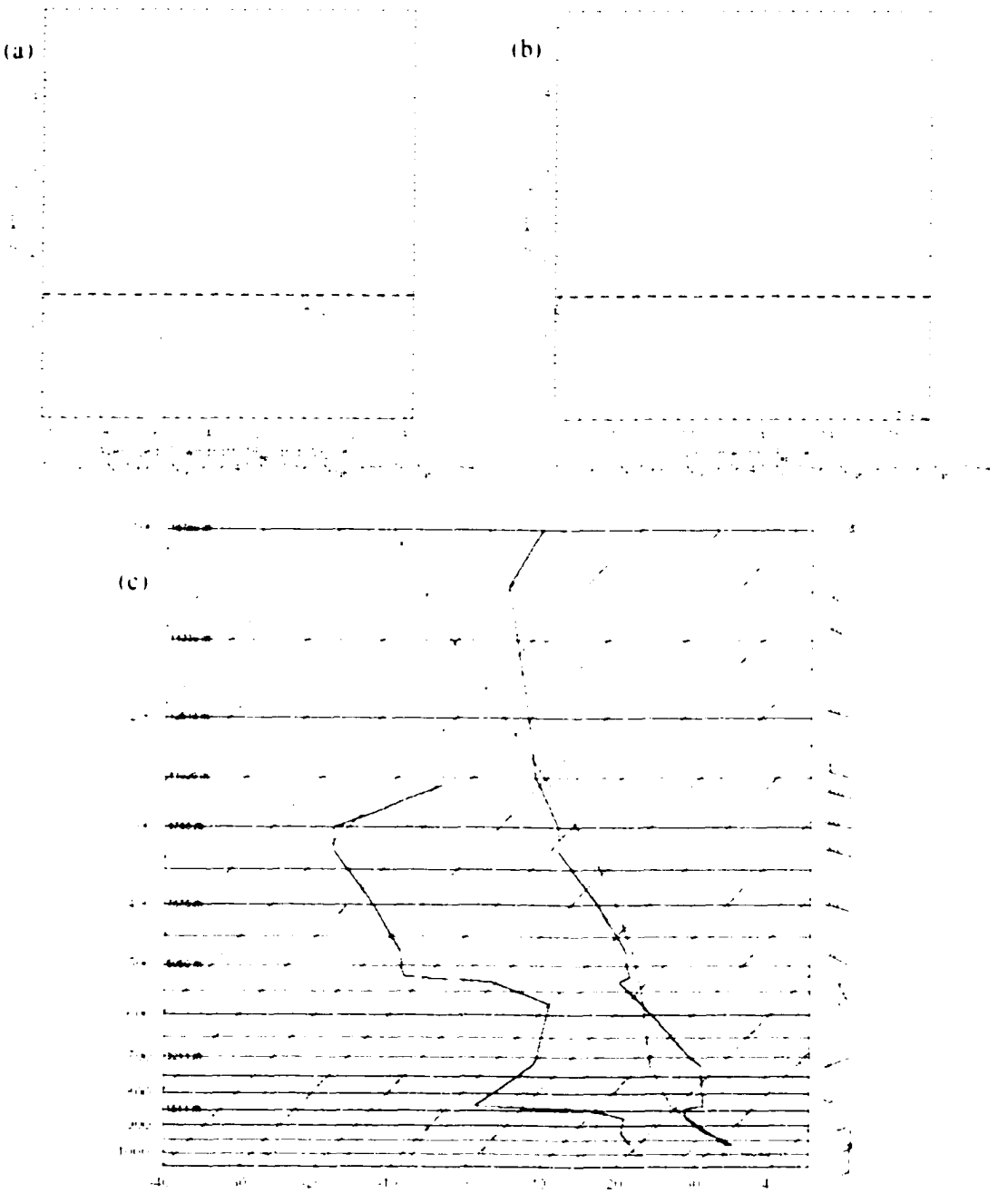

FIG. 3.16. (a) As in Fig. 3.14a. (b) Environmental θ_e profile for the 00 UTC 19 June 1992 Stephenville, TX sounding (c) used in the 18 June 1992 simulation.

3.3.3 Effects of Within-Hook Variability

In the selection of the radar data that were used to drive the 1.5-dimension downdraft model, care was taken to choose values that are characteristic of the respective hook echoes. Brief oscillations and spikes were ignored. Values were preferentially taken from regions having larger Z_h values since these regions should provide the strongest forcing of the RFDs. Values were taken from both the necks and tips of the hook echoes.

An important question is whether variability in the hydrometeor fields of hook echoes can significantly affect RFDs. Previous research concerning precipitation-driven downdrafts (e.g., Hookings 1965; Srivastava 1985, 1987; Proctor 1989) indicates that the properties of hydrometeor fields should be important to RFDs. To answer this question, however, tests using soundings for tornadic and nontornadic storms should be performed. A parameter space study of the effects of different hydrometeor size distributions, microphysical processes, etc., on RFDs is beyond the scope of this study but is planned for the future. At the present time, effects of hydrometeor variability within an observed hook echo are considered.

The hook echo that is considered is that from the tornadic 4 October 1998 case. Of those studied, this hook echo exhibited the greatest variability in terms of both Z_h and Z_{DR}. Three simulations, the parameters for which are shown in Table 3.2, were performed. The first simulation in Table 3.2, the 'control' simulation, corresponds to that performed for the 4 October 1998 case in the previous section. The other two are

for a region of relatively high Z_h and low Z_{DR} and a region of relatively low Z_h and high Z_{DR}.

Results for vertical velocity are shown in Fig. 3.17. The control simulation and the low Z_h-high Z_{DR} simulation produce nearly the same results. The high Z_h-low Z_{DR} simulation, however, produces a much stronger downdraft that reaches a maximum of -2.0 m s^{-1} as compared to -0.6 m s^{-1} in the control simulation. The rounded shape of downdraft profile from the high Z_h-low Z_{DR} simulation is similar to that observed in the high altitude simulation (Fig. 3.5). Consequently, it appears as if the melting of graupel and hail is important in the production of this stronger downdraft.

Results for θ_e and θ_v differences are shown in Fig. 3.18. As in the case of vertical velocity, the control simulation and the low Z_h-high Z_{DR} simulation produce nearly the same results. The high Z_h-low Z_{DR} simulation produces larger θ_e differences except at the ground, where the θ_e difference is approximately equal to that in the control simulation. Therefore, it is apparent that θ_e differences are also sensitive to the properties of the hydrometeor field.

This very limited set of simulations illustrates that RFDs are likely sensitive to the properties of the hydrometeor fields that drive them. As expected, increased hydrometeor loading and greater amounts of graupel/hail can be more effective at driving the RFD and at bringing lower-θ_e air downward towards the surface.

TABLE 3.2. As in Table 3.1 except for the hook-echo variability simulations for the 4 October 1998 case. The first row is for the 'control' simulation, the second is for the high Z_h-low Z_{DR} simulation, and the third is for the low Z_h-high Z_{DR} simulation.

z AGL (km)	Z_h (dBZ)	Z_{DR} (dB)	K_{DP} ($^\circ$ km^{-1})	F_r	F_{rh}	F_i	Z_{hr} (dBZ)	$Z_{DR,r}$ (dB)	Λ_r (mm^{-1})	N_{0r} (m^{-3} mm^{-1})	Z_{hi} (dBZ)	Λ_{ch} (mm^{-1})
1.25	40.0	2.25	0.5	0.0	0.0	0.0	40.0	2.25	1.74	424.93	--	--
1.34	47.0	0.8	0.09	0.51	0.95	0.6	43.0	2.38	1.67	620.14	44.79	1.12
1.29	31.0	1.2	0.4	0.0	0.0	0.0	31.0	1.2	2.74	1736.41	--	--

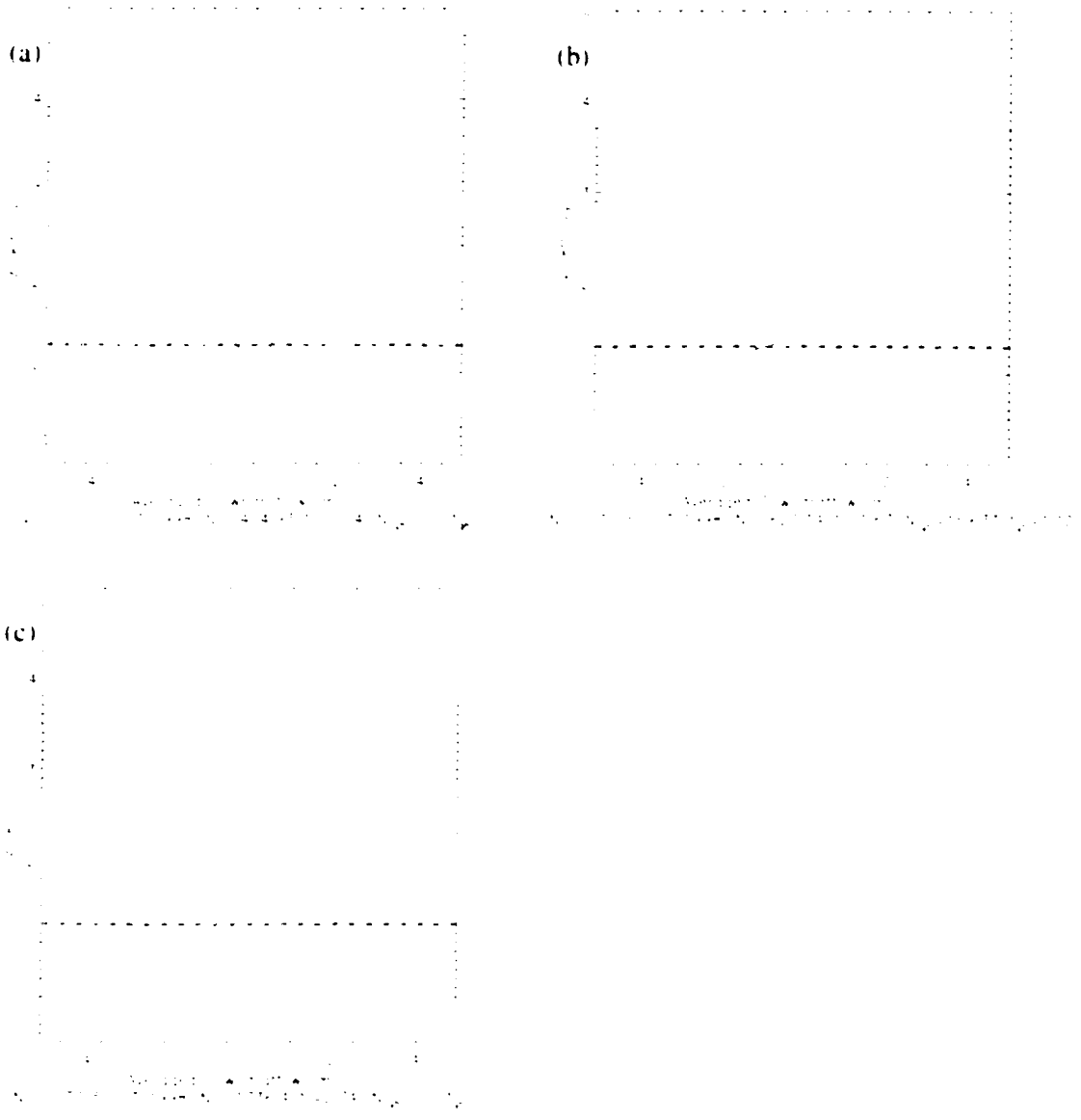

FIG. 3.17. As in Fig. 3.10 except for the 4 October 1998 hook echo variability simulations listed in Table 3.2. Results are for the (a) 'control' simulation presented in Fig. 3.10, (b) relatively high Z_h and low Z_{DR} region, and (c) relatively low Z_h and high Z_{DR} region.

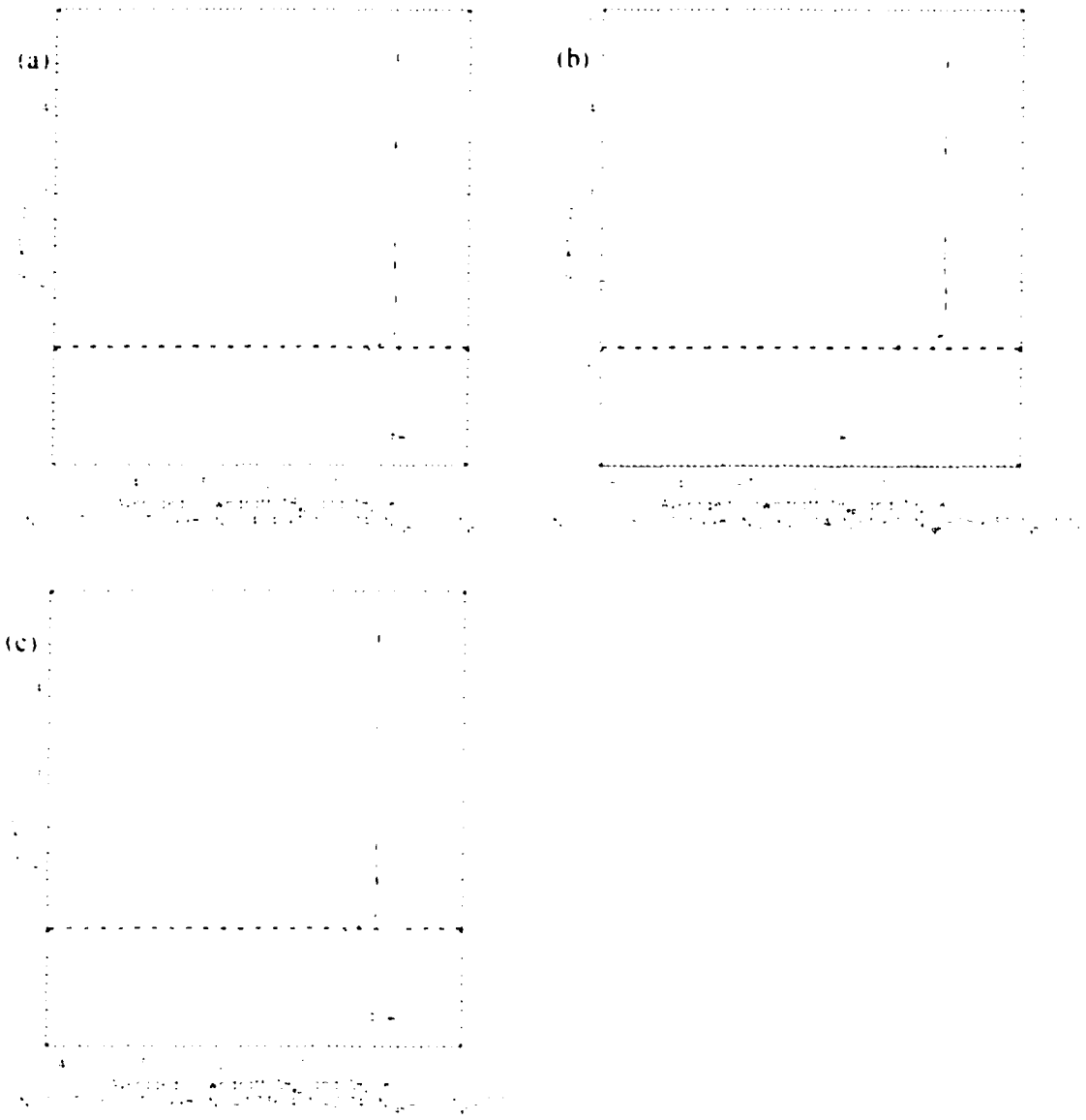

FIG. 3.18. As in Fig. 3.17 except for differences between downdraft and environmental θ_e (solid line) and θ_v (dashed line) values. Differences are computed as downdraft value minus environmental value.

3.3.4 VORTEX Cases

A subset of the VORTEX cases analyzed by MSR02 is studied here. Three tornadic and three nontornadic cases were randomly chosen for study. To initialize these simulations, soundings from MSR02 and radar observed Z_h values are used. Because polarimetric radar data are not available for these cases, a spectrum of possible hydrometeor types is considered by performing three simulations for each case: mixture of rain and graupel/hail (mix), all rain (rain), and all graupel/hail (ice). It is hoped that the variety of downdrafts produced might encompass the actual downdraft. The parameters for the eighteen simulations are provided in Tables 3.3 and 3.4.

It is noted that because this model works only if the graupel and hail are melting, in two of the nontornadic cases (Sidney, NE and Carlsbad, NM) precipitation had to be inserted below its observation altitude. In the Sidney, NE case the impact is expected to be minimal since the insertion altitude is only 0.1 km below the observation altitude. In the Carlsbad, NM case, however, the difference between insertion and observation altitude is large (2.7 km). Unfortunately, for this case the lowest-altitude radar data intercepts the hook echo at a relatively high altitude (4.8 km). The discrepancy between insertion and observation altitude may have important consequences in this case, especially if the insertion-altitude Z_h was significantly different from the observation-altitude Z_h. If not, then the difference between the insertion and observation altitudes may be unimportant since significant downdraft may have commenced only once melting ensued (the forcing of the downdraft by loading and sublimation of graupel and hail would likely have been relatively weak).

Vertical velocities for the nontornadic mix simulations are shown in Fig. 3.19. The mix, rain, and ice simulations are similar for each of the nontornadic cases. Consequently, only the mix results are shown. A comparison to Figs. 3.10 and 3.11 shows that the structure of these downdrafts is similar to that simulated in the polarimetric cases.

Vertical velocities for tornadic simulations are shown in Fig. 3.20. Some significant differences between the mix, rain, and ice simulations arose in the tornadic cases. In Fig. 3.20, the simulation that produced the strongest downdraft for each case is presented. As with the polarimetric cases, no consistent differences in the downdraft structures of the tornadic and nontornadic are apparent.

Differences between downdraft and environmental θ_e and θ_v values for nontornadic and tornadic cases are depicted in Figs. 3.21 and 3.22, respectively. For the nontornadic cases, the θ_e differences at the surface are relatively large, although the large differences for the Carlsbad case are restricted to a very narrow surface layer. In addition, the surface θ_e differences for two of the three nontornadic cases, Jetmore and Nazareth, are also large. These results are consistent with the findings of MSR02, who found that θ_e differences were relatively large for both nontornadic cases and weakly tornadic (defined as) cases.[37] The strongly tornadic case, Allison, has a small θ_e difference at the surface. This, too, is consistent with the findings of MSR02, who found that surface θ_e deficits were generally small for strongly tornadic supercells.

[37] MSR02 defined weakly tornadic events as those that produced F0-F1 tornadoes that persisted for 5 minutes or less. They defined strongly tornadic events as those that produced F2 or greater intensity tornadoes that lasted at least 5 minutes.

For the Allison case, however, MSR02 did observe large θ_e deficits (up to 18 K) in the surface RFD. Reasons for the difference between the simulation performed here and the observations can be surmised by considering the environmental θ_e profile (Fig. 3.23) and the (strongest) simulated downdraft for this case (Fig. 3.20b). In the simulation, precipitation was inserted at an altitude that would enable the transport of low θ_e air to the surface. However, because the simulated downdraft subsided at about 1.3 km AGL and then resumed in the boundary layer, it was not able perform this transport. Since θ_e is nearly constant in the lowest 1.3 km of this sounding, the simulated downdraft produced a surface θ_e difference close to zero. The observation of large θ_e deficits in the surface RFD of the Allison storm indicates that air from the elevated, low-θ_e reservoir was drawn to the surface. This could have been accomplished if, perhaps, larger hailstones or dynamically-induced pressure perturbations contributed to a stronger downdraft above the boundary layer. The role larger hailstones play in transporting mid-level, low-θ_e air to the surface will be investigated in future work.

A comparison between the surface θ_e differences observed by MSR02 and those modeled herein is provided in Table 3.5. The model results are generally close to the range of observed values. Exceptions are the Allison case, which has already been discussed, and the Sidney case, in which the mix simulation produced a θ_e difference 5.4 K higher than the maximum θ_e difference that was observed. Considering the simplicity of the downdraft model, uncertainties in determining environmental conditions, and the difficulties involved in obtaining complete measurements of the surface RFD, the agreement between observations and model results is encouraging.

Sensitivities that arose in the Jetmore and Nazareth simulations are illustrated in Figs. 3.24 and 3.25. For the Jetmore case, the rain simulation (Fig. 3.24a,b) produced a downdraft that is three times stronger and a surface θ_e deficit that is ~14 K greater than in the ice simulation (Fig. 3.24c,d). This illustrates that the strength and thermodynamic properties of precipitation-driven downdrafts can be quite sensitive to the characteristics of the precipitation that drives them. One might also conclude that the evaporation of rain is more efficient at driving low-level downdrafts than the melting of graupel and hail. This does not necessarily follow from these results, however, because the mixing ratios of the rain and hail fields are not the same at the insertion level. Because the rain and graupel/hail fields are estimated using observations of Z_h, this is the quantity that the precipitation fields in the two simulations have in common at the insertion level. The rain and graupel/hail fields produce the same Z_h value but do not have the same mixing ratio. In fact, at the insertion level the mixing ratio of graupel/hail in the ice simulation is about half the mixing ratio of rain in the rain simulation.

The sensitivity illustrated in Fig. 3.25 is particularly interesting. The Nazareth rain and mix simulations produce downdrafts that have similar maximum intensities. Their structures, however, are significantly different at low altitudes. In the mix simulation the downdraft weakens considerably at ~0.4 km AGL and then accelerates towards the surface. In the rain simulation the downdraft weakens more gradually from 0.6 km AGL to the surface without the acceleration at very low altitudes. These differences in low-level downdraft structure have a large impact on low-level θ_e difference profiles, as is apparent in Fig. 3.25. For instance, the surface θ_e difference in

the mix simulation is -2.7 K whereas the surface θ_e difference in the rain simulation is -12.6 K.

Dynamic entrainment may be an important factor in the creation of the dissimilar low-level θ_e difference profiles in Fig. 3.25. In the mix simulation the deceleration at ~0.4 km AGL slows the descent of the low-θ_e air from above. Owing to continuity, the subsequent downdraft acceleration then results in entrainment of environmental air that dilutes the low-θ_e air in the downdraft. This dilution contributes to much smaller low-level θ_e deficits.

TABLE 3.3. As in Table 3.1 except for three nontornadic VORTEX cases. Parameters for three simulations, mixture of rain and graupel/hail, rain only, and graupel/hail only, are provided for each case. For cases in which the precipitation insertion altitude differs from the observation altitude, the observation and insertion altitudes are given in the form observation altitude/insertion altitude.

CASE	z AGL (km)	Z_h (dBZ)	Z_{DR} (dB)	K_{DP} ($^\circ$ km^{-1})	F_r	F_{gh}	F_i	Z_{hr} (dBZ)	Z_{DRr} (dB)	Λ_r (mm^{-1})	N_{0r} (m^{-3} mm^{-1})	Z_{hi} (dBZ)	Λ_{gh} (mm^{-1})
8 June 1995 Elmwood, OK	2.3	45.0	1.0	0.3	0.39	0.61	0.43	42.55	1.95	1.93	1695.47	41.35	1.54
	2.3	45.0	2.0	0.6	0.0	0.0	0.0	45.0	2.0	1.89	2579.28	--	--
	2.3	45.0	0.0	0.0	1.0	1.0	1.0	--	--	--	--	45.0	1.1
19 May 1998 Sidney, NE	2.8/2.7	30.0	0.6	0.01	0.37	0.5	0.4	27.8	1.05	3.01	1760.39	26.0	5.25
	2.8/2.7	30.0	1.1	0.1	0.0	0.0	0.0	30.0	1.1	2.91	2232.8	--	--
	2.8/2.7	30.0	0.0	0.0	1.0	1.0	1.0	--	--	--	--	30.0	3.82
26 May 1999 Carlsbad, NM	4.8/2.1	37.5	0.7	0.1	0.43	0.53	0.45	34.93	1.36	2.5	2146.71	34.0	2.78
	4.8/2.1	37.5	1.5	0.2	0.0	0.0	0.0	37.5	1.5	2.33	2255.06	--	--
	4.8/2.1	37.5	0.0	0.0	1.0	1.0	1.0	--	--	--	--	37.5	2.1

TABLE 3.4. As in Table 3.3 except for three tornadic VORTEX cases. As in Table 3.1, the Fujita rating and duration (in minutes) of each tornado are indicated in parentheses in the form Fujita rating/duration.

CASE	z AGL (km)	Z_h (dBZ)	Z_{DR} (dB)	K_{DP} (° km^{-1})	F_L	F_A	F_I	Z_{hr} (dBZ)	Z_{DRr} (dB)	Λ_r (mm^{-1})	N_{0r} (m^{-3} mm^{-1})	Z_{hi} (dBZ)	Λ_{gh} (mm^{-1})
16 May 1995 Jetmore, KS (F0/5)	1.8	45.0	1.0	0.3	0.39	0.61	0.43	42.55	1.95	1.93	1695.47	41.35	1.54
	1.8	45.0	2.0	0.6	0.0	0.0	0.0	45.0	2.0	1.89	2579.28	--	--
	1.8	45.0	0.0	0.0	1.0	1.0	1.0	--	--	--	--	45.0	1.1
8 June 1995 Allison, TX (F4/46)	2.4	50.0	1.2	0.8	0.39	0.52	0.46	47.36	2.54	1.59	1171.1	46.58	0.9
	2.4	50.0	2.4	1.5	0.0	0.0	0.0	50.0	2.4	1.66	2972.7	--	--
	2.4	50.0	0.0	0.0	1.0	1.0	1.0	--	--	--	--	50.0	-0.06
2 June 1999 Nazareth, TX (F0/1)	1.5	50.0	1.2	0.8	0.39	0.52	0.46	47.36	2.54	1.59	1171.1	46.58	0.9
	1.5	50.0	2.4	1.5	0.0	0.0	0.0	50.0	2.4	1.66	2972.7	--	--
	1.5	50.0	0.0	0.0	1.0	1.0	1.0	--	--	--	--	50.0	-0.06

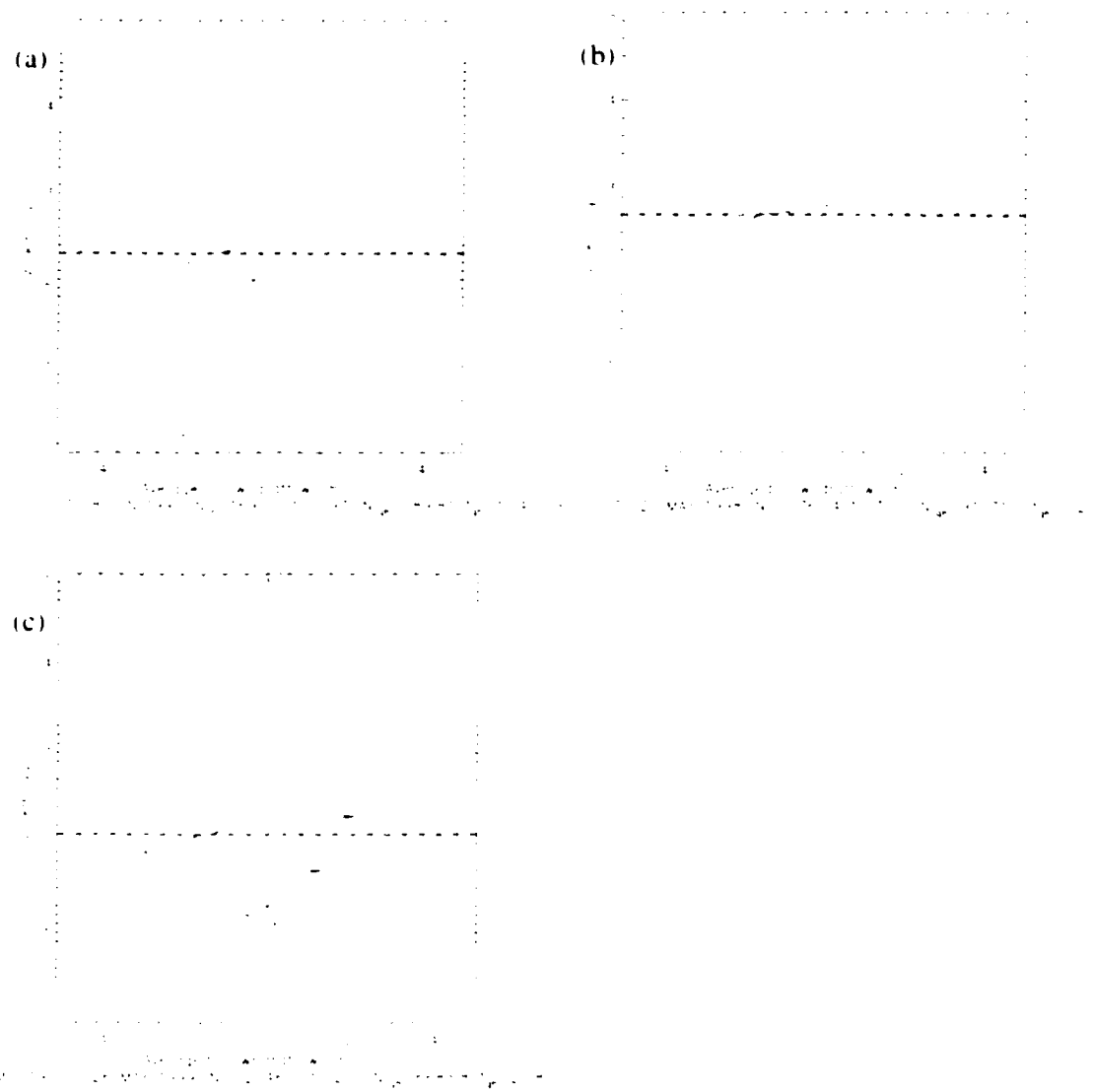

FIG. 3.19. Vertical velocity (m s^{-1}) versus altitude (km AGL) for the mix simulations for the (a) 8 June 1995 Elmwood, OK, (b) 19 May 1998 Sidney, NE, and (c) 26 May 1999 Carlsbad, NM, nontornadic VORTEX cases. In order to decrease the impact of buoyancy oscillations, model results are averaged over a five minute interval from t = 1950 to t = 2250 seconds (centered on t = 35 minutes). Thick, dashed, grey lines indicate the precipitation insertion altitude.

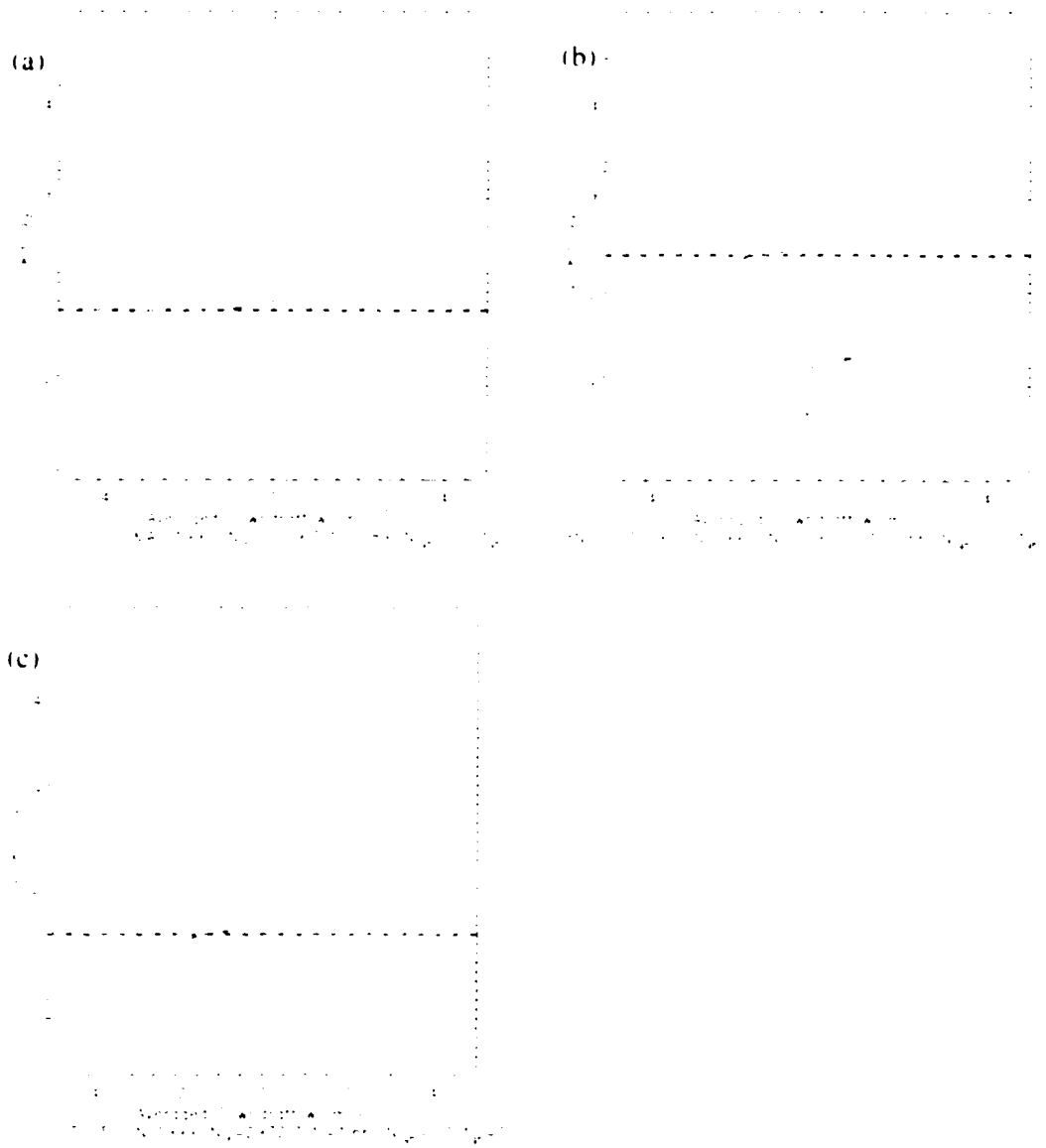

FIG. 3.20. As in Fig. 3.19 except for the (a) 16 May 1995 Jetmore, KS, rain simulation, (b) 8 June 1995 Allison, TX, rain simulation, and (c) 2 June 1999 Nazareth, TX, rain simulation.

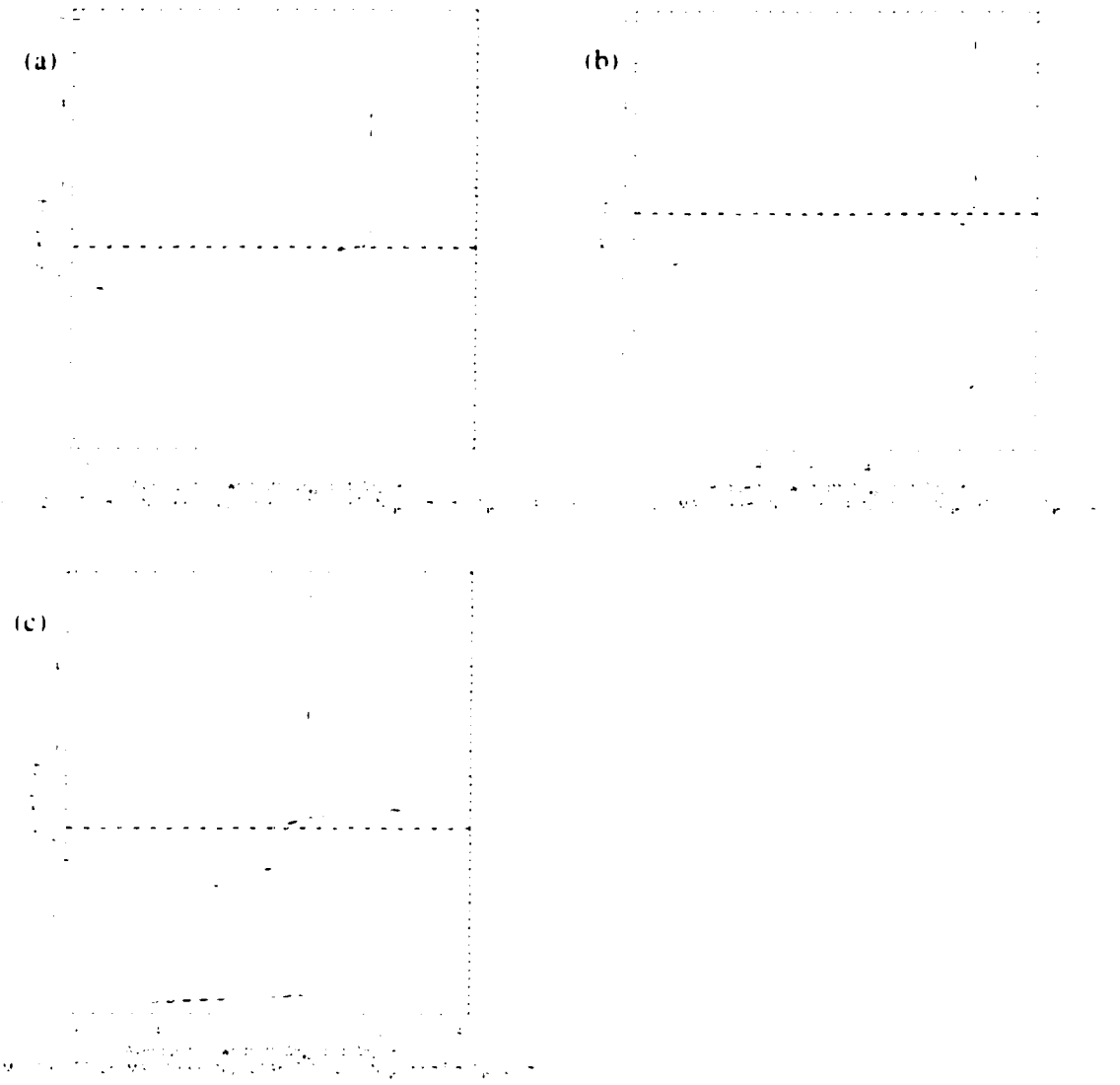

FIG. 3.21. As in Fig. 3.19 (mix simulation results for nontornadic VORTEX cases) except for differences between downdraft and environmental θ_e (solid line) and θ_v (dashed line) values. Differences are computed as downdraft value minus environmental value.

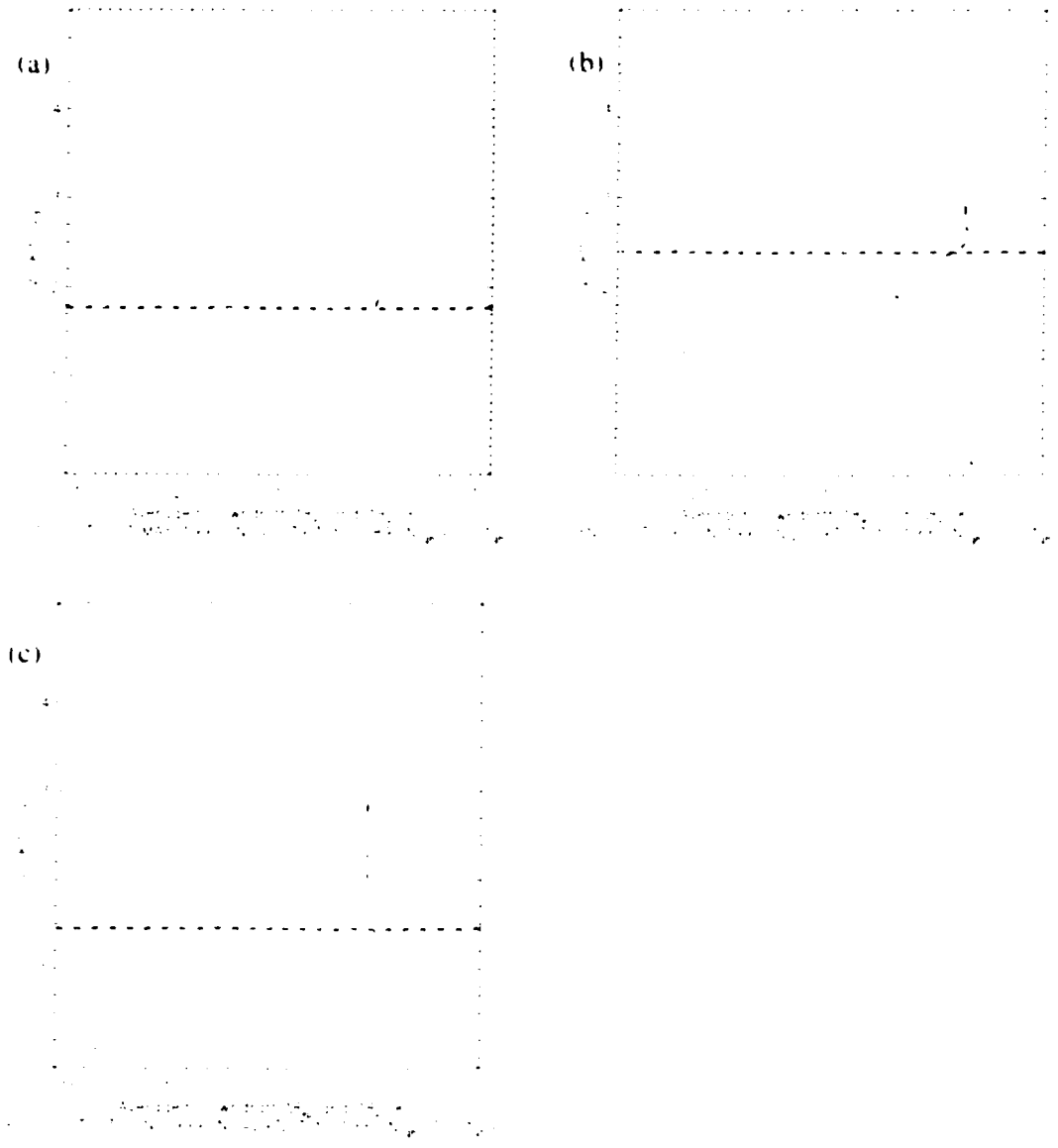

FIG. 3.22. As in Fig. 3.21 except for the (a) 16 May 1995 Jetmore, KS, rain simulation, (b) 8 June 1995 Allison, TX, rain simulation, and (c) 2 June 1999 Nazareth, TX, rain simulation.

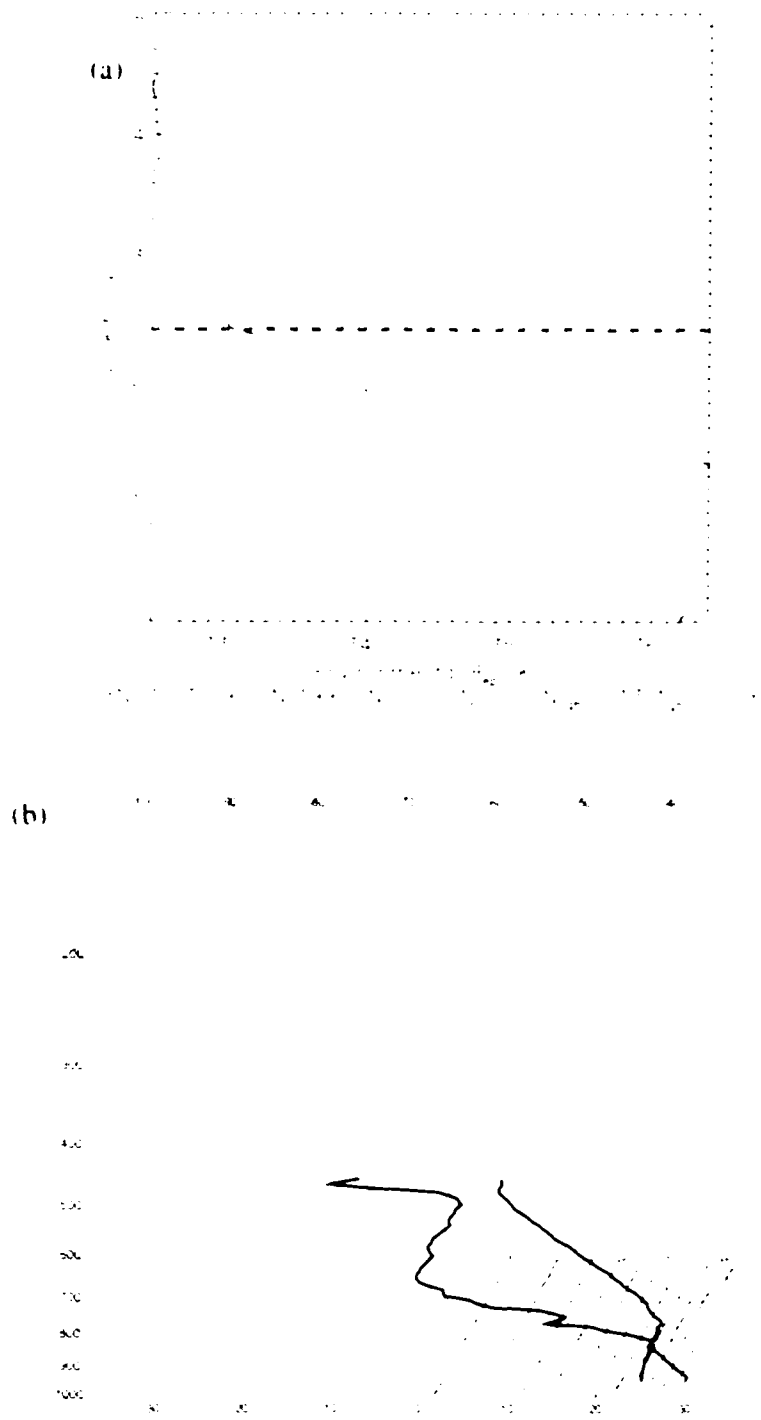

FIG. 3.23. (a) Environmental θ_e profile for the 8 June 1995 Allison, TX, case (b) and the associated sounding. Sounding courtesy of P. Markowski.

TABLE 3.5. Comparison between the θ_e differences observed by Markowski et al. (2002) and those modeled herein (for model results shown in Figs. 3.19-3.22). The θ_e differences are computed as downdraft value minus environmental value. The dashed line separates the tornadic VORTEX cases from the nontornadic VORTEX cases. Fujita rating and duration (minutes) of each tornado are indicated in parentheses in the form Fujita rating/duration.

Case	Observed Surface θ_e Differences (K)	Modeled Surface θ_e Differences (K)
Elmwood, OK	-12.1 to -8.0	-8.0
Sidney, NE	-13.5 to -9.5	-4.1
Carlsbad, NM	-4.0 to +5.0	-5.6
Jetmore, KS (F0/5)	-16.1 to -10.1	-16.7
Allison, TX (F4/46)	-19.2 to -2.2	0.0
Nazareth, TX (F0/1)	-12.2 to -8.2	-12.6

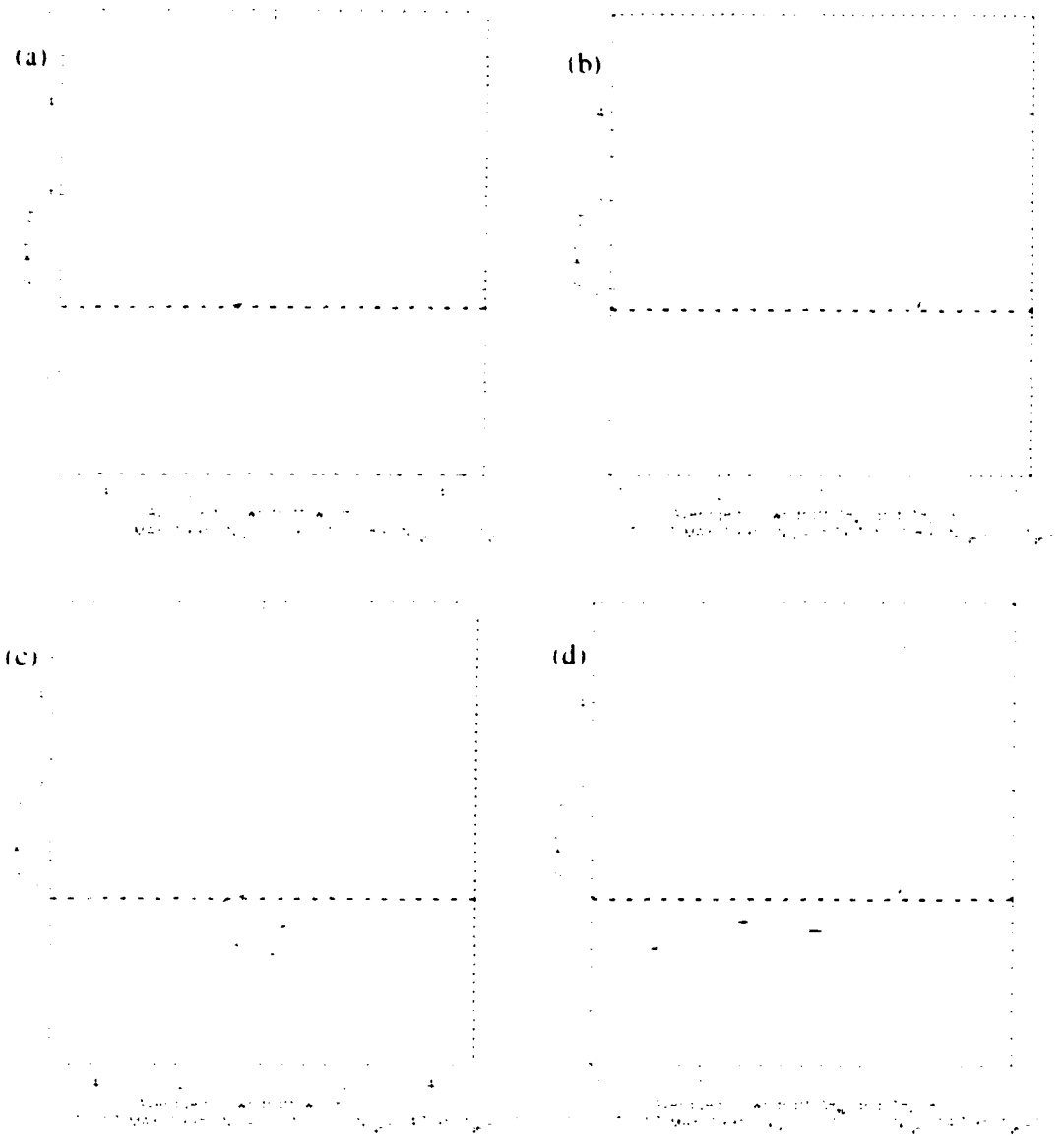

FIG. 3.24. Vertical velocity [(a) and (c)] and θ_e and θ_i difference values [(b) and (d)] as in Figs. 3.19 and 3.21. Results from the Jetmore rain simulation are in (a) and (b) while those from the Jetmore ice simulation are in (c) and (d).

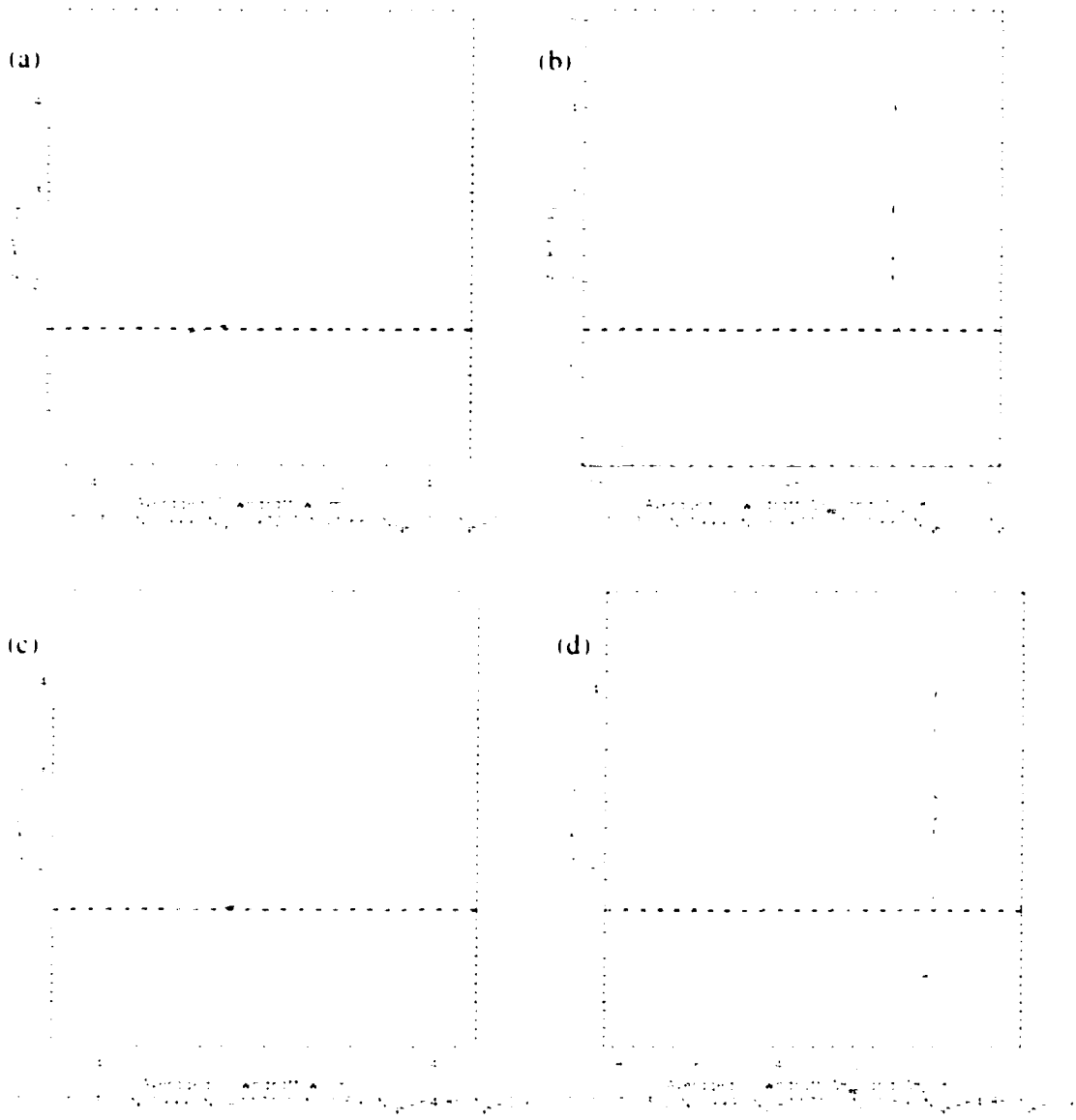

FIG. 3.25. As in Fig. 3.24 except for the Nazareth rain simulation [(a) and (b)] and the Nazareth mix simulation [(c) and (d)].

3.4 Discussion

In their comprehensive review of downdrafts, Knupp and Cotton (1985) list precipitation-driven downdraft velocities as ranging from 1 to 15 m s^{-1}. The downdrafts simulated herein are skewed towards smaller values but are consistent with this range. While this is reassuring, the validity of these simulations cannot be assured without a comprehensive set of *in situ* measurements, which is not available. Surface observations are available for the VORTEX cases, however, and the simulation results generally agree with those observations.

Above the boundary layer, supercell environments are often relatively resistant to precipitation-driven downdrafts. This resistance results from downdraft descent and the environmental temperature profile (e.g., Figs. 3.6, 3.7a, 3.8, 3.9, and 3.23b) being between dry and moist adiabatic (Das and Subba Rao 1972; Srivastava 1987). This is consistent with the finding of previous studies [e.g., Kamburova and Ludlam (1966), Girard and List (1975), Harris (1977), Srivastava (1987), and Proctor (1989)] that downdraft intensity depends strongly on environmental stability. As the stability of the environment increases, the downdraft temperature rises relative to the environment and the downdraft weakens.

Highly stable layers are often present in supercell environments just above the boundary layer (Figs. 3.8a and 3.23b). These layers deter mid-level downdrafts from penetrating into the boundary layer and, thus, deter midlevel, low-θ_e air from reaching the surface.

In supercell environments, downdrafts tended to develop and accelerate readily within the boundary layer (Figs. 3.5, 3.10-11, 3.19-20). The dry-adiabatic lapse rate that is typically present in these boundary layers provides minimal resistance to the downdrafts.

The relative stability above the boundary layer and instability within the boundary layer to precipitation-driven downdrafts may explain why MSR02 found that surface RFD parcels originated from within ~1 km of the surface in many of the VORTEX cases. This study shows that in the absence of other processes (e.g., effects of larger hail or pressure perturbation forces) hook-echo hydrometeor fields will often be unable to force midlevel air to the surface. Of course, a major limitation (to be addressed in future work) is the lack of larger hail in the downdraft model.

The lack of differences between tornadic and nontornadic downdraft vertical velocity profiles is consistent with the observation that, with the exception of the tornado itself, tornadic and nontornadic supercells often have similar low-level wind fields (e.g., Trapp 1999, MSR02). If the tilting of horizontal vorticity by the RFD is important to tornadogenesis, then a distinguishing wind field characteristic may be the intensity of an RFD. The results of this study, however, are insufficient to support or refute this hypothesis.

MSR02 tentatively concluded that "Evaporative cooling and entrainment of midlevel potentially cold air play smaller roles in the formation of RFDs associated with tornadic supercells compared to nontornadic supercells." The findings of this study support their conclusion and suggest that RFDs that reach the ground are often generated or at the very least significantly intensified within the boundary layer. If

generated within the boundary layer, then the surface θ_e deficit is limited by the minimum θ_e value within the boundary layer. If midlevel air is able to penetrate to the surface, then intensification of the RFD within the boundary layer should result in significant dilution of this air through dynamic entrainment.[38] If either generation or intensification occurs in the boundary layer, then the boundary layer θ_e profile will be critical to the surface θ_e deficit. It appears, therefore, that the boundary layer θ_e profile may be important to tornadogenesis.

These results indicate that the environment plays a large role in determining the low-level thermodynamic characteristics of precipitation-driven RFDs. This does not mean, however, that precipitation characteristics are unimportant. On the contrary, the sensitivity tests of §3.3.3 and the VORTEX simulations (§3.3.4) indicate that properties of precipitation-driven downdrafts can be quite sensitive to the characteristics of the precipitation fields that drive them. This suggests that knowledge of hook echo hydrometeor fields could be very useful in anticipating the tornadic potential of a supercell storm.

It is interesting that in the VORTEX simulations significant sensitivity was observed in the weakly tornadic cases but not in the nontornadic cases or in the strongly tornadic case. It is possible that the environments of nontornadic and strongly tornadic storms are such that the RFD has similar thermodynamic characteristics at the surface for a variety of hook-echo hydrometeor fields. The tornadic fate of these storms may be ordained by their environment. In the same vein, the environments of weakly tornadic storms may be such that the surface thermodynamic characteristics of the RFD depend

[38] This assumes that the downdraft maintains roughly the same cross-sectional area. If so, then continuity

strongly upon the properties of the hook-echo hydrometeors. If the right conditions are met, tornadogenesis can ensue.

The results of this study are generally consistent with the observations of MSR02. This is encouraging since it suggests that a simple model like the one used herein might be useful in forecasting (or nowcasting) surface RFD characteristics and, potentially, tornado likelihood. The efficacy of such an approach could be significantly limited, however, by uncertainties concerning important parameters like maximum hailstone size and the environment in which a storm resides.

Limitations of this work include the following:

1) the absence of larger (> 9 mm diameter) hailstones in the simulations,
2) difficulties in determining actual downdraft environments,
3) uncertainties in the estimation of precipitation characteristics,
4) the simple 1.5 dimensional framework of the downdraft model,
5) the absence of perturbation pressure effects, and
6) the limited number of cases studied.

Because of these limitations, the results of this study must be considered with caution. The above limitations need to be examined to evaluate their importance. Plans are already underway to examine one and three.

Issue two is a well known problem for which there is no simple solution. First, there is the issue of mesoscale variability (see, for example, MSR02 and references cited therein). Because mesoscale variability may be significant, it is difficult to know whether any of the soundings used are representative. Moreover, for some cases

---

requires downdraft accelerations to be accompanied by the intake of environmental air.

soundings from either the previous day or an adjacent site were used because of convective contamination of the soundings closest to the storms. This exacerbates this problem for these cases. Alternatively, forecast soundings could have been used. These, however, have their own set of uncertainties (accuracy of predicted cap strength, lapse rates above the boundary layer, etc.). Neither choice is optimal. Herein, alternative observed soundings were used because at least with this approach the modeled downdrafts occur in an actual sounding.

In addition to mesoscale variability, the issue of convective contamination is critically important. When given the choice of a proximity sounding that exhibits little (or no) convective contamination or a convectively altered sounding, which should be used as the environmental sounding for an RFD? It can be argued that either may be more representative of the RFD environment. For instance, if the rear of the storm is strongly ventilated by the environmental flow, then the proximity sounding may be more appropriate. On the other hand, if this is not the case, then the alterations of the proximity sounding by the storm may be important in defining the true environment of the RFD. This is a difficult issue for which there is no easy answer. Herein, non-contaminated environments were used. In future work, idealized soundings that represent multiple possibilities will be used. With this approach, the issue of convective contamination will be explored and the issue of mesoscale variability will be alleviated.

Regarding issue four, this simple downdraft model was used in order to scale down the problem so that it was more manageable. While the second and third dimensions are undoubtedly fundamentally important to supercell processes, it is

believed that many of the important features of RFDs can be elucidated by focusing on processes occurring in the vertical direction.

Concerning five, this study shows that hook-echo hydrometeors can drive RFDs without pressure perturbations. It has been shown [e.g., Klemp and Rotunno (1983)] that the perturbation pressure field can have important impacts on the RFD. *In fact, the impacts of the perturbation pressure field can be at least on the same order of the impacts of hydrometeors* [e.g., Klemp and Rotunno (1983); Houze (1993, §7.1)]. The lack of perturbation pressure fields, therefore, is a significant limitation of this work. A complete understanding of the RFD will require comprehension of the roles of hydrometeors, the pressure field, and their interactions.

Limitation six is the standard limitation innate to all studies like this one. Indisputably, more cases are needed to verify or refute the findings of this study. Towards this goal, an analysis of the complete set of VORTEX cases is planned.

These uncertainties mean that none of the modeled RFDs can be viewed as replicating the true RFDs that occurred in any of the cases. However, by using this set of radar and environmental data attention has been focused on a subset of the large parameter space that applies to this problem. It is hoped that in doing so this effort has identified physical processes that are important to both the RFD and tornadogenesis.

Chapter 4: Conclusion

Polarimetric radar data have been utilized to investigate properties of precipitation-driven rear flank downdrafts. Because this required the quantitative utilization of radar data, aspects of this have been studied.

It has been shown that the commonly-used assumption that radar rays follow paths of constant curvature can be utilized to compute heights and great circle distances of radar data without resorting to the equivalent-earth model. The new technique produces results similar to those obtained using the equivalent-earth model but may be preferable since it utilizes a less complicated model for the propagation of radar rays.

The transformation equations for a spherical curvilinear coordinate system have also been derived. It is known that these equations have been derived previously by others (R. Brown 2000, personal communication). Because they have not been published in the formal literature, however, the intent is to do so as a service to the meteorological community.

The objective analysis of radar data has been investigated. The first effort in this vein regards an analysis technique, named the adaptive Barnes (A-B) scheme, that automatically adapts to the characteristics of radar data. This work has already been published. The conclusions, taken directly from Askelson et al. (2000), are

"1) The A-B filter can directly account for the dependence of radar data spacing on direction and for the tendency of radar data density to decrease with range. Within the confines of one-pass DDWA schemes, the A-B filter facilitates the retention of the maximum amount of information.

2) Consistent with the anisotropy of radar data spacing, more information concerning waves with short to medium wavelengths in the highly resolved direction can be retained by decreasing the smoothing in that direction using the direction-splitting design of the A-B filter. This occurs without egregious phase shifts or orientation changes of input waves.

3) Because the weight assigned to an observation depends upon the differences in the coordinates of the observation and analysis points, the A-B filter automatically adapts to the systematically decreasing radar data density with range. With the A-B filter information content at close ranges does not have to be sacrificed because of poor resolution at more distant ranges.

4) Windowing weight functions produces ringing in their response functions. Effects on the main lobe of the one-dimensional, Barnes response function are small when the weight function is windowed at or below 0.05.

5) For radar data, postanalysis gradient fields of analyses produced using an isotropic weight function will generally suffer from contributions by gradients in the analysis weights. Because of its consistency with radar data, the direction-splitting A-B filter, when applied away from data boundaries and to radar data that are at regular radial, azimuthal, and elevational intervals, results in postanalysis gradient fields that have virtually no contribution from gradients in analysis weights. However, even when the additional restriction of collocated observation and analysis points is imposed, postanalysis gradients are not equal to analyses of gradients because of the scale factors associated with the spherical coordinate system of radar data.

6) The A-B filter should be used with caution since imbalances in the data, including preferential orientation of finescale structure and decreasing finescale structure with range, can be retained by the A-B filter. The retention of these imbalances is what ironically produces both the potential benefits and detriments of the A-B scheme. Potential detriments arise since retention of data imbalances could lead unwary analysts to form incorrect conclusions concerning the phenomena being studied. Isotropic schemes, at the cost of information loss, attempt to normalize these imbalances."

In the investigation of the A-B scheme, the issue of response functions for arbitrary weight functions and data distributions arose. The subsequent investigation proved fruitful. The conclusions are:

1) The local response function for DDWA schemes is the complex conjugate of the normalized Fourier transform of the effective weight function. Complex conjugation arises because DDWA is, in general, a cross correlation, not a convolution. Normalization is imposed by the DDWA normalization factor. The effective weight function is the product of the weight function and the function, or generalized function (also called a distribution), that describes the distribution of the observations.

2) To obtain the local response function by way of the convolution theorem the concept of an equivalent analysis is needed. In an equivalent analysis a hypothetical analysis field is produced by using, throughout the entire domain, the same weight function and data distribution that apply to the point of interest. This

artifice enables the convolution-theorem based derivation of the response function by altering the mathematical form that describes the analysis field.

3) The local response function generally depends upon the weight function, frequency, and location.

4) Response functions can be eloquently described in terms of the amplitude and phase modulations of the input waves.

5) Boundaries significantly affect response functions. In their vicinity they produce significant phase shifts and appreciable alterations of amplitude modulations relative to the ideal response function, which holds for continuous, infinite data.

6) Phase shift information provides a straightforward interpretation for extrapolation. It illustrates the movement, or shift, of information that seems to be fundamental to all extrapolation schemes. During extrapolation analysis values are produced by taking information and *moving it* to the analysis locations.

7) Irregular data spacing can result in significant phase shifts and significant departures from the ideal amplitude modulation. The degree of filtering at a particular frequency can be either greater or less than that imposed under ideal conditions.

8) The framework for determining the local response function is also valid in two dimensions. It appears as if the extension to three or more dimensions can be accomplished by simply generalizing the methods utilized herein

The conclusions regarding precipitation-driven RFDs are

1) Hook-echo hydrometeor fields inferred from radar data are able to drive significant downdrafts without the influence of vertical perturbation pressure gradients.

2) Supercell environments are often relatively resistant to downdrafts above the boundary layer and supportive of them within the boundary layer.

3) In many supercell environments, large hail or vertical perturbation pressure gradients may be needed to produce deep midlevel downdrafts that penetrate into the boundary layer.

4) In supercell environments it appears as if RFDs are typically either generated or intensified significantly within the boundary layer. Consequently, the boundary layer θ_v profile appears to be very important to the surface RFD θ_v deficit and, from the findings of Markowski et al. (2002), to tornadogenesis.

5) In some supercell environments precipitation-driven RFDs are relatively insensitive to the characteristics of the precipitation fields that drive them while in other environments significant sensitivity exists.

In closing, it is noted that this research has raised some important questions and has in the process opened some new research avenues. Regarding response functions for arbitrary weight functions and data distributions, efforts to apply the response function in filter design are already underway. Moreover, the incorporation of larger hail in the 1.5 dimension downdraft model is already being planned. It is hoped that these research efforts will not only build upon the foundation laid before them by countless others, but also serve in the foundation for future endeavors.

References

Abraham, F. F., 1970: Functional dependence of drag coefficient of a sphere on Reynolds number. *Phys. Fluids*, **13**, 2194-2195.

Achtemeier, G. L., 1986: The impact of data boundaries upon a successive corrections objective analysis of limited-area datasets. *Mon. Wea. Rev.*, **114**, 40-49.

Adlerman, E. J., K. K. Droegemeier, and R. Davies-Jones, 1999: A numerical simulation of cyclic mesocyclogenesis. *J. Atmos. Sci.*, **56**, 2045-2069.

Andsager, K., K. V. Beard, and N. F. Laird, 1999: Laboratory measurements of axis ratios for large raindrops. *J. Atmos. Sci.*, **56**, 2673-2683.

Askelson, M. A., J. P. Aubagnac, and J. M. Straka, 2000: An adaptation of the Barnes filter applied to the objective analysis of radar data. *Mon. Wea. Rev.*, **128**, 3050-3082.

Asai, T., and A. Kasahara, 1967: A theoretical study of the compensating downward motions associated with cumulus clouds. *J. Atmos. Sci.*, **24**, 487-496.

Atlas, D., R. C. Srivastava, and R. S. Sekhon, 1973: Doppler radar characteristics of precipitation at vertical incidence. *Rev. Geophys. Space Phys.*, **11**, 1-35.

Aubagnac, J. P., and D. S. Zrnić, 1995: Identification and quantification of hydrometeors in a supercell storm using radar polarimetry. Preprints, *27th Conf. on Radar Meteor.*, Vail, CO, Amer. Meteor. Soc., 105-107.

Auer, A. H., Jr., 1972: Distribution of graupel and hail with size. *Mon. Wea. Rev.*, **100**, 325-328.

Aydin, K., and Y. Zhao, 1990: A computational study of polarimetric radar observables in hail. *IEEE Trans. Geosci. Remote Sens.*, **28**, 412-422.

———, and V. Giridhar, 1992: C-band dual-polarization radar observables in rain. *J. Atmos. Oceanic Technol.*, **9**, 383-390.

Ayres, F., Jr., 1954: *Theory and Problems of Plane and Spherical Trigonometry*. Schaum's Outline Series, McGraw-Hill, 207 pp.

Balakrishnan, N., and D. S. Zrnić, 1990a: Estimation of rain and hail rates in mixed-phase precipitation. *J. Atmos. Sci.*, **47**, 565-583.

———, and ———, 1990b: Use of polarization to characterize precipitation and discriminate large hail. *J. Atmos. Sci.*, **47**, 1525-1540.

Barnes, S. L., 1964: A technique for maximizing details in numerical weather map analysis. *J. Appl. Meteor.*, **3**, 396-409.

———, 1978a: Oklahoma thunderstorms on 29-30 April 1970. Part I: Morphology of a tornadic storm. *Mon. Wea. Rev.*, **106**, 673-684.

———, 1978b: Oklahoma thunderstorms on 29-30 April 1970. Part II: Radar-observed merger of twin hook echoes. *Mon. Wea. Rev.*, **106**, 685-696.

Battan, L. J., 1973: *Radar Observation of the Atmosphere*. University of Chicago Press, 324 pp.

Bean, B. R., and E. J. Dutton, 1966: *Radio Meteorology*, Natl. Bur. Stand. Monogr., No. 92, 435 pp.

Beard, K. V., 1976: Terminal velocity and shape of cloud and precipitation drops aloft. *J. Atmos. Sci.*, **33**, 851-864.

———, 1977: Terminal velocity adjustment for cloud and precipitation drops aloft. *J. Atmos. Sci.*, **34**, 1293-1298.

———, 1980: The effects of altitude and electrical force on the terminal velocity of hydrometeors. *J. Atmos. Sci.*, **37**, 1363-1374.

———, 1985: Simple altitude adjustments to raindrop velocities for Doppler radar analysis. *J. Atmos. Oceanic Technol.*, **2**, 468-471.

———, and H. R. Pruppacher, 1971: A wind tunnel investigation of the rate of evaporation of small water drops falling at terminal velocity in air. *J. Atmos. Sci.*, **28**, 1455-1464.

———, and A. R. Jameson, 1983: Raindrop canting. *J. Atmos. Sci.*, **40**, 448-454.

———, and C. Chuang, 1987: A new model for the equilibrium shape of raindrops. *J. Atmos. Sci.*, **44**, 1509-1524.

———, D. B. Johnson, and A. R. Jameson, 1983: Collisional forcing of raindrop oscillations. *J. Atmos. Sci.*, **40**, 455-462.

Bent, A. E., P. M. Austin, and M. L. Stone, 1950: Beam Width and Pulse Length in Radar Weather Detection. MIT Dept. of Meteor. Tech. Rep. No. 12, 61 pp.

Berry, E. X., and M. R. Pranger, 1974: Equations for calculating the terminal velocities of water drops. *J. Appl. Meteor.*, **13**, 108-113.

Betts, A. K., and M. F. Silva Dias, 1979: Unsaturated downdraft thermodynamics in cumulonimbus. *J. Atmos. Sci.*, **36**, 1061-1071.

Böhm, H. P., 1989: A general equation for the terminal fall speed of solid hydrometeors. *J. Atmos. Sci.*, **46**, 2419-2427.

Bohren, C. F., and L. J. Battan, 1980: Radar backscattering by inhomogeneous precipitation particles. *J. Atmos. Sci.*, **37**, 1821-1827.

Bolton, D., 1980: The computation of equivalent potential temperature. *Mon. Wea. Rev.*, **108**, 1046-1053.

Bracewell, R. N., 2000: *The Fourier Transform and its Applications*, 3rd ed. McGraw-Hill Series in Electrical and Computer Engineering, McGraw-Hill, 616 pp.

Braham, R. R., Jr., 1963: Some measurements of snow pellet bulk-densities. *J. Appl. Meteor.*, **2**, 498-500.

———, 1964: What is the role of ice in summer rain-showers? *J. Atmos. Sci.*, **21**, 640-645.

———, 1986: Coalescence-freezing precipitation mechanism. Preprints, *Tenth Conf. on Weather Modification*, Arlington, VA, Amer. Meteor. Soc., 142-145.

Brandes, E. A., 1978: Mesocyclone evolution and tornadogenesis: Some observations. *Mon. Wea. Rev.*, **106**, 995-1011.

———, 1981: Finestructure of the Del City-Edmond tornadic mesocirculation. *Mon. Wea. Rev.*, **109**, 635-647.

———, 1984: Relationships between radar-derived thermodynamic variables and tornadogenesis. *Mon. Wea. Rev.*, **112**, 1033-1052.

———, A. V. Ryzhkov, and D. S. Zrnić, 2001: An evaluation of radar rainfall estimates from specific differential phase. *J. Atmos. Oceanic Technol.*, **18**, 363-375.

Bringi, V. N., T. A. Seliga, and K. Aydin, 1984: Hail detection with a differential reflectivity radar. *Science*, **225**, 1145-1147.

———, R. M. Rasmussen, and J. Vivekanandan, 1986a: Multiparameter radar measurements in Colorado convective storms. Part I: Graupel melting studies. *J. Atmos. Sci.*, **43**, 2545-2563.

———, J. Vivekanandan, and J. D. Tuttle, 1986b: Multiparameter radar measurements in Colorado convective storms. Part II: Hail detection studies. *J. Atmos. Sci.*, **43**, 2564-2577.

———, V. Chandrasekar, N. Balakrishnan, and D. S. Zrnić, 1990: An examination of propagation effects in rainfall on radar measurements at microwave frequencies. *J. Atmos. Oceanic Technol.*, **7**, 829-840.

———, L. Liu, P. C. Kennedy, V. Chandrasekar, and S. A. Rutledge, 1996: Dual multiparameter radar observations of intense convective storms: The 24 June 1992 case study. *Meteor. Atmos. Phys.*, **59**, 3-31.

Brooks, H. E., C. A. Doswell III, and R. B. Wilhelmson, 1994: The role of midtropospheric winds in the evolution and maintenance of low-level mesocyclones. *Mon. Wea. Rev.*, **122**, 126-136.

Brown, R. A., C. R. Safford, S. P. Nelson, D. W. Burgess, W. C. Bumgarner, M. L. Weible, and L. C. Fortner, 1981: Multiple Doppler radar analysis of severe thunderstorms: Designing a general analysis system. NOAA Tech. Memo. ERL NSSL-92, 21 pp. [Available from NSSL Library, 1313 Halley Circle, Norman, OK 73069.]

Browning, K. A., 1962: Cellular nature of convective storms. *Meteor. Mag.*, **91**, 341-350.

———, 1964: Airflow and precipitation trajectories within severe local storms which travel to the right of the winds. *J. Atmos. Sci.*, **21**, 634-639.

———, and F. H. Ludlam, 1962: Airflow in convective storms. *Quart. J. Roy. Meteor. Soc.*, **88**, 117-135.

Buzzi, A., D. Gomis, M. A. Pedder, and S. Alonso, 1991: A method to reduce the adverse impact that inhomogeneous station distributions have on spatial interpolation. *Mon. Wea. Rev.*, **119**, 2465-2491.

Caracena, F., 1987: Analytic approximation of discrete field samples with weighted sums and the gridless computation of field derivatives. *J. Atmos. Sci.*, **44**, 3753-3768.

———, S. L. Barnes, and C. A. Doswell III, 1984: Weighting function parameters for objective interpolation of meteorological data. *Proc. 10th Conference Weather Forecasting and Analysis*, Clearwater Beach, FL, Amer. Meteor. Soc., 109-116.

Carey, L. D., and S. A. Rutledge, 1996: A multiparameter radar case study of the microphysical and kinematic evolution of a lightning producing storm. *Meteor. Atmos. Phys.*, **59**, 33-64.

Carr, F. H., P. L. Spencer, C. A. Doswell III, and J. D. Powell, 1995: A comparison of two objective analysis techniques for profiler time-height data. *Mon. Wea. Rev.*, **123**, 2165-2180.

Chandrasekar, V., W. A. Cooper, and V. N. Bringi, 1988: Axis ratios and oscillations of raindrops. *J. Atmos. Sci.*, **45**, 1323-1333.

Cheng, L., and M. English, 1983: A relationship between hailstone concentration and size. *J. Atmos. Sci.*, **40**, 204-213.

———, ———, and R. Wong, 1985: Hailstone size distributions and their relationship to storm thermodynamics. *J. Climate Appl. Meteor.*, **24**, 1059-1067.

Chong, S.-L., and C. S. Chen, 1974: Water shells on ice pellets and hailstones. *J. Atmos. Sci.*, **31**, 1384-1391.

Conway, J. W., and D. S. Zrnić, 1993: A study of embryo production and hail growth using dual-Doppler and multiparameter radars. *Mon. Wea. Rev.*, **121**, 2511-2528.

Daley, R., 1991: *Atmospheric Data Analysis*. Cambridge Atmospheric and Space Science Series, Vol. 2, Cambridge University Press, 457 pp.

Das, P., and M. C. Subba Rao, 1972: The unsaturated downdraught. *Indian J. Meteor. Geophys.*, **23**, 135-144.

Davies, C. N., 1945: Definitive equations for the fluid resistance of spheres. *Proc. Phys. Soc. London*, **A57**, 259-270.

Davies-Jones, R. P., 1982: A new look at the vorticity equation with application to tornadogenesis. *Proc. 12th Conf. Severe Local Storms*, San Antonio, TX, Amer. Meteor. Soc., 249-252.

———, R. P., 2000: Can the hook echo instigate tornadogenesis barotropically? *Proc. 20th Conf. Severe Local Storms*, Orlando, FL, Amer. Meteor. Soc., 269-272.

———, and H. Brooks, 1993: Mesocyclogenesis from a theoretical perspective. *The Tornado: Its Structure, Dynamics, Prediction, and Hazards, Geophys. Monogr.*, No. 79, Amer. Geophys. Union, 105-114.

Debye, P., 1929: *Polar Molecules*. The Chemical Catalog Company, 172 pp.

Doswell, C. A., III, and F. Caracena, 1988: Derivative estimation from marginally sampled vector point functions. *J. Atmos. Sci.*, **45**, 242-253.

———, and D. W. Burgess, 1993: Tornadoes and tornadic storms: A review of conceptual models. *The Tornado: Its Structure, Dynamics, Prediction, and Hazards, Geophys. Monogr.*, No. 79, Amer. Geophys. Union, 161-172.

———, and S. Lasher-Trapp, 1997: On measuring the degree of irregularity in an observing network. *J. Atmos. Oceanic Technol.*, **14**, 120-132.

Doviak, R. J., and D. S. Zrnić, 1993: *Doppler Radar and Weather Observations*. 2nd Ed. Academic Press, 562 pp.

Dowell, D. C., and H. B. Bluestein, 1997: The Arcadia, Oklahoma, storm of 17 May 1981: Analysis of a supercell during tornadogenesis. *Mon. Wea. Rev.*, **125**, 2562-2582.

———, H. B. Bluestein, and D. P. Jorgensen, 1997: Airborne Doppler radar analysis of supercells during COPS-91. *Mon. Wea. Rev.*, **125**, 365-383.

Dutton, J. A., 1995: *Dynamics of Atmospheric Motion*. Dover, 617 pp.

Emanuel, K. A., 1994: *Atmospheric Convection*. Oxford University Press, 580 pp.

English, M., 1973: Alberta hailstorms part II: Growth of large hail in the storm. *Alberta Hailstorms, Meteor. Monogr.*, No. 36, Amer. Meteor. Soc., 37-98.

Federer, B., and A. Waldvogel, 1975: Hail and raindrop size distributions from a Swiss multicell storm. *J. Appl. Meteor.*, **14**, 91-97.

Flora, S. D., 1956: *Hailstorms of the United States*. University of Oklahoma Press, Norman, OK, 201 pp.

Foote, G. B., and P. S. Du Toit, 1969: Terminal velocity of raindrops aloft. *J. Appl. Meteor.*, **8**, 249-253.

Girard, C., and R. List, 1975: Thermodynamics of falling precipitation zones. *Pure Appl. Geophys.*, **113**, 1035-1053.

Golestani, Y., V. Chandrasekar, and V. N. Bringi, 1989: Intercomparison of multiparameter radar measurements. Preprints, *24th Conf. on Radar Meteor.*, Tallahassee, FL, Amer. Meteor. Soc., 309-314.

Grazulis, T. P., 1993: *Significant Tornadoes, 1680-1991*. Environmental Films, St. Johnsbury, Vermont, 1326 pp.

———, 2001: *The Tornado: Nature's Ultimate Windstorm*. University of Oklahoma Press, Norman, Oklahoma, 324 pp.

Green, A. W., 1975: An approximation for the shapes of large raindrops. *J. Appl. Meteor.*, **14**, 1578-1583.

Gunn, K. L. S., and T. W. R. East, 1954: The microwave properties of precipitation particles. *Quart. J. Roy. Meteor. Soc.*, **80**, 522-545.

Gunn, R., and G. D. Kinzer, 1949: The terminal velocity of fall for water droplets in stagnant air. *J. Meteor.*, **6**, 243-248.

Hall, M. P. M., S. M. Cherry, J. W. F. Goddard, and G. R. Kennedy, 1980: Rain drop sizes and rainfall rate measured by dual-polarization radar. *Nature*, **285**, 195-198.

———, J. W. F. Goddard, and S. M. Cherry, 1984: Identification of hydrometeors and other targets by dual-polarization radar. *Radio Sci.*, **19**, 132-140.

Hall, W. D., and H. R. Pruppacher, 1976: The survival of ice particles falling from cirrus clouds in subsaturated air. *J. Atmos. Sci.*, **33**, 1995-2006.

Hamming, R. W., 1998: *Digital Filters*, 3d ed. Dover, 284 pp.

Hane, C. E., and P. S. Ray, 1985: Pressure and buoyancy fields derived from Doppler radar data in a tornadic thunderstorm. *J. Atmos. Sci.*, **42**, 18-35.

Harris, F. I., 1977: The effects of evaporation at the base of ice precipitation layers: Theory and radar observations. *J. Atmos. Sci.*, **34**, 651-672.

Herman, B. M., and L. J. Battan, 1961: Calculations of Mie back-scattering from melting ice spheres. *J. Meteor.*, **18**, 468-478.

Herzegh, P. H., and A. R. Jameson, 1992: Observing precipitation through dual-polarization radar measurements. *Bull. Amer. Meteor. Soc.*, **73**, 1365-1374.

Heymsfield, A. J., 1978: The characteristics of graupel particles in northeastern Colorado cumulus congestus clouds. *J. Atmos. Sci.*, **35**, 284-295.

Höller, H., V. N. Bringi, J. Hubbert, M. Hagen, and P. F. Meischner, 1994: Life cycle and precipitation formation in a hybrid-type hailstorm revealed by polarimetric and Doppler radar measurements. *J. Atmos. Sci.*, **51**, 2500-2522.

Hookings, G. A., 1965: Precipitation-maintained downdrafts. *J. Appl. Meteor.*, **4**, 190-195.

Houze, R. A., Jr., 1993: *Cloud Dynamics*. International Geophysical Series, Vol. 53, Academic Press, 573 pp.

Hubbert, J., and V. N. Bringi, 1995: An iterative filtering technique for the analysis of copolar differential phase and dual-frequency radar measurements. *J. Atmos. Oceanic Technol.*, **12**, 643-648.

———, and ———, 2000: The effects of three-body scattering on differential reflectivity signatures. *J. Atmos. Oceanic Technol.*, **17**, 51-61.

Jameson, A. R., 1985: Microphysical interpretation of multiparameter radar measurements in rain. Part III: Interpretation and measurement of propagation differential phase shift between orthogonal linear polarizations. *J. Atmos. Sci.*, **42**, 607-614.

———, 1987: Relations among linear and circular polarization parameters measured in canted hydrometeors. *J. Atmos. Oceanic Technol.*, **4**, 634-645.

———, and K. V. Beard, 1982: Raindrop axial ratios. *J. Appl. Meteor.*, **21**, 257-259.

———, and D. B. Johnson, 1990: Cloud microphysics and radar. *Radar in Meteorology: Battan Memorial and 40th Anniversary Radar Meteorology Conference*. D. Atlas, Ed., American Meteorological Society, 323-340.

———, and I. J. Caylor, 1994: A new approach to estimating rainwater content by radar using propagation differential phase shift. *J. Atmos. Oceanic Technol.*, **11**, 311-322.

Jones, D. M. A., 1959: The shape of raindrops. *J. Meteor.*, **16**, 504-510.

Jones, R. H., 1972: Aliasing with unequally spaced observations. *J. Appl. Meteor.*, **11**, 245-254.

Kamburova, P. L., and F. H. Ludlam, 1966: Rainfall evaporation in thunderstorm downdraughts. *Quart. J. Roy. Meteor. Soc.*, **92**, 510-518.

Kerker, M., P. Langleben, and K. L. S. Gunn, 1951: Scattering of microwaves by a melting, spherical ice particle. *J. Meteor.*, **8**, 424.

Klemp, J. B., and R. Rotunno, 1983: A study of the tornadic region within a supercell thunderstorm. *J. Atmos. Sci.*, **40**, 359-377.

Knight, N. C., 1981: The climatology of hailstone embryos. *J. Appl. Meteor.*, **20**, 750-755.

———, and A. J. Heymsfield, 1983: Measurement and interpretation of hailstone density and terminal velocity. *J. Atmos. Sci.*, **40**, 1510-1516.

Knupp, K. R., and W. R. Cotton, 1985: Convective cloud downdraft structure: An interpretive study. *Rev. Geophys.*, **23**, 183-215.

Koch, S. E., M. DesJardins, and P. J. Kocin, 1983: An interactive Barnes objective map analysis scheme for use with satellite and conventional data. *J. Climate Appl. Meteor.*, **22**, 1487-1503.

Koenig, L. R., 1963: The glaciating behavior of small cumulonimbus clouds. *J. Atmos. Sci.*, **20**, 29-47.

Komabayasi, M., T. Gonda, and K. Isono, 1964: Life time of water drops before breaking and size distribution of fragment droplets. *J. Meteor. Soc. Japan*, **42**, 330-340.

Lemon, L. R., and C. A. Doswell III, 1979: Severe thunderstorm evolution and mesocyclone structure as related to tornadogenesis. *Mon. Wea. Rev.*, **107**, 1184-1197.

Lin, Y. L., R. D. Farley, and H. D. Orville, 1983: Bulk parameterization of the snow field in a cloud model. *J. Climate Appl. Meteor.*, **22**, 1065-1092.

List, R. J., 1951: *Smithsonian Meteorological Tables*. 6th ed. Smithsonian Institution, 527 pp.

———, and R. S. Schemenauer, 1971: Free-fall behavior of planar snow crystals, conical graupel and small hail. *J. Atmos. Sci.*, **28**, 110-115.

———, U. W. Rentsch, A. C. Byram, and E. P. Lozowski, 1973: On the aerodynamics of spheroidal hailstone models. *J. Atmos. Sci.*, **30**, 653-661.

Liu, H., and V. Chandrasekar, 2000: Classification of hydrometeors based on polarimetric radar measurements: Development of fuzzy logic and neuro-fuzzy systems, and in situ verification. *J. Atmos. Oceanic Technol.*, **17**, 140-164.

Liu, L., V. N. Bringi, V. Chandrasekar, E. A. Mueller, and A. Mudukutore, 1994: Analysis of the copolar correlation coefficient between horizontal and vertical polarizations. *J. Atmos. Oceanic Technol.*, **11**, 950-963.

Ludlam, F. H., 1980: *Clouds and Storms*. The Pennsylvania State University Press, 405 pp.

Macklin, W. C., and F. H. Ludlam, 1961: The fallspeeds of hailstones. *Quart. J. Roy. Meteor. Soc.*, **87**, 72-81.

Markowski, P. M., J. M. Straka, and E. N. Rasmussen, 2002: Direct surface thermodynamic observations within the rear-flank downdrafts of nontornadic and tornadic supercells. *Mon. Wea. Rev.*, **130**, 1692-1721.

Marshall, J. S., and W. McK. Palmer, 1948: The distribution of raindrops with size. *J. Meteor.*, **5**, 165-166.

———, and K. L. S. Gunn, 1952: Measurement of snow parameters by radar. *J. Meteor.*, **9**, 322-327.

———, W. Hitschfeld, and K. L. S. Gunn, 1955: Advances in radar weather. *Advances in Geophysics*, Vol. 2, H. E. Landsberg, Ed., Academic Press, 1-56.

Mason, B. J., 1956: On the melting of hailstone. *Quart. J. Roy. Meteor. Soc.*, **82**, 209-216.

Matson, R. J., and A. W. Huggins, 1980: The direct measurement of the sizes, shapes and kinematics of falling hailstones. *J. Atmos. Sci.*, **37**, 1107-1125

Meischner, P. F., V. N. Bringi, D. Heimann, and H. Höller, 1991: A squall line in Southern Germany: Kinematics and precipitation formation as deduced by advanced polarimetric and Doppler radar measurements. *Mon. Wea. Rev.*, **119**, 678-701.

Moller, A. R., C. A. Doswell III, and R. Przybylinski, 1990: High-precipitation supercells: A conceptual model and documentation. *Proc. 16th Conf. Severe Local Storms*, Kananaskis Park, Alberta, Canada, Amer. Meteor. Soc., 52-57.

———, ———, M. P. Foster, and G. R. Woodall, 1994: The operational recognition of supercell thunderstorm environments and storm structures. *Wea. Forecasting*, **9**, 327-347.

Ogura, Y., and T. Takahashi, 1971: Numerical simulation of the life cycle of a thunderstorm cell. *Mon. Wea. Rev.*, **99**, 895-911.

———, and ———, 1973: The development of warm rain in a cumulus model. *J. Atmos. Sci.*, **30**, 262-277.

Papoulis, A., 1962: *The Fourier Integral and its Applications*. McGraw-Hill Electronic Sciences Series, McGraw-Hill, 318 pp.

Pauley, P. M., 1990: On the evaluation of boundary errors in the Barnes objective analysis scheme. *Mon. Wea. Rev.*, **118**, 1203-1210.

———, and X. Wu, 1990: The theoretical, discrete, and actual response of the Barnes objective analysis scheme for one- and two-dimensional fields. *Mon. Wea. Rev.*, **118**, 1145-1163.

Pellet, J. L., and A. S. Dennis, 1974: Effects of heat storage in hailstones. Preprints, *Conference on Cloud Physics*, Tuscon, AZ, Amer. Meteor. Soc., 63-66.

Pointin, Y., D. Ramond, and J. Fournet-Fayard, 1988: Radar differential reflectivity Z_{DR}: A real-case evaluation of errors induced by antenna characteristics. *J. Atmos. Oceanic Technol.*, **5**, 416-423.

Proctor, F. H., 1989: Numerical simulations of an isolated microburst. Part II: Sensitivity experiments. *J. Atmos. Sci.*, **46**, 2143-2165.

Pruppacher, H. R., and K. V. Beard, 1970: A wind tunnel investigation of the internal circulation and shape of water drops falling at terminal velocity in air. *Quart. J. Roy. Meteor. Soc.*, **96**, 247-256.

———, and R. Rasmussen, 1979: A wind tunnel investigation of the rate of evaporation of large water drops falling at terminal velocity in air. *J. Atmos. Sci.*, **36**, 1255-1260.

———, and J. D. Klett, 1997: *Microphysics of Clouds and Precipitation*. 2nd Ed. Atmospheric and Oceanographic Sciences Library, Vol. 18, Kluwer Academic Publishers, 954 pp.

Ramachandran, R., A. Detwiler, J. Helsdon Jr., P. L. Smith, and V. N. Bringi, 1996: Precipitation development and electrification in Florida thunderstorm cells during Convection and Precipitation/Electrification Project. *J. Geophys. Res.*, **101**, 1599-1619.

Rasmussen, E. N., and D. O. Blanchard, 1998: A baseline climatology of sounding-derived supercell and tornado forecast parameters. *Wea. Forecasting*, **13**, 1148-1164.

———, J. M. Straka, R. Davies-Jones, C. A. Doswell III, F. H. Carr, M. D. Eilts, and D. R. MacGorman, 1994: Verifications of the origins of rotation in tornadoes experiment: VORTEX. *Bull. Amer. Meteor. Soc.*, **75**, 995-1006.

Rasmussen, R. M., and A. J. Heymsfield, 1987: Melting and shedding of graupel and hail. Part I: Model physics. *J. Atmos. Sci.*, **44**, 2754-2763.

———, V. Levizzani, and H. R. Pruppacher, 1984a: A wind tunnel and theoretical study of the melting behavior of atmospheric ice particles. II: A theoretical study for frozen drops of radius < 500 μm. *J. Atmos. Sci.*, **41**, 374-380.

———, ———, and ———, 1984b: A wind tunnel and theoretical study on the melting behavior of atmospheric ice particles. III: Experiment and theory for spherical ice particles of radius > 500 μm. *J. Atmos. Sci.*, **41**, 381-388.

Reddy, J. N., and M. L. Rasmussen, 1990: *Advanced Engineering Analysis*. Robert E. Krieger, 488 pp.

Richner, H., and P. Viatte, 1995: The hydrostatic equation in the evaluation algorithm for radiosonde data. *J. Atmos. Oceanic Technol.*, **12**, 649-656.

Rogers, R. R., and M. K. Yau, 1989: *A Short Course in Cloud Physics*. International Series in Natural Philosophy, Vol. 113, Pergamon Press, 293 pp.

Rotunno, R., 1993: Supercell thunderstorm modeling and theory. *The Tornado: Its Structure, Dynamics, Prediction, and Hazards, Geophys. Monogr.*, No. 79, Amer. Geophys. Union, 57-73.

———, and J. B. Klemp, 1982: The influence of the shear-induced pressure gradient on thunderstorm motion. *Mon. Wea. Rev.*, **110**, 136-151.

———, and ———, 1985: On the rotation and propagation of simulated supercell thunderstorms. *J. Atmos. Sci.*, **42**, 271-292.

Ryzhkov, A. V., and D. S. Zrnić, 1995a: Comparison of dual-polarization radar estimators of rain. *J. Atmos. Oceanic Technol.*, **12**, 249-256.

———, and ———, 1995b: Precipitation and attenuation measurements at a 10-cm wavelength. *J. Appl. Meteor.*, **34**, 2121-2134.

———, and ———, 1996: Assessment of rainfall measurement that uses specific differential phase. *J. Appl. Meteor.*, **35**, 2080-2090.

———, and ———, 1998: Beamwidth effects on the differential phase measurement of rain. *J. Atmos. Oceanic Technol.*, **15**, 624-634.

———, ———, and B. A. Gordon, 1998: Polarimetric method for ice water content determination. *J. Appl. Meteor.*, **37**, 125-134.

Sachidananda, M., and D. S. Zrnić, 1986: Differential propagation phase shift and rainfall rate estimation. *Radio Sci.*, **21**, 235-247.

———, and ———, 1987: Rain rate estimates from differential polarization measurements. *J. Atmos. Oceanic Technol.*, **4**, 588-598.

Schlax, M. G., and D. B. Chelton, 1992: Frequency domain diagnostics for linear smoothers. *J. Amer. Stat. Assoc.*, **87**, 1070-1081.

———, and ———, 2002: Filter transfer functions for the method of successive corrections. *Mon. Wea. Rev.*, **130**, 372-385.

Sears, F. W., M. W. Zemansky, and H. D. Young, 1987: *University Physics*. 7th Ed. Addison-Wesley Series in Physics, Addison-Wesley, 1096 pp.

Seliga, T. A., and V. N. Bringi, 1976: Potential use of radar differential reflectivity measurements at orthogonal polarizations for measuring precipitation. *J. Appl. Meteor.*, **15**, 69-76.

———, and ———, 1978: Differential reflectivity and differential phase shift: Applications in radar meteorology. *Radio Sci.*, **13**, 271-275.

———, ———, and H. H. Al-Khatib, 1979: Differential reflectivity measurements in rain: First experiments. *IEEE Trans. Geosci. Electron.*, **GE-17**, 240-244.

———, ———, and ———, 1981: A preliminary study of comparative measurements of rainfall rate using the differential reflectivity radar technique and a raingage network. *J. Appl. Meteor.*, **20**, 1362-1368.

———, K. Aydin, and H. Direskeneli, 1986: Disdrometer measurements during an intense rainfall event in central Illinois: Implications for differential reflectivity radar observations. *J. Climate Appl. Meteor.*, **25**, 835-846.

Shelleng, J. C., C. R. Burrows, and E. B. Ferrell, 1933: Ultra-short-wave propagation, *Proc. Inst. Radio Eng.*, **21**, 427-463.

Smith, P. L., 1984: Equivalent radar reflectivity factors for snow and ice particles. *J. Climate Appl. Meteor.*, **23**, 1258-1260.

Soong, S.-T., and Y. Ogura, 1973: A comparison between axisymmetric and slab-symmetric cumulus cloud models. *J. Atmos. Sci.*, **30**, 879-893.

Srivastava, R. C., 1985: A simple model of evaporatively driven downdraft: Application to microburst downdraft. *J. Atmos. Sci.*, **42**, 1004-1023.

———, 1987: A model of intense downdrafts driven by the melting and evaporation of precipitation. *J. Atmos. Sci.*, **44**, 1752-1773.

———, and J. L. Coen, 1992: New explicit equations for the accurate calculation of the growth and evaporation of hydrometeors by the diffusion of water vapor. *J. Atmos. Sci.*, **49**, 1643-1651.

Stapor, D. P., and T. Pratt, 1984: A generalized analysis of dual-polarization radar measurements of rain. *Radio Sci.*, **19**, 90-98.

Stephens, J. J., 1967: Filtering responses of selected distance-dependent weight functions. *Mon. Wea. Rev.*, **95**, 45-46.

———, and A. L. Polan, 1971: Spectral modification by objective analysis. *Mon. Wea. Rev.*, **99**, 374-378.

Straka, J. M., 1996: Hydrometeor fields in a supercell storm as deduced from dual-polarization radar. *Proc. 18th Conf. on Severe Local Storms*, San Francisco, CA, Amer. Meteor. Soc., 551-554.

———, D. S. Zrnić, and A. V. Ryzhkov, 2000: Bulk hydrometeor classification and quantification using polarimetric radar data: Synthesis of relations. *J. Appl. Meteor.*, **39**, 1341-1372.

Testud, J., and M. Chong, 1983: Three-dimensional wind field analysis from dual-Doppler radar data. Part I: Filtering, interpolating and differentiating the raw data. *J. Climate Appl. Meteor.*, **22**, 1204-1215.

Thiébaux, H. J., and M. A. Pedder, 1987: *Spatial Objective Analysis: With Applications in Atmospheric Science*. Academic Press, 299 pp.

Tong, H., V. Chandrasekar, K. R. Knupp, and J. Stalker, 1998: Multiparameter radar observations of time evolution of convective storms: Evaluation of water budgets and latent heating rates. *J. Atmos. Oceanic Technol.*, **15**, 1097-1109.

Trapp, R. J., 1999: Observations of nontornadic low-level mesocyclones and attendant tornadogenesis failure during VORTEX. *Mon. Wea. Rev.*, **127**, 1693-1705.

Ulbrich, C. W., 1983: Natural variations in the analytical form of the raindrop size distribution. *J. Climate Appl. Meteor.*, **22**, 1764-1775.

———, and D. Atlas, 1984: Assessment of the contribution of differential polarization to improved rainfall measurements. *Radio Sci.*, **19**, 49-57.

Vivekanandan, J., D. S. Zrnić, S. M. Ellis, R. Oye, A. V. Ryzhkov, and J. Straka, 1999: Cloud microphysics retrieval using S-band dual-polarization radar measurements. *Bull. Amer. Meteor. Soc.*, **80**, 381-388.

Walko, R. L., 1993: Tornado spin-up beneath a convective cell: Required basic structure of the near-field boundary layer winds. *The Tornado: Its Structure, Dynamics, Prediction, and Hazards, Geophys. Monogr.*, No. 79, Amer. Geophys. Union, 89-95.

Warner, C., and A. Hizal, 1976: Scattering and depolarization of microwaves by spheroidal raindrops. *Radio Sci.*, **11**, 921-930.

Weaver, H. J., 1983: *Applications of Discrete and Continuous Fourier Analysis*. Wiley & Sons, 375 pp.

Weisman, M. L., and J. B. Klemp, 1984: The structure and classification of numerically simulated convective storms in directionally varying wind shears. *Mon. Wea. Rev.*, **112**, 2479-2498.

Wicker, L. J., and R. B. Wilhelmson, 1995: Simulation and analysis of tornado development and decay within a three-dimensional supercell thunderstorm. *J. Atmos. Sci.*, **52**, 2675-2703.

Xu, J. L., 1983: Some hail research in China. *Bull. Amer. Meteor. Soc.*, **64**, 124-132.

Yang, C., and R. Shapiro, 1973: The effects of the observational system and the method of interpolation on the computation of spectra. *J. Atmos. Sci.*, **30**, 530-536.

Zahrai, A., and D. S. Zrnić, 1993: The 10-cm-wavelength polarimetric weather radar at NOAA's National Severe Storms Laboratory. *J. Atmos. Oceanic Technol.*, **10**, 649-662.

Ziegler, C. L., P. S. Ray, and N. C. Knight, 1983: Hail growth in an Oklahoma multicell storm. *J. Atmos. Sci.*, **40**, 1768-1791.

Zrnić, D. S., and R. J. Doviak, 1989: Effect of drop oscillations on spectral moments and differential reflectivity measurements. *J. Atmos. Oceanic Technol.*, **6**, 532-536.

———, and A. Ryzhkov, 1996: Advantages of rain measurements using specific differential phase. *J. Atmos. Oceanic Technol.*, **13**, 454-464.

———, and ———, 1999: Polarimetry for weather surveillance radars. *Bull. Amer. Meteor. Soc.*, **80**, 389-406.

———, V. N. Bringi, N. Balakrishnan, K. Aydin, V. Chandrasekar, and J. Hubbert, 1993: Polarimetric measurements in a severe hailstorm. *Mon. Wea. Rev.*, **121**, 2223-2238.

Appendix A: Amplitude and Phase Representation of Fourier Content

The Fourier content of a real function $f(x)$ can be expressed in terms of the amplitudes and phases of the one-sided spectrum. The starting point for this derivation is the (indirect) Fourier transform

$$f(x) = \int_{-\infty}^{\infty} F(v)\exp(j2\pi vx)dv, \tag{A1}$$

where

$$F(v) = \int_{-\infty}^{\infty} f(x)\exp(-j2\pi vx)dx = F_{\mathrm{Re}}(v) + jF_{\mathrm{Im}}(v). \tag{A2}$$

An important property of $F(v)$, for $f(x)$ real, is that it is hermitian (Bracewell 2000, 13-14), which means that

$$\begin{aligned} F_{\mathrm{Re}}(v) &= F_{\mathrm{Re}}(-v) \\ F_{\mathrm{Im}}(v) &= -F_{\mathrm{Im}}(-v). \end{aligned} \tag{A3}$$

Under the appropriate conditions (discussed at the end of this derivation), the integral in (A1) can be split at $v = 0$ to produce

$$f(x) = \int_{-\infty}^{0} F(v)\exp(j2\pi vx)dv + \int_{0}^{\infty} F(v)\exp(j2\pi vx)dv. \tag{A4}$$

By considering the integrand in the first integral of (A4) it is obvious that (A4) can be written as

$$f(x) = \int_{0}^{\infty} F(v)\exp(j2\pi vx) + F(-v)\exp(-j2\pi vx)dv, \tag{A5}$$

a result that can be obtained mathematically through the substitution $u = -v$ in the first integral in (A4). Moreover, $F(v)$ and $F(-v)$ can be expressed in polar coordinates as

$$F(v) = \left[F_{\mathrm{Re}}(v)^2 + F_{\mathrm{Im}}(v)^2\right]^{1/2} \exp\left[j\varphi_{F(v)}\right] \tag{A6}$$

and

$$F(-v) = \left[F_{\mathrm{Re}}(v)^2 + F_{\mathrm{Im}}(v)^2\right]^{1/2} \exp\left[j\varphi_{F(-v)}\right], \tag{A7}$$

where $\varphi_{F(v)} = \arg[F(v); F_{\mathrm{Re}}(v), F_{\mathrm{Im}}(v)]$, $\varphi_{F(-v)} = \arg[F(-v); F_{\mathrm{Re}}(v), -F_{\mathrm{Im}}(v)]$, and (A3) has been utilized.[A1] [Note that v is restricted to be greater than or equal to zero from (A5) onward in this derivation.] Because $\varphi_{F(-v)} = -\varphi_{F(v)}$, (A5) can be written, using (A6) and (A7), as

$$f(x) = \int_0^{\infty} \left[F_{\mathrm{Re}}(v)^2 + F_{\mathrm{Im}}(v)^2\right]^{1/2} \left\{\exp\left[j(2\pi vx + \varphi_{F(v)})\right] + \exp\left[-j(2\pi vx + \varphi_{F(v)})\right]\right\} dv . \tag{A8}$$

Since $e^{j\theta} + e^{-j\theta} = 2\cos\theta$, (A8) simplifies to

$$f(x) = \int_0^{\infty} 2\left[F_{\mathrm{Re}}(v)^2 + F_{\mathrm{Im}}(v)^2\right]^{1/2} \cos(2\pi vx + \varphi_{F(v)})\, dv . \tag{A9}$$

This result is valid for many situations that are encountered. It is not valid, however, when the mean value of $f(x)$ is not equal to zero. In that case, $F(0) = \left(\int_{-\infty}^{\infty} f(x)dx \Big/ \int_{-\infty}^{\infty} dx \right) \int_{-\infty}^{\infty} dx = C_m \delta(0)$ [the ratio of the integrals must be considered in the sense of a limit as the integration limits approach $\pm\infty$ while the Dirac distribution arises from definition (Bracewell 2000, 74-106)]. Insertion of this result into (A1) produces $f(x) = C_m + \mathrm{OF}$, where OF represents the contribution from the

other frequencies (other than the frequency 0) and the sifting property of the Dirac distribution, $\int_{-\infty}^{\infty}\delta(x-a)f(x)dx = f(a)$ (Bracewell 2000, p. 79), has been applied. Insertion of this result into (A4) or (A9), on the other hand, produces $f(x) = 2C_m + \mathrm{OF}$. [For a concrete example, consider what happens when $f(x) = C$, where C is a constant. Then, $F(\nu) = C\delta(\nu)$, (A1) produces $f(x) = C$, and (A4) or (A9) produce $f(x) = 2C$.] The reason for this discrepancy is the split of the (indirect) Fourier transform at $\nu = 0$. Normally, this would have no impact since the value of the integrand at one location usually does not alter the value of the integral (differences must normally be spread out over a finite range). Here, however, the Fourier transforms of elements such as periodic and constant functions (over infinite domains) are of theoretical interest. To deal with these Fourier transforms, distributions like the Dirac distribution are needed. When the Dirac distribution is utilized, its sifting property can result in differences in integrands at individual points being of consequence. This is what occurs at $\nu = 0$ in the above example. To correct for the above problem, the magnitude in (A9) is altered by the appropriate factor, resulting in

$$f(x) = \int_{\nu=0}^{\infty} \frac{2}{1+\delta^0(\nu)}\left[F_{\mathrm{Re}}(\nu)^2 + F_{\mathrm{Im}}(\nu)^2\right]^{1/2}\cos\left(2\pi\nu x + \varphi_{F(\nu)}\right)d\nu, \qquad \text{(A10)}$$

where $\delta^0(x)$ is defined as in Bracewell (2000, p. 87)

$$\delta^0(x) = \begin{cases} 0 & x \neq 0 \\ 1 & x = 0. \end{cases} \qquad \text{(A11)}$$

[A1] See footnote 13.

It is noted that the adjustment in (A10) could be rendered unnecessary by adapting the convention $\int_{x=0}^{x=\infty}\delta(x)dx=\frac{1}{2}$, which is mentioned by Bracewell (2000, p. 104). Herein, the convention $\int_{x=0}^{x=\infty}\delta(x)dx=1$ is used.

The fundamental result of this analysis is that the real function $f(x)$ can be expressed in terms of the amplitudes $|F(\nu)|=\left[F_{\mathrm{Re}}(\nu)^2+F_{\mathrm{Im}}(\nu)^2\right]^{1/2}$ and phases $\varphi_{F(\nu)}=\arg\left[F(\nu);F_{\mathrm{Re}}(\nu),F_{\mathrm{Im}}(\nu)\right]$ of the one sided $(\nu\geq 0)$ Fourier coefficients.

Appendix B: Amplitude and Phase Representation of Two-Dimensional Fourier Content

The Fourier content of a real function $f(x,y)$ can be expressed in terms of the amplitudes and phases of its Fourier coefficients. The approach for obtaining this result herein is much the same as that used for one-dimensional data. The starting point for this derivation is the (indirect) Fourier transform

$$f(x,y) = \int_{-\infty}^{\infty}\int_{-\infty}^{\infty} F(u,v)\exp[j2\pi(ux+vy)]\,du\,dv\,. \tag{B1}$$

where

$$F(u,v) = \int_{-\infty}^{\infty}\int_{-\infty}^{\infty} f(x,y)\exp[-j2\pi(ux+vy)]\,dx\,dy = F_{\mathrm{Re}}(u,v) + jF_{\mathrm{Im}}(u,v)\,. \tag{B2}$$

The hermitian property described by Bracewell (2000, 13-14) for one-dimensional Fourier transforms extends to two-dimensional Fourier transforms. This means that for $f(x,y)$ real,

$$\begin{aligned} F_{\mathrm{Re}}(u,v) &= F_{\mathrm{Re}}(-u,-v) \\ F_{\mathrm{Re}}(-u,v) &= F_{\mathrm{Re}}(u,-v) \\ F_{\mathrm{Im}}(u,v) &= -F_{\mathrm{Im}}(-u,-v) \\ F_{\mathrm{Im}}(-u,v) &= -F_{\mathrm{Im}}(u,-v)\,, \end{aligned} \tag{B3}$$

which are easily verified using (B2).

The integral in (B1) can be split to produce

$$
\begin{aligned}
f(x,y) = & \int_{-\infty}^{0}\int_{-\infty}^{0} F(u,v)\exp[j2\pi(ux+vy)]\,du\,dv \\
& + \int_{-\infty}^{0}\int_{0}^{\infty} F(u,v)\exp[j2\pi(ux+vy)]\,du\,dv \\
& + \int_{0}^{\infty}\int_{-\infty}^{0} F(u,v)\exp[j2\pi(ux+vy)]\,du\,dv \\
& + \int_{0}^{\infty}\int_{0}^{\infty} F(u,v)\exp[j2\pi(ux+vy)]\,du\,dv.
\end{aligned}
\tag{B4}
$$

By applying the change of variables $u = -s$, $v = -t$ to the third and fourth double integrals in (B4) and changing the directions of integration in the resultant integrals, the third double integral can be combined with the second and the fourth double integral can be combined with the first to produce

$$
\begin{aligned}
f(x,y) = & \int_{-\infty}^{0}\int_{-\infty}^{0} F(u,v)\exp[j2\pi(ux+vy)] + F(-u,-v)\exp[-j2\pi(ux+vy)]\,du\,dv \\
& + \int_{0}^{\infty}\int_{-\infty}^{0} F(u,v)\exp[j2\pi(ux+vy)] + F(-u,-v)\exp[-j2\pi(ux+vy)]\,du\,dv.
\end{aligned}
\tag{B5}
$$

which can be written as

$$
f(x,y) = \int_{-\infty}^{\infty}\int_{-\infty}^{0} F(u,v)\exp[j2\pi(ux+vy)] + F(-u,-v)\exp[-j2\pi(ux+vy)]\,du\,dv. \tag{B6}
$$

Moreover, $F(u,v)$ and $F(-u,-v)$ can be expressed in polar coordinates as

$$
F(u,v) = \left[F_{\mathrm{Re}}(u,v)^2 + F_{\mathrm{Im}}(u,v)^2\right]^{1/2}\exp[j\varphi_{F(u,v)}] = |F(u,v)|\exp[j\varphi_{F(u,v)}] \tag{B7}
$$

and

$$
F(-u,-v) = \left[F_{\mathrm{Re}}(u,v)^2 + F_{\mathrm{Im}}(u,v)^2\right]^{1/2}\exp[j\varphi_{F(-u,-v)}] = |F(u,v)|\exp[j\varphi_{F(-u,-v)}], \tag{B8}
$$

where $|F(u,v)| = \left[F_{Re}(u,v)^2 + F_{Im}(u,v)^2\right]^{1/2}$ is the magnitude of $F(u,v)$, $\varphi_{F(u,v)} = \arg[F(u,v); F_{Re}(u,v), F_{Im}(u,v)]$, $\varphi_{F(-u,-v)} = \arg[F(-u,-v); F_{Re}(-u,-v), F_{Im}(-u,-v)]$, and (B3) has been utilized.[B1] Since, from (B3), $\varphi_{F(-u,-v)} = \arg[F(-u,-v); F_{Re}(u,v), -F_{Im}(u,v)]$ and, thus, $\varphi_{F(-u,-v)} = -\varphi_{F(u,v)}$, (B8) can be written as

$$F(-u,-v) = |F(u,v)|\exp[-j\varphi_{F(u,v)}]. \tag{B9}$$

Inserting (B7) and (B9) into (B6) produces

$$f(x,y) = \int_{0}^{\infty}\int_{-\infty}^{\infty}|F(u,v)|\left(\exp\{j[2\pi(ux+vy)+\varphi_{F(u,v)}]\} + \exp\{-j[2\pi(ux+vy)+\varphi_{F(u,v)}]\}\right)dudv. \tag{B10}$$

Since $e^{\theta} + e^{-\theta} = 2\cos\theta$, (B10) simplifies to

$$f(x,y) = \int_{0}^{\infty}\int_{-\infty}^{\infty}2|F(u,v)|\cos[2\pi(ux+vy)+\varphi_{F(u,v)}]dudv. \tag{B11}$$

As in the one-dimensional case, an adjustment to (B11) is required. However, in contrast to the one-dimensional case where the adjustment was required only at a point, the adjustment here is required along the line $v = 0$. Because the behavior at the point $(u,v) = (0,0)$ is slightly different from the other points on this line, it is considered first. When the mean value of $f(x,y)$ is not equal to zero,

---

[B1] The representation of the argument function arg in the form $\arg[F(u,v); F_{Re}(u,v), F_{Im}(u,v)]$ means the argument of $F(u,v)$, which depends upon $F_{Re}(u,v)$ and $F_{Im}(u,v)$. The argument of $F(u,v)$ is the angle $\varphi_{F(u,v)}$ such that $|F(u,v)|\cos\varphi_{F(u,v)}$ is the real part of $F(u,v)$ and $|F(u,v)|\sin\varphi_{F(u,v)}$ is the imaginary part of $F(u,v)$; it is the angle in the complex plane that the vector, originating from zero and ending at $F(u,v)$, makes with the positive x-axis.

$$F(0,0)=\left(\int_{-\infty}^{\infty}\int_{-\infty}^{\infty}f(x,y)dxdy\Big/\int_{-\infty}^{\infty}\int_{-\infty}^{\infty}dxdy\right)\int_{-\infty}^{\infty}\int_{-\infty}^{\infty}dxdy=C_m\,{}^{2}\delta(0,0)$$ [the ratio of the integrals must be considered in the sense of a limit as the integration limits approach $\pm\infty$ while the Dirac distribution arises from the definition of the Dirac distribution and from the relation ${}^{2}\delta(u,v)=\delta(u)\delta(v)$ (Bracewell 2000, 74-106)]. Insertion of this result into (B1) produces $f(x,y)=C_m+\mathrm{OF}$, where OF represents the contribution from the other frequencies [other than the frequency (0,0)] and the sifting property of ${}^{2}\delta(x,y)$, $\int_{-\infty}^{\infty}\int_{-\infty}^{\infty}{}^{2}\delta(x-a,y-b)f(x,y)dx\,dy=f(a,b)$, has been applied. Insertion of this result into (B11), on the other hand, produces $f(x,y)=2C_m+\mathrm{OF}$. Consequently, the magnitude of the zero frequency component is too large by a factor of two when (B11) is used. The same problem arises for the other points along the line $v=0$. To illustrate this, consider the situation where the input is given by $f(x,y)=A_1\cos[2\pi(u_1x+v_1y)]$. In this case $F_{\mathrm{Re}}(u,v)=\frac{A_1}{2}\,{}^{2}\delta(u-u_1,v-v_1)+\frac{A_1}{2}\,{}^{2}\delta(u+u_1,v+v_1)$ and $F_{\mathrm{Im}}(v)=0$, which can be verified by insertion into (B1). When $v_1=0$, (B1) produces $f(x,y)=A_1\cos(2\pi u_1x)$ while (B11) produces $f(x,y)=2A_1\cos(2\pi u_1x)$, which is too large by a factor of two. Tests for points away from the line $v=0$ indicate that (B11) is correct for those points. Consequently, an adjusted form of (B11) that produces results consistent with (B1) is

$$f(x,y)=\int_{v=0}\int_{u=-\infty}^{u=\infty}\frac{2}{1+\delta^{0}(v)}|F(u,v)|\cos[2\pi(ux+vy)+\varphi_{F(u,v)}]dudv, \qquad \text{(B12)}$$

where $\delta^{(0)}(x)$ is defined as in Bracewell (2000, p. 87)

$$\delta^{(0)}(x) = \begin{cases} 0 & x \neq 0 \\ 1 & x = 0. \end{cases} \tag{B13}$$

The fundamental result of this analysis is that the real function $f(x, y)$ can be expressed in terms of the amplitudes $|F(u,v)| = \left[F_{\mathrm{Re}}(u,v)^2 + F_{\mathrm{Im}}(u,v)^2\right]^{1/2}$ and phases $\varphi_{F(u,v)} = \arg[F(u,v); F_{\mathrm{Re}}(u,v), F_{\mathrm{Im}}(u,v)]$ of the half-plane $(v \geq 0)$ Fourier coefficients.

Appendix C: The Classification and Quantification of Bulk Hydrometeor Fields Using Polarimetric Radar Data

The purpose is to acquaint the reader with polarimetric variables and with standard techniques that are used to classify and quantify bulk hydrometeor characteristics. The emphasis is upon polarimetric variables collected using the Cimarron radar (Zahrai and Zrnić 1993).

C.1 Polarimetric Variables Collected with the Cimarron Radar

The polarimetric variables collected using the Cimarron radar include Z_h, Z_{DR}, $|\rho_{hv}(0)|$, and ϕ_{dp}. The variable Z_h (dBZ) is the reflectivity factor at horizontal polarization (the polarization is determined by the electric component of the electromagnetic wave) and, since many radars utilize horizontally polarized waves, is the reflectivity factor that has customarily been used in meteorology. It is given by

$$Z_h = Z_h^{int} - \alpha_h(r) + OES \,, \tag{C1}$$

where Z_h^{int} is the intrinsic Z_h (depends only upon the properties of the scatterers in the radar resolution volume), $\alpha_h(r)$ is the two-way attenuation at horizontal polarization (a function of range r), and OES stands for other error sources. Provided that all of the scatterers are of the same thermodynamic phase and are small enough such that they behave as Rayleigh scatterers [$D_{eh}/\lambda \le 16$, where D_{eh} is the equivalent diameter of the hydrometeor for horizontally polarized waves and λ is the radar wavelength (Doviak and Zrnić 1993, p. 35)], Z_h^{int} is

$$Z_h^{int} = 10\log\left[\frac{\lambda^4}{\pi^5|K|^2}\int_{D_{min}}^{D_{max}}\sigma(D_{eq})N(D_{eq})dD_{eq}\right]. \quad \text{(C2)}$$

where $|K|^2$ is a factor related to the complex refractive index of the scatterers (~0.93 for liquid hydrometeors and ~0.18 for ice hydrometeors), $\sigma(D_{eq})$ is the backscattering cross section for horizontally polarized waves, and $N(D_{eq})$ is the hydrometeor size distribution. The attenuation $\alpha_h(r)$ is related to the one-way, specific attenuation at horizontal polarization A_h (dB km^{-1}) by

$$\alpha_h(r) = 2\int_0^r A_h(r')dr'. \quad \text{(C3)}$$

Because $\alpha_h(r)$ generally is not known, it is assumed to be zero when the radar equation is solved for Z_h and is thus a source of error. [Note that with polarimetric radars reasonable estimates of $\alpha_h(r)$ in rain can be obtained using ϕ_{DP} (Bringi et al. 1990)]. Other error sources (*OES*) include system noise, calibration errors, sidelobe contamination, and statistical uncertainty of the estimate (Doviak and Zrnić 1993, 54, 74-75, 197, 125-129).

The differential reflectivity Z_{DR} is equal to the difference, in dB, between Z_h and Z_v ($Z_{DR} = Z_h - Z_v$), with Z_v being the reflectivity factor at vertical polarization. Relations for Z_v are equivalent to those for Z_h [(C1)-(C3)], with subscript-*v*s replacing the subscript-*h*s. Differential reflectivity can be expressed as

$$Z_{DR} = Z_{DR}^{int} - \alpha_{dp}(r) + OES. \quad \text{(C4)}$$

where Z_{DR}^{int} is the intrinsic Z_{DR}, $\alpha_{dp}(r)$ is the two-way differential attenuation, and OES again stands for other error sources. The two-way differential attenuation $\alpha_{dp}(r)$ is related to the one-way, specific attenuations for horizontally and vertically polarized waves A_h and A_v through the relation

$$\alpha_{dp}(r) = 2\int_0^r [A_h(r') - A_v(r')]dr' = 2\int_0^r A_{dp}(r')dr', \qquad \text{(C5)}$$

where $A_{dp}(r)$ (dB km $^{-1}$) is the one-way, specific differential attenuation. As in the case for Z_h, $\alpha_{dp}(r)$ is not generally known and thus is a source of error in Z_{DR} estimates [if ϕ_{DP} is available, one can obtain reasonable estimates of $\alpha_{dp}(r)$ in rain (Bringi et al. 1990)]. Other error sources for Z_{DR} include system noise, mismatched main-lobe power patterns (Pointin et al. 1988), mismatched sidelobe power patterns, and statistical uncertainty in the estimate (Doviak and Zrnić 1993, 54, 197, 146-147).

The magnitude of the correlation coefficient at zero lag $|\rho_{hv}(0)|$ measures the magnitude of the correlation, at zero time lag, of returned horizontally and vertically polarized signals. It can be expressed as

$$|\rho_{hv}(0)| = |\rho_{hv}(0)|^{int} + ES, \qquad \text{(C6)}$$

where $|\rho_{hv}(0)|^{int}$ is the intrinsic $|\rho_{hv}(0)|$ and ES stands for error sources. Because $|\rho_{hv}(0)|$ depends upon power measurements, errors affecting Z_h and Z_v can also affect $|\rho_{hv}(0)|$. Balakrishnan and Zrnić (1990b) specifically noted the potential sidelobe contamination and low signal to noise ratios (SNRs) have for degrading the quality of $|\rho_{hv}(0)|$ measurements. Liu et al. (1994) illustrated the effects spectral shape, SNR,

phase noise (non-constant phases of transmitted waves), and the spatial phase pattern of the transmitted signal (primarily within the main lobe) have upon $|\rho_{hv}(0)|$. For the estimation method used with the Cimarron radar (Zahrai and Zrnić 1993), Liu et al. (1994) found that non-Gaussian spectra, low SNR (<20 dB), and high phase noise (≥ ~5°) can significantly degrade $|\rho_{hv}(0)|$.

The polarimetric variables discussed to this point depend upon backscattering properties of hydrometeors. The differential phase between returned horizontally and vertically polarized signals ϕ_{DP}, however, depends primarily upon forward scattering properties of hydrometeors. It can be expressed as

$$\phi_{DP} = \phi_{DP}^{sys} + \phi_{DP}^{m} + \delta + ES , \tag{C7}$$

where ϕ_{DP}^{sys} is the system, or initial ($r = 0$), ϕ_{DP}, ϕ_{DP}^{m} is the ϕ_{DP} owing to the intervening propagation medium between the radar and the sample volume, δ is the backscatter differential phase, and *ES* stands for error sources. The (two-way) differential phase ϕ_{DP}^{m} is related to the (one-way) intrinsic specific differential phase K_{DP}^{int} through the relation

$$\phi_{DP}^{m} = 2 \int_{r'=0}^{r} K_{DP}^{int}(r')dr' . \tag{C8}$$

The specific differential phase K_{DP} results from forward scattering by hydrometeors [depends upon hydrometeor properties, like oblateness (e.g., Jameson 1985)] and is very useful in rainfall estimation (e.g., Zrnić and Ryzhkov 1996). Consequently, ϕ_{DP} is typically measured so that estimates of K_{DP} can be obtained. The backscatter differential phase δ results from backscattering properties of hydrometeors and is

indicative of resonant scattering (e.g., Bringi et al. 1996). It can be estimated through iterative range filtering of ϕ_{DP} (Hubbert and Bringi 1995). Error sources for ϕ_{DP} include system noise (Sachidananda and Zrnić 1986), nonuniform beamfilling (Ryzhkov and Zrnić 1998), sidelobe contamination (Sachidnanda and Zrnić 1987), and statistical uncertainty of the estimate (Sachidananda and Zrnić 1986).

Within the meteorological community, the level of understanding of the processes that result in $|\rho_{hv}(0)|$ and K_{DP} is relatively low compared to that for Z_h, Z_v, and, thus, Z_{DR} (i.e., the transmitted wave produces electric dipoles in hydrometeors which then radiate electromagnetic energy back to the radar). For $|\rho_{hv}(0)|$, decorrelation, or the lack thereof, is what provides most of the useful information. In rain, $|\rho_{hv}(0)|$ is very high ($\geq$ ~0.97) (Doviak and Zrnić 1993, p. 271). Decreased correlation is expected for more diverse hydrometeor sizes, shapes, canting angles, and types as well as for increasing hail size and diversity of δ (Balakrishnan and Zrnić 1990b). Decreased $|\rho_{hv}(0)|$ values arise when the co-variation between backscatter fields for horizontally and vertically polarized waves decreases (i.e., when fluctuations in Z_h do not correspond as well to fluctuations in Z_v and vice-versa). As indicated earlier, the specific differential phase K_{DP} results from forward scattering by hydrometeors. Specifically, it results because the frequency of an electromagnetic wave is independent of the medium while the speed is not (the speed of an electromagnetic wave in a medium is smaller than in a vacuum). From the relation between wave speed v, frequency f, and wavelength λ, $v = \lambda f$, it is apparent that in a medium the wavelength must be smaller than in a vacuum. When, for instance, horizontally and vertically

polarized waves travel through hydrometeors whose major axes are in the horizontal plane (wider than they are tall), the horizontally polarized wave is slowed more than the vertically polarized wave and, thus, its wavelength is smaller than that of the vertically polarized wave. This results in the horizontally polarized wave having to go through more phase (more degrees) than the vertically polarized wave when traveling through these hydrometeors. The situation for hydrometeors whose major axes are in the vertical plane is just the opposite. This is the physical cause of the differential phase ϕ_{DP}^{m} and is what is typically measured using ϕ_{DP}.

C.2 Physical Bases for the Classification of Bulk Hydrometeor Types Using Polarimetric Radar Data

The determination of bulk hydrometeor types using radar has been a long-standing goal of meteorologists. With polarization diversity radars, this feat is much more attainable (Straka et al. 2000). Bulk hydrometeor types can be inferred using polarization diversity radars because of hydrometeor properties that result in identifiable polarimetric signatures. Straka et al. (2000) have provided a comprehensive review of this topic[C1]; herein the purpose is to provide a brief summary so as to acclimate the reader.

A balance between surface tension, aerodynamic pressure, and hydrostatic pressure results in raindrops having flattened equilibrium shapes (approximately oblate), with the degree of flattening (eccentricity) increasing with size (Beard and

[C1] Other principal works in this area include Liu and Chandrasekar (2000), Vivekanandan et al. (1999), Zrnić and Ryzhkov (1999), Straka (1996), Aubagnac and Zrnić (1995), Holler et al. (1994), Zrnić et al. (1993), Doviak and Zrnić (1993, 239-271), Hall et al. (1984), and Hall et al. (1980).

Chuang 1987).[C2] Moreover, raindrops tend to fall with their minor axes vertical. Because of their oblateness and preferred orientation, raindrops backscatter relatively more horizontally-polarized power than vertically-polarized power and thus produce positive Z_{DR} values [0.5 to 4.0 dB are likely values (Doviak and Zrnić 1993, 248-252, 271)]. In addition, the oblateness and preferred orientation of raindrops results in positive K_{DP} values [0 to 10^{-1} km^{-1} are likely values (Doviak and Zrnić 1993, p. 271)]. Modeling and observational studies (e.g., Balakrishnan and Zrnić 1990b) indicate that in pure rain $|\rho_{hv}(0)|$ values are high ($\geq$ ~0.97).

In contrast to raindrops, dry graupel and small ($D < 2$ cm) hail have irregular shapes and often tumble. As a consequence, they usually appear to be isotropic to the horizontal and vertical polarization states (Bringi et al. 1984). This, combined with decreased Z_{DR} sensitivity to shape for ice water relative to liquid water, results in Z_{DR} values for dry graupel and hail that are typically less than 1 dB (Herzegh and Jameson 1992). Observations have indicated that larger hailstones (those with equivolume diameters of ~1.5 cm or greater) can produce Z_{DR} values of -0.5 dB or less (e.g., Zrnić et al. 1993). Proposed explanations for these observations include hailstones that are falling with their major axes primarily vertical (e.g., Zrnić et al. 1993), resonant scattering from large (equivolume diameter greater than ~4.0 cm) hailstones whose major axes are primarily horizontal (e.g., Aydin and Zhao 1990), three-body scattering (Hubbert and Bringi 2000), and antenna illumination differences for horizontally and vertically polarized waves (e.g., Pointin et al. 1988). Owing to their relatively low

[C2] Beard and Chuang (1987) indicate that internal circulations and electric stress may also affect equilibrium raindrop shapes.

concentrations, near isotropy, and relatively weak dielectric constants, dry and wet[c3] graupel and hail produce small ($\leq \sim 1.5^{\circ}$ km^{-1}) K_{DP} values (Balakrishnan and Zrnić 1990a; Straka et al. 2000). Because of the relative smoothness of and lack of resonant scattering by graupel and small ($D < 2$ cm) hail, the amount of decorrelation resulting from these hydrometeors is expected to be limited [$|\rho_{hv}(0)| \geq \sim 0.92$] (Straka et al. 2000). Giant ($D > 4$ cm), wet hailstones with random canting angles can produce significant decorrelation [$\sim 0.6 \leq |\rho_{hv}(0)| \leq \sim 0.95$], while smaller ($\sim 2$ cm $\leq D \leq \sim 4$ cm), randomly oriented wet hailstones are expected to result in $\sim 0.88 \leq |\rho_{hv}(0)| \leq \sim 0.95$. Spongy hail with $D \approx 2$ cm can produce $|\rho_{hv}(0)| \approx 0.92$ while spongy hail with $D > \sim 4.3$ cm can result in $\sim 0.84 \leq |\rho_{hv}(0)| \leq \sim 0.96$. Moreover, giant hailstones, which can have relatively large (~0.1) protuberance-to-diameter ratios, can produce significant decorrelation [$|\rho_{hv}(0)| \approx 0.92$] (Balakrishnan and Zrnić 1990b).

Rain-hail-graupel mixtures and mixed-phase hydrometeors (e.g., melting graupel with ice-water cores and liquid-water shells) produce polarimetric signals that are often intermediate between the signals resulting from the individual hydrometeor species. Exceptions include Z_{DR} values resulting from melting graupel and small hail and $|\rho_{hv}(0)|$ values of mixtures. When graupel and small hail melt, both tori and shells (depending upon the degree of melting) of liquid water form around ice-water cores (Rasmussen et al. 1984b). Because the ice-water cores discourage breakup, these mixed-phase hydrometeors can have axis ratios comparable to those of the largest

[c3] Provided either the amount of melting is limited or the ice-particle is large ($D \geq \sim 1.5$ cm) so that water coatings are thin (Rasmussen et al. 1984b).

raindrops ($D \approx 0.8$ cm) and can thus produce very high (>5 dB) Z_{DR} values (Rasmussen et al. 1984b; Aydin and Zhao 1990; Ryzhkov and Zrnić 1995b). In mixtures, Balakrishnan and Zrnić (1990b) found that $|\rho_{hv}(0)|$ values can be significantly depressed (<0.95), especially when the returned powers from the different types of hydrometeors are comparable.

Because of their low densities and small dielectric constants, snow crystals and aggregates produce relatively weak polarimetric signals [$Z_{DR} \leq \sim 3\,dB$, although sometimes larger, $|\rho_{hv}(0)| \geq \sim 0.95$, except for wet crystals and aggregates (as low as 0.5), and $K_{DP} \leq \sim 1^{\circ}\,\mathrm{km}^{-1}$]. Much work remains to be done concerning the utilization of polarimetric radar data to infer properties of bulk snow-crystal and aggregate fields (Straka et al. 2000).

C.3 Estimation of Quantitative Bulk Hydrometeor Information

The Z_h, Z_{DR}, $|\rho_{hv}(0)|$, K_{DP}, and δ of bulk hydrometeor fields are, in themselves, quantitative information. For analysis, modeling, and other purposes, however, other types of quantitative information (e.g., rainrates, contents, fall velocities, etc.) are desired. A logical step in the estimation of these quantities is the determination, in hydrometeor mixtures, of the polarimetric values associated with the different hydrometeor types.

The hydrometeor mixture that has received the most intense scrutiny is the rather common rain-hail-graupel mixture. Two methods exist for separating the total reflectivity factor at horizontal polarization Z_h into those for rain Z_{hr} and hail (ice) Z_{hi}.

The first method was introduced by Golestani et al. (1989) and utilizes the reflectivity difference Z_{DP} (dBZ), which is defined as

$$Z_{DP} = 10\log(Z_{\eta} - Z_{\nu}) = 10\log|(Z_{hr} + Z_{ht}) - (Z_{vr} + Z_{vt})|. \qquad \text{(C9)}$$

In (C9) $Z_{\eta} > Z_{\nu}$, $Z_{\eta} = Z_{hr} + Z_{ht}$, $Z_{\nu} = Z_{vr} + Z_{vt}$, where Z_{vr} and Z_{vt} are the reflectivity factors at vertical polarization for rain and hail (ice), respectively, and the reflectivity factors have units of $mm^6\ m^{-3}$. By assuming that raindrop size distributions conform to the gamma distribution (Ulbrich 1983) and by varying the parameters thereof, Golestani et al. (1989) obtained the relation

$$Z_{hr}\,(\text{dBZ}) = a\,Z_{DP_r} + b, \qquad \text{(C10)}$$

where $Z_{DP_r}\,(\text{dBZ}) = 10\log(Z_{hr} - Z_{vr})$ is the Z_{DP} corresponding to rain and a and b are constants.[C4] Observations from regions dominated by rain have confirmed the validity of (C10) (Golestani et al. 1989; Meischner et al. 1991; Conway and Zrnić 1993; Carey and Rutledge 1996; Tong et al. 1998). With the key assumption that the ice-water hydrometeors are effectively isotropic with respect to reflectivity factor and thus that $Z_{ht} = Z_{vt}$, $Z_{DP} = Z_{DP_r}$ and through (C9) one can obtain Z_{hr} from Z_h and Z_v. With this, one can determine Z_{ht} (and Z_{vt} and Z_{vr}).

The second method for separating Z_h into Z_{hr} and Z_{ht} was introduced by Balakrishnan and Zrnić (1990a) and, as with Z_{DP}, depends upon the ice hydrometeors

---

[C4] From their rainfall observations Golestani et al. (1989) obtained $a = 0.84$ and $b = 13.0$ dB. Because Z_{DP} depends upon radar calibration, however, a and b may be different for each data set. Other published values of a and b include $a = 0.64$, $b = 14.73$ dB for $1 < Z_{DP} \le 20$ and $a = 0.87$, $b = 10.1$ dB for $20 < Z_{DP} < 52$ (Aydin and Giridhar 1992), $a = 0.88$, $b = 8.05$ dB (Conway and Zrnić 1993), $a = 0.91$, $b = 8.51$ dB (Carey and Rutledge 1996), and $a = 0.87$, $b = 7.85$ dB (Tong et al. 1998). The Aydin and Giridhar (1992) values are for C-band, while values from the others are for S-band. Aydin and Giridhar

being essentially isotropic with respect to horizontal and vertical polarization states. In this method, however, it is presumed that the ice hydrometeors do not affect K_{DP}. Utilization of K_{DP}-R and R-Z_{hr} relations, where R is rainrate, then produces an estimate of Z_{hr}. From the $R = 37.1(K_{DP})^{0.866}$ K_{DP}-R relation proposed by Sachidananda and Zrnić (1987) and the Marshall-Palmer $Z_{hr} = 200R^{1.6}$ R-Z_{hr} relation (Marshall et al. 1955), Balakrishnan and Zrnić (1990a) obtained

$$Z_{hr} = 64.840(K_{DP})^{1.356}, \tag{C11}$$

where Z_{hr} is in mm^6 m^{-3} and K_{DP} is in $^\circ$ km^{-1}. Methods for separating rain and hail-graupel contributions to $|\rho_{hv}(0)|$ have not been developed. On the other hand, since δ results from resonant scattering, it is expected to be negligible for S-band radars unless graupel or hail are present (Straka et al. 2000).

Other hydrometeor mixtures (e.g., graupel and snow crystals, snow crystals and aggregates, etc.) have not received as much attention as rain-hail-graupel mixtures. The separation of polarimetric values according to hydrometeor type may be more difficult for these mixtures because of forward- and back-scattering similarities of the constituent hydrometeors.

Among the bulk hydrometeor quantities desired are rate R (units of depth time^{-1}), content M (units of mass volume^{-1}), and fall velocity V (units of distance time^{-1}). Because of its tremendous hydrologic utility, a great deal of attention has been focused upon the use of polarimetric data to estimate R (e.g, Ryzhkov and Zrnić 1995a).

(1992) provide S-band values that are nearly equivalent to their C-band values, with $a = 0.64$, $b = 14.8$ dB for $1 < Z_{DR} \le 20$ and $a = 0.88$, $b = 10.0$ dB for $20 < Z_{DR} < 52$.

Relatively less attention has been given to other quantities, like M and V, although they have been considered (e.g., Conway and Zrnić 1993; Jameson and Caylor 1994; Ryzhkov and Zrnić 1995a; Ryzhkov et al. 1998). Straka et al. (2000) provide a comprehensive review of relations that can be used to estimate quantities like R, M, and V from polarimetric variables.

The relations between polarimetric variables and quantities like R, M, and V generally require assumptions concerning the hydrometeor size distributions. The most popular distributions are exponential (e.g., Marshall and Palmer 1948) and gamma (e.g., Ulbrich 1983).[5] Exponential distributions are four parameter distributions (minimum and maximum diameters D_{min} and D_{max}, intercept N_0, and slope Λ) while gamma distributions depend upon five parameters (minimum and maximum diameters D_{min} and D_{max}, intercept N_0, slope Λ, and shape parameter μ). With some very reasonable assumptions, parameters of exponential and gamma distributions can be estimated using polarimetric variables. The hydrometeor types of primary concern are rain and graupel/hail. For raindrops, $D_{min} \approx 0$ mm and $D_{max} \approx 8$ mm (Komabayasi et al. 1964). With knowledge of raindrop shape as a function of size (e.g., Beard and Chuang 1987), Z_h and Z_{DR} can be used to determine the remaining two parameters N_0 and Λ of the exponential distribution (Seliga and Bringi 1976; Seliga and Bringi 1978; Seliga et al. 1979). If instead it is assumed that the raindrops conform to the gamma distribution, then Z_h, Z_{DR}, and K_{DP} can be used to determine N_0, Λ, and μ (Aubagnac and Zrnić 1995). For graupel/hail, the Cheng and English (1983) exponential distribution [also

see Cheng et al. (1985)], in which the intercept and slope are related, has gained some acceptance. With assumptions concerning graupel/hail D_{min}, D_{max}, shape (e.g., spherical), and orientation, only one parameter, Z_h, is needed to determine the parameters of the Cheng-English distribution.

---

[65] Exponential and gamma distributions can be expressed as $N(D) = N_0 D^{\mu} \exp(-\Lambda D)$, where $N(D)$ is the number of drops of diameter D per unit volume per unit size interval, N_0 is the intercept, μ is the shape parameter, and Λ is the slope. In the exponential distribution, $\mu = 0$.

Appendix D: Reflectivity Factor of Snow, Graupel, and Hail (Ice/Air Mixtures) and of Melting Graupel and Hail (High Density Ice/Air Mixtures with a Water Coating)

The weather radar equation can be expressed as

$$\bar{P}(r_0) = \frac{C\eta}{r_0^2}, \tag{D1}$$

where $C = \frac{P_t g^2 g_r^2 \lambda^2 c\tau\pi\theta_1^2}{(4\pi)^3 (16\ln 2) l_s l^2}$ is a constant, η is the reflectivity, and r_0 is range. The reflectivity is

$$\eta = \int_{D_{min}}^{D_{max}} \sigma(D) N(D) dD, \tag{D2}$$

where D is diameter, D_{min} and D_{max} are the minimum and maximum particle diameters, respectively, σ is the backscattering cross section, and $N(D)$ is the size distribution. For spherical particles that are small relative to the radar wavelength such that Rayleigh scattering applies,[D1]

$$\sigma(D) = \frac{\pi^5}{\lambda^4} |K|^2 D^6, \tag{D3}$$

where λ is the radar wavelength, $K = (\varepsilon - 1)/(\varepsilon + 2)$, $\varepsilon = m^2$ is the dielectric constant, and $m = n - jn_K$ is the complex refractive index (Battan 1973, §4.5; Doviak and Zrnić 1993, p. 35). Inserting (D3) and (D2) into (D1), we have

[D1] The requirement for Rayleigh scattering by spherical, liquid-water drops is $D \le \lambda/16$ (e.g., Battan 1973, §4.7; Doviak and Zrnić 1993, p. 35), where λ is the radar wavelength. For spherical, solid-water (ice) hydrometeors, the requirement is $D \le \lambda/4$ (Battan 1973, §4.7; Jameson and Johnson 1990, p. 329).

$$Z = \int_{D_{min}}^{D_{max}} N(D) D^6 \, dD = \frac{\lambda^4 r_0^2 \overline{P}(r_0)}{\pi^5 C |K|^2}. \qquad \text{(D4)}$$

where Z is the reflectivity factor and it is assumed that all of the particles have the same K value. This works fine if we are dealing with hydrometeors that are all liquid water or that are all solid ice. If a hydrometeor is composed of a mixture (ice/air, water/ice, etc.), then determination (and definition) of Z is more complicated.

If a hydrometeor is composed of a mixture, its dielectric constant (and, thus, K) depends upon the relative amounts and dielectric constants of the materials in the mixture (Bohren and Battan 1980). As Bohren and Battan discuss, there are several functions for determining effective dielectric constants. They show that for ice/air mixtures, the Debye (1929) relation that estimates the ice/air mixture dielectric constant ε_{ia} as

$$\frac{\varepsilon_{ia} - 1}{\varepsilon_{ia} + 2} = \left(\frac{V_a}{V_a + V_i} \right) \left(\frac{\varepsilon_a - 1}{\varepsilon_a + 2} \right) + \left(\frac{V_i}{V_a + V_i} \right) \left(\frac{\varepsilon_i - 1}{\varepsilon_i + 2} \right). \qquad \text{(D5)}$$

where V is volume and subscript *as* and *is* indicate air and ice, respectively, performs well. [It does not generally perform well, however, for water/ice mixtures (Bohren and Battan 1980)]. Because $\varepsilon_a = 1$ [at a pressure of 1013.25 mb and temperature of 20 °C, $\varepsilon_a = 1.00059$ (Sears et al. 1987, p. 612)] while the real part of ε_i is about 3.168 (Battan 1973; §4.6), the first term on the rhs of (D5) can be neglected and

$$K_{ia} = \frac{\varepsilon_{ia} - 1}{\varepsilon_{ia} + 2} \approx \left(\frac{V_i}{V_a + V_i} \right) \left(\frac{\varepsilon_i - 1}{\varepsilon_i + 2} \right) = \left(\frac{V_i}{V_a + V_i} \right) K_i. \qquad \text{(D6)}$$

The backscattering cross section for an (assumed spherical) ice/air mixture particle is thus

$$\sigma_{ia}(D_{ia},\rho_{ia}) = \frac{\pi^5}{\lambda^4}|K_{ia}|^2 D_{ia}^6 = \frac{\pi^5}{\lambda^4}\left(\frac{V_i}{V_a + V_i}\right)^2 |K_i|^2 D_{ia}^6 . \tag{D7}$$

where ρ_{ia} is the density of the ice/air particle [$\rho_{ia} = (m_i + m_a)/(V_i + V_a)$, where m_i and m_a are the masses of the ice and air, respectively]. (The dependence of σ_{ia} upon D_{ia} and ρ_{ia} will soon become apparent.) Since a spherical shape is assumed, $D_{ia}^6 = \left(\frac{6}{\pi}\right)^2 (V_a + V_i)^2$ and

$$\sigma_{ia}(D_{ia},\rho_{ia}) = \frac{\pi^5}{\lambda^4}\left(\frac{6}{\pi}\right)^2 V_i^2 |K_i|^2 . \tag{D8}$$

This can be expressed in terms of D_i, the diameter of a sphere of (solid) ice having volume V_i. With $V_i = \frac{\pi}{6} D_i^3$, (D8) becomes

$$\sigma_{ia}(D_{ia},\rho_{ia}) = \frac{\pi^5}{\lambda^4}|K_{ia}|^2 D_{ia}^6 = \frac{\pi^5}{\lambda^4}|K_i|^2 D_i^6 . \tag{D9}$$

The backscattering cross section of an ice/air hydrometeor, therefore, is equal to the backscattering cross section of a spherical, solid-ice hydrometeor that occupies the same volume as the ice in the ice/air hydrometeor. [From the data of Gunn and East (1954), $|K_i|^2 = 0.176$, which agrees with the 0.18 value quoted by Doviak and Zrnić (1993, p. 36) and with the value quoted by Smith (1984).] The equi-ice-volume diameter D_i is related to D_{ia} and ρ_{ia} through

$$D_i^3 = \frac{D_{ia}^3(\rho_{ia} - \rho_a)}{(\rho_i - \rho_a)} \approx \frac{D_{ia}^3 \rho_{ia}}{\rho_i} , \tag{D10}$$

where ρ_i and ρ_a are the densities of ice and air, respectively. Calculations indicate that the approximation in (D10) is accurate to within roughly 2.5% of D_i^3 for extreme

conditions of $\rho_{ai} = 1.3$ kg m^{-3}, $\rho_i = 932.0$ kg m^{-3}, and $\rho_{mi} = 50.0$ kg m^{-3}. For $\rho_{mi} = 100.0$ kg m^{-3} and $\rho_{mi} = 500.0$ kg m^{-3}, the accuracies are 1.2% and 0.12%, respectively. It is noted that the approximation in (D10) corresponds to ignoring the mass of the air in the ice/air mixture.

In meteorology the convention is to define the reflectivity factor of ice/air hydrometeors as $Z_{mi} \equiv \int_{D} N(D_i) D_i^6 \, dD_i$ instead of as $\int_{D_{mi}} N(D_{mi}) D_{mi}^6 \, dD_{mi}$. This way, the variability of the dielectric constant is cast into the reflectivity factor and thus one dielectric constant (and, thus, one K) is used. This is similar to what is done with virtual temperature and the gas constant.

Marshall and Gunn (1952) introduced the idea of collapsing an ice hydrometeor into a sphere having a density of 1 g cm^{-3} (akin to melting the particle). Since the same mass of ice must be present whether the density is that of ice (0.92 g cm^{-3}) or 1 g cm^{-3}, $D_1^6 = \left(\frac{\rho_i}{\rho_1} \right)^2 D_i^6$, where $\rho_1 = 1$ g cm^{-3}. Inserting this into (D9),

$$\sigma_{mi}(D_{mi}, \rho_{mi}) = \frac{\pi^5}{\lambda^4} |K_{mi}|^2 D_{mi}^6 = \frac{\pi^5}{\lambda^4} |K_i|^2 \left(\frac{\rho_i}{\rho_1} \right)^2 D_1^6 . \qquad \text{(D11)}$$

The backscattering cross section of an ice/air hydrometeor, therefore, is also equal to the backscattering cross section of a spherical, solid-ice hydrometeor that has the same mass as the ice in the ice/air hydrometeor, a density of 1 g cm^{-3},[D2] and a K given by

[D2] The diameter of this fictitious ice hydrometeor is equal to that of the melted hydrometeor since it has the same mass as the ice in the ice/air hydrometeor and the density of liquid water.

$$K_{ai} = |K_i|^2 \left(\frac{\rho_i}{\rho_i} \right)^2 = 1.18 |K_i|^2 = 0.208 . \qquad \text{(D12)}$$

This K value is the same as that quoted by Smith (1984) and agrees with the value calculated using the $K_{ai}/\rho_{ai} \approx K_i/\rho_i = C_1$ (C_1 is a constant) approximation of Marshall and Gunn (1952) and the data from Gunn and East (1954).

Consequently, there are two possible definitions for the reflectivity factor of snow (and dry graupel and hail), $Z_{ai} \equiv \int_{D_{i,min}}^{D_{i,max}} N(D_i) D_i^6 \, dD_i$ and $Z_{ai1} \equiv \int_{D_{1,min}}^{D_{1,max}} N(D_1) D_1^6 \, dD_1$.

It seems that the Z_{ai} definition is preferable because it does not require the artifice of 1 g cm^{-3} ice. This artifice is useful in practice, however, since D_1 can be easily estimated by melting the ice/air hydrometeor. The determination of D_i is not as easy. For practical applications, one can determine D_1 and scale it by $(\rho_1/\rho_i)^2$ to determine D_i and thus Z_{ai} [thus, in (D11) the $(\rho_1/\rho_i)^2$ factor is associated with D_1 instead of with $|K_i|^2$].

For ice/air hydrometeors,

$$Z_{ai} = \int_{D_{i,min}}^{D_{i,max}} N(D_i) D_i^6 \, dD_i = \frac{\lambda^4 r_0^2 \bar{P}(r_0)}{\pi^5 C |K_i|^2} . \qquad \text{(D13)}$$

When data are collected using weather radars, λ, π, and C are known and r_0 and $\bar{P}(r_0)$ are measured. Since it is not known whether rain or snow (graupel, hail, etc.) is being observed, the $|K|^2 = 0.93 \equiv |K_w|^2$ value is typically assumed. Thus, one obtains an equivalent reflectivity factor Z_e defined by

$$Z_e = \frac{\lambda^4 r_0^2 \bar{P}(r_0)}{\pi^5 C |K_w|^2} = \frac{\lambda^4}{\pi^5 |K_w|^2} \eta . \tag{D14}$$

If all of the hydrometeors are ice/air mixtures, then

$$Z_{ia} = \int_{D=D_{ia,min}}^{D=D_{ia,max}} N(D_i) D_i^6 \, dD_i = \frac{|K_w|^2}{|K_i|^2} Z_e . \tag{D15}$$

For a mixture of liquid and ice/air hydrometeors,

$$Z_r + \frac{|K_i|^2}{|K_w|^2} Z_{ia} = Z_e , \tag{D16}$$

where Z_r is the reflectivity factor of rain.

It is noted that the above analysis is essentially drawn from Marshall and Gunn (1952) and Smith (1984). The purpose here was to combine relevant portions of their work into a cohesive exposition.

The situation for melting graupel and hail is more complex. The investigations of Kerker et al. (1951) and Herman and Battan (1961) indicate that relatively thin (~0.1 mm) water shells rapidly increase the backscattering cross sections of melting graupel and hail towards the values of liquid-water spheres of the same size. The results of Herman and Battan (1961) can be expressed as

$$\sigma_{ia,w}(D_{ia,w}, D_{sh}, \rho_{ia}) = \sigma_{ia}(D_{ia,w}, \rho_{ia}) + f\left[\sigma_w(D_{ia,w}) - \sigma_{ia}(D_{ia,w}, \rho_{ia})\right], \tag{D17}$$

where $\sigma_{ia,w}(D_{ia,w}, D_{sh}, \rho_{ia})$ is the backscattering cross section of a water-coated ice/air hydrometeor of diameter $D_{ia,w}$, D_{sh} is the thickness of the water shell, $\sigma_{ia}(D_{ia,w}, \rho_{ia})$ is the backscattering cross section of an ice/air hydrometeor having diameter $D_{ia,w}$ and density ρ_{ia}, $\sigma_w(D_{ia,w})$ is the backscattering cross section of a liquid hydrometeor having diameter $D_{ia,w}$, and f is the fractional backscattering cross section relative to the

difference in the backscattering cross sections of all liquid water and ρ_{ia}-density ice spheres of diameter $D_{ia,wt}$. In this context, then, the backscattering cross section of a water coated ice/air hydrometeor is expressed in terms of its diameter $D_{ia,wt}$. This depends upon the diameter and density of the initial ice/air hydrometeor D_{ia_init} and ρ_{ia} and upon D_{sh} through the relation

$$\rho_w D_{ia,wt}^3 + (\rho_{ia} - \rho_w)(D_{ia,wt} - D_{sh})^3 = \rho_{ia} D_{ia\_init}^3 . \qquad \text{(D18)}$$

where ρ_w is the density of liquid water. (If $D_{sh} << D_{ia,wt}$, then $D_{ia,wt} \approx D_{ia\_init}$.) The results of Herman and Battan (1961) indicate that for Rayleigh scatterers and a fixed radar wavelength the f in (D17) depends upon D_{sh} and weakly upon $D_{ia,wt}$. One caveat is that in past studies like those of Kerker et al. (1951) and Herman and Battan (1961) the melting graupel or hailstone was considered to be composed of solid ice. In (D17), an approximation that strictly holds for solid ice hydrometeors coated by water shells is extended to ice/air hydrometeors that are coated by water shells. This approach is believed to be valid since the transition from ice to liquid-water backscattering can be viewed as resulting from increasing shielding (by the liquid-water coat) of the ice from the incident radiation (Herman and Battan 1961). The same behavior is expected for ice/air hydrometeors covered by water shells, with the $|K|^2$ of the underlying material smaller owing to the presence of air. (Note that if the original ice/air hydrometeor is porous, then melt water will soak into the hydrometeor before collecting on the surface. In this case, the $|K|^2$ of the underlying hydrometeor is that of an ice/water mixture.)

The reflectivity of a mixture of liquid hydrometeors and water-coated ice/air hydrometeors is thus

$$\eta = \int_{D_{ice,min}}^{D_{ice,max}} \int_{D_{ice,min}}^{D_{ice,max}} \sigma_{ice,wet}(D_{ice,wet}, D_{ice}, \rho_{ice}) N(D_{ice,wet}) dD_{ice,wet} + \frac{\pi^5}{\lambda^4} |K_w|^2 Z_e \,. \qquad \text{(D19)}$$

With (D9), (D10), and (D14), (D19) becomes

$$Z_e = Z_e + \frac{|K_i|^2}{|K_w|^2} \int_{D_{ice,min}}^{D_{ice,max}} \int_{D_{ice,min}}^{D_{ice,max}} \left(\frac{\rho_{ice}}{\rho_w}\right)^2 (1-f) D_{ice,wet}^6 \, N(D_{ice,wet}) dD_{ice,wet} + \int_{D_{ice,min}}^{D_{ice,max}} f \, D_{ice,wet}^6 \, N(D_{ice,wet}) dD_{ice,wet} \,. \qquad \text{(D20)}$$